

THESIS

GEOLOGY OF THE FOOTWALL OF THE NORTHERN PLOMOSA MOUNTAINS  
METAMORPHIC CORE COMPLEX, WEST-CENTRAL ARIZONA

Submitted by

Evan Strickland

Department of Geosciences

In partial fulfillment of the requirements

For the Degree of Master of Science

Colorado State University

Fort Collins, Colorado

Fall 2017

Master's Committee:

Advisor: John Singleton

Jerry Magloughlin  
Rocky Coleman

Copyright by Evan Douglas Strickland 2017

All Rights Reserved

## ABSTRACT

### GEOLOGY OF THE FOOTWALL OF THE NORTHERN PLOMOSA MOUNTAINS METAMORPHIC CORE COMPLEX, WEST-CENTRAL ARIZONA

The northern Plomosa Mountains is a N-S trending range in the lower Colorado River Extensional Corridor, west-central Arizona – a region which hosts several highly extended terrains known as metamorphic core complexes. Metamorphic core complexes are characterized by low-angle normal faults (detachment faults) which have accommodated tens of kilometers of extension, and juxtapose a brittlely-deformed hanging wall against a ductilely-deformed footwall. The primary structural feature of the northern Plomosa Mountains is the Plomosa detachment fault, a gently-dipping low-angle normal fault. Though 1:24,000 scale geologic mapping had previously been conducted in the northern Plomosa Mountains, little work had been done in the metamorphic footwall of the Plomosa detachment fault, which was the focus of this study.

New 1:10,000-scale geologic mapping, structural and microstructural analysis, and U-Pb zircon geochronology reveals that the footwall of the Plomosa detachment fault is dominated by early Miocene mylonitic fabrics associated with detachment faulting, demonstrating that the northern Plomosa Mountains is a metamorphic core complex similar to adjacent core complexes in the region. Three mylonitic units dominate the footwall of the Plomosa Mountains core complex: 1) Orocopia Schist, 2) an early Miocene intrusive complex, and 3) gneiss. The quartzofeldspathic Orocopia Schist encompasses 10.5 km<sup>2</sup> of the northern Plomosa Mountains, and locally contains graphitic plagioclase

porphyroblasts, and coarse-grained green actinolite pods 0.2–1.5 m wide are scattered throughout the Orocopia Schist. These pods are high in Mg, Cr, and Ni, strongly suggesting derivation from an ultramafic protolith. A laterally continuous unit of amphibolite (~3.5 km long, 10–150 m thick), interpreted as Orocopia metabasalt, is localized along a moderately SE-dipping contact between the Orocopia Schist and the gneiss, and contains metachert layers 3–30 cm thick. L>S mylonitic fabrics are common throughout the Orocopia Schist and gneiss, and a zone of L-tectonites is localized along their contact. The Miocene intrusive complex, which is dominated by biotite granodiorite and hornblende diorite, parallels the detachment fault along its eastern margin, and the gneiss is corrugated about a NE-trending subhorizontal axis.

Mylonitic fabrics have systematic NE-SW-trending lineations (average T/P = [220/09]), and record top-to-the-NE shear. The Plomosa detachment fault defines a broad NE-trending corrugation parallel to its slip direction, and on average dips ~12° to the NE. NW-striking normal faults, joints, and dikes throughout the footwall record NE-SW extension consistent with that of the mylonitic fabrics, indicating there was no change in extension direction between the ductile and brittle regimes. Dynamically recrystallized quartz grain sizes and mechanisms suggest the gneiss and the Orocopia Schist underwent amphibolite-facies mylonitization, locally with evidence of overprinting by upper- to middle-greenschist-facies mylonitization, whereas the Miocene intrusive complex dominantly records upper- to middle-greenschist-facies mylonitization. Based on the geometry and deformation conditions of footwall fabrics, three separate mylonitic shear zones were identified: I) A pre-Miocene, originally moderately NE-dipping (~50°) normal-sense shear zone which deformed the corrugated gneiss. II) An originally shallowly NE-

dipping ( $\sim 25^\circ$ ) normal-displacement Miocene shear zone, active before initiation of the detachment fault, and which primarily deformed the Orocopia Schist and Miocene intrusive complex. III) A detachment-subparallel Miocene shear zone that deformed rocks adjacent to the Plomosa detachment fault. The Miocene intrusive complex was mylonitized prior to exhumation by the Plomosa detachment fault, suggesting that magmatism slightly predated or was coeval with initiation of detachment faulting.

U-Pb zircon geochronology of the Orocopia Schist reveals an abrupt drop-off of Th/U ratios  $>0.1$  at 68–70 Ma, which demarcates the maximum depositional age of the Schist. A high density of Th/U ratios  $<0.1$  between 75–50 Ma zircons record metamorphism of the Schist after it was subducted. Xenocrystic zircons in the Miocene intrusive complex have an identical distribution of ages and Th/U ratios as the Orocopia Schist, indicating that the Schist was melted or assimilated during early Miocene plutonism. The early Miocene pre-detachment paleo-depth of the top of the Orocopia Schist is 3–4 km, suggesting a Paleogene exhumation event brought the Schist to upper-crustal depths after it was subducted beneath the crust

Late-stage dextral and sinistral faults strike N and ENE, respectively, and associated barite and carbonate veins strike NE. These faults locally cut moderately-consolidated colluvium, and veins cut NW-striking joints and faults associated with detachment faulting. Together these structures record a minor phase of WNW-ESE extension, which is attributed to regional post-middle Miocene dextral faulting, with the northern Plomosa Mountains having occupied a transtensional step.

## ACKNOWLEDGEMENTS

First and foremost, I thank my advisor, Dr. John Singleton. I worked with John as an undergraduate prior to graduating in 2010, and he invited me to work with him again for my Master's degree. He was constantly involved in my project, pushed me to create the quality products that resulted, and personally made sure I completed on time. I also thank him and his family for inviting me into their home during my transition in living arrangements nearing the completion of this thesis and my degree.

I thank Andrew Griffin and Justin Hufford for their time conducting field work with me. Justin joined me for eight days in the Spring Break of 2016, and Andrew joined me for a month between October and November, 2016. Both are talented geologists who contributed many important observations.

I thank my committee members Jerry Magloughlin and Rocky Coleman for their time and input, and for the skills I learned from each of them which aided this project.

I give special thanks to Carl Jacobson and Gordon Haxel for their continued assistance throughout the project regarding the Orocopia Schist. They provided valuable discussion and insight to many of my interpretations.

I thank my friend Nikki Seymour, who was instrumental to my understanding and implementation of U-Pb zircon geochronology.

I thank the Arizona Geological Survey for hosting my geologic map on their website. Several AZGS geologists attended our two-day field trip to the northern Plomosa Mountains, including many other geologists, whom I give thanks for their time and interest.

Finally I thank my family, especially my parents, whom have supported me throughout my graduate career. They provided a peaceful work environment in our Austin, Texas home where I finished much of this thesis. I look forward to the opportunities I will find in Austin, where I will have the pleasure to again live close to home and spend time with them, as well as my older brother Colin and his wife Guin.

## TABLE OF CONTENTS

ABSTRACT .....	ii
ACKNOWLEDGEMENTS.....	v
LIST OF TABLES .....	xi
LIST OF FIGURES .....	xii
Introduction.....	1
1. Geologic Background.....	3
1.1. Metamorphic Core Complexes .....	3
1.2. Lower Colorado River Extensional Corridor.....	7
1.3. Northern Plomosa Mountains .....	12
1.4. Pelona-Orocopia-Rand schists .....	13
2. Previous Studies of the Northern Plomosa Mountains.....	16
Methods .....	18
3. Geologic Mapping.....	18
4. U-Pb Zircon and Geochemical Analyses .....	19
4.1 U-Pb zircon geochronology .....	19
4.1.1 Samples .....	19
4.1.2 Separation .....	20
4.1.3 Cathodoluminescence imaging.....	20
4.1.4 Laser ablation .....	20
4.2 Geochemistry.....	21
Results .....	22
5. Geologic Units.....	22
5.1. Orocopia Schist (KPGos) .....	22
5.2. Miocene Intrusive Complex (Nic) .....	36
5.3. Gneiss (KXgn) .....	43
5.4. Other units .....	47
5.4.1. Interlayered mylonitic quartzite and marble (MzPzq) .....	47
5.4.2. Nonmylonitic Miocene dikes (Nd).....	47



5.4.3. Miocene sedimentary units (Ncg).....	48
5.4.4. Pliocene to Quaternary(?) conglomerates (PlQcg) .....	49
5.4.5. Quaternary sediments (Qal, Qeol, Qoal) .....	49
6. Mineralization and Alteration .....	55
6.1. Syn-detachment mineralization and alteration.....	55
6.2. Post-detachment veining.....	62
7. Mylonitization and Metamorphism.....	64
7.1. Mylonitic fabric field observations.....	64
7.2. Mylonitic fabric microstructural observations .....	69
7.3. Mylonitization conditions .....	71
7.4. Metamorphic conditions.....	75
8. Structural Data.....	78
8.1. Metamorphic fabrics.....	78
8.1.1. Mylonitic foliations .....	78
8.1.2. Mylonitic lineations .....	79
8.1.3. Gneissic foliation in Orocopia metabasalt.....	83
8.1.4. Folded mylonitic fabric .....	83
8.2. Faults, joints, and dikes .....	84
8.2.1. Plomosa detachment fault .....	84
8.2.2. All other faults.....	85
8.2.3. Normal faults .....	85
8.2.4. Joints.....	85
8.2.5. Dikes .....	85
8.3. Barite and carbonate veins, and kinematically-related post-detachment faults .....	88
8.3.1. Barite veins.....	88
8.3.2. Carbonate veins .....	89
8.3.3. Post-detachment faults .....	89
9. U-Pb Zircon Geochronology.....	91
9.1. Orocopia Schist .....	91
9.2. Miocene intrusive complex.....	98

Discussion.....	104
10. The Northern Plomosa Mountains Metamorphic Core Complex.....	104
10.1. Geometry and kinematics of extension .....	104
10.2. Timing of mylonitization and extension .....	106
10.2.1. Early Miocene mylonitic fabrics .....	106
10.2.2. Synkinematic intrusions .....	106
10.2.3. Pre-Miocene mylonitic fabrics.....	107
10.3. Relationships of amphibolite- and greenschist-facies deformation fabrics .....	108
10.4. Possible origins of mylonitic fabrics .....	111
10.5. Geometric relationship of mylonitic fabrics and the Plomosa detachment fault	113
10.6. Three mylonitic shear zones .....	115
10.7. Relationship of Miocene intrusive complex to the Plomosa detachment fault ...	121
10.8. Implications of the Miocene intrusive complex .....	122
10.9. Topographic trends .....	124
10.10. Comparison of northern Plomosa Mountains to other core complexes in the LCREC .....	125
11. Orocopia Schist at the Northern Plomosa Mountains .....	129
11.1. Deposition, subduction, and metamorphism of the Orocopia Schist.....	129
11.2. Implications for emplacement of the Orocopia Schist .....	131
11.3. Xenocrystic zircons: Melting of Orocopia Schist?.....	134
12. Post-detachment Faulting and Barite Mineralization .....	138
12.1. Barite mineralization.....	138
12.2. Causes for post-detachment faulting and veining.....	139
Conclusions .....	143
References .....	147
Appendices .....	156
Appendix 1: Locations of thin section samples.....	156
Appendix 2: Thin section analysis spreadsheet.....	157
Appendix 3: Locations of geochronology samples .....	163
Appendix 4: Actinolite geochemical data .....	164
Appendix 5: Metabasalt and metachert geochemical data .....	165

Appendix 6: Zircon U-Pb weighted mean and tuff-zircon ages for igneous intrusions....	167
Appendix 7: Raw zircon U-Pb ages for intrusions .....	169
Appendix 8: Raw zircon U-Pb ages for Orocopia Schist.....	179
Appendix 9: CL Imagery of zircons from Orocopia Schist.....	205
Sample 15-5-P9 .....	205
Sample 1015-P57 .....	214
Sample 0316-P80a.....	223
Appendix 10: CL Imagery of zircons from Igneous Intrusions.....	235
Sample 0217-P43 .....	235
Sample 0217-P47 .....	239

## LIST OF TABLES

Table 1- Chemical formulas and ppm Ni and Cr for samples of actinolite .....	36
Table 2- Zircon U-Pb ages of intrusive samples.....	99

## LIST OF FIGURES

Figure 1- Location of map area for this study .....	2
Figure 2- Simplified geologic map of the lower Colorado River extensional corridor.....	2
Figure 3- Schematic cross-section of a metamorphic core complex.....	4
Figure 4- Distribution of metamorphic core complexes in the western U.S.....	5
Figure 5- Schematic cross-section of antithetic shears within a metamorphic core complex .....	5
Figure 6- Structural belts of the lower Colorado River extensional corridor .....	11
Figure 7- Distribution of Pelona-Orocopia-Rand schists .....	16
Figure 8- Simplified geologic map of the northern Plomosa Mountains.....	25
Figure 9- Cross-sections through the footwall of the Plomosa Mountains detachment fault .....	26
Figure 10- Photographs of Orocopia Schist .....	27
Figure 11- Photomicrographs of Orocopia Schist .....	28
Figure 12- Photographs and photomicrographs of features in Orocopia Schist .....	29
Figure 13- Photograph and photomicrographs of meta-arkose in Orocopia Schist .....	30
Figure 14- Photograph and photomicrographs of Orocopia metabasalt .....	31
Figure 15- Ternary ratios of Th, Hf, and Ta from Orocopia metabasalt .....	32
Figure 16- Photographs and photomicrographs of metachert.....	33
Figure 17- PAAS-normalized rare earth element spectra of metachert.....	34
Figure 18- Photographs and photomicrograph of actinolite.....	35
Figure 19- QAP ternary plot of samples of the Miocene intrusive complex .....	37
Figure 20- Photographs and photomicrographs of the Miocene intrusive complex .....	38
Figure 21- Photographs and photomicrographs of diorites.....	39
Figure 22- Photographs and photomicrographs of leucocratic intrusions .....	40
Figure 23- Photographs and photomicrographs of intrusions.....	41
Figure 24- Photographs and photomicrographs of intrusions in Orocopia Schist .....	42
Figure 25- Photographs of gneiss.....	45
Figure 26- Photomicrographs of gneiss.....	46

Figure 27- Photographs and photomicrographs of mylonitic quartzite and marble.....	51
Figure 28- Photographs and photomicrographs of postmylonitic dikes .....	52
Figure 29- Photographs of conglomerates and siltstone (unit Ncg) .....	53
Figure 30- Photographs of units PIQcg, Qoal, and Qoel .....	54
Figure 31- Degree of chloritization in the footwall of the Plomosa detachment fault .....	57
Figure 32- Degree of sericitization in the footwall of the Plomosa detachment fault .....	58
Figure 33- Photographs and photomicrographs of alteration in dikes vs Orocopia Schist ...	59
Figure 34- Photomicrographs of veins.....	60
Figure 35- Photographs of extension-related mineralization and alteration .....	61
Figure 36- Photographs of post-detachment veining.....	63
Figure 37- Photographs of foliation and lineation fabrics.....	66–67
Figure 38- Compilation map and cross-section of the northern Plomosa Mountains.....	68
Figure 39- Photomicrographs of mylonitic fabrics.....	70
Figure 40- Distribution of dynamically recrystallized quartz grain sizes and mechanisms .	73
Figure 41- Plot of modal % mica and quartz vs dynamically recrystallized quartz grain sizes.....	74
Figure 42- Plot of degree of chloritization vs dynamically recrystallized quartz grain sizes .....	77
Figure 43- Distribution of mylonitic foliations and lineations .....	80
Figure 44- Stereoplots of poles to mylonitic foliations.....	81
Figure 45- Stereoplots of mylonitic lineations .....	82
Figure 46- Stereoplots of gneissic foliations and fold axes of meter-scale folds .....	84
Figure 47- Stereoplots of faults.....	87
Figure 48- Stereoplots of joints and poles to dikes .....	88
Figure 49- Stereoplots of barite veins, carbonate veins, and post-detachment faults.....	90
Figure 50- Zircon U-Pb age density plots of Orocopia Schist.....	93
Figure 51- Zircon U-Pb age density plots of individual samples of Orocopia Schist.....	92–94
Figure 52- Plots of Th/U ratios vs age.....	95
Figure 53- CL-images of polished zircon grains for samples of Orocopia Schist.....	96–97
Figure 54- Plot of Th/U ratio vs age for zircon rims <5 $\mu\text{m}$ thick .....	98
Figure 55- Zircon U-Pb age density plots of two intrusive samples.....	100

Figure 56- Zircon U-Pb age density plots of Orocopia Schist and xenocrystic zircons .....	100
Figure 57- CL-images of polished zircons for two intrusive samples .....	103
Figure 58- Approximate early Miocene pre-detachment paleo-depths of the footwall of the Plomosa detachment fault.....	110
Figure 59- Three shear-zone domains interpreted in the footwall of the Plomosa detachment fault .....	118
Figure 60- Structural evolution cross-sections of the three mylonitic shear zones ...	119–120
Figure 61- Map of exposed mylonitic footwalls of metamorphic core complexes in the LCREC with the average slip direction of the detachment faults.....	128
Figure 62- Plot of Th/U ratios and ppm Ce vs age for a sample of Orocopia Schist.....	131
Figure 63- Plot of Th/U ratios vs age for an igneous sample with annotated hypothetical tectonic events .....	137
Figure 64- Plot of temperature vs weight % equivalent NaCl for barite from the Bouse Hills .....	139
Figure 65- Schematic illustration of transtension at the northern Plomosa Mountains.....	142

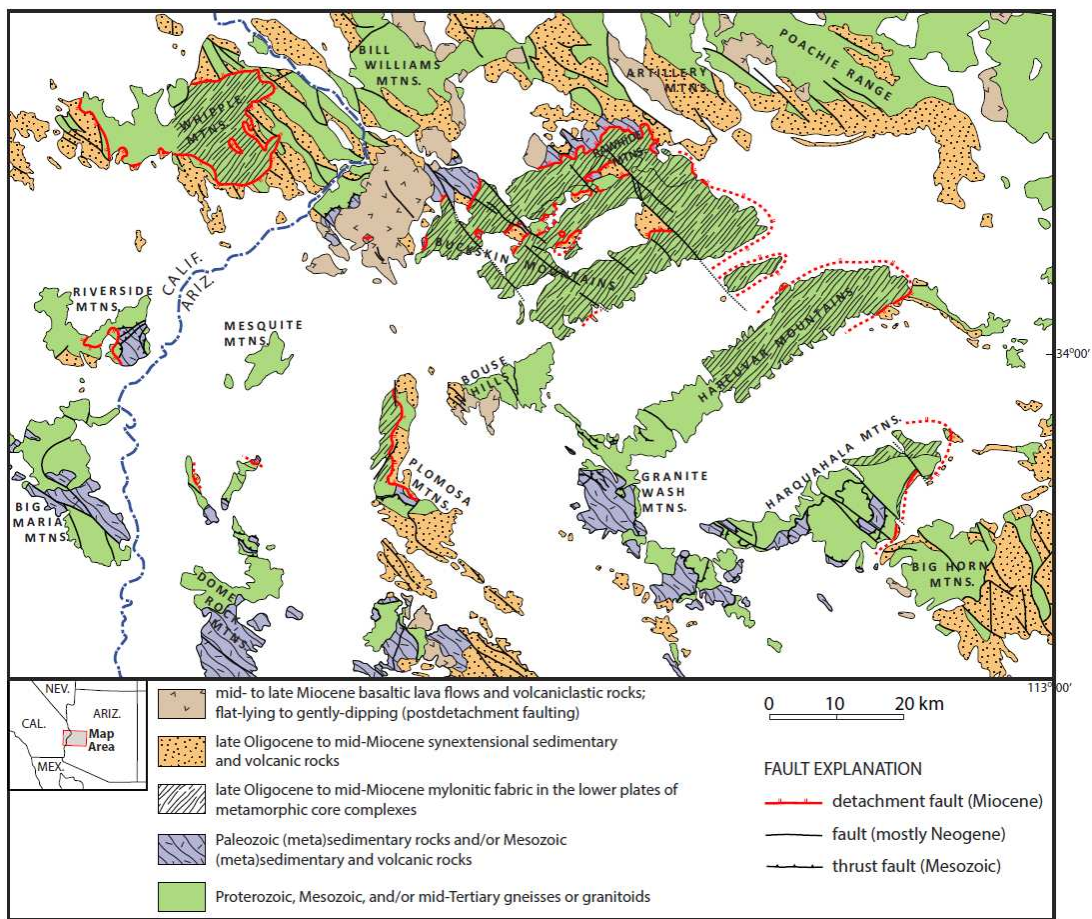
## Introduction

The northern Plomosa Mountains are a N-S trending range within the Basin and Range Province of Arizona (Figure 1), located in La Paz county, ~30 km SE of the town of Parker and immediately west of the town of Bouse. The primary structural feature of the northern Plomosa Mountains is the Plomosa detachment fault (Scarborough and Meader, 1983), a gently-dipping normal fault responsible for the exhumation of mid-crustal mylonitic rocks that comprise most of the footwall of the northern Plomosa Mountains metamorphic core complex (Figure 2). Though several workers have conducted geologic mapping in this area (Jemmett, 1966; Scarborough and Meader, 1983; Spencer et al., 2015), prior to this study no detailed mapping or significant structural analysis had been done within the mylonitic footwall, nor had the age of footwall fabrics been documented. The goal of this study is to better understand the deformation and metamorphic history of the northern Plomosa Mountains metamorphic core complex, which was accomplished through 1:10,000-scale geologic mapping, collection of structural measurements of both ductile and brittle features, and analysis of petrographic thin sections from samples collected across the footwall. In addition, zircon U-Pb geochronology was used to determine the age of footwall mylonitization and to understand the age and provenance of a quartzofeldspathic schist unit that dominates the northern half of the study area. This study was funded by the USGS EDMAP grant G16AC00142 and NSF Tectonics Program award 1557265 to J. Singleton.





**Figure 1:** Location of the map area for this study. Geologic province outlines are from Spencer and Reynolds (1989).



**Figure 2:** Simplified geologic and structural elements of the lower Colorado River extensional corridor. The northern Plomosa Mountains is located to the lower left of center. Modified from Singleton and Mosher (2012) (originally modified from Spencer and Reynolds 1989).

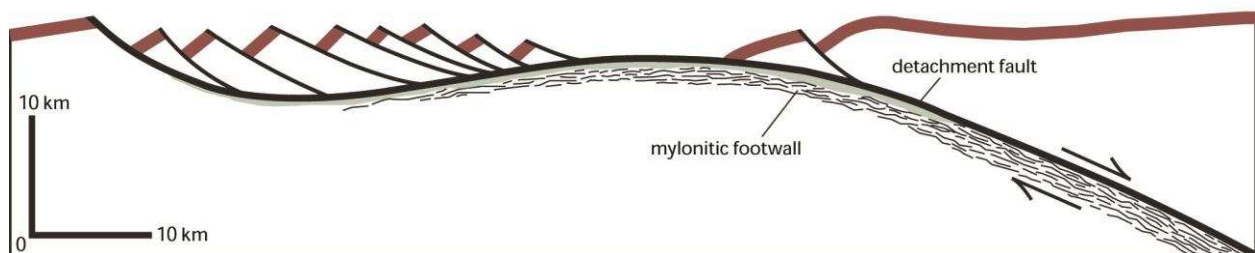
# 1. Geologic Background

## 1.1. Metamorphic Core Complexes

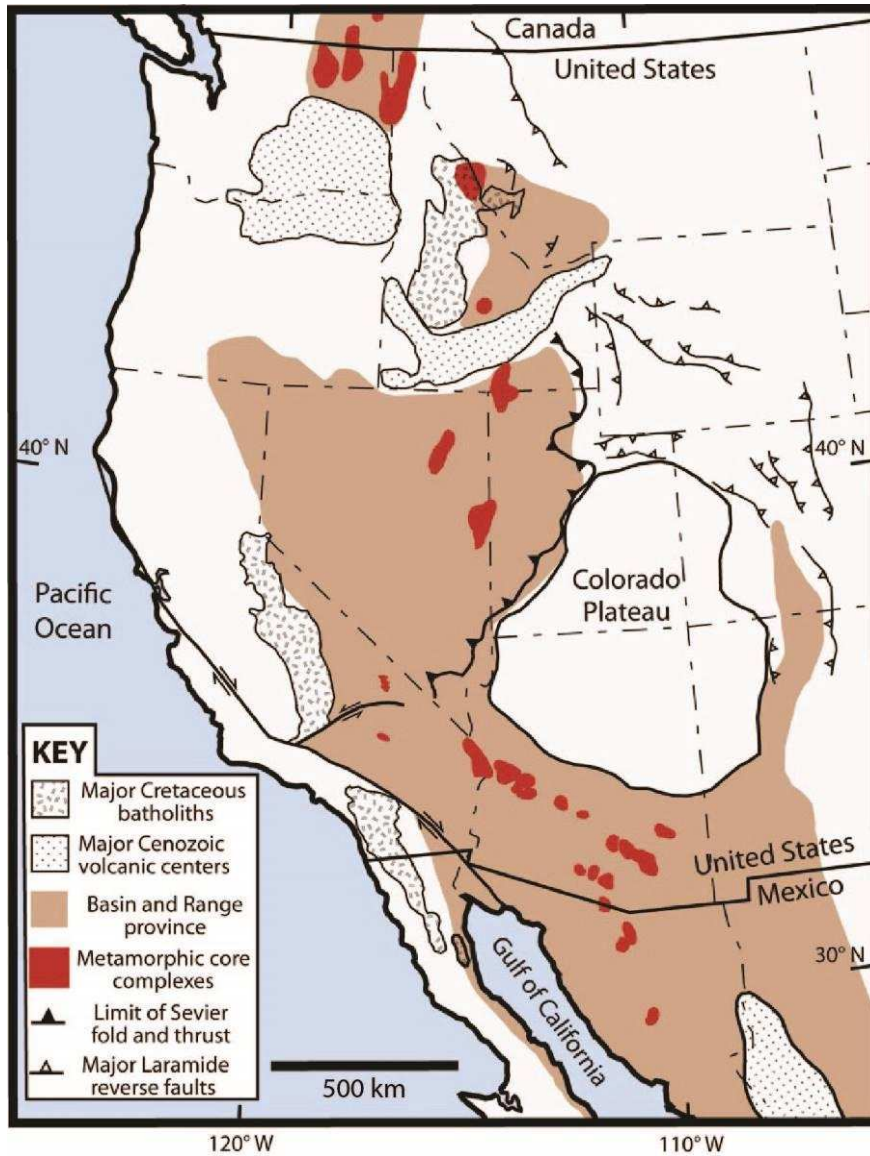
Metamorphic core complexes are terrains of large-magnitude extension (tens of kilometers) accommodated by low-angle ( $<30^\circ$ ), normal-offset detachment faults. In most core complexes detachment faults juxtapose mylonitized mid-to-lower-crustal rocks against upper-crustal rocks that have undergone intense brittle deformation and dissection by normal faults (Figure 3) (Lister and Davis, 1989). Western North America hosts many classic core complexes that form a discontinuous, sinuous belt extending from British Columbia to Sonora Mexico (Coney, 1978, 1980) (Figure 4). Confined within the Cordilleran orogen, Cordilleran metamorphic core complexes have diachronous formation ages that are predominantly Eocene north of the Snake River Plain, and Oligocene to Miocene south of the Plain (Coney 1978, 1980). Though they post-date Mesozoic shortening, north of Arizona, Cordilleran core complexes consistently lie immediately west of the front of the Mesozoic Sevier folds and thrusts. To explain the association between Mesozoic contraction and associated crustal thickening with Cenozoic extension, Coney and Harms (1984) proposed the crustal welt hypothesis, which states that major continental extension is driven by gravitational collapse of locally over-thickened crust (crustal welts) that develop during orogenesis.

A popular model for the evolution of metamorphic core complexes involves a low-angle detachment fault (though perhaps high-angle near surface) that cuts down into the mid-to-lower crust and soles into a near-horizontal mylonitic shear zone that records a sense of shear parallel to the detachment slip direction (e.g. Lister and Davis, 1989, Singleton and Mosher, 2012). As the mylonitic shear zone is exhumed to the brittle regime,

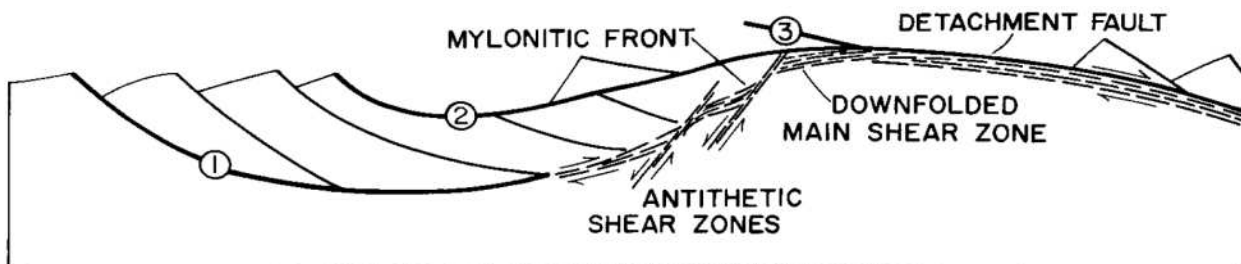
deformation is localized along the detachment fault, beneath which mylonitic fabrics are locally overprinted by cataclastic deformation and intense chloritic alteration (e.g. Davis et al., 1986). Additionally, the detachment fault may incise into the footwall or excise into the hanging wall, creating more complicated relationships than shown in Figure 3 (Lister and Davis, 1989). Another important concept for the development of core complexes (illustrated in Figure 3) is footwall arching via isostatic rebound in response to removal of the overlying hanging wall, resulting in a broadly folded mylonitic shear zone with a fold axis trending perpendicular to the displacement direction. Reynolds and Lister (1990) documented the association of folded mylonitic shear zones with antithetic shears (shears with oppositely directed normal displacement than the overall normal displacement) that occur near the back-dipping mylonitic front (Figure 5). Because these antithetic shears formed during the late-stage of mylonitization, Reynolds and Lister (1990) concluded that the arching of the mylonitic shear zones occurs when the shear zone is dragged through the brittle-ductile transition.



**Figure 3:** A schematic cross-section of a metamorphic core complex. From Singleton and Mosher (2012).



**Figure 4:** Distribution of metamorphic core complexes and other structural elements in the western U.S. Modified from Wong and Gans (2008).



**Figure 5:** A schematic cross-section of antithetic shears within a metamorphic core complex. From Reynolds and Lister (1990).

Another common feature of metamorphic core complexes is the corrugated geometries of their detachment faults and underlying mylonitic fabrics. These corrugations are particularly pronounced in the Buckskin-Rawhide and Harcuvar Mountains, just NE of the northern Plomosa Mountains (Figure 2), which have nearly horizontal, NE-trending corrugation axes approximately parallel to the direction of extension. Based on observations in the central Mojave metamorphic core complex, Fletcher and Bartley (1994) proposed a model where corrugations form in response to non-coaxial constrictional strain during mylonitization, and they suggest that because corrugations are common throughout core complexes, constrictional strain may also be a common result of large-magnitude extension. Singleton (2013) documented constrictional strain in the Buckskin-Rawhide Mountains in the form of L>S tectonites within a homogenous Miocene mylonitic granitoid (the Swansea Plutonic Suite), and upright meter- and kilometer-scale folds in well-layered pre-Tertiary rocks of the lower plate, similar to what was observed by Fletcher and Bartley (1994) in the central Mojave. However, Singleton (2013) proposed that the corrugations in the Buckskin-Rawhide core complex are late-stage features because of the observation that most lower-plate folding occurred by post-mylonitic flexural slip in the well-layered rocks. Another model proposed to explain corrugations is the “continuous casting” model by Spencer (1999), which states that corrugations are imprinted onto the plastically deforming footwall by initially corrugated detachment faults.

Metamorphic core complexes in southeastern California and southwestern Arizona are commonly associated with synmylonitic igneous intrusions (e.g. in the South Mountains, Reynolds, 1986, the Buckskin-Rawhide Mountains, Bryant and Wooden, 2008, Whipple Mountains, Gans and Gentry, 2016), though their exact temporal relationships

remain debated. Coney and Harms (1984) state that their proposed crustal welts would have remained stable until post-Laramide magmatism lowered the viscosity of the crust, suggesting that large-magnitude extension initiated in response to magmatism. Spencer et al. (1995) agree with the crustal welt hypothesis, concluding that extension in southwestern Arizona initiated in response to magmatism, and that the local magnitude and duration of extension was primarily controlled by preexisting crustal thickness and topography. Also, Lister and Baldwin (1993) state that there are strong spatial and temporal associations of shear zones with intruded igneous bodies in core complexes, and that viewing ductile deformation as a response to plutonic activity may better explain documented pulses of ductile shearing.

## **1.2. Lower Colorado River Extensional Corridor**

The northern Plomosa Mountains are located within the lower Colorado River Extensional Corridor (LCREC), a tilt-domain of the southern Basin and Range Province (Figures 2 and 5) (Howard and John, 1987). Late Oligocene to Miocene extensional deformation within the Basin and Range province of Arizona was accomplished by low-angle normal faults associated with metamorphic core complexes and high-angle normal faults that form the typical basin-and-range topography (Spencer and Reynolds, 1989). Within Arizona, low-angle normal faulting accommodated NE-SW directed extension (Zoback et al, 1981; Spencer and Reynolds, 1991), and kinematic data from the Buckskin-Rawhide Mountains indicate that near the end of detachment faulting the extension direction rotated clockwise from NE-SW to ENE-WNW and E-W, with E-W extension accommodated primarily by NE-dipping dextral and oblique dextral-normal faults (Singleton, 2015). The clockwise rotation in extension direction is attributed to the

superposition of dextral shear from the San Andreas fault system onto the Basin and Range extensional system (Singleton, 2015).

The LCREC is divided into several structural belts as described by Spencer and Reynolds (1990a) (Figure 6). The southwestern-most belt of extension (labeled B in Figure 6) in which the northern Plomosa Mountains lies is described as a “synformal keel of extended upper-plate rocks separated from the [southerly] adjacent unextended area by a breakaway fault” (Spencer and Reynolds, 1990a). To the northeast is a belt of metamorphic core complexes (labeled C) which includes the Chemehuevi Mountains, Whipple Mountains, Buckskin-Rawhide Mountains, and Harcuvar Mountains. The northeastern-most extensional domain of the LCREC is an extended wedge of hanging wall rocks (labeled D) which lie structurally above low-angle detachment faults, and grades into a region of large fault blocks (labeled E) bounded by high-angle normal faults (Spencer and Reynolds, 1990a). Mylonitic crystalline rocks of the Whipple Mountains, Buckskin-Rawhide Mountains, and Harcuvar Mountains metamorphic core complexes (extensional belt C in Figure 6) comprise the footwall of the regionally extensive Whipple-Buckskin-Rawhide-Bullard detachment fault system. This detachment fault system is estimated to have accommodated 40–60 km of NE-directed extension, having exhumed rocks from 10–15 km depth (Spencer and Reynolds, 1991; Singleton et al., 2014; Prior et al., 2016). Mylonitic rocks in the footwall have well-developed stretching lineations trending 040–060 and record top-to-the-NE shear parallel to the detachment fault slip direction (Spencer and Reynolds, 1989; Singleton, 2015). Extension along these core complexes initiated in the early Miocene and ended prior to the late Miocene (Spencer and Reynolds, 1989), and low-temperature thermochronology and geochronology conducted by Singleton et al. 2014

indicate that slip on the Buckskin detachment fault system initiated between ~21–20 Ma and continued until ~12–11 Ma, with a spatially variable time-average slip rate of ~2–6 km/Myr.

The extensional belts of the LCREC trend SE and overlap an E-W trending zone of Cretaceous shortening known as the Maria fold-and-thrust belt (MFTB) (Reynolds et al., 1986) (Figure 6). Thrusts of the MFTB primarily verge SW, S, or SE, away from the North American craton (Reynolds et al., 1986; Laubach et al., 1989; Spencer and Reynolds, 1990a), in contrast to the rest of the ~N-S-trending Cordillera where thrusts typically verge towards the craton. The MFTB is also characterized by large-scale ENE- to E-trending south-facing folds (Reynolds et al., 1986). Deformation in the MFTB was commonly ductile in nature. For example, in the Granite Wash Mountains (just east of the northern Plomosa Mountains) the Hercules thrust zone was active under greenschist facies metamorphic conditions (Laubach et al., 1989), and the Tyson thrust in the Dome Rock Mountains (just southwest of the northern Plomosa Mountains) has mylonitized Proterozoic Gneiss in the hanging wall (Boettcher and Mosher, 1989).

An explanation for the anomalous E-W to ENE-WNW trend of the MFTB proposed by Dickinson and Lawton (2001) and Spencer and Reynolds (1990a) is that the MFTB may have activated along a failed rift of the Bisbee-McCoy basin, which formed in the Late Jurassic presumably in response to slab-roll back of the Farallon Plate (Decelles, 2004). Coincidentally, where the MFTB is cross-cut by the extensional belts of the LCREC, the trends of the extensional belts and exposures of metamorphic core complexes along the Cordilleran orogen change from N-S trending to WNW-ESE trending. An explanation for the coincidence between the change in orientation of extensional belts at the intersection of



the MFTB is that the orientation of the LCREC may have been primarily controlled by the orientation of a crustal welt that formed from Mesozoic shortening along the MFTB (Spencer and Reynolds, 1990a). Interestingly, evidence for Cretaceous gravitational collapse of a crustal welt may be recorded in the Dome Rock Mountains, where Boettcher and Mosher (1998) documented ductile thrust zones that were reactivated as NE-directed normal-sense shear zones shortly after (0–10 million years) peak metamorphism in the Late Cretaceous. Recent geo/thermochronology and microstructural studies suggest that latest Cretaceous to early Paleogene NE-directed normal-sense shear zones are also present in the Harcuvar Mountains and Buckskin-Rawhide Mountains (Wong et al., 2013; Singleton and Wong, 2016).



### **1.3. Northern Plomosa Mountains**

Within the study area, the bedrock geology of the northern Plomosa Mountains consists primarily of hanging wall sedimentary, metasedimentary, volcanic, and granitic rocks juxtaposed along the Plomosa detachment fault against footwall metamorphic rocks. Most Miocene sedimentary and volcanic rocks were deposited in syn-extensional basins that formed between rotating fault blocks in the dissected hanging wall of the Plomosa detachment fault. Pre-Cenozoic hanging wall rocks have also undergone complex faulting prior to Miocene extension (Spencer et al. 2015), and sedimentary and volcanic rocks of the upper-plate host mid-Miocene Au-Cu mineral deposits of the Northern Plomosa Mineral District, which included twelve small mines that operated in the first half of 20<sup>th</sup> century extracting copper ore (up to 7.6% Cu) with minor gold and silver (Duncan, 1990). The Plomosa detachment fault is the middle of three imbricate low-angle detachment fault systems that were active during the early to middle Miocene in west-central Arizona (Spencer and Reynolds, 1991). Based on tectonic reconstructions, the Plomosa detachment fault accommodated ~15–30 km of NE-directed extension, whereas the Buckskin-Rawhide detachment fault (the structurally highest of the three imbricate detachment faults) accommodated up to 60 km of extension (Spencer and Reynolds 1991). Apatite and zircon fission-track dates suggest that the footwall of the Plomosa detachment fault was exhumed between 23–15 Ma, similar to the initiation and end of detachment faulting of nearby core complexes (Foster and Spencer, 1992).

Approximately 3.5 km south of the study area is the Cretaceous Plomosa Pass thrust zone, a portion of the MFTB comprised of N- and NE-verging thrust faults and mylonite zones, and E- and SE-trending folds within Paleozoic to Mesozoic sedimentary units

(Spencer and Reynolds, 2015). The largest structure in this zone is the NE-vergent Deadman thrust, which bounds a mylonite zone up to ~500 m thick (Scarborough and Meader, 1983; Steinke, 1997).  $^{40}\text{Ar}/^{39}\text{Ar}$  thermochronologic data from the Plomosa Pass area document a period of Cretaceous to Miocene cooling at the Plomosa Mountains (Knapp and Heizler, 1990). Based on this data, Knapp and Heizler (1990) concluded that there was a period of regional heating in the Late Cretaceous, slow cooling during the early Tertiary, and rapid cooling in the late Oligocene to early Miocene. In addition, they inferred that partial resetting of K-feldspar in the northern Plomosa Mountains may have been caused by a renewed heating event during Tertiary detachment faulting.

#### **1.4. Pelona-Orocopia-Rand schists**

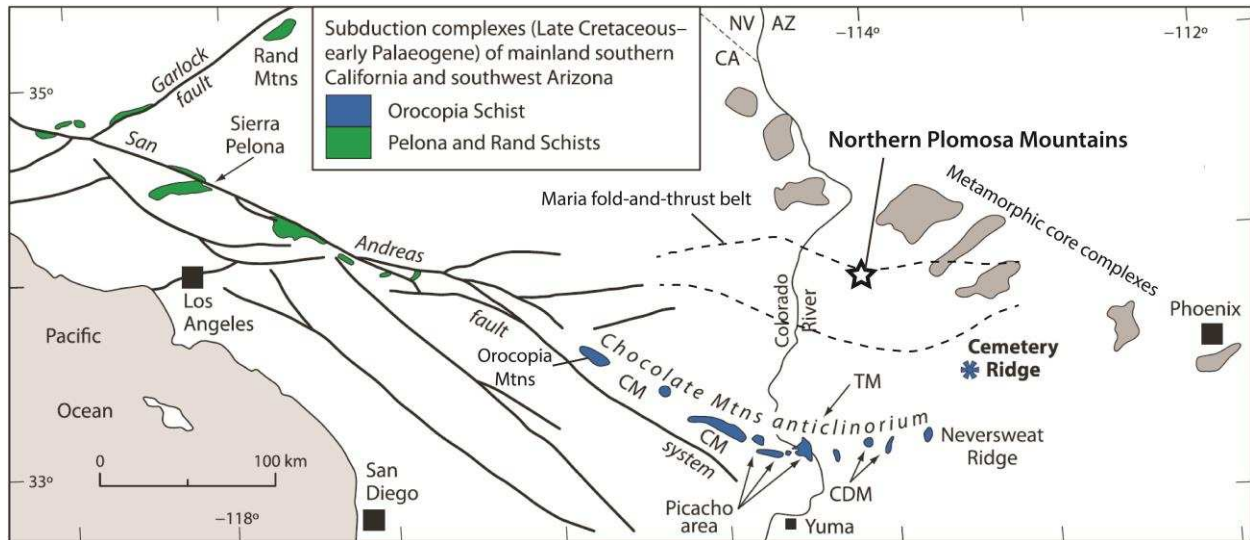
An exposure of Orocopia Schist was recently discovered at Cemetery Ridge in SW Arizona, ~70 km SE of the northern Plomosa Mountains (Haxel et al., 2014). Because the emplacement of the Pelona-Orocopia-Rand (POR) schists of southeastern California and southwestern Arizona (Figure 7) was a wide-spread tectonic event, the close proximity of the new exposure of Orocopia Schist to the northern Plomosa Mountains warrants their discussion. The POR schists are interpreted as Late-Cretaceous to early Paleogene metamorphosed trench sediments (Jacobson et al., 2000) subducted during the Laramide Orogeny and likely accreted beneath the lower continental crust during slab flattening of a segment of the Farallon plate (Saleeby, 2003). The recognition of POR schists as exhumed subduction complexes occurred nearly 50 years ago (Crowell, 1968; Yeats, 1968), yet the exposure of Orocopia Schist at Cemetery Ridge was not discovered until over 40 years later (Haxel et al., 2014). The POR schists are intriguing because they were exhumed over 100 km inland from the oceanic trench (Jacobson et al., 2000), whereas the likely correlative

Franciscan assemblages, a Cretaceous accretionary complex of deformed greywackes, shales, and exotic blocks, crop-out in the Coast Ranges and Great Valley of California, in close proximity to the paleo-oceanic trench (Taliaferro, 1943; Ernst, 1970; Chapman et al., 2016).

The Orocochia Schist comprises the bodies of POR schists nearest to the Plomosa Mountains (Figure 7), and is thought to have a younger depositional age than the Pelona and Rand Schists in southern California (Barth et al., 2003; Grove et al., 2003, 2008; Jacobson et al., 2011, Chapman et al., 2013, 2016; Dumitru et al., 2016). Characteristics of the Orocochia Schist include the quartzofeldspathic nature of the schist itself, the inclusion of porphyroblasts of graphitic albite within the schist, and the association of the Orocochia schist with metabasalt (amphibolite), ferromanganiferous metachert (quartzite), siliceous marble, and layers, lenses, and/or pods of coarse-grained actinolite-talc rock and talc-actinolite schist scattered in minor quantities (Haxel and Dillon, 1978; Haxel et al., 2002). The interpretation of oceanic origins for the Orocochia Schist, metabasalt, and metachert is supported by geochemical evidence; bulk major element composition of the Orocochia Schist is similar to unmetamorphosed graywacke (Haxel et al., 1987), ratios of immobile key trace elements of the metabasalt are similar to normal- to enriched-type MORB, and metachert generally has a negative cerium (Ce) anomaly, characteristic of seawater and many oceanic nondetrital sedimentary rocks (Haxel et al., 2002). The Orocochia Schist at Cemetery Ridge of SW Arizona (Figure 7) is unique because of its extreme inboard location compared to other POR schist localities (~300 km from the paleo-continental margin), and by the inclusion of numerous large blocks ( $\leq 300$  m) of variably serpentinized mantle peridotite, which is often rimmed by metasomatic rock of actinolite (Haxel et al., 2014). The

rims of metasomatic actinolite around ultramafic rock at Cemetery Ridge are identical to actinolite found as pods scattered throughout other Orocopia Schist localities, revealing that the scattered actinolite pods are likely also metasomatized ultramafic rocks. Another similarity between exposures of Pelona and Orocopia Schist is they have been exhumed along normal faults and are typically juxtaposed against gneissic and granitic rock (Haxel and Dillon, 1978).

Detailed thermochronologic studies of Orocopia Schist at the Gavilan Hills (Picacho area in Figure 7) and Orocopia Mountains revealed two distinct periods of rapid cooling which took place during the Eocene and latest Oligocene to early Miocene (Jacobson et al., 2002, 2007), leading to the inference that the Orocopia Schist has undergone two phases of exhumation. Chapman (2016) summarizes explanations for the Eocene cooling event into four models. The first two models are the “isostasy” model (Jacobson et al., 1996, 2007) and the “passive roof thrust” model (Yin, 2002) which involve schist rising from the subduction channel through the lower crust at the location they are currently exhumed. The second two models are the “Extrusion” model (Chapman, 2010) and the “Return Flow” model (Cloos, 1982) which involve schist migrating in the subduction channel back towards the oceanic trench. The second cooling event is accepted to be the result of exhumation of the schist to the surface or near surface along normal faults.



**Figure 7:** Locations of POR schists in southeast California and southwest Arizona. Modified from Haxel et al. (2014). Maria fold-and-thrust belt outline from Spencer and Reynolds (1990a).

## 2. Previous Studies of the Northern Plomosa Mountains

The first comprehensive geologic study of the northern Plomosa Mountains was by Jemmett (1966) who assessed the stratigraphy, faulting, and mineralization in the area. He identified a group of “younger” metamorphic rocks, which make up the footwall of the Plomosa detachment fault, and described the unit as predominantly gneiss in the southern portion, and schist toward the north, which agrees with the results of this most recent mapping.

Scarborough & Meader (1983) conducted reconnaissance mapping of the northern Plomosa Mountains. They described the metamorphic footwall as predominantly compositionally layered gneisses, and they interpreted several NE-trending folds based on sparse measurements of metamorphic fabrics. They also inferred the Plomosa detachment fault and its footwall to be arched along a large NE-trending antiform, the axis of which they projected just north of the Plomosa Pass area.

Duncan (1990) conducted a detailed study of the mineralization and alteration in the Northern Plomosa district, an economic-mineralized area in the hanging-wall of the Plomosa detachment fault just NNE of this study area. Duncan (1990) determined the sequence of extension-related mineralization and alteration in the hanging wall Tertiary units, including pervasive potassium metasomatism, and he suggested that a late-stage rejuvenation of mineralizing fluids and increase in temperature were possibly due to an unidentified igneous source. He also noted that samples of barite from the footwall of the Plomosa detachment fault have different sulfur isotope values than the barite in the hanging wall, suggesting at least two sources of sulfate.

Spencer et al. (2015) present the most comprehensive geologic map of the northern Plomosa Mountains, which includes detailed stratigraphy and structures of the hanging wall. This map was the first to describe the northern Plomosa Mountains as a metamorphic core complex, although it includes little detail of the footwall mylonitic units and structures, which was the motivation of our study.

Additional work in the Plomosa Mountains conducted south of our study area includes mapping by Miller (1970) and Miller and Mckee (1971) who documented thrust and strike-slip faulting in the southern two-thirds of the Plomosa Mountains, and Steinke (1997) who produced a detailed geologic map the Plomosa Pass area, including a portion of the Deadman thrust mylonite zone and complex Cretaceous folds that mostly trend NW-SE.



## Methods

### 3. Geologic Mapping

Geologic mapping of the mylonitic footwall of the northern Plomosa Mountains was conducted at a scale of 1:10,000, and the units Qal, Qeol, Qoal, and Nic<sub>a</sub> were mapped primarily via aerial imagery (Plate 1: Geologic Map of the Northern Plomosa Mountains Metamorphic Core Complex, Arizona – available as supplemental file). Jeep trails provide access to the eastern side of the range from the town of Bouse. My field work for this study totaled ~48 days spread out between October 2015 and November 2016. Justin Hufford served as a field assistant during a week in March 2016, and Andrew Griffin served as a field assistant for over a month from October through November 2016. Dr. Singleton helped define the scope of the project and aided in mapping and sample collection numerous times throughout the project. A review of the geologic mapping took place during a two-day field trip in early November 2016 which was attended by geologists Jon Spencer, Stephen Reynolds, Sue Beard, Brad Johnson, Charles Ferguson, Gordon Haxel, Carl Jacobson, and others.

The locations of observations and measurements were recorded with a hand-held GPS, and geolocated in ArcGIS allowing for quick analysis of spatial patterns. GPS locations, contours, and imagery were exported from ArcGIS and imported into Adobe Illustrator for digitization of the final geologic map.

The primary objectives of this study were to map distinct units in the mylonitic footwall, and to collect and map structural data including orientations of mylonitic foliations and lineations, the sense of shear, the orientations and kinematics of brittle

faults, and the orientations of joints and veins. A secondary objective was to document mineralization in the area and the structural controls on mineralization. Additionally, thin sections were created for 85 samples across the footwall of the Plomosa detachment fault (Appendices 1 and 2), and a variety of rock types were collected to characterize the mylonitic units. The degree of chloritization and sericitization, and the dynamic recrystallization mechanisms and sizes of dynamically recrystallized quartz were determined where possible. The degree of chloritization was defined simply as the modal percent of chlorite relative to biotite. The degree of sericitization was purely qualitative, based on my impression of whether sericitization was weak, moderate, strong, or intense. The size of dynamically recrystallized quartz was estimated optically, and samples were categorized into average quartz grain-size bins defined as <20  $\mu\text{m}$ , 20-70  $\mu\text{m}$ , 70-120  $\mu\text{m}$ , 120-200  $\mu\text{m}$ , and >200  $\mu\text{m}$ .

## **4. U-Pb Zircon and Geochemical Analyses**

### **4.1 U-Pb zircon geochronology**

#### ***4.1.1 Samples***

U-Pb zircon ages were determined for 12 samples (Appendix 3); seven samples of mylonitic quartzofeldspathic schist, five mylonitic to protomylonitic granodiorite/quartz diorite intrusions, and one nonmylonitic diorite intrusion. Approximately 30–50 zircons were analyzed for each of the intrusions. For the mylonitic schist, ~110–140 zircons were analyzed for each sample, yielding a robust age distribution to compare with detrital zircon ages from other schists in the region, namely the Pelona-Orocopia-Rand schists of southeastern California and southwestern Arizona (Jacobson et al. 1996).

#### ***4.1.2 Separation***

Zircons were separated for each sample by the following steps: 1) Samples were crushed using a jaw-crusher, 2) crushed samples were sieved below 850  $\mu\text{m}$ , 3)  $<850 \mu\text{m}$  samples were mixed with water, and the clay-sized particles were poured out, 4) the samples were further sieved to  $<300 \mu\text{m}$  and panned to concentrate denser minerals, 5) magnetic minerals were removed utilizing a Frantz operating to a maximum of  $\sim 1.7$  amps, 6) the remaining non-magnetic minerals underwent density separation in MEI heavy liquid. This last step usually yielded a high concentration of zircons.

#### ***4.1.3 Cathodoluminescence imaging***

Zircons for five samples (three quartzofeldspathic schists, and two intrusions) were mounted in epoxy and polished to expose a cross-section of their rims and cores. The polished mounts were imaged utilizing cathodoluminescence (CL) on an SEM. This imaging allowed for direct targeting of the rims and cores of individual samples during laser ablation. Three schist samples (15-5-P9, 1015-P57, and 0316-P80a) were imaged by Martin Wong at Colgate University, and two intrusive samples (0217-P43 and 0217-P47) were imaged at the USGS facility in Denver, Colorado, by Nikki Seymour and the author.

#### ***4.1.4 Laser ablation***

U-Pb zircon ages of the samples were determined at the Laser Ablation ICPMS lab at the University of Texas at Austin, run by Dr. Daniel Stockli. Reduction of the data was done by Nikki Seymour, a Ph.D. candidate at Colorado State University. The resulting age data were analyzed in Isoplot (Ludwig, 2003), and detrital zircon age distributions were created with Density Plotter (Vermeesch, 2012).

For the polished samples, 30  $\mu\text{m}$ -wide laser ablation spots were targeted for cores and 20  $\mu\text{m}$  spots were targeted for rims. The remaining samples were analyzed using the laser ablation depth-profiling method developed by the lab of Dr. Stockli. In this method, unpolished zircons on tape mounts are ablated through their outer rim into the core producing a depth vs. age profile. During reduction of the data, distinct periods of zircon growth can be identified and reported as separate ages. For some of the schist samples this technique allowed for the determination of U-Pb ages of very thin metamorphic rims, commonly  $<4 \mu\text{m}$  thick.

## **4.2 Geochemistry**

Three samples of actinolite were processed for whole rock geochemical XRF analysis by ALS minerals (Appendix 4). Four samples of amphibolite and five samples of quartzite were processed by Gordon Haxel and analyzed by AGAT Labs via XRF for major elements, and sinter and acid dissolution for trace and rare-earth elements (Appendix 5).

# Results

## 5. Geologic Units

This section addresses the key units identified in the footwall of the Plomosa detachment fault, for which there are three dominant units: 1) Orocopia Schist (unit KPGos), 2) a Miocene intrusive complex (unit Nic), and 3) gneiss (unit KXgn) (Plate 1; Figures 8 and 9).

### 5.1. Orocopia Schist (KPGos)

The predominant unit of the northern half of the field area is a mylonitic quartzofeldspathic schist (unit KPGos), which was determined to be the Orocopia Schist by field observations and U-Pb zircon ages (presented in the section “U-Pb Zircon Geochronology”). Figures 10 and 11 are photos and photomicrographs of Orocopia Schist from the northern Plomosa Mountains. The Orocopia Schist most often crops out as gray flaggy layers with well-developed cm-scale layering, or is homogenous with a purple-red color, and commonly has very well developed S-C fabric. The mineralogy is dominantly quartz (26–50%) and plagioclase (24–50%), with biotite (8–34%, variably chloritized), locally muscovite (2–20%, generally ~10%), minor opaque minerals (up to 4%, mostly graphite), accessory apatite (up to 1%), rutile, zircon, and local accessory garnet (up to 0.5%). Muscovite is locally not present in the schist, though it is the most ubiquitous identifier of this unit, as intrusions of the unit Nic may often look similar but mostly lack significant muscovite. Locally there are 0.1–2 m-thick packages of actinolite-bearing schist, which appears golden and flaky (Figure 12 A & B). In plane-polarized light, the biotite is typically brown to reddish brown and may even be red, and rutile needles are common in

areas where biotite has retrograded into chlorite (Figure 12 C & D). 2–50 cm thick milky quartz lenses/pods, and quartz-feldspar veins with up to ~10% feldspar are common throughout the Orocopia Schist (Figure 12 E & F). Locally the unit contains gray metasandstone layers, 10–30 cm thick, that have <10% total mica, and >60% feldspar (Figure 13).

Five hallmarks of the Orocopia Schist as described by Haxel and Dillon (1978) are present in the schist of the northern Plomosa Mountains:

1) The dominantly quartzofeldspathic composition and gray flaggy appearance of the schist in the northern Plomosa Mountains is consistent with that of the Orocopia Schist.

2) Poikiloblastic graphitic plagioclase porphyroblasts as described by Haxel and Dillon (1978) are widespread throughout the schist in the field area (Figures 10 E & F, and 11 C & D). They are generally 1–5 mm in size, and have a dark gray color, locally with a bluish tint. A foliation defined by graphite is preserved within the porphyroblasts of some samples as observed in thin section. The presence of graphitic plagioclase is a key identifier of Orocopia Schist in the field area.

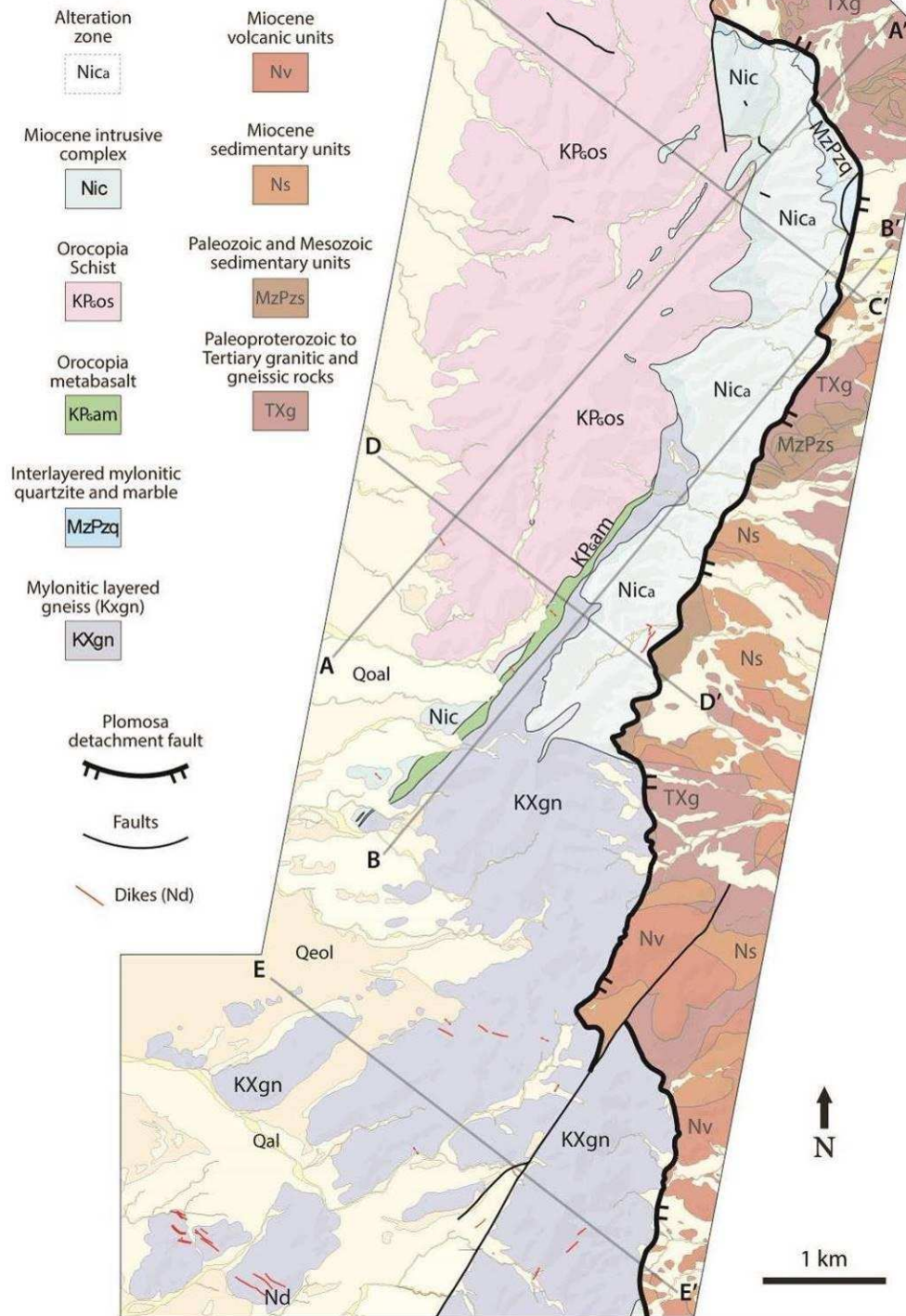
3) A ~4 km long layered unit of amphibolite interlayered with Orocopia Schist occupies the central field area (unit KPGam) (Figure 8 and 14; Plate 1). This unit is similar to amphibolite layers observed in Orocopia Schist of other localities, which are generally interpreted as metamorphosed basalt, consistent with geochemical analysis of four samples from the northern Plomosa Mountains (Figure 15)

4) Quartzite layers 3–30 cm thick with small (~0.5 mm) reddish-orange Mn-rich garnets are common within unit KPGam (Plate 1). The quartzite is generally weathered to a rusty red color, though some outcrops have clear alternating white and dark gray layers

(Figure 16), and is commonly observed to be ductily deformed and folded within unit KPGam (Figure 14 A). Garnets also locally appear as masses within the quartzite (Figure 16 F). The quartzite is interpreted as metachert (e.g. Haxel and Dillon, 1978), which is supported by the geochemical analysis of five samples from the northern Plomosa Mountains (Figure 17).

5) Scattered pods of coarse-grained green magnesian actinolite, 5 cm to 1.5 m wide, are present in the schist (Figure 18); locally, several smaller pods may be aligned parallel to the trend of mylonitic lineations. ~0.1–2 m-thick layers of actinolite-bearing schist with minor talc and rare talc schist commonly include actinolite pods within them. In one location, a ~40 cm-wide tabular body of the actinolite is present (Figure 16 F). Whole-rock geochemical analyses of three samples of the green actinolite indicate a Mg/(Mg+Fe) ratio of 0.84–0.88, 413–1290 ppm Ni, and 1580–2330 ppm Cr (Table 1), suggesting an ultramafic protolith (e.g. Oze et al., 2004). Recent work by Haxel et al. (2014) demonstrated that the actinolite at Cemetery Ridge in Arizona, and likely of all POR schists, is derived from peridotite, consistent with the geochemistry of the samples in the northern Plomosa Mountains, and they suggest the Mg-rich peridotite was metasomatized to actinolite by the interaction with Ca-bearing fluids from the schist (e.g. Harlow and Sorensen, 2005).

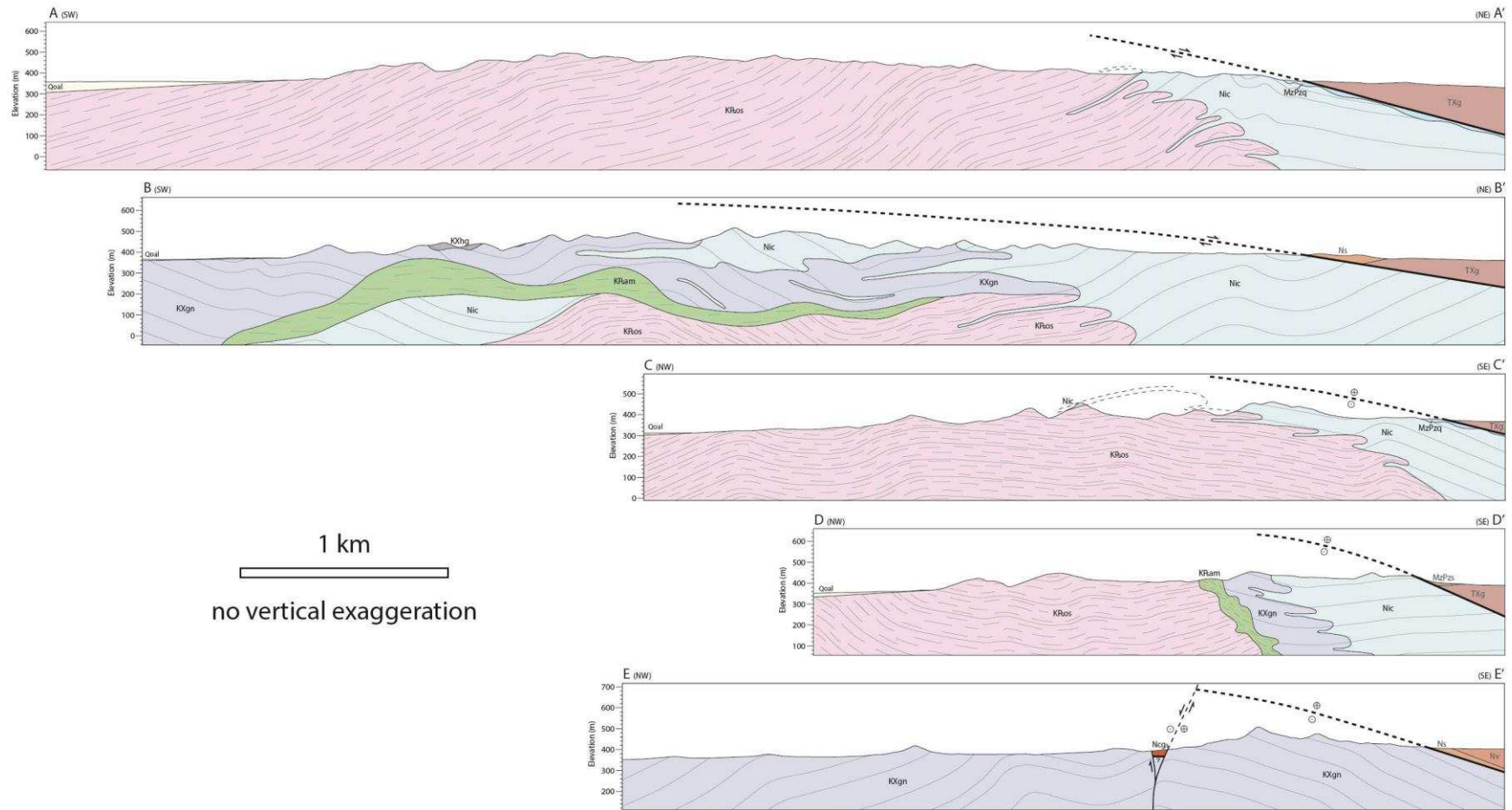
Simplified geologic map of the northern Plomosa Mountains  
(results of this study)



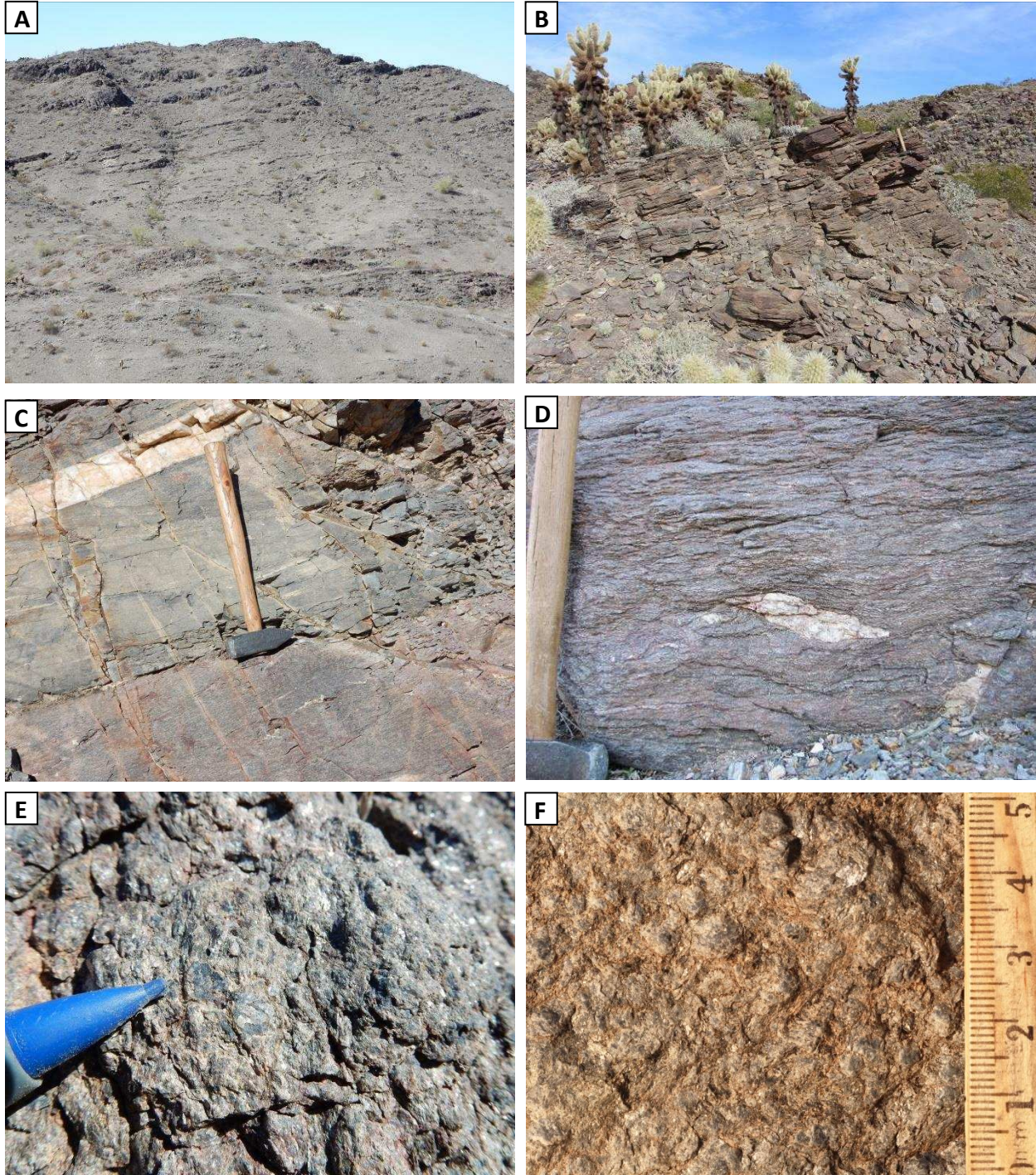
**Figure 8:** Simplified geologic map of the northern Plomosa Mountains. Units in the left-hand column are the results of this study. Units in the right-hand column are simplified from the geologic map of Spencer et al. 2015.



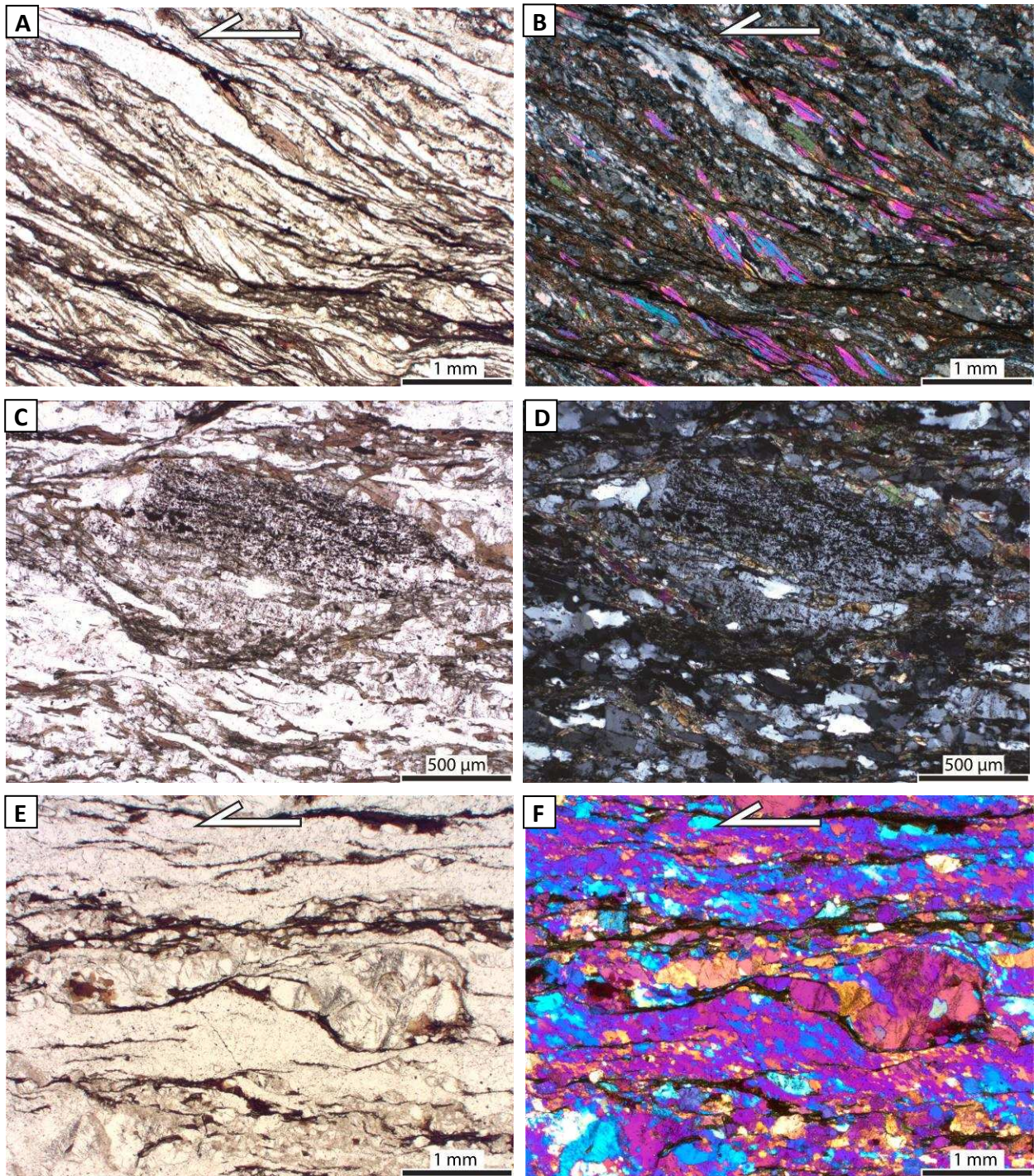
# Cross-sections through the footwall of the Plomosa Mountains detachment fault



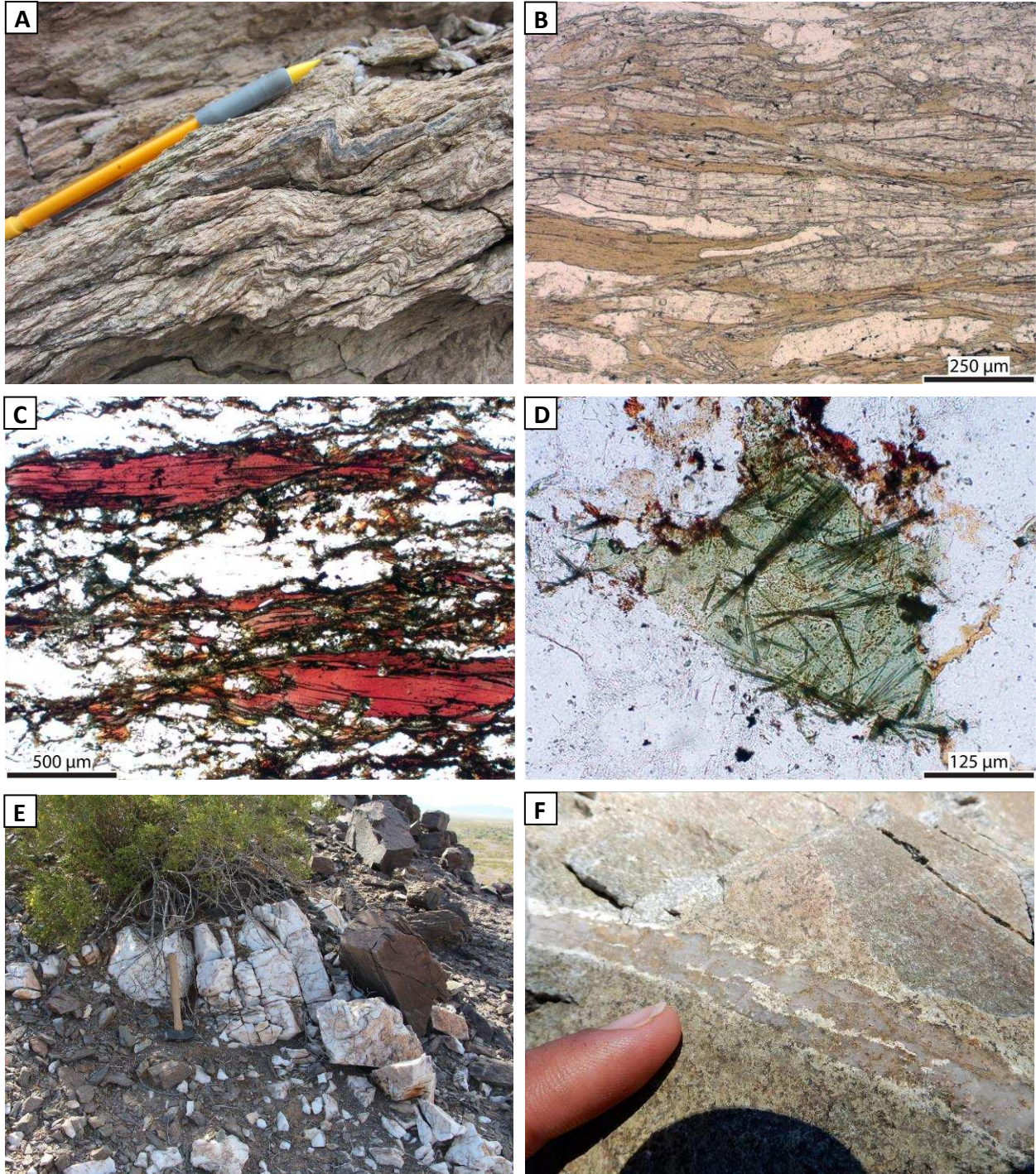
**Figure 9:** Cross-sections through the footwall of the Plomosa detachment fault. Cross-section lines are shown in Figure 8.



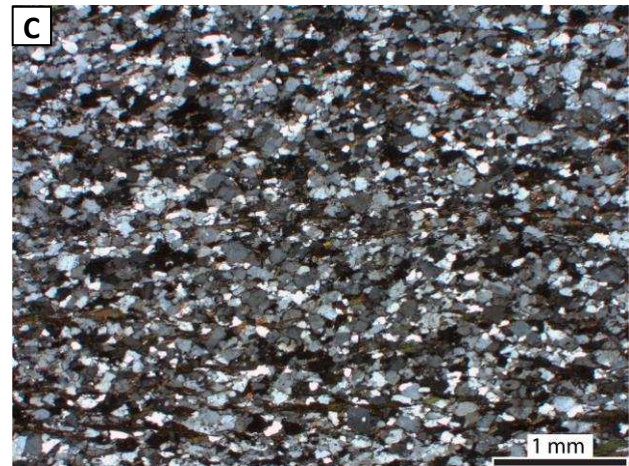
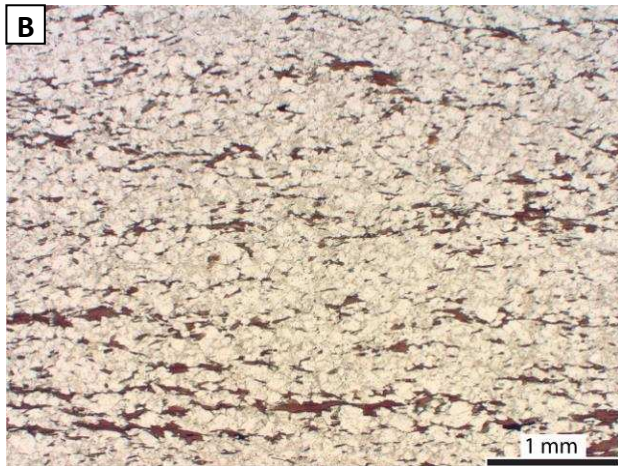
**Figure 10:** Photographs of the Orocopia Schist from the northern Plomosa Mountains. **A)** Typical exposure viewed from a distance, with foliation dipping to the left (SW). The hill is ~40 m high. **B)** Gray flaggy layers of Orocopia Schist, with a brown to tan desert varnish. **C)** Massive and homogenous Orocopia Schist, with gray on top and purple-red on bottom. A quartz vein with minor feldspar intersects the hammer handle. **D)** Typical appearance of homogenous purple-red Orocopia Schist. A close-up would reveal an S-C fabric which is very common. The asymmetric leucocratic lens near center records top-to-the NE sense of shear (NE to left). **E)** Pencil is pointing to an example of graphitic plagioclase. **F)** Another example of graphitic plagioclase. The largest in the photo is ~0.5 mm wide.



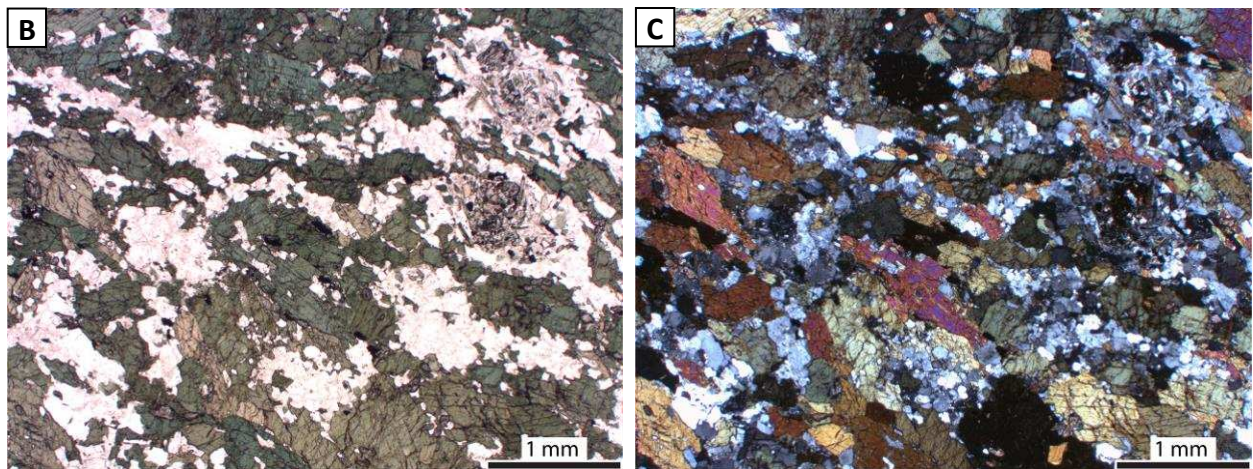
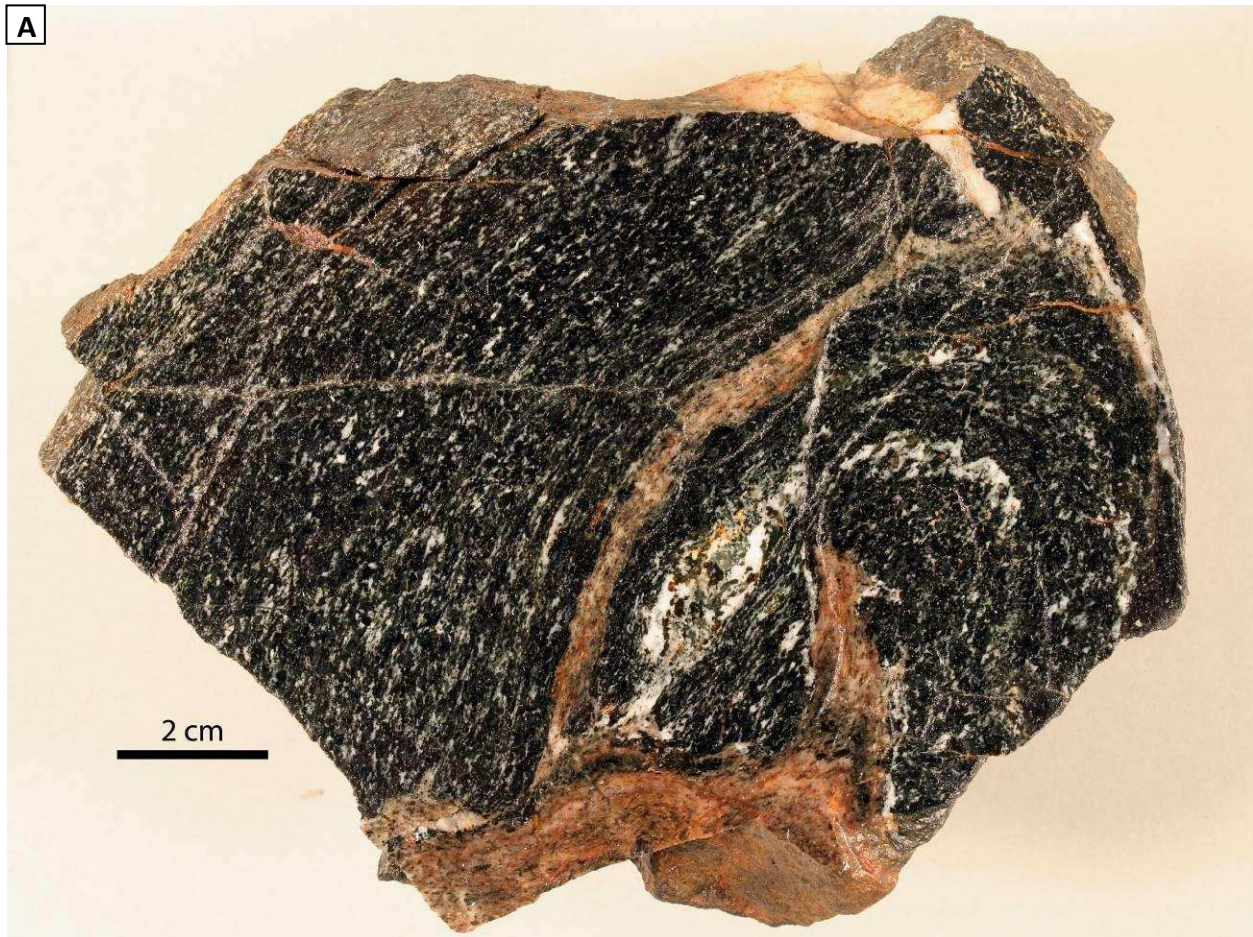
**Figure 11:** Photomicrographs of samples of Orocopia Schist collected from the northern Plomosa Mountains. **A)** Quartzofeldspathic schist with biotite and muscovite (PPL) [155-P9]. S-C fabric is visible which records top-to-the NE sense of shear. **B)** Same as A (XPL). **C)** Orocopia Schist with graphitic plagioclase (graphite is the disseminated opaque mineral) (PPL) [1115-P57c]. **D)** Same as C (XPL). **E)** Quartz- and feldspar-rich example of Orocopia Schist. Sigma-clast bordered by oblique quartz grain-shape fabric records top-to-the NE sense of shear (PPL) [1116-P9]. **F)** Same as E ( $1\lambda$  plate).



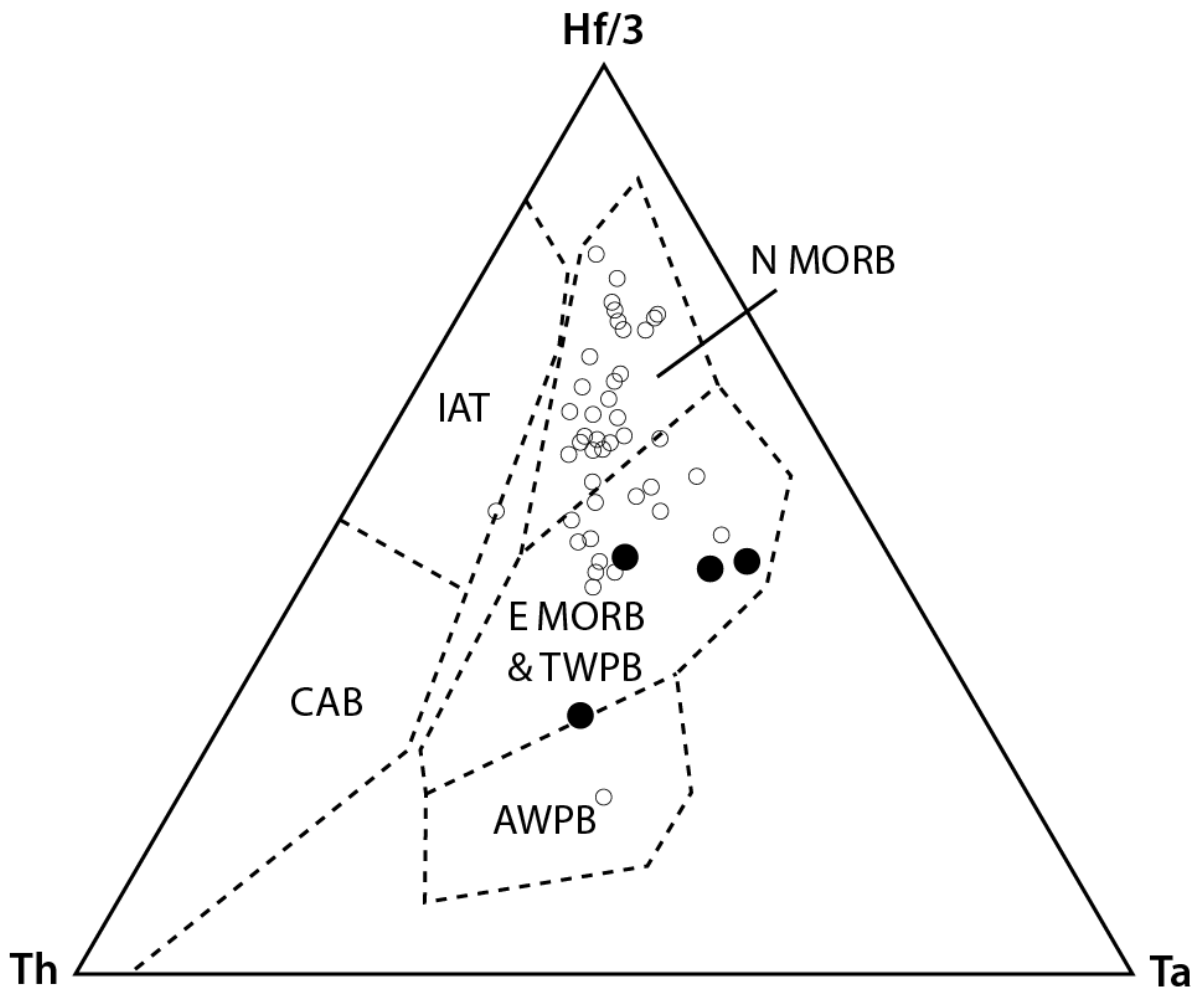
**Figure 12:** Photographs and photomicrographs of features observed in the Orocopia Schist of the northern Plomosa Mountains. **A)** Actinolite-bearing schist of the Orocopia Schist. Asymmetric fold (below pencil tip) records top-to-the-NE sense of shear (NE to the right). **B)** Photomicrograph (PPL) of a sample of actinolite-bearing schist [1016-P259], collected from an outcrop of golden-flaky schist similar to that shown in A. **C)** Photomicrograph (PPL) of red biotite somewhat common in samples of Orocopia Schist [1115-P20a]. **D)** Photomicrograph (PPL) of rutile needles in chlorite (after biotite) commonly observed in samples of Orocopia Schist [1115-P61a]. **E)** Milky-quartz lens within the Orocopia Schist, located just a few meters from a pod of actinolite. **F)** Quartz vein with minor feldspar in the Orocopia Schist.



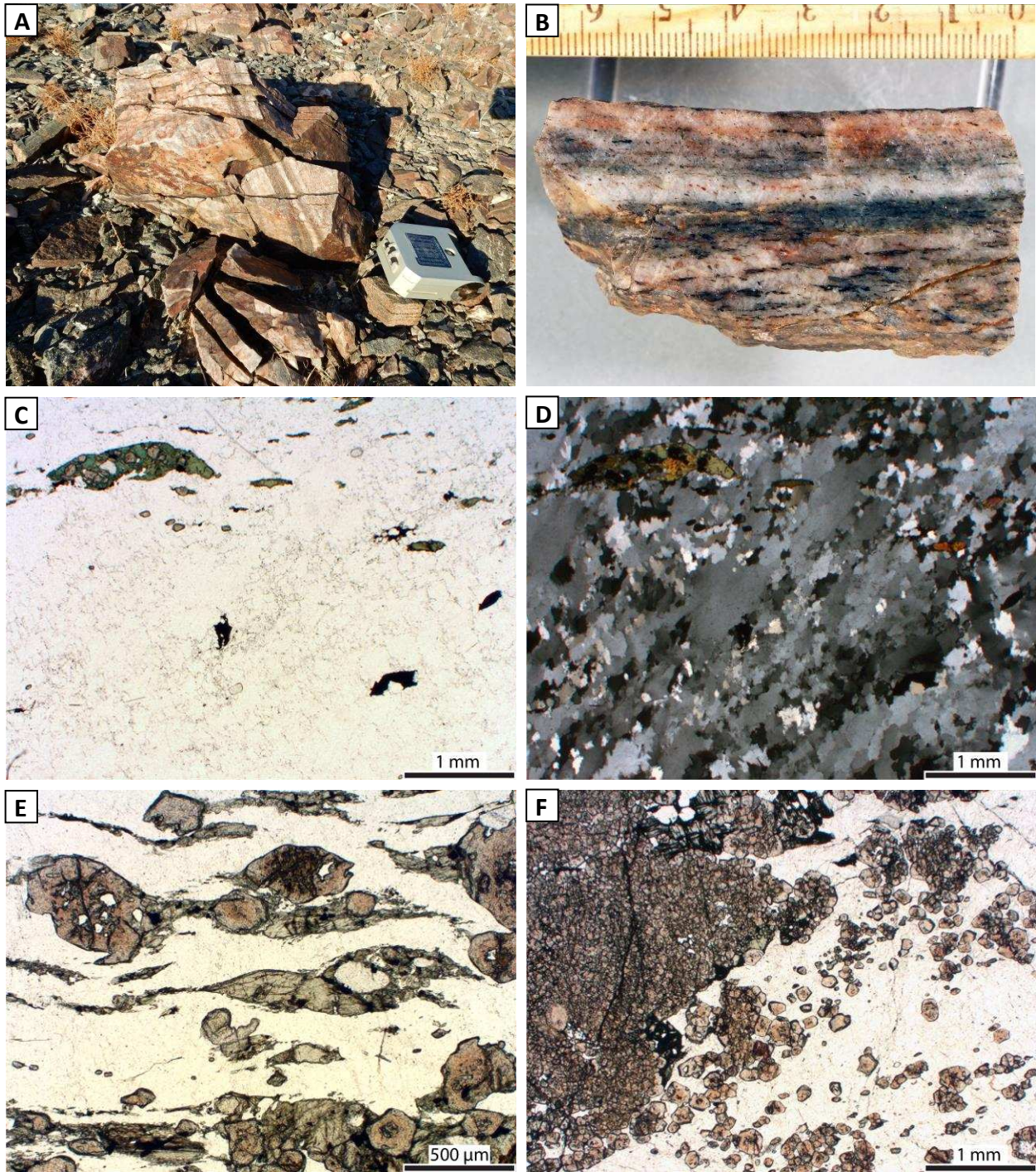
**Figure 13: A)** Photograph of two layers of meta-arkose within Orocopia Schist in the northern Plomosa Mountains (above the hammer handle, extending from the left- to right-hand side of the photo). The lower layer is ~5 cm thick, the upper layer is ~15 cm thick, and both are parallel to the mylonitic foliation. Ribbons of quartz + feldspar intersect the hammer handle. **B)** Photomicrograph (PPL) of a sample of meta-arkose showing a composition dominantly of feldspar, with minor biotite and quartz [0316-P81b]. **C)** Same as B (XPL).



**Figure 14: A)** Photograph of a slab of Orocopia metabasalt from the northern Plomosa Mountains, with folded foliation. The orange/red portion on the bottom is metachert, which has been squeezed into the fold hinge of the metabasalt, and incorporated into one of the limbs. **B)** Photomicrograph (PPL) of Orocopia metabasalt from the northern Plomosa Mountains, showing mineralogy dominantly of hornblende and feldspar, with minor quartz and titanite [0217-P41]. The remnants of two resorbed garnets are seen in in the upper-right corner. **C)** Same as B (XPL).

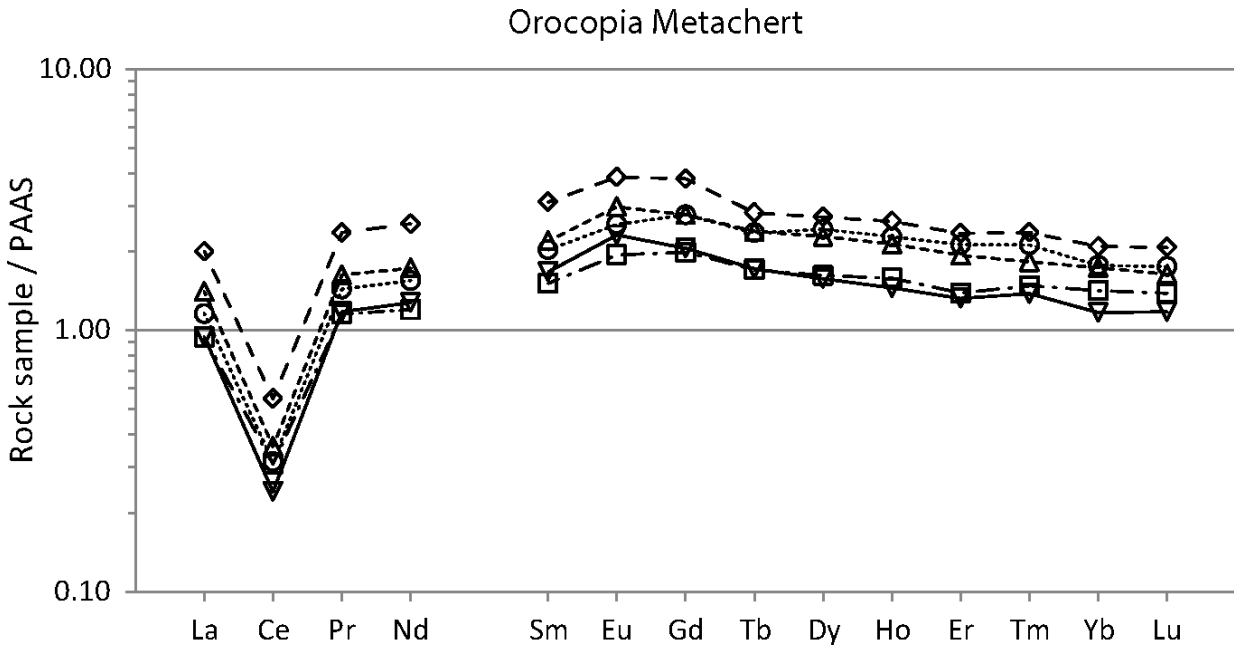


**Figure 15:** Ternary diagram of Th, Hf, and Ta from samples of amphibolite schist interlayered with Orocopia Schist (Appendix 5). Solid black circles are data from amphibolite interlayered with Orocopia Schist from the northern Plomosa Mountains, which plot in the E MORB space, consistent with the interpretation of the amphibolite as metabasalt. Small open circles are data points from Haxel et al. (2002) of metabasalt from Orocopia, Pelona, and Rand schists (Haxel et al., 1987; Dawson and Jacobson, 1989; Moran, 1993). N-, E-MORB: normal- and enriched-type mid-ocean ridge basalt; TWPB, AWPB: tholeiitic, alkaline within-plate basalt; IAT, CAB: island-arc tholeiite, calcalkaline basalt. Basalt categories (dashed lines) are copied from Haxel et al., (2002). Ternary plots in this thesis were created with the Excel spreadsheet of Graham and Midgley (2000).

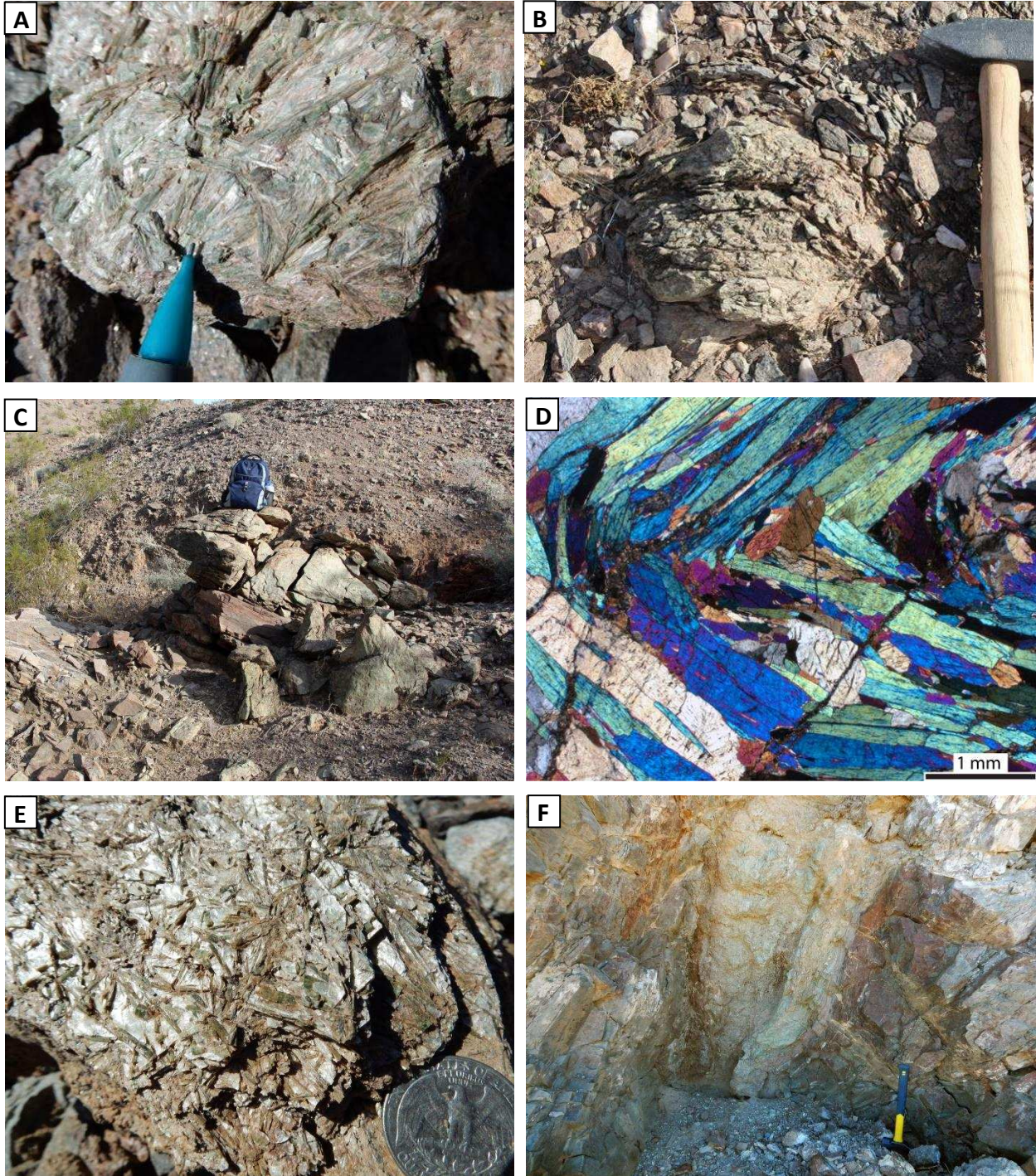


**Figure 16:** Photographs and photomicrographs of metachert from the northern Plomosa Mountains. **A)** Photograph of an exposure of metachert located within unit KPGam. This example displays light and dark banding parallel to the mylonitic foliation. **B)** Photograph of a slab of metachert with light and dark banding. **C)** Photomicrograph (PPL) of metachert with a composition dominantly of quartz [1116-P62]. Minor garnet is observed clustered in the upper-left corner, overgrown by hornblende, and minor opaque minerals are isolated within quartz in the lower-right of the photo. **D)** Same as C (XPL), with the grain boundaries of dynamically recrystallized quartz visible. **E)** Photomicrograph (PPL) of metachert with garnet and foliated actinolite [1016-P274]. The garnet in the upper-left corner is ~0.5 mm wide, and displays a zonation of color: darker in the center and pale on the rim. **F)** Photomicrograph (PPL) of metachert showing masses of very fine-grained garnet [1016-P178].





**Figure 17:** PAAS (post-Archean Australian shale)-normalized rare earth element spectra of five samples of quartzite interlayered with metabasalt from the northern Plomosa Mountains (Appendix 5). The negative cerium (Ce) anomaly exhibited by these samples is characteristic of seawater and many oceanic nondetrital sedimentary rocks (e.g. Haxel et al., 2002), supporting the interpretation that the quartzite is metamorphosed chert.



**Figure 18:** Examples of actinolite found in the Orocopia Schist of the northern Plomosa Mountains. **A)** Coarse-grained green actinolite pod within the Orocopia Schist. **B)** An *in-situ* actinolite pod within the schist. **C)** An *in-situ*, asymmetric actinolite pod  $\sim 1.5$  m long (backpack for scale, set on top of pod), with asymmetry consistent with top-to-the-NE shear. NE is to the left. **D)** Photomicrograph (XPL) of folded actinolite [1115-P57T1]. **E)** An example of uncommon actinolite-talc schist. **F)** A  $\sim 0.4$  m-wide tabular body of actinolite (vertical and centered). This actinolite is more friable than the actinolite found as pods.

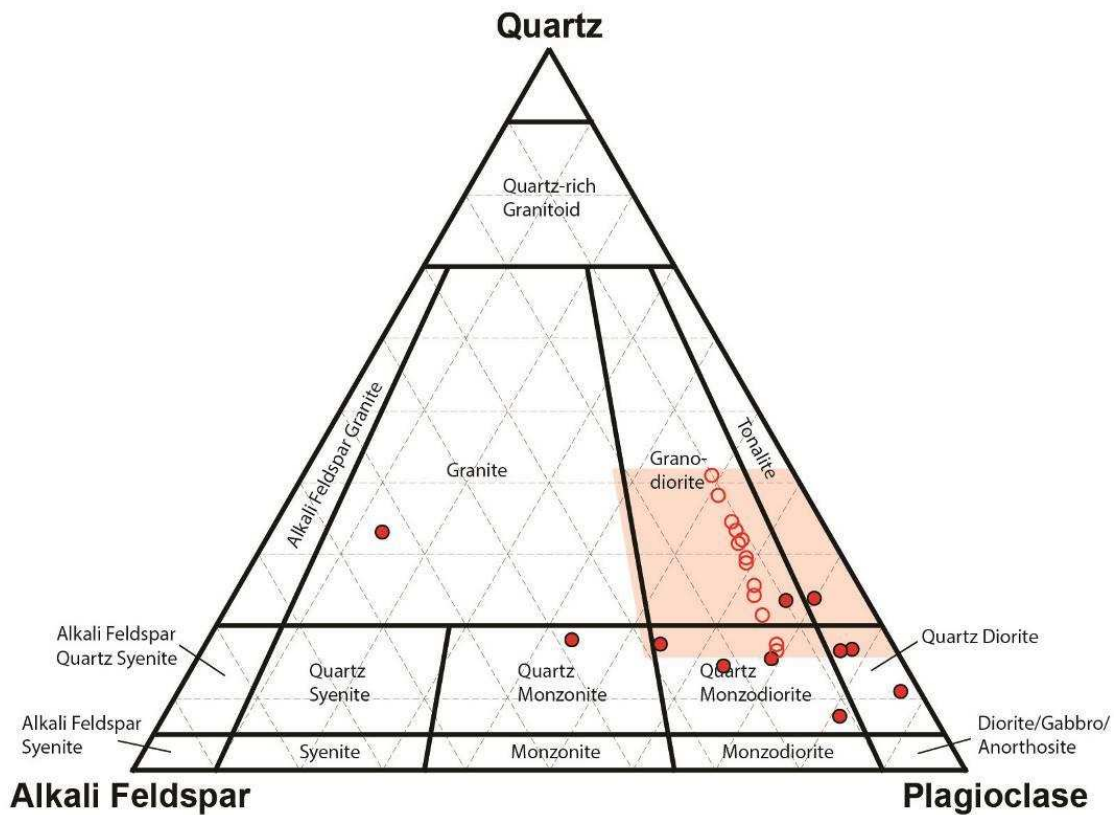
**Table 1:** Chemical formulas and ppm Ni and Cr for three actinolite samples collected within the Orocopia Schist from the northern Plomosa Mountains, derived from whole-rock geochemical results (Appendix 4).

<b>Actinolite sample P57T1</b>			
Chemical Formula	$(\text{Ca}_{1.57}\text{Na}_{0.08}\text{K}_{0.01})(\text{Mg}_{3.83}, \text{Fe}_{0.72}, \text{Mn}_{0.03})\text{Al}_{0.46}\text{Si}_{7.57}\text{O}_{22}(\text{OH})_{1.85}$		
PPM Ni	1290	PPM Cr	1700
<b>Actinolite sample P71</b>			
Chemical Formula	$(\text{Ca}_{1.42}\text{Na}_{0.08}\text{K}_{0.01})(\text{Mg}_{3.67}, \text{Fe}_{0.64}, \text{Mn}_{0.02})\text{Al}_{0.47}\text{Si}_{7.81}\text{O}_{22}(\text{OH})_{1.63}$		
PPM Ni	413	PPM Cr	2330
<b>Actinolite sample P421</b>			
Chemical Formula	$(\text{Ca}_{1.61}, \text{Na}_{0.26}, \text{K}_{0.04})(\text{Mg}_{4.07}, \text{Fe}_{0.57}, \text{Mn}_{0.03})\text{Al}_{0.57}\text{Si}_{7.40}\text{O}_{22}(\text{OH})_{1.83}$		
PPM Ni	1080	PPM Cr	1580

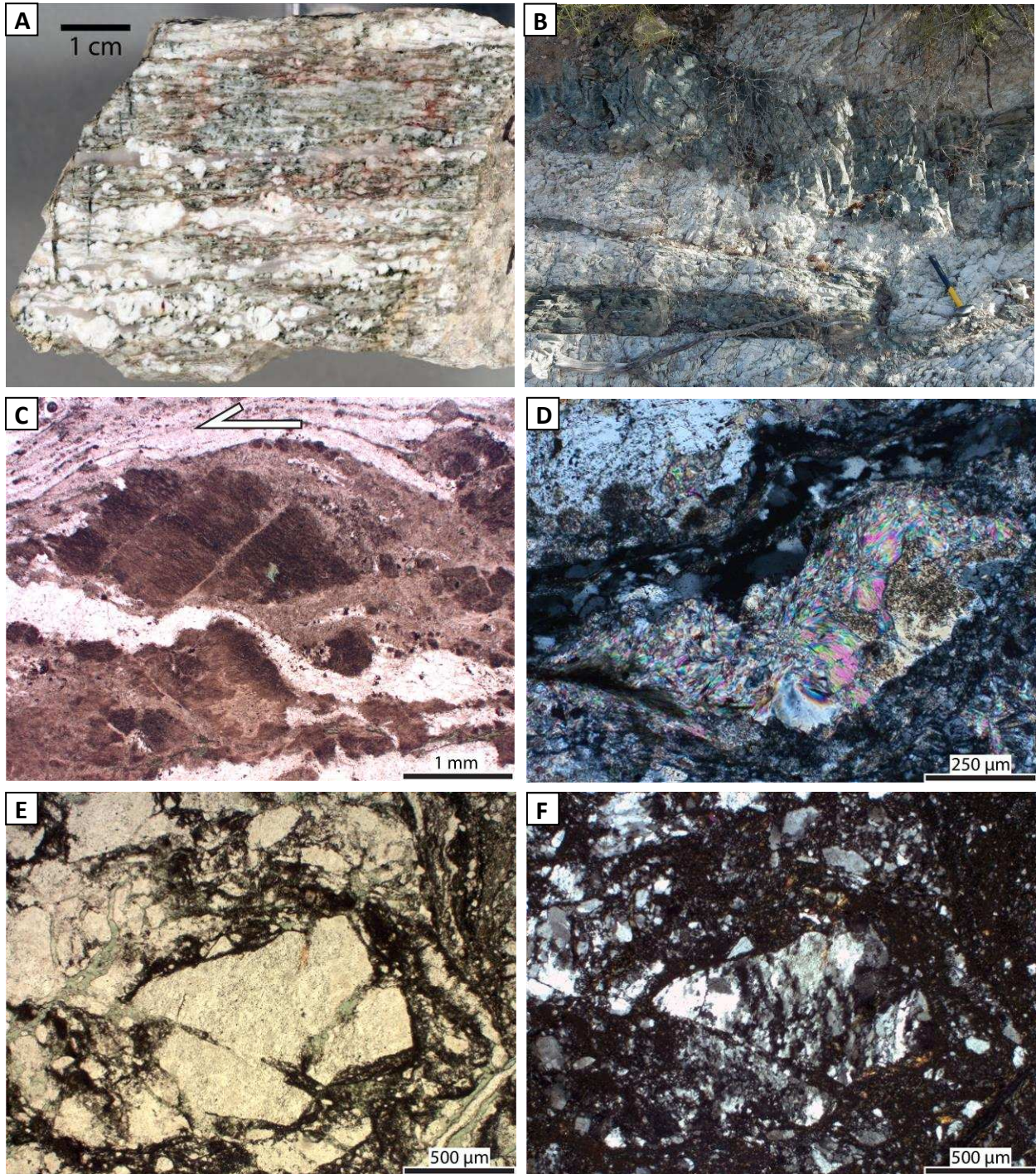
## 5.2. Miocene Intrusive Complex (Nic)

A newly recognized Miocene intrusive complex (unit Nic) borders the Plomosa detachment fault in the northern half of the field area (Plate 1; Figures 8 and 9). The intrusive complex has a bimodal composition of leucocratic biotite tonalite, granodiorite, and uncommon granite (totaling ~60% of the unit) and intermediate hornblende-biotite diorite, with lesser quartz diorite, quartz monzodiorite, and rare quartz monzonite (Figure 19). Figures 20 to 24 are photographs and photomicrographs of unit Nic. The bulk of this unit appears as layered tabular bodies approximately parallel to mylonitic foliation, though nonmylonitic diorite/quartz diorite dikes locally cut across well-foliated layers (Figure 20 B and 21 C). Much of the unit is marked by a pale-colored zone (unit Nic<sub>a</sub>) corresponding to pervasive chloritization and alteration (Plate 1; Figure 8), described further in the section “Mineralization and Alteration”. Miocene intrusive rocks are also present outside of the mapped Nic area as mylonitic to protomylonitic leucocratic dikes and sills 3 cm to 2 m thick

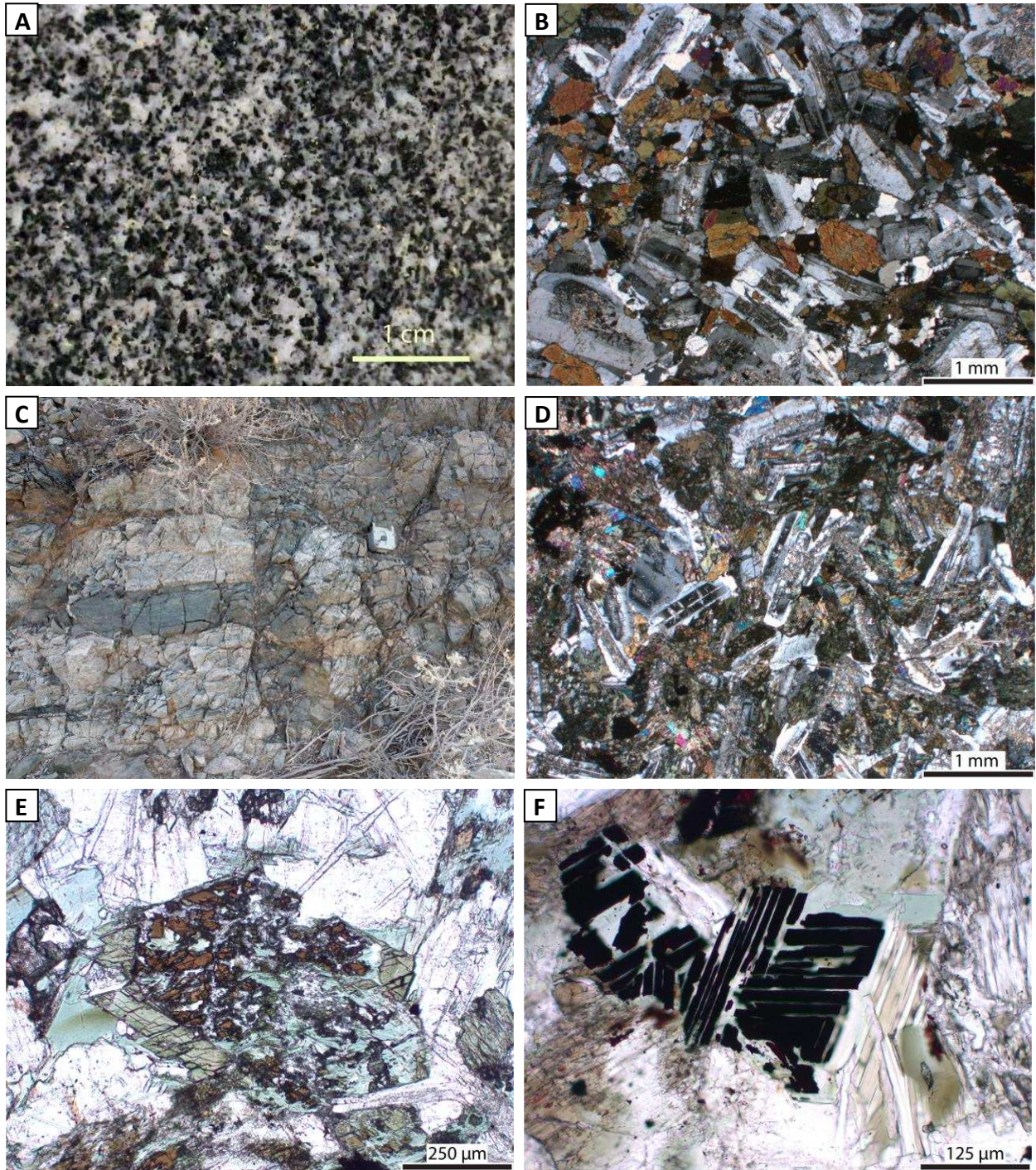
(Figure 22), most commonly observed within the Orocopia Schist. Intermediate compositions are rare outside of the mapped Nic unit, and some appear to have undergone magma mingling (Figure 23 A). In outcrop, intrusions often appear to have undergone high amounts of strain, yet a thin section of an apparent high-strain intrusion revealed it is actually protomylonitic (Figure 23 B, E & F), suggesting it intruded synmylonitically and deformed as a magma or crystal mush. Unit Nic is in some locations hard to distinguish from mica-poor Orocopia Schist, as it may be relatively rich in quartz with a similarly homogenous appearance (Figure 24).



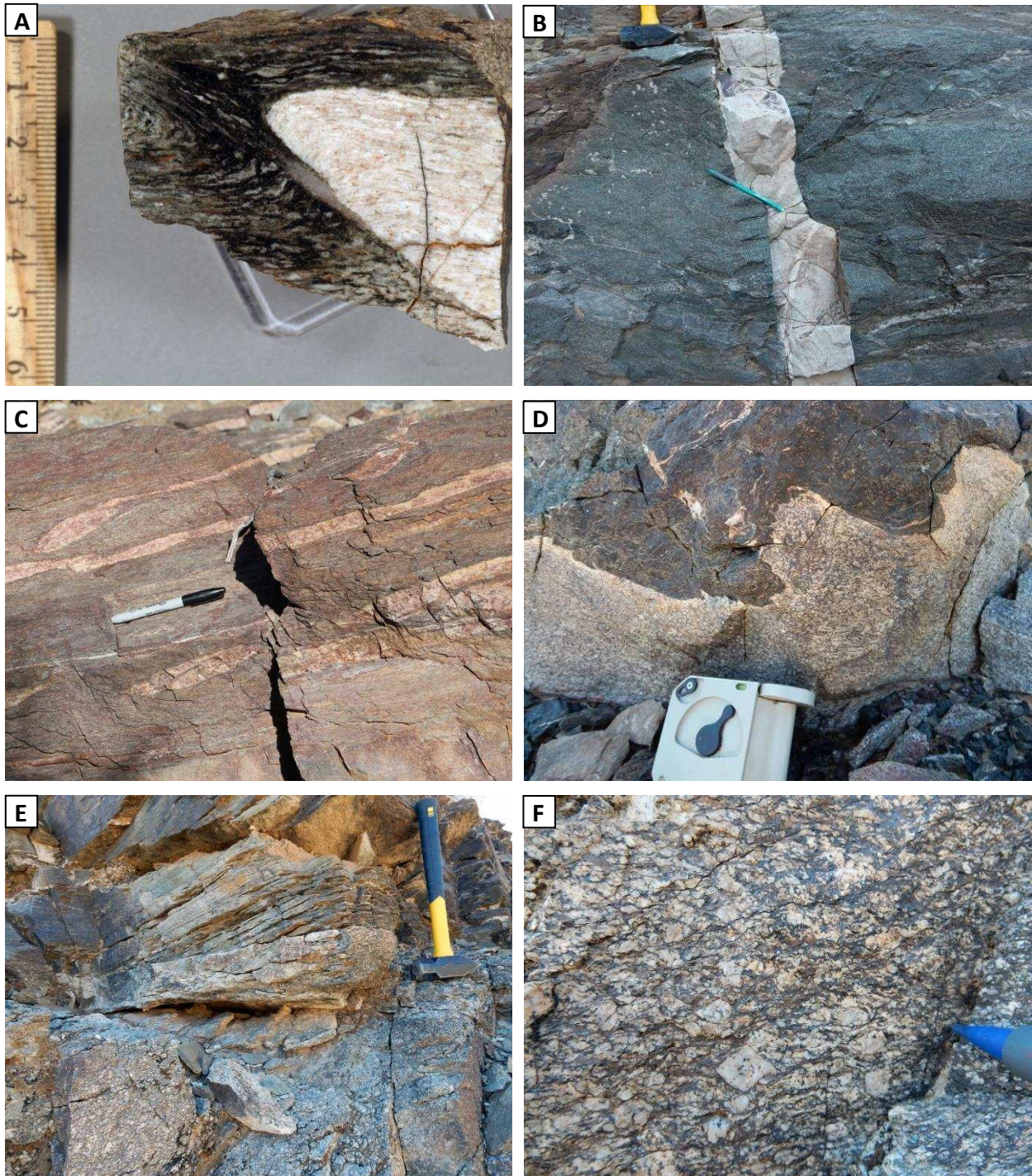
**Figure 19:** QAP diagram of samples of the unit Nic. Solid red circles are for samples where plagioclase and k-spar could be distinguished (n = 11). Hollow circles are for samples where the type of feldspar could not be distinguished (n = 13), and the ratio of plagioclase and k-feldspar used in the plot is the average of the solid circle samples, excluding the highly alkaline granite sample. The red box represents the reasonable range of feldspar compositions for the hollow circles as determined in the field (mainly tonalite and granodiorite with rare granite).



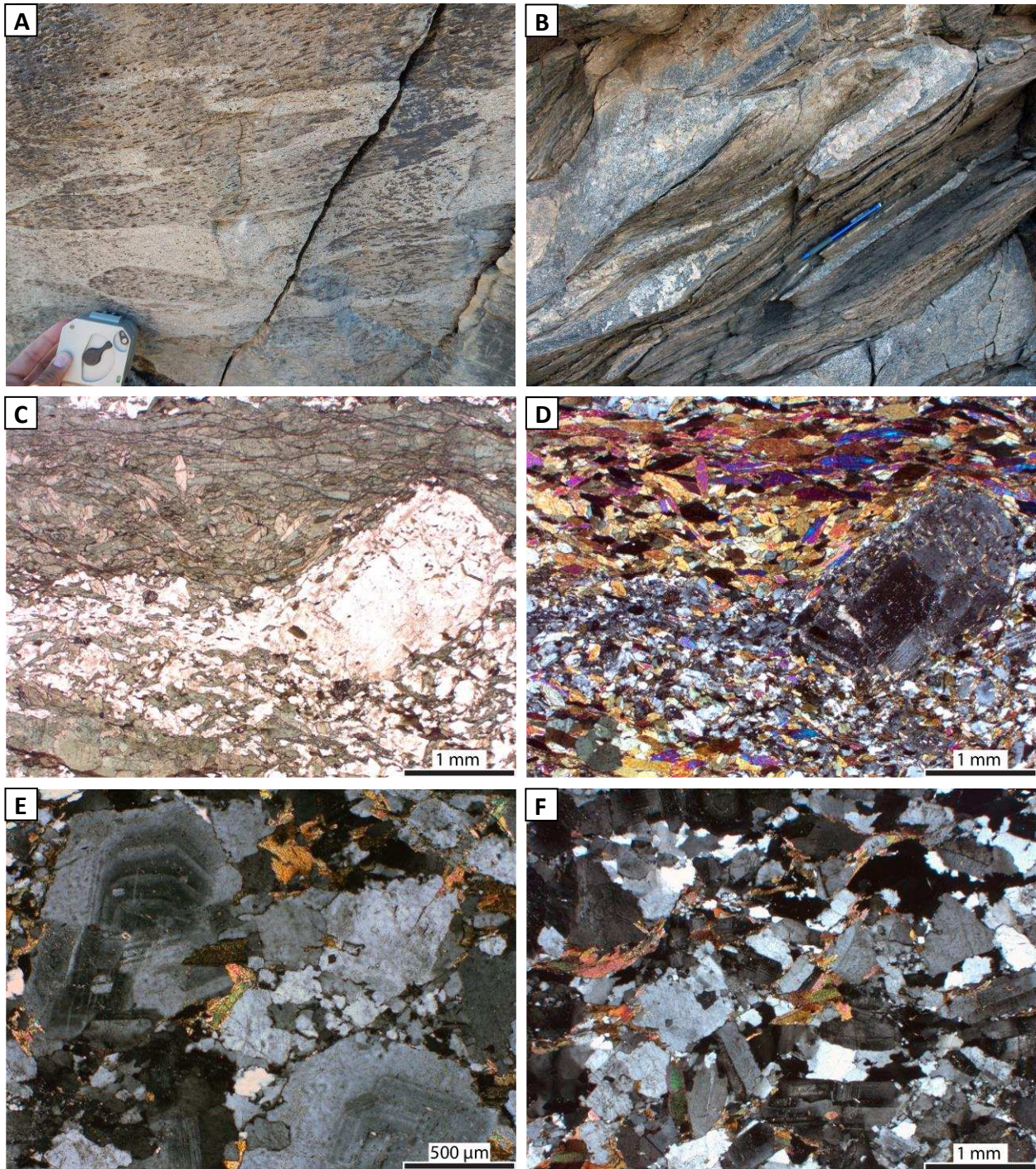
**Figure 20:** Photographs and photomicrographs of unit Nic of the northern Plomosa Mountains. **A)** Photo of a slab of a leucocratic mylonitic/protomylonitic sample collected to represent the “core” of the intrusive complex within unit Nic<sub>a</sub>. Zircon U-Pb geochronology was applied to this sample (0217-P43), including CL-imaging of a polished mount. **B)** An example of the layered tabular bodies of alternating leucocratic and intermediate compositions, characteristic of unit Nic. These layers are parallel to the mylonitic foliation, and may have been transposed during mylonitization. **C)** Photomicrograph (PPL) of the sample from A, showing intensely sericitized feldspars, to the point where the original feldspar is no longer visible [0217-P43]. **D)** Photomicrograph (XPL) of radiating white mica in the same sample. **E)** Photomicrograph (PPL) of the cataclasized and intensely chloritized rock found within the mapped alteration zone (unit Nic<sub>a</sub>) [1016-P278]. **F)** Same as E (XPL).



**Figure 21:** Photographs and photomicrographs of diorites of the unit Nic from the northern Plomosa Mountains. **A)** Photograph of a slab of diorite collected south of the mapping area. **B)** Photomicrograph (XPL) of A [0217-P16]. Zircon U-Pb geochronology was applied to this sample. **C)** Photograph of non-foliated diorite dikes (right side) cutting across foliated layers of alternating leucocratic and intermediate compositions (left side). Brunton for scale. **D)** Photomicrograph (XPL) of the non-foliated diorite dike from photo C [1116-P187e]. This sample is proximal to the detachment fault within the alteration zone (Nic<sub>a</sub>), and has a grungy appearance compared to B, but otherwise they appear identical. **E)** Photomicrograph from the same sample as D, showing the remnants of a brown amphibole, partially replaced by chlorite, and rimmed with green hornblende. **F)** Another photomicrograph of the same sample, showing opaque minerals which have replaced the brown amphibole.

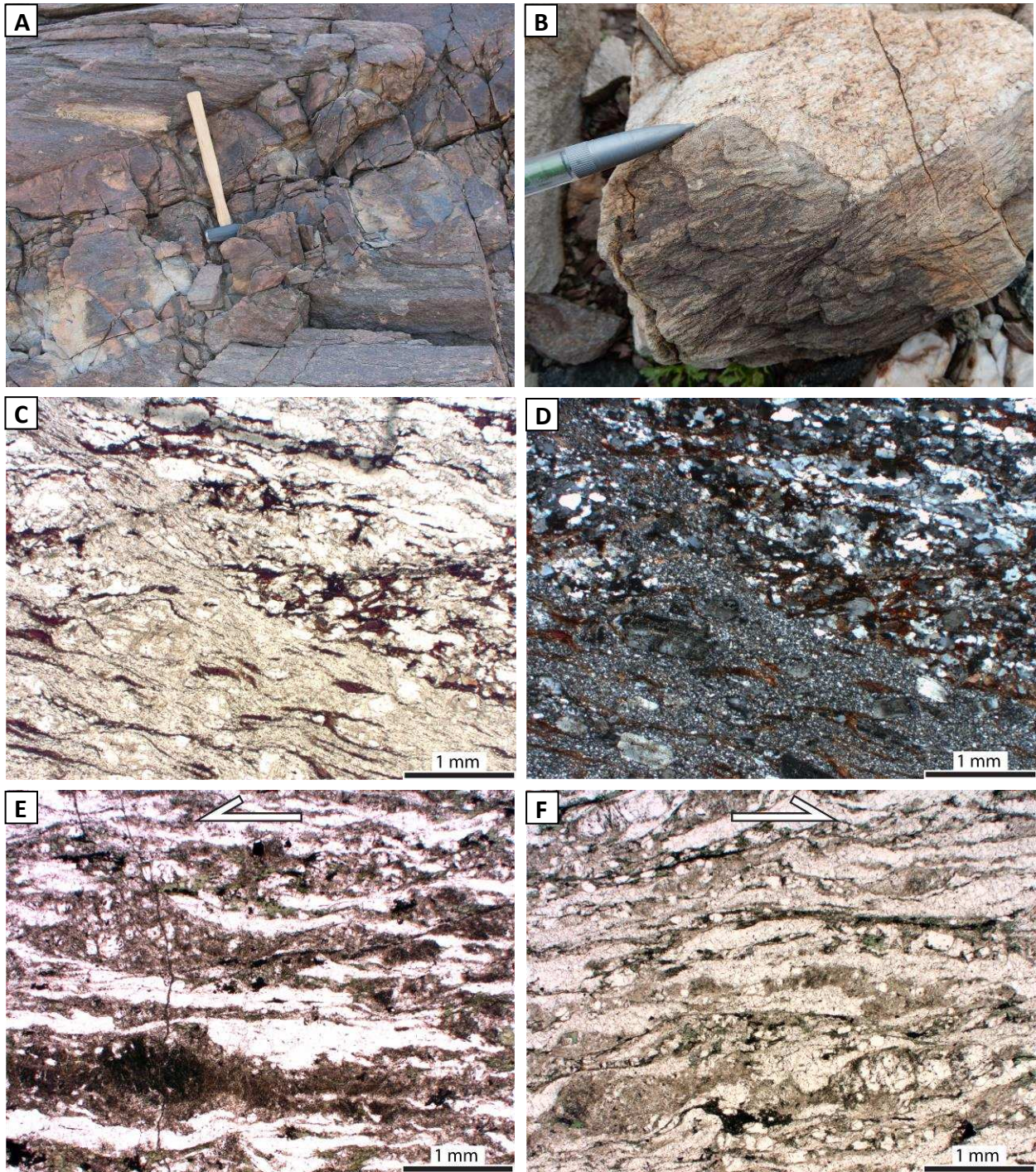


**Figure 22:** Photographs of leucocratic intrusions of the unit Nic from the northern Plomosa Mountains. **A)** Slab of a foliated leucocratic intrusion in Orocopia Schist. Drag-folding in the foliation of the intrusion records top-to-the NE displacement along a SW-dipping shear zone, NE to the left. **B)** Leucocratic intrusion within unit KXgn, offset with top-to-the NE displacement, NE to the left. **C)** Leucocratic intrusions in the form of sills and asymmetric lenses within Orocopia Schist. Asymmetry of the lenses records top to-the NE sense of shear, NE to the right. **D)** Deformed leucocratic intrusion (bottom) in contact with Orocopia metabasalt (top). **E)** A protomylonitic, leucocratic, shallowly-dipping dike (bottom) intruded into Orocopia Schist (top). Note how the orientation of the contact of the dike with the schist is oblique to the mylonitic foliation of the schist. **F)** Close-up of the protomylonitic dike from photo E.



**Figure 23:** Photographs and photomicrographs of intrusions from the northern Plomosa Mountains. **A)** Photograph of an intermediate hornblende-bearing intrusion which appears to have undergone magma mingling. **B)** Photograph of an apparently high-strained intrusion within Orocopia Schist. **C)** Photomicrograph (PPL) of A, showing layer of foliated hornblende [1116-P7]. **D)** Same as C (XPL), showing typical zonation of a feldspar as found in unit Nic. **E)** Photomicrograph (XPL) of an intrusive sample similar to and nearby photo B, showing well-zoned feldspars typical of unit Nic [0316-P71x]. **F)** Same as E (XPL), showing protomylonitic appearance of the rock as a whole with a weak foliation defined by aligned biotite, in contrast to the high-strained appearance of the rock in outcrop.





**Figure 24:** **A)** Photograph of an intrusion within Orocopia Schist. **B)** Photograph of an intrusive contact of unit Nic (top) with Orocopia Schist (bottom). **C)** Photomicrograph (PPL) of A, showing intrusive contact (intrusion bottom, Orocopia Schist top) [0316-P40a]. **D)** Same as D (XPL). Zoned feldspar porphyroblasts of the intrusion are within a matrix of fine-grained feldspars, which is clearly distinct from the Orocopia Schist. **E)** Photomicrograph of a quartz-rich granitic intrusion, with highly sericitized feldspars typical of unit Nic, as well as chlorite [0217-P47]. S-C' fabric records top-NE sense of shear. **F)** Photomicrograph of a sample which was determined to be Orocopia Schist from the presence of graphitic plagioclase and rutile needles in chlorite [1016-P300a]. Note the similarity between this sample and the sample in E, though E is an intrusion and F is Orocopia Schist. Rocks such as E and F were often difficult to distinguish in the field. S-C fabric records top-NE sense of shear.

### 5.3. Gneiss (KXgn)

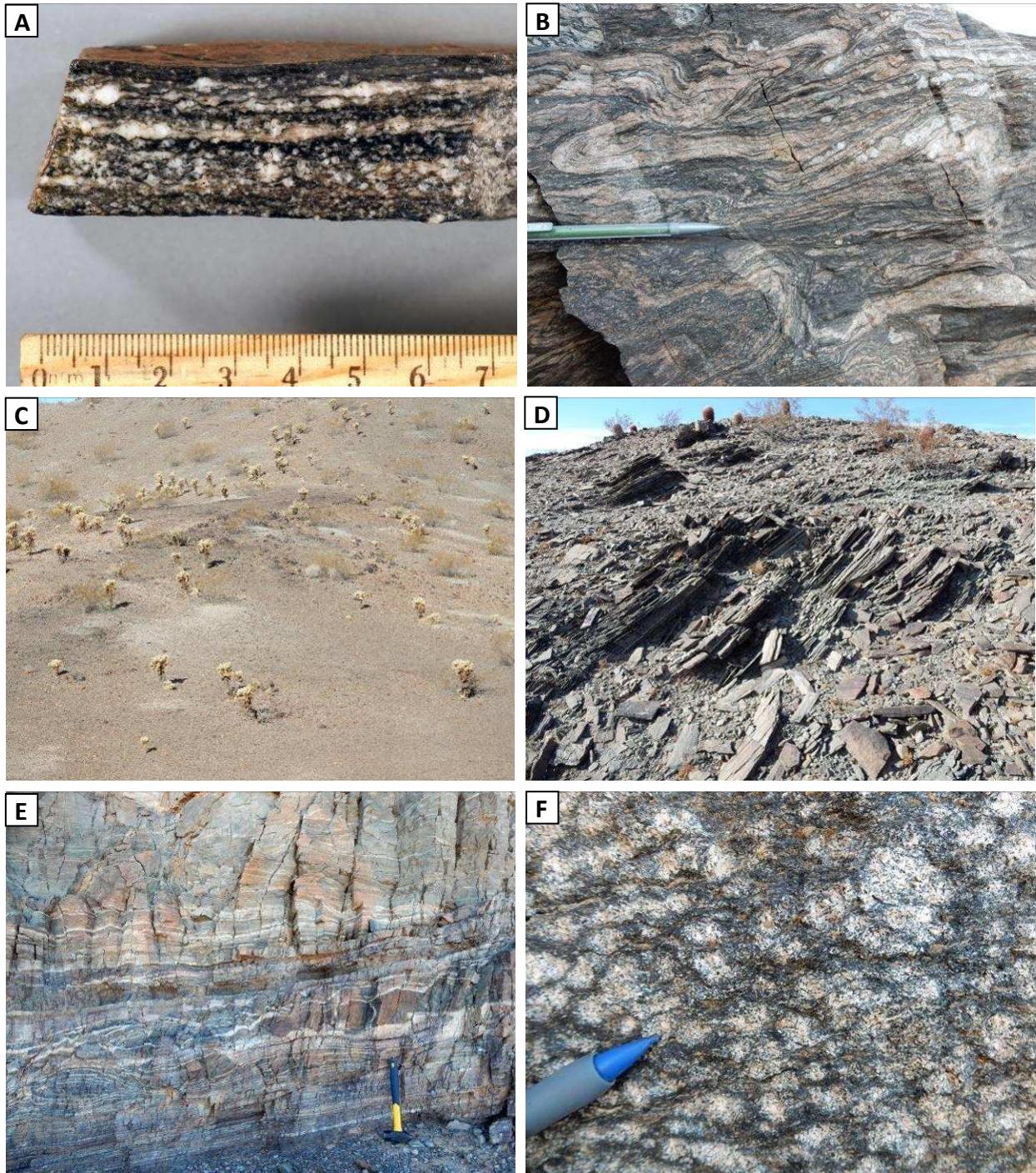
Crystalline gneiss (Figures 25 and 26) dominates the southern half of the map area (unit KXgn), and is juxtaposed against the Orocopia Schist to the north along a tectonic contact with the unit KPGam (Orocopia metabasalt) (Plate 1; Figures 8 and 9). Based on the similarity of this unit to other crystalline gneisses in west-central Arizona (e.g. Bryant and Wooden, 2008), the protolith age is likely a mix of Proterozoic, Jurassic, and Cretaceous rocks. The unit is dominantly mylonitic within the map area, though locally it contains 5–30 cm-thick protomylonitic layers. Mylonitic lineations are typically defined by stretched quartz, aligned hornblende, and streaks of biotite. The fabric becomes predominantly protomylonitic towards the southern end of the field area, which is ~2 km NNE of a mylonitic front.

1) The gneiss most commonly appears as alternating layers ~3–30 cm thick, composed of hornblende amphibolite, biotite-poor tonalite or granodiorite, and gray to tan-gray, well-foliated and lineated hornblende biotite tonalite or granodiorite. The well-foliated gneiss commonly appears as several meter-thick packages (locally >10 m), with 1 mm to 1.5 cm-thick layering defined by alternating felsic and mafic compositions. Amphibolite and hornblende-rich tonalite/granodiorite may be several meters thick, and the amphibolite commonly form boudins or exhibit pinch-and-swell structures. The unit locally includes 1–10 cm thick leucogranite layers with recrystallized ribbons of quartz and plagioclase.

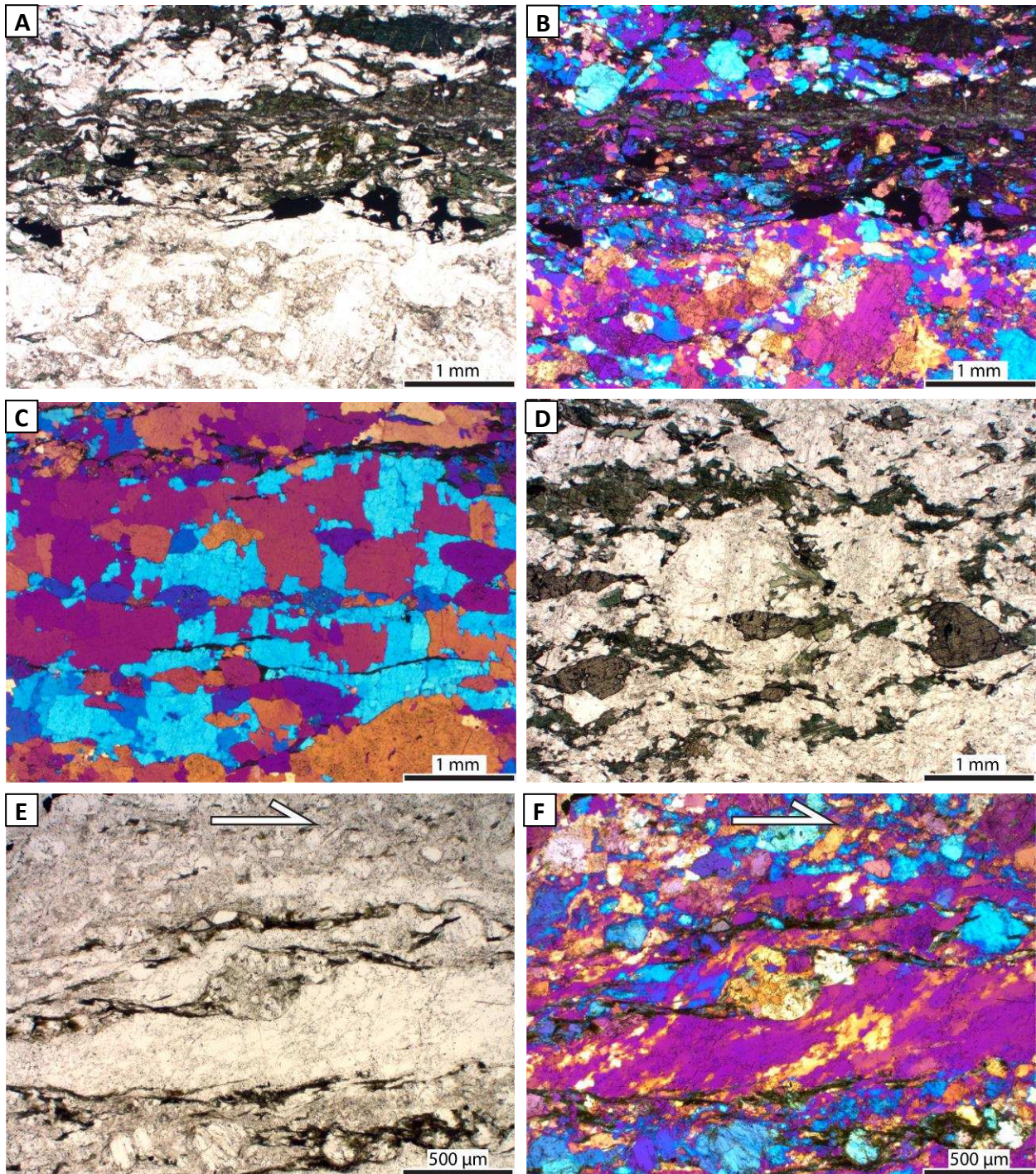
2) The SW portion of the gneissic unit commonly has an outcrop-scale “salt-and-pepper” appearance as viewed from a distance (Figure 25 C), which is fine-grained

hornblende amphibolite adjacent to leucocratic biotite-poor tonalite/granodiorite, commonly interlayered with the well-foliated gneiss.

3) A nonmylonitic gneiss with a spotted appearance is found in the very SE portion of the unit, on the east side of the mapped NE-striking fault. It has white poikiloblastic plagioclase ~3 mm to 1 cm in diameter and a weakly-developed foliation defined by aligned hornblende and biotite, all of which is overgrown by randomly-oriented hornblende  $\leq 0.5$  cm long (Figure 25 F). Minor titanite up to 2 mm long and quartz are also present. This spotted gneiss occurs as several repeated layers that vary from 3–8 meters thick and is laterally continuous for  $\geq 400$  m.



**Figure 25:** Photographs of gneiss from the northern Plomosa Mountains. **A)** Photograph of a slab of mylonitic gneiss. **B)** Isoclinally-folded gneiss. Folds are consistent with top-to-the-NE sense of shear (NE to the right). **C)** Photograph of the “salt-and-pepper” appearance of the gneiss, as viewed from a distance. Cholla cactus are ~1 m tall. **D)** Typical well-foliated gneiss. **E)** Compositional layers of the gneiss, including amphibolite layers which exhibit pinch-and-swell structures. **F)** The gneiss with a spotted appearance. A crude foliation is defined by aligned hornblende between the plagioclase porphyroblasts.



**Figure 26:** Photomicrographs of gneiss from the northern Plomosa Mountains. **A)** Mafic hornblende-bearing layer (top) and leucocratic layer (bottom), with layer of relatively abundant opaque minerals in the middle (PPL) [1016-P37]. **B)** Same as A ( $1\lambda$  plate). **C)** Dynamically recrystallized quartz exhibiting a chessboard pattern from the southern end of the mapping area ( $1\lambda$  plate) [0316-P94]. **D)** Example of relatively abundant titanite (PPL) [0316-P116]. **E)** Sigma clast that records top-to-the-NE sense of shear (PPL) [1016-P67]. **F)** Same as F ( $1\lambda$  plate). Dynamically recrystallized quartz with oblique grain-shape fabric also records top-to-the-NE sense of shear.

## **5.4. Other units**

### ***5.4.1. Interlayered mylonitic quartzite and marble (MzPzq)***

The smallest mapped unit in the footwall of the Plomosa detachment fault is interlayered mylonitic quartzite and marble (unit MzPzq, previously identified by Scarborough and Meader, 1983), located in the NE end of the map area along the Plomosa detachment fault (Plate 1; Figures 8 and 27). Marble layers are typically 0.5–1 m thick, while quartzite layers may be up to several meters thick. The interlayered marble and quartzite are not continuous throughout the map unit, but are interlayered with sections of granodiorite and tonalite intrusions of the unit Nic.

The rheological contrast between the marble and quartzite layers is very clear. Adjacent to the detachment fault, the relatively strong quartzite layers interlayered within the marble are intensely fractured, whereas the marble primarily lacks brittle deformation and has very well-developed mylonitic foliation (Figure 27 A & B). Because of the spatial relationship of the quartzite and marble to the Plomosa detachment fault, the Plomosa detachment may have been at least partially localized along this unit, as ductile strain could be accommodated by the quartzite at relatively low temperatures (~300°C), and later accommodated by the marble at shallower depths and even lower temperatures (~200–250°C). However, the foliation of this unit is often discordant to the detachment fault, which is counter to that interpretation.

### ***5.4.2. Nonmylonitic Miocene dikes (Nd)***

Nonmylonitic rhyo-dacite dikes ~0.2–3 meter wide are somewhat common throughout the footwall, and are most abundant in the southern third of the map area (unit Nd; Plate 1; Figure 28). These dikes contain up to 65% groundmass consisting primarily of

plagioclase laths. Weathered surfaces of non-mylonitic dikes are pitted (0.2–1 cm wide pits). A few of the mapped dikes are phaneritic, mylonitic quartz diorite, which are likely late-stage intrusions of unit Nic.

#### **5.4.3. Miocene sedimentary units (Ncg)**

Concealed mostly beneath Qoal, Miocene sedimentary rocks (unit Ncg) are exposed within three drainages just NNE of the unit PIQcg (Plate 1). There are three subunits: **Ncgt**: The southernmost and youngest subunit is a poorly-consolidated, clast-supported, pale salmon to tan conglomerate, with a silty to sandy matrix (Figure 29 A). Clasts are mostly subangular, with 50–60% gravel to cobble in size (5–10% of the total volume are cobble clasts >10 cm in diameter), and sparse boulders 0.4–1m in diameter. Clast lithologies include volcanic (including rhyolitic tuff and vesicular basalt), plutonic (medium-grained granite and diorite), and quartz-pebble conglomerate. This subunit lacks mylonite clasts, but is overlain by a sedimentary breccia consisting entirely of mylonite clasts (Figure 29 B), likely the same breccia as PIQcg<sub>m</sub> (described below). **Ncgr**: The middle subunit is a moderately- to well-consolidated, matrix-supported, reddish-tan conglomerate, with a sand and pebble matrix (~60%), and mostly rounded to subrounded cobble-sized clasts (~30%). Clasts include volcanic and plutonic lithologies similar to those in subunit Ncgt, but also sparse, well-rounded pegmatitic granite boulders (up to 50 cm), and rare mylonite (Figure 29 C & D). The well-rounded pegmatitic granite boulders seem to match the description of boulders found in a nearby unit called the Plomosa conglomerate, described by Jemmett (1966) and mapped by Duncan (1990). **Ncgs**: The oldest and northernmost subunit is a well-consolidated (though fractured and friable) brownish-red and tan siltstone, with bedding ranging from 0.5 mm to ~5 cm thick. Resistant, cobble-sized oblate

nodules are common, and sparse 1–2 cm-thick manganiferous(?) to ferruginous sandstone layers are present (Figure 29 E & F).

#### ***5.4.4. Pliocene to Quaternary(?) conglomerates (PIQcg)***

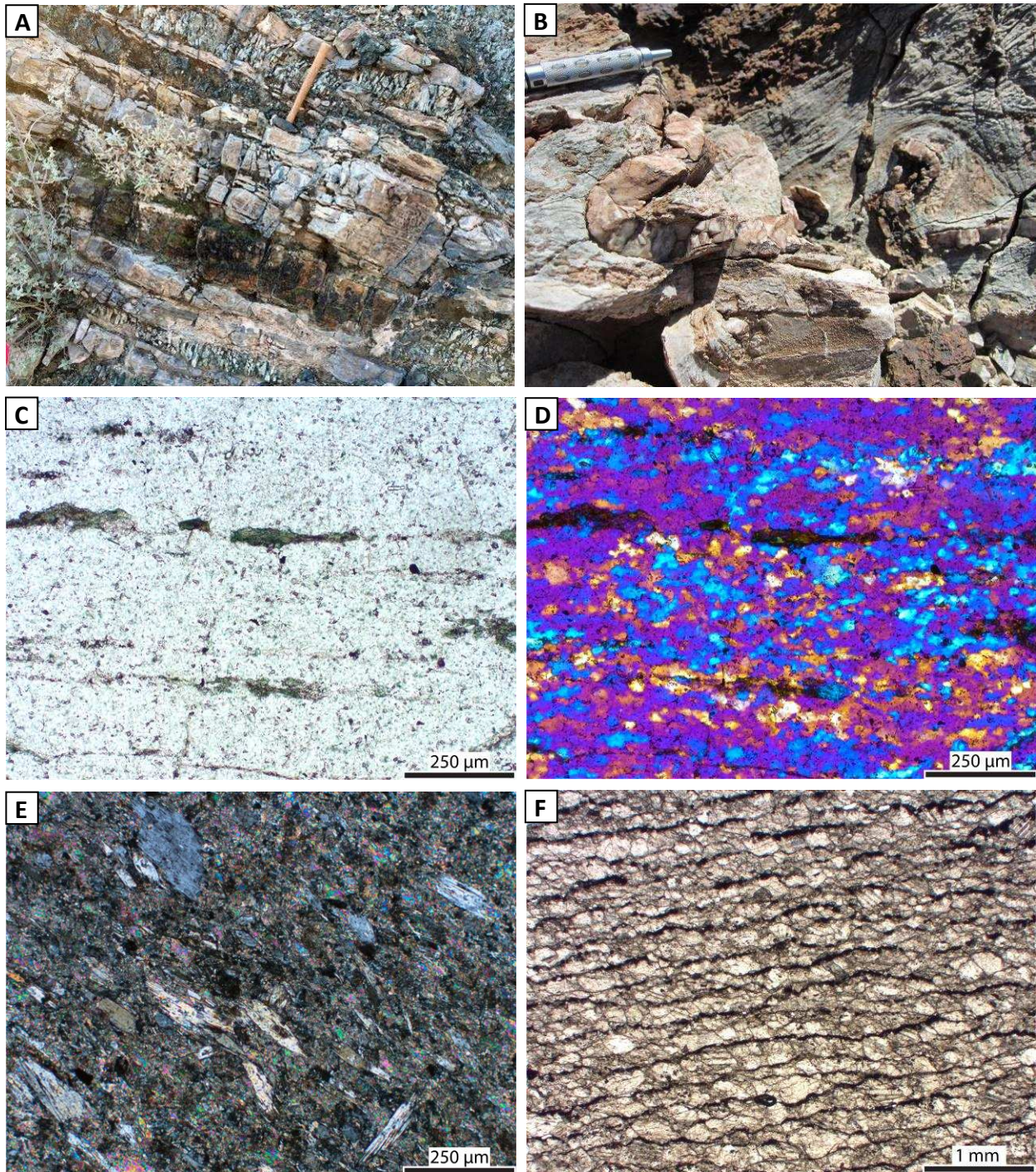
Mostly concealed beneath Qoal, Pliocene to Quaternary(?) conglomerates (unit PIQcg) are exposed within two main drainages in the southernmost map area, and bounded on their SE side by the mapped NE-striking fault (Plate 1). There are two subunits: **PIQcg<sub>s</sub>**: The southernmost subunit, interpreted as the youngest, is a tan-colored, moderately-consolidated silty sandstone, with 5–20% pebble to boulder-sized (up to 30 cm) angular clasts of mylonite (Figure 30 A & B). The depositional environment for the silt and sand comprising subunit PIQcg<sub>s</sub> is not known. **PIQcg<sub>m</sub>**: To the north is a well-consolidated, angular, clast-supported sedimentary breccia (Figure 30 C). Clasts are mostly pebble to cobble in size, and are sourced from the surrounding mylonitic gneisses (unit KXgn). Compared to Qoal, unit PIQcg<sub>m</sub> has much more sand and gravel in the matrix (up to 30–40%), is more well consolidated, and clasts have a higher degree of angularity. Unit PIQcg may have been deposited synkinematically with movement on the mapped NE-striking fault, as this unit is faulted against unit KXgn (Figure 30 D) and contains highly angular clasts of mylonitic gneiss equivalent to the gneiss across the fault.

#### ***5.4.5. Quaternary sediments (Qal, Qeol, Qoal)***

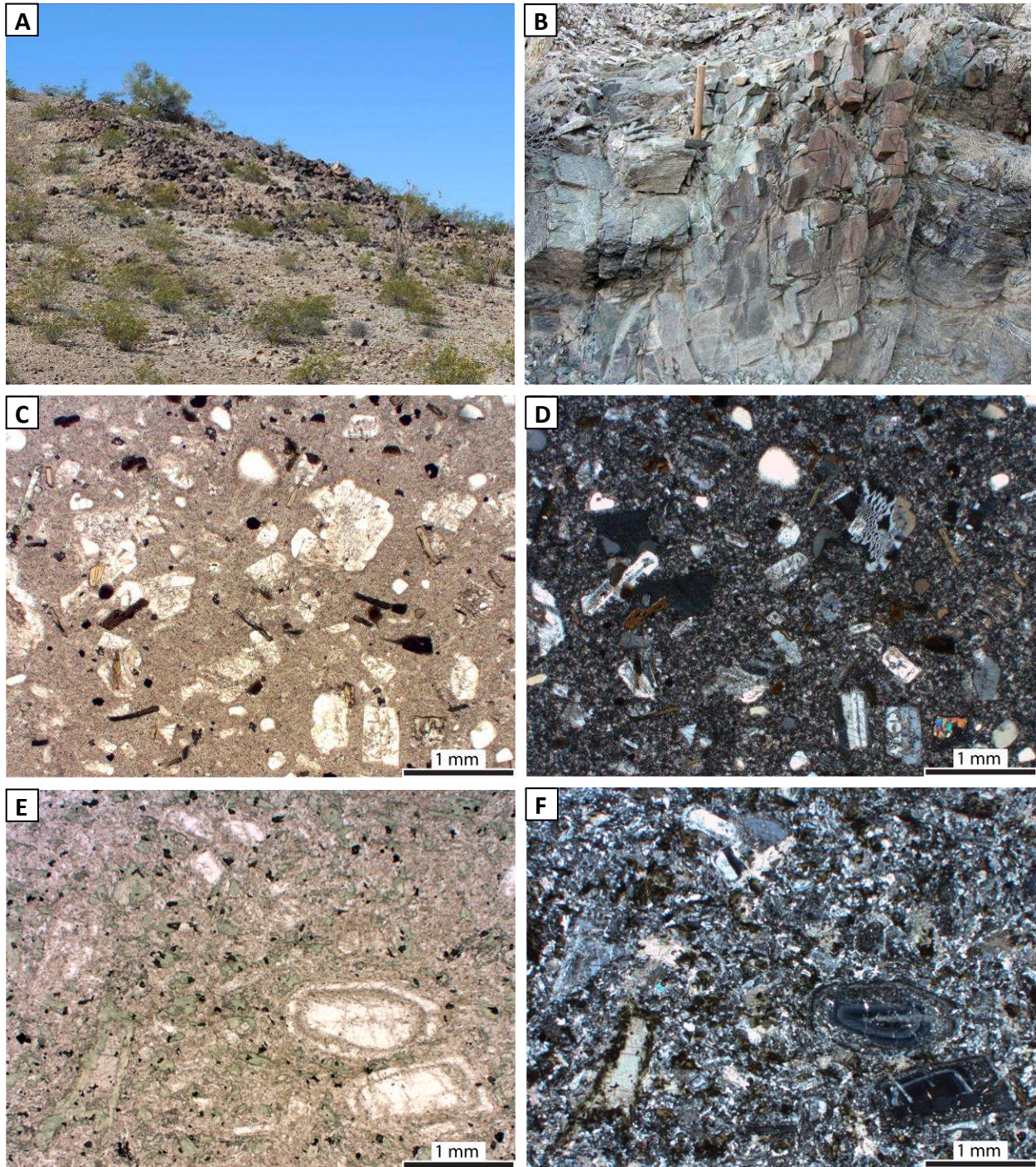
Three quaternary sediments were mapped primarily from aerial imagery: **Qal** is poorly-sorted, unconsolidated, angular to subrounded sediment deposited within unvegetated to lightly vegetated active channels. Sediment is derived from the surrounding bedrock and consists primarily of sand, gravel, and cobbles with minor silt and sparse



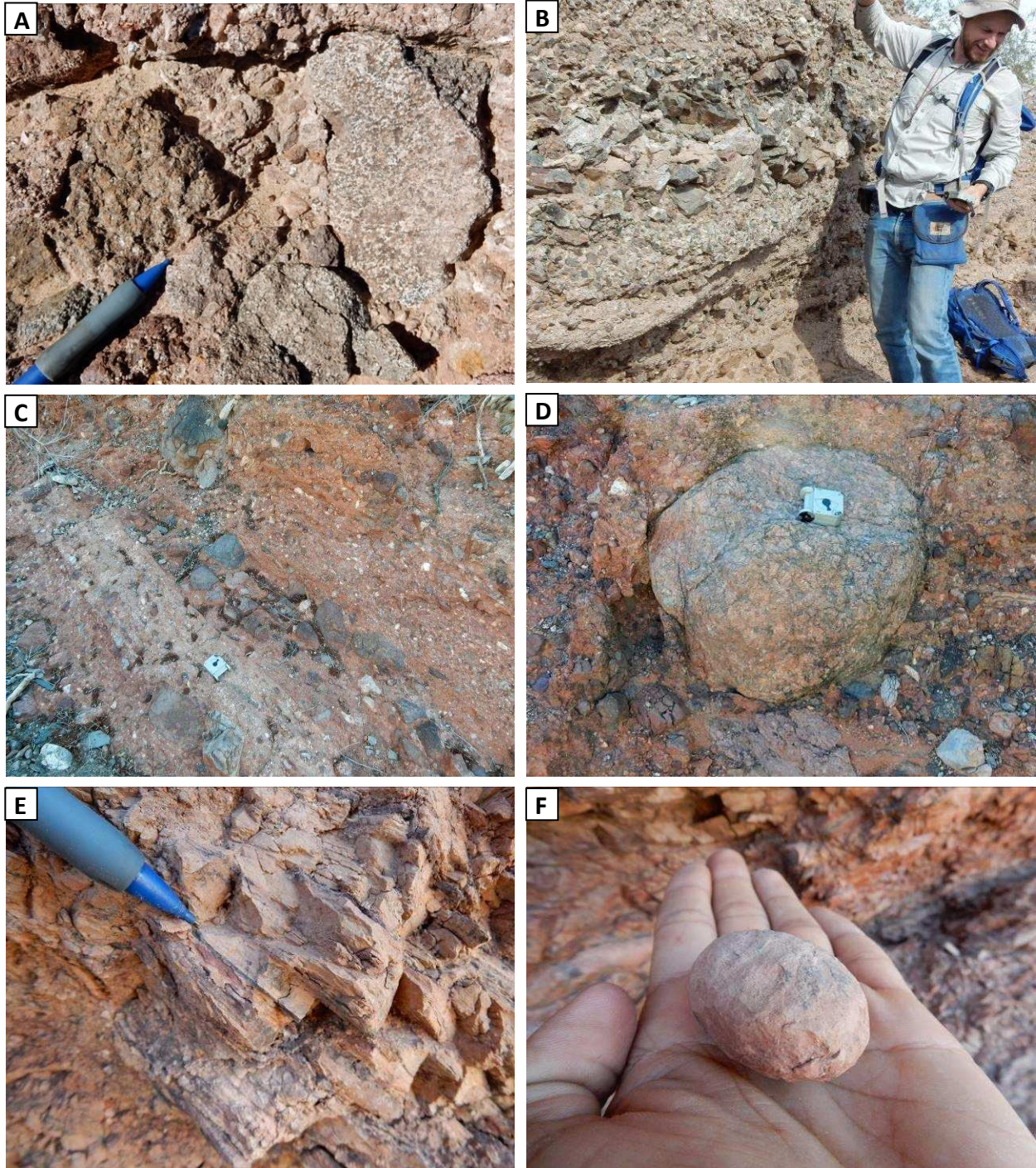
boulders. Channels are incised 0.5–6 m into bedrock and Qoal. **Qeol** is unconsolidated, moderately vegetated, tan-colored, fine- to very-fine sand deposits consisting of ~97% quartz. Most sand is subangular to subrounded and well sorted. This unit is deposited on Qoal, contains scattered colluvium clasts, and has locally accumulated into dunes, typically on the flanks of colluvium mounds or bedrock slopes (Figure 30 E). Locally a weakly-consolidated, 1–3 mm-thick crust is developed a few centimeters beneath the surface. **Qoal** is mostly paleo-terraces composed of weakly-consolidated, clast-supported colluvium and alluvium with a silt matrix. Clasts are mostly angular to subangular, pebble to cobble in size with sparse boulders, and are commonly imbricated. Terraces are locally >6 m thick where incised by active channels (Figure 30 F). This unit is moderately vegetated in most areas, but lightly to scarcely vegetated where desert pavement is developed. On the northwest side of the range colluvium and alluvium terraces are locally moderately to well consolidated.



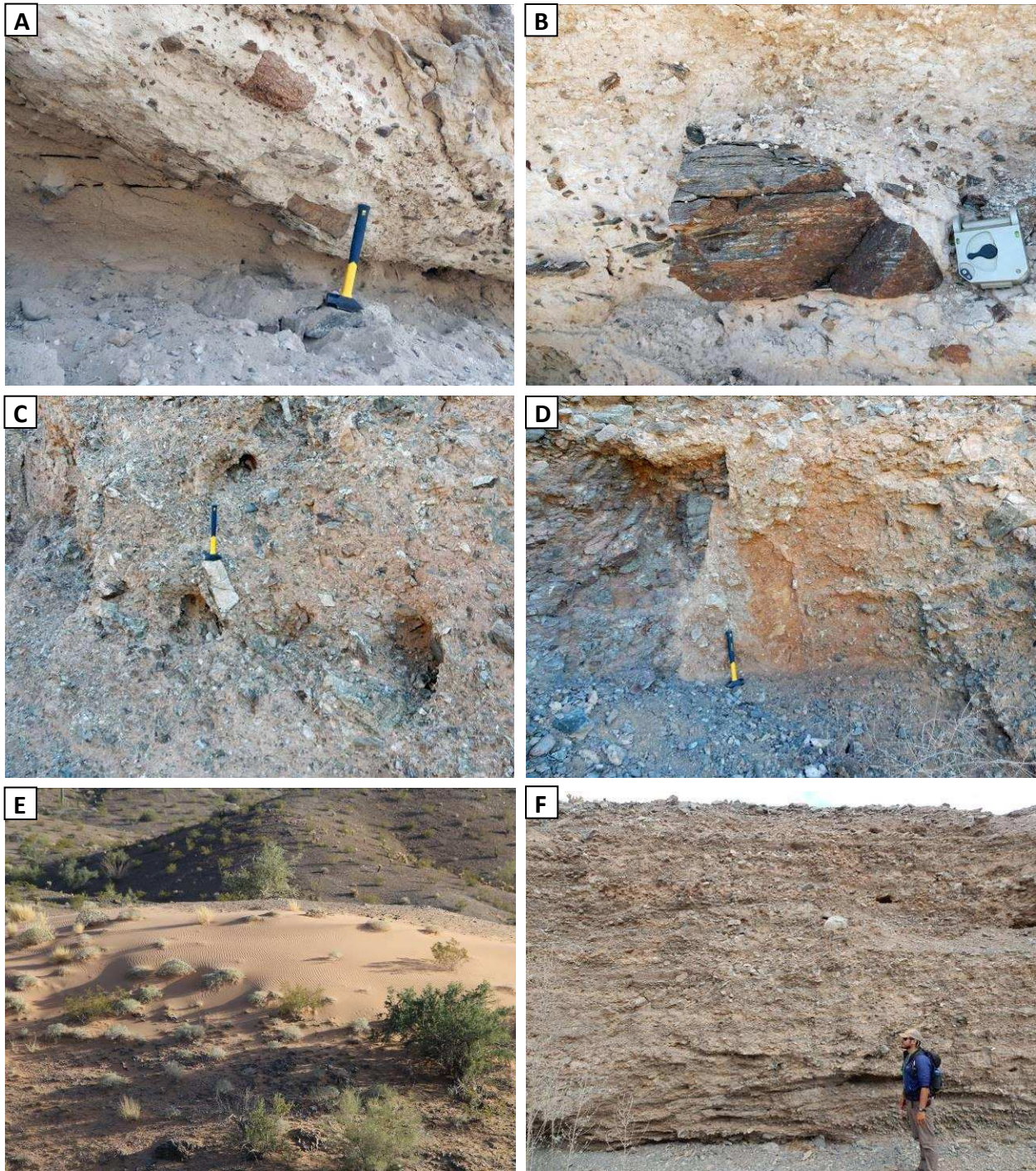
**Figure 27:** Photographs and photomicrographs of mylonitic quartzite and marble from the northern Plomosa Mountains. **A)** Interlayered mylonitic quartzite and marble showing clear rheological differences between the two. An intensely fractured quartzite layer intersects the hammer handle. More coherent, non-intensely fractured layers are marble. **B)** Isoclinally folded marble (gray) with thin layers of quartzite (tan). The marble is commonly cherty as seen below the pencil. Foliation in the marble can be seen in the upper-right of the photograph. **C)** Photomicrograph (PPL) of quartzite with minor chlorite [115-P1a]. **D)** Same as C ( $1\lambda$  plate), showing dynamically recrystallized quartz with roughly equant polygonal shapes, indicative of subgrain rotation. **E)** Photomicrograph of marble with abundant tremolite [115-P15]. **F)** Photomicrograph of marble dominantly of calcite, showing pressure solution cleavage where opaque minerals have been concentrated [115-P15].



**Figure 28:** Photographs and photomicrographs of postmylonitic dikes from the northern Plomosa Mountains. **A)** Example of a typical outcrop of rhyo-dacite dikes as linear piles of angular boulders. **B)** Near-vertical nonmylonitic dike (parallel to and right of hammer handle) cutting through foliated rock (foliation is approximately horizontal). **C)** Photomicrograph (PPL) of a rhyo-dacite dike collected from around photograph A [0316-P119]. **D)** Same as C (XPL). **E)** Photomicrograph of the nonmylonitic dike from B [1115-P25a]. **F)** Same as E (XPL). In the lower-left is a relic euhedral grain, with a core entirely replaced by calcite, and a rim of chlorite. This sample from within the alteration zone  $Nic_a$  is intensely chloritized and strongly sericitized, and has calcite mineralization.



**Figure 29:** Photographs of unit Ncg from the northern Plomosa Mountains. **A)** The pale salmon to tan conglomerate Ncg<sub>t</sub>. **B)** John Singleton standing on unit Ncg<sub>t</sub>, measuring the orientation of an overlying sedimentary breccia, likely the same breccia as subunit PIQcg<sub>m</sub>. **C)** The reddish-tan conglomerate Ncg<sub>r</sub>, Brunton for scale. **D)** Example of a well-rounded pegmatitic granite boulder in unit Ncg<sub>r</sub>. **E)** Close-up of the siltstone Ncg<sub>s</sub>. **F)** Example of a nodule found within the siltstone.



**Figure 30:** Photographs of units PIQcg, Qoal, and Qoel from the northern Plomosa Mountains. **A)** The silty sandstone PIQcg<sub>s</sub> with clasts of mylonite. **B)** A close up of a mylonite clast in unit PIQcg<sub>s</sub>. **C)** The sedimentary breccia PIQcg<sub>mv</sub>, about 10 m east of the fault contact in photograph D. **D)** Fault contact of unit PIQcg<sub>m</sub> (right) with unit KXgn (left). **E)** An isolated accumulation of sand of unit Qoel. **F)** Deeply incised alluvium/colluvium of unit Qoal. Andrew Griffin for scale.

## **6. Mineralization and Alteration**

Two periods of mineralization and alteration are interpreted to have occurred in the footwall of the Plomosa Mountains detachment fault: 1) syn-detachment mineralization and alteration, and 2) post-detachment veining.

### **6.1. Syn-detachment mineralization and alteration**

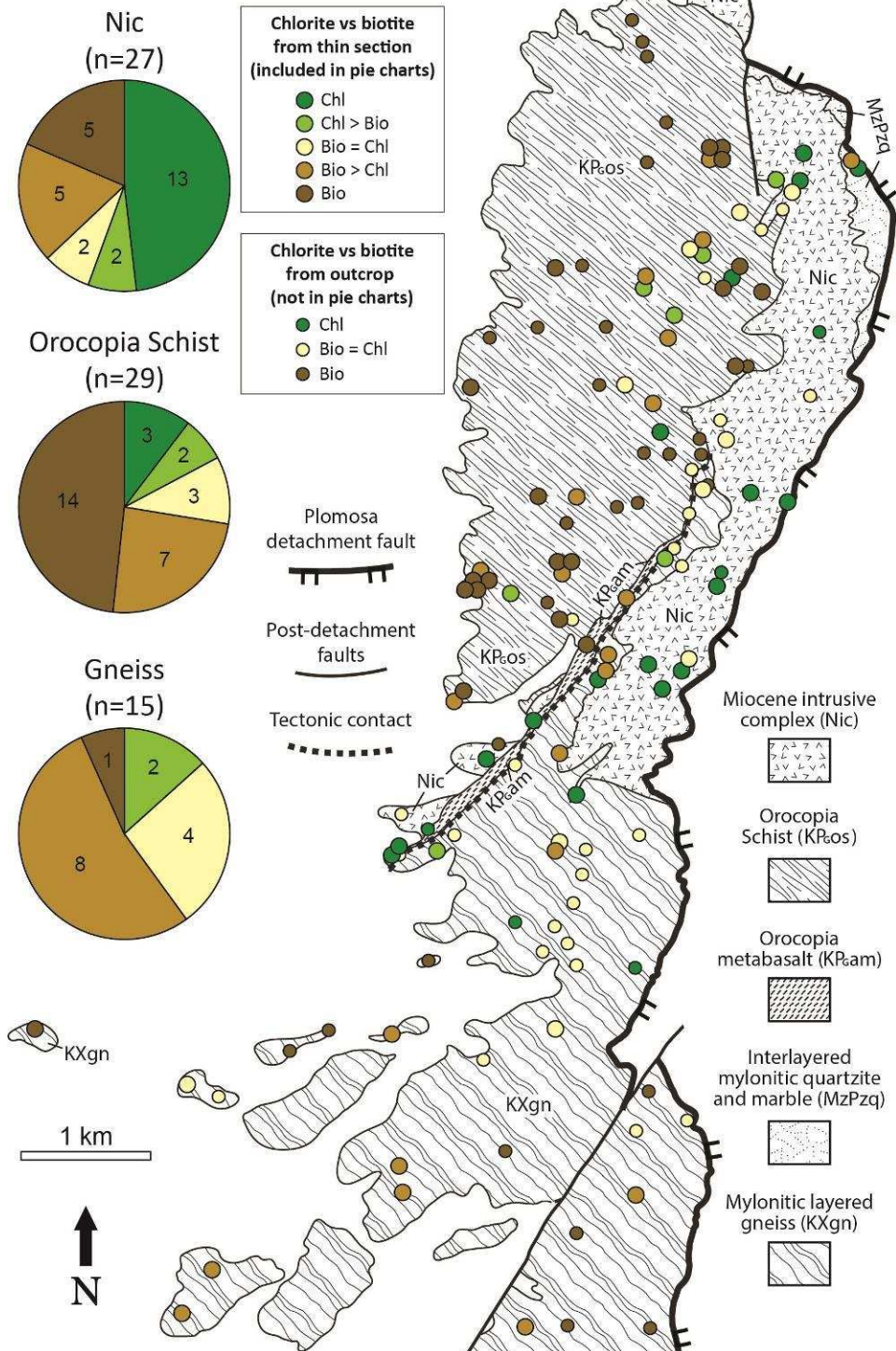
A pale-colored zone (unit Nic<sub>a</sub>, Plate 1; Figure 8) that corresponds to pervasive chloritization and sericitization is present throughout most of unit Nic. It was determined that the degree of chloritization and sericitization within footwall units correlates most clearly with the rock type, with a strong association of alteration with the unit Nic (Figures 31 and 32). Dikes and sills of the unit Nic outside of the mapped area of unit Nic (and outside of the alteration zone Nic<sub>a</sub>) are commonly completely chloritized and moderately to strongly sericitized, while the host rock (i.e. Orocopia Schist) is often entirely unaltered (Figure 33). The association of chloritization and sericitization with the intrusions suggests that they were the focus of substantial fluid flow, and perhaps acted as conduits for fluids escaping magma from greater depth, and the association of the alteration zone (Nic<sub>a</sub>) with the Miocene intrusive complex suggests that alteration is Miocene in age and was driven by magmatically-derived hydrothermal fluids. The alteration zone (Nic<sub>a</sub>) is spatially associated with the detachment fault only inasmuch that it directly overlaps with the Miocene intrusive complex that borders the detachment fault, which would have been the locus of the most fluid flow.

Figure 34 are photomicrographs of veins inferred to be associated with detachment faulting observed in the footwall of Plomosa detachment fault. Mineralization throughout the footwall includes chlorite and lesser calcite, epidote, allanite, and uncommon pale

fibrous amphibole as veins and fracture coatings (chlorite and epidote are predominantly observed to coat fractures), though this mineralization is greatest in unit Nic<sub>a</sub>. Locally, veins of feldspar were also observed in thin section, and are assumed to have formed prior to the previously mentioned mineralization, though still during detachment faulting. Mylonitized quartz veins are also locally present, and may be evidence of a synmylonitic fluid system.

Earthy and specular hematite, and local copper mineralization (mostly chrysocolla ± malachite, Figure 35 A), occurs along steeply- to moderately-dipping normal faults that have accommodated NE-SW extension, and thus this mineralization is inferred to have occurred during detachment-related extension. This mineralization also occurs in smaller fractures, is often exposed in prospect excavations, and is present throughout the footwall with no apparent spatial relationship to the Plomosa detachment fault, nor did the detachment fault seem to host such mineralization (Figure 35 C). Joints and fractures commonly have a 1–5 cm-thick bleached zones which commonly contain disseminated pyrite visible with a hand-lens (Figure 35 B). These bleached zones are more resistant than the surrounding rock, suggesting the rock has had a loss of mica and/or an increase in quartz, and are interpreted to have undergone quartz-sericite-pyrite (QSP) alteration.

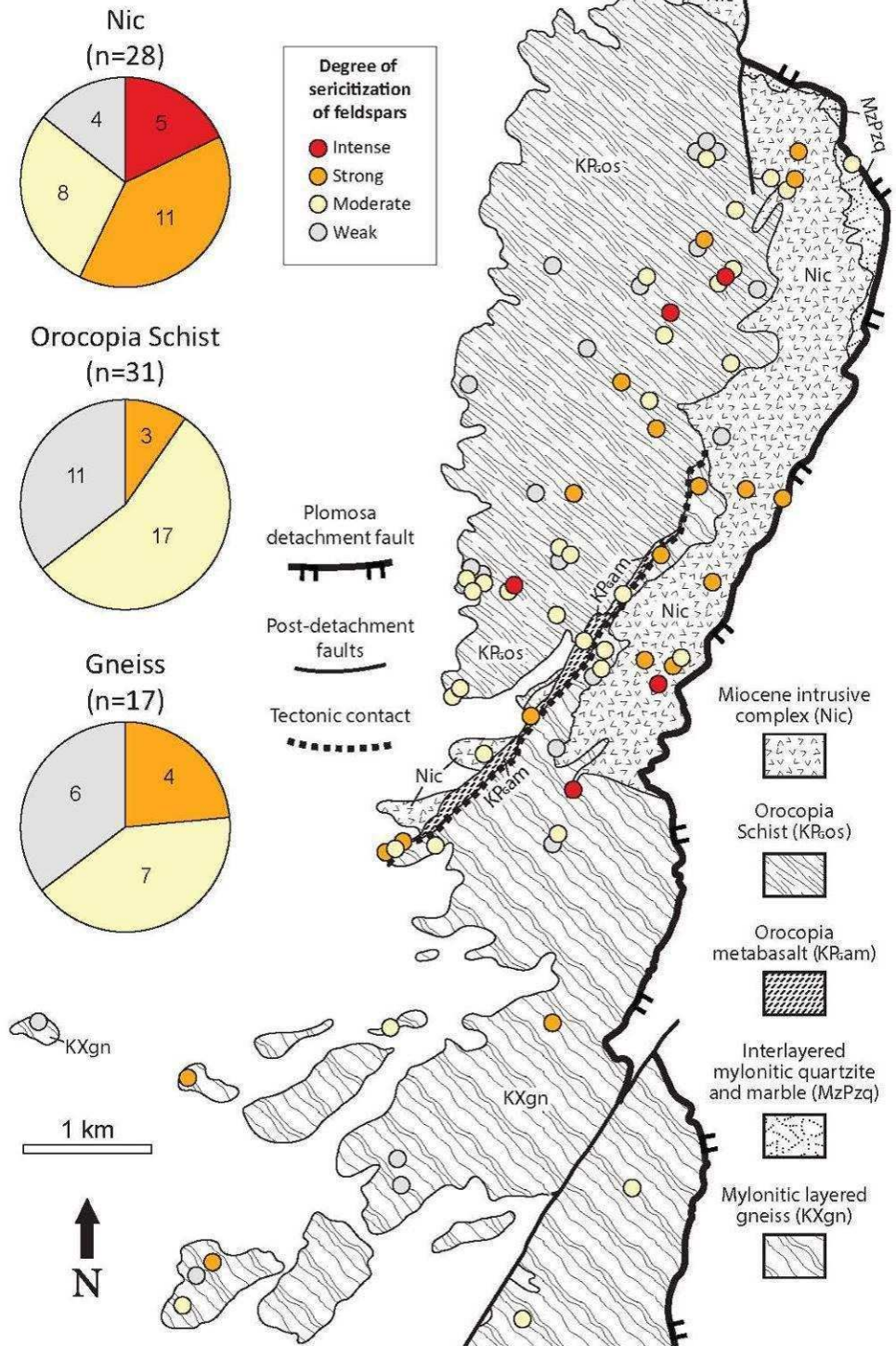
## Degree of chloritization



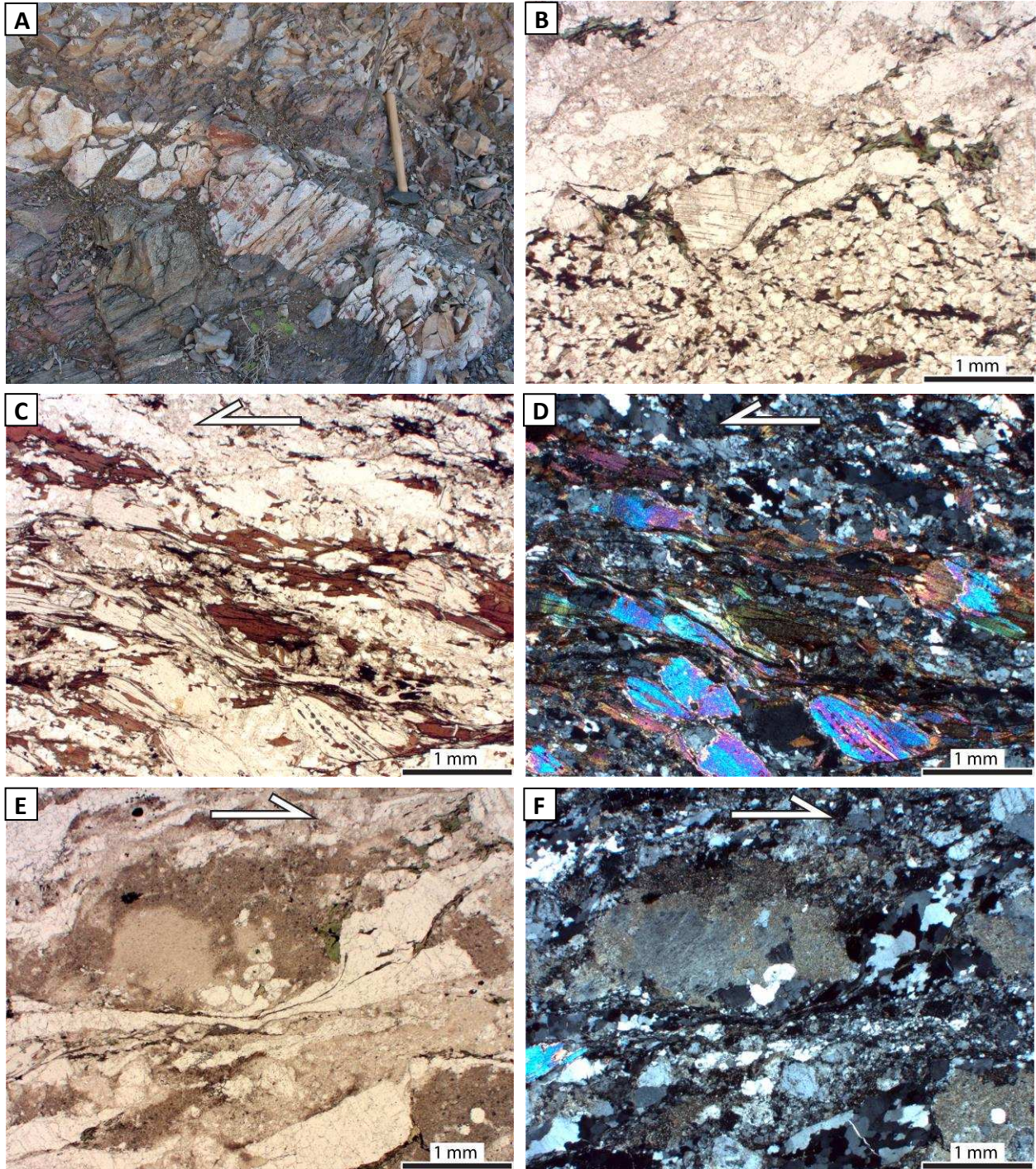
**Figure 31:** The degree of chloritization in the footwall of the Plomosa detachment fault, as determined from thin section (larger circles) and outcrop (smaller circles). Pie charts display the degree of chloritization as separated by the three main units (including only the data derived from thin sections), illustrating that unit Nic is commonly completely chloritized.



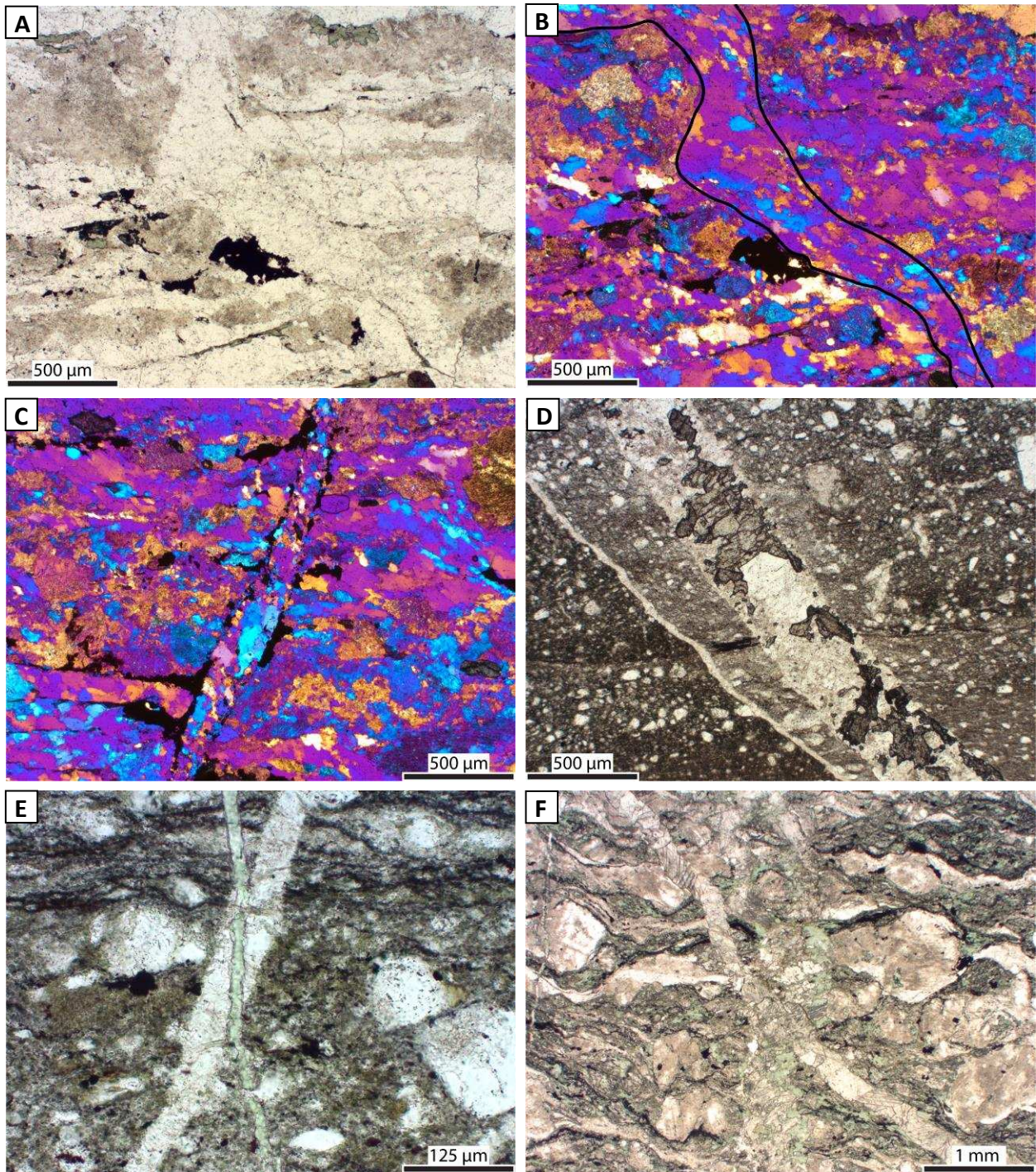
### Degree of sericitization



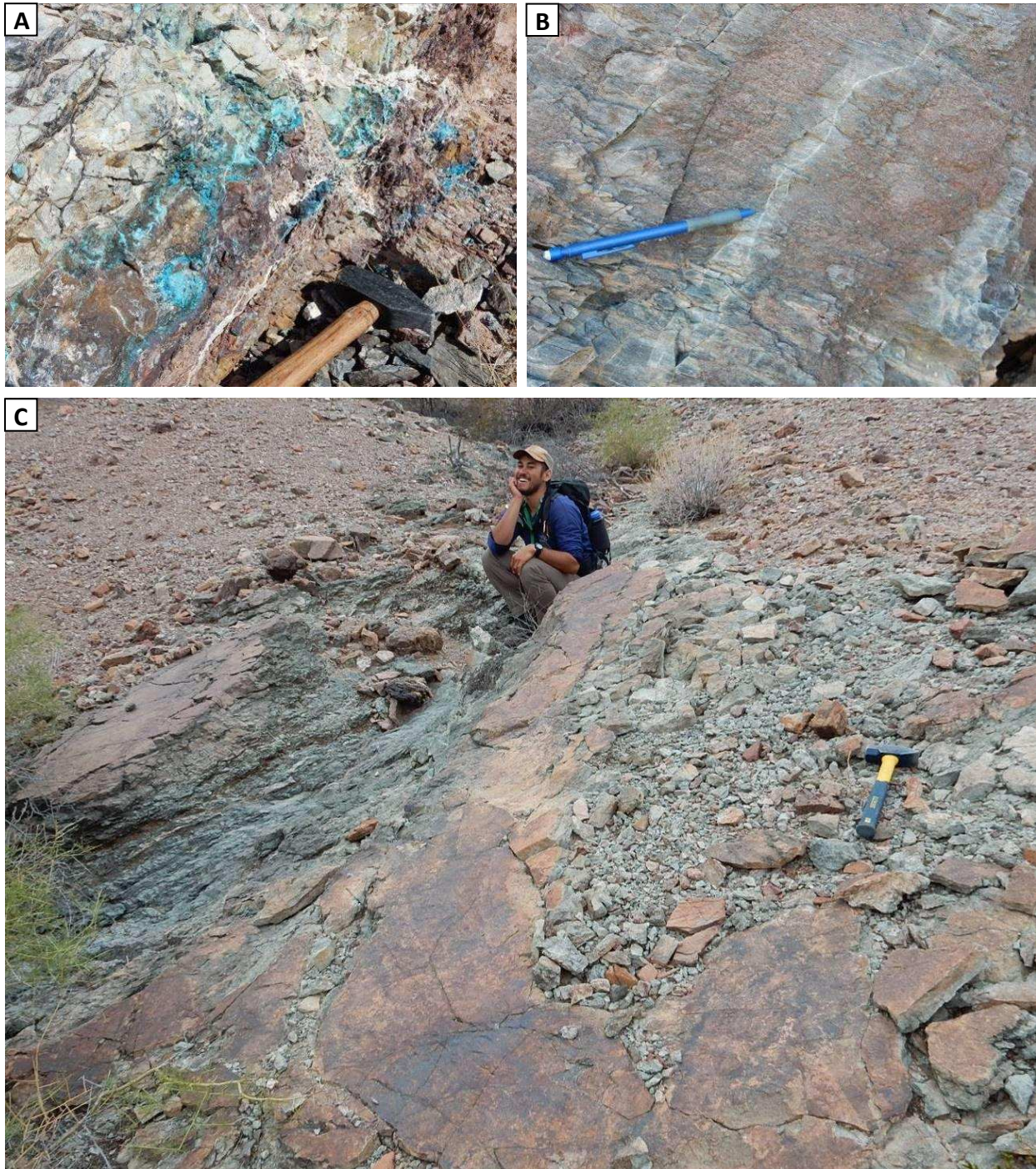
**Figure 32:** The degree of sericitization in the footwall of the Plomosa detachment fault, as determined from thin section. Pie charts display the degree of sericitization as separated by the three main units, illustrating that unit Nic is usually strongly to intensely sericitized, and is the only unit to have undergone intense sericitization.



**Figure 33: A)** Photograph of a leucocratic dike intruded into Orocopia Schist. **B)** Photomicrograph (PPL) of the contact between the dike (top) with Orocopia Schist (bottom) from A [0316-P80ab]. Within the dike biotite is mostly chloritized, whereas abruptly into the Orocopia Schist the biotite is not at all chloritized. **C)** Photomicrograph (PPL) of Orocopia Schist collected directly adjacent to the dike in A, exhibiting completely fresh biotite [0316-P80a]. **D)** Same as C (XPL). **E)** Photomicrograph (PPL) of the dike in photo A, exhibiting strongly sericitized feldspars, and a minor amount of chlorite with no biotite present [0316-P80b]. **F)** Same as E (XPL). There is minor muscovite in this intrusion, visible in the bottom left corner.



**Figure 34:** Photomicrographs of veins in the northern Plomosa Mountains. **A)** Mylonitic quartz vein (PPL) in unit Nic [1016-P368]. **B)** Same as A (XPL), with the edges of the quartz vein traced. **C)** A feldspar vein in unit Nic (same sample as A) along the edges of which opaque minerals have been concentrated, as well as within foliation intersecting the vein. **D)** A vein of feldspar (light colored) and epidote (darker colored) in Orocopia Schist [1016-P194]. **E)** A feldspar vein (white) cut by a chlorite vein (pale green) in Orocopia Schist (same sample as D). **F)** A vein of calcite + chlorite (centered and vertical) in unit Nic, cut by a vein purely of calcite (extending from upper left to lower right) [PI-65]. This sample is from directly adjacent to the Plomosa detachment fault within unit Nic<sub>a</sub>, whereas the other samples are from just west of unit Nic<sub>a</sub>.



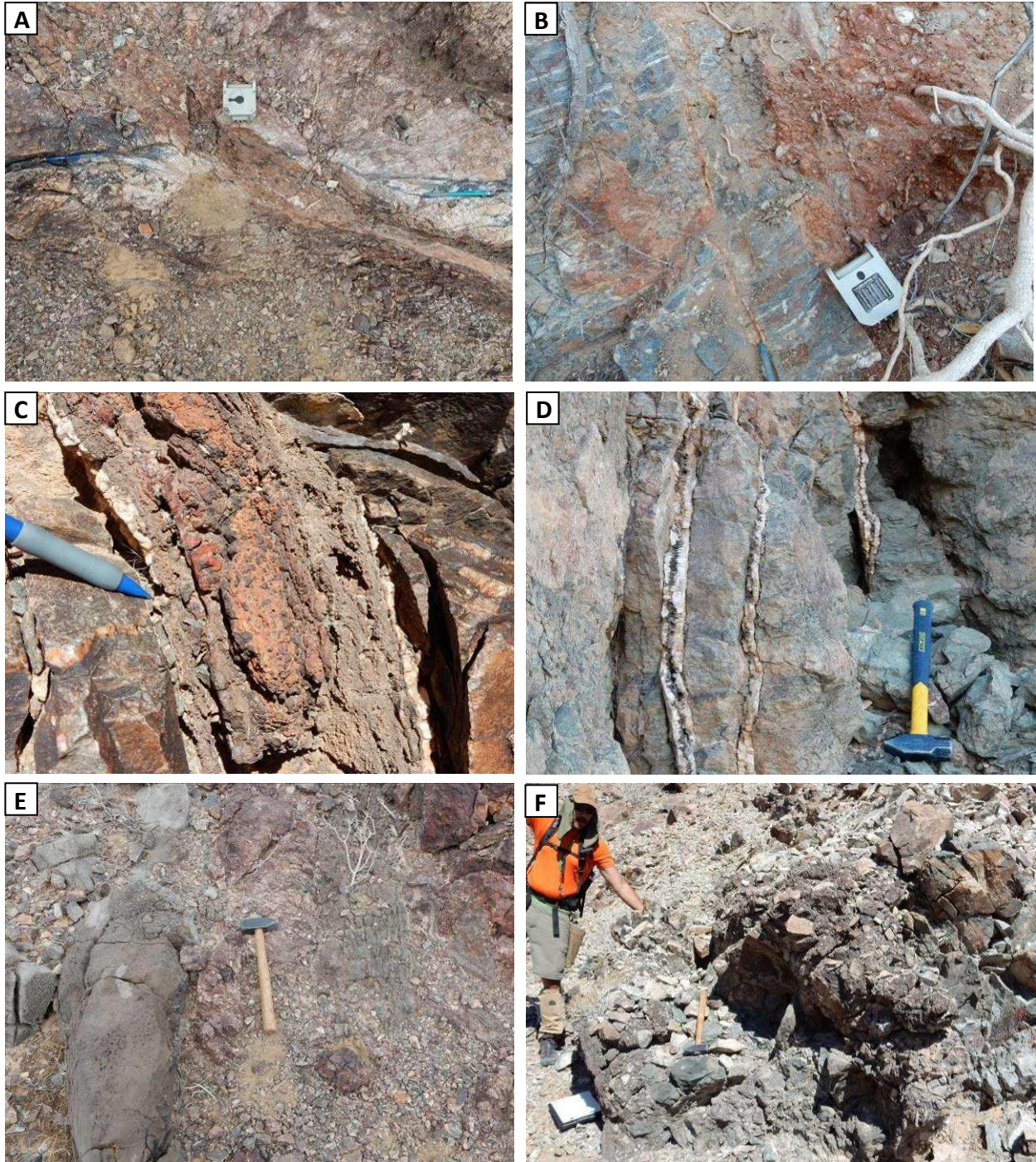
**Figure 35:** Photographs of extension-related mineralization and alteration. **A)** Chrysocolla mineralization along the damage zone of a normal fault with hematite mineralization concentrated near the fault plane. **B)** A fracture in Orocopia Schist along which the rock has been bleached and has become more resistant due to a loss of mica and increase in quartz. **C)** Principal slip plane of the Plomosa detachment fault (the orange-tan surface above the greenish-gray brecciated rock below) dipping shallowly to the ESE (left). Note there is a lack of significant mineralization (such as copper mineralization) below the detachment surface except for moderate chloritization of the brecciated footwall.

## 6.2. Post-detachment veining

In two locations, barite veins are observed to cut brittle structures associated with NE-SW extension, and the veins are generally parallel to a NE-striking fault, and locally parallel to a N-striking fault, both of which cut the Plomosa detachment fault (Figure 36 A & B). The carbonate veins have a similar orientation, and are locally observed to be parallel to the N-striking post-detachment fault. These relationships, in conjunction with the unique orientations of these features, strongly suggest the barite and carbonate veins are the result of post-detachment mineralization.

Figure 36 C and D are photographs of barite veins observed in the footwall of the Plomosa detachment fault. The typical mineralization of these veins is barite ± hematite ± carbonate ± carbonate-cemented breccia ± agate/chalcedony, with barite typically on the outer edges, and carbonate and carbonate-cemented breccia towards the center. Veins are generally 1–10 cm thick; barite is 0.5–1 cm thick on either edge of a vein, and hematite where present commonly constitutes the breccia. Minor Mn-mineralization was identified via a portable XRF (pXRF) analysis of hematite encrusting barite, which reported ~50% Fe and 7.5% Mn.

Figure 36 E and F are photos of carbonate veins and carbonate-cemented breccia zones in the footwall of the Plomosa detachment fault. These carbonate veins and breccia zones are generally 0.2–1.5 m wide and appear to lack other mineralization, though a pXRF analysis of a sample of calcite from a vein reported >9000 ppm S, >8000 ppm Mn, and >3000 ppm Fe.



**Figure 36:** Photographs of post-detachment veining. **A)** A barite-mineralized dextral fault (extending from upper-left to lower-right) cutting across a hematite-mineralized normal fault (horizontal on page). Two pencils mark the offset portions of the normal fault. **B)** The NE-striking sinistral-normal fault that cuts the detachment (Brunton leaning against fault plane). The pencil points to a thin barite vein that parallels the fault plane. **C)** Barite + agate + hematite + carbonate vein exhibiting the typical zonation; thin barite on the edges, and brecciated hematite cemented by carbonate in the center. **D)** Fairly typical barite veins, though these veins have a coating of hematite in the center, which is not always present. **E)** Left of the hammer is a ~30 cm thick carbonate vein, and to the right is a parallel vein of similar thickness comprised of repeated carbonate veins each a few cm wide. **F)** A carbonate-cemented breccia zone, centered and to the lower-right, casting the large shadow.

## 7. Mylonitization and Metamorphism

### 7.1. Mylonitic fabric field observations

Within the map area mylonitic fabrics are pervasive throughout the footwall of the Plomosa detachment fault, which include L-S tectonites, L>S tectonites, and localized L-tectonites (Figure 37 A, B, & I). L>S fabrics are observed to occur throughout the Orocopia Schist and the gneiss, indicative of a component of constriction during mylonitization, and include “contorted” foliation that wraps around tight/isoclinally folded coherent layers, often observed in the Orocopia Schist (Figure 37 C–F). Fold axes of the folded coherent layers are observed to be parallel to the mylonitic lineations, and these folds often have attenuated and thickened limbs. Mylonitic leucocratic dikes of unit Nic are often observed to be isoclinally folded within the schist (Figure 37 D), and also have attenuated and thickened limbs, indicating these dikes are pre- or synmylonitic. The formation of such ductile folds during noncoaxial-dominated shear in a constrictional setting is consistent with deformation in the in the Central Mojave metamorphic core complex in southern California, where Fletcher and Bartley (1994) interpret footwall folds to have initiated as upright open folds, progressing to inclined tight folds, and finally becoming recumbent isoclinal folds, with fold axes parallel to the stretching direction.

Within unit KXgn, well-foliated and -lineated granitoid layers were preferentially measured over gneissic foliation of amphibolite layers, which parallel the mylonitic foliation. Gneissic foliation of unit KXgn was observed to be discordant to the mylonitic foliation in one location (Figure 37 G). Gneissic layering of the Orocopia amphibolite (unit KPGam) has a very different orientation than the overall mylonitic fabric throughout the footwall; it dips moderately/steeply to the SE, and is undulatory with recumbent open-fold

axes parallel to strike (Figure 37 H). However, mylonitic foliation of interlayered Orocopia Schist and intrusions locally conforms to the gneissic layering within and adjacent to the unit KPGam. A zone of L-tectonites is present within the gneiss and unit Nic directly adjacent to unit KPGam (Plate 1; Figure 37 I). Regional constrictional strain may have been concentrated along unit KPGam due to rheological differences between the Orocopia Schist and gneiss, creating L-tectonites rather than L>S tectonites at this boundary.

Based on reconnaissance mapping the mylonitic front is located ~2 km south of the mapping area (Figure 38), which is the structurally highest limit of mylonitic fabrics. The mylonitic front is gradational, transitioning from mylonite to protomylonite to nonmylonite, with sparse discrete shear zones within the protomylonite and nonmylonite concentrated near the mylonitic front. Within 500 m of the mylonitic front, SW-dipping shear zones were observed with top-to-the-SW displacement (Figure 36 J), and a sample of mylonitic gneiss records top-to-the-SW shear at the microscale. Similar antithetic shear zones concentrated adjacent to the mylonitic front are documented in nearby metamorphic core complexes (Figure 5; Reynolds and Lister, 2000).



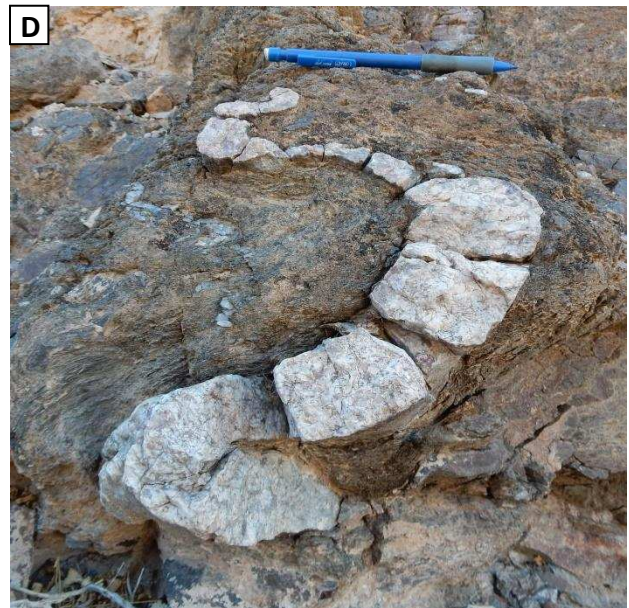
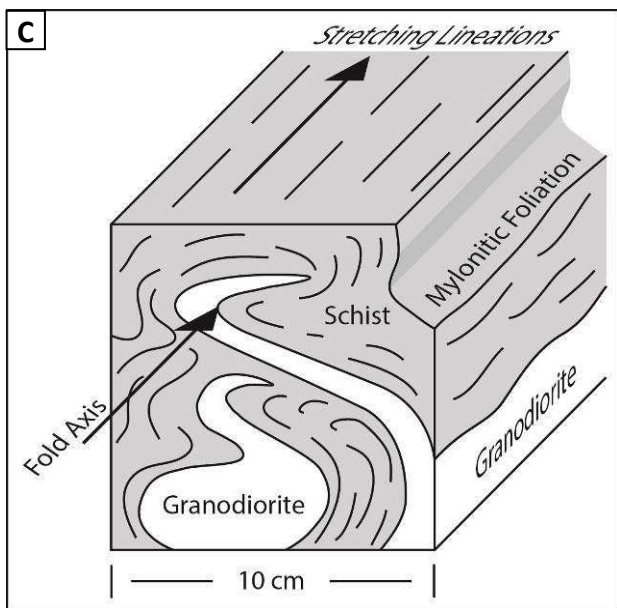
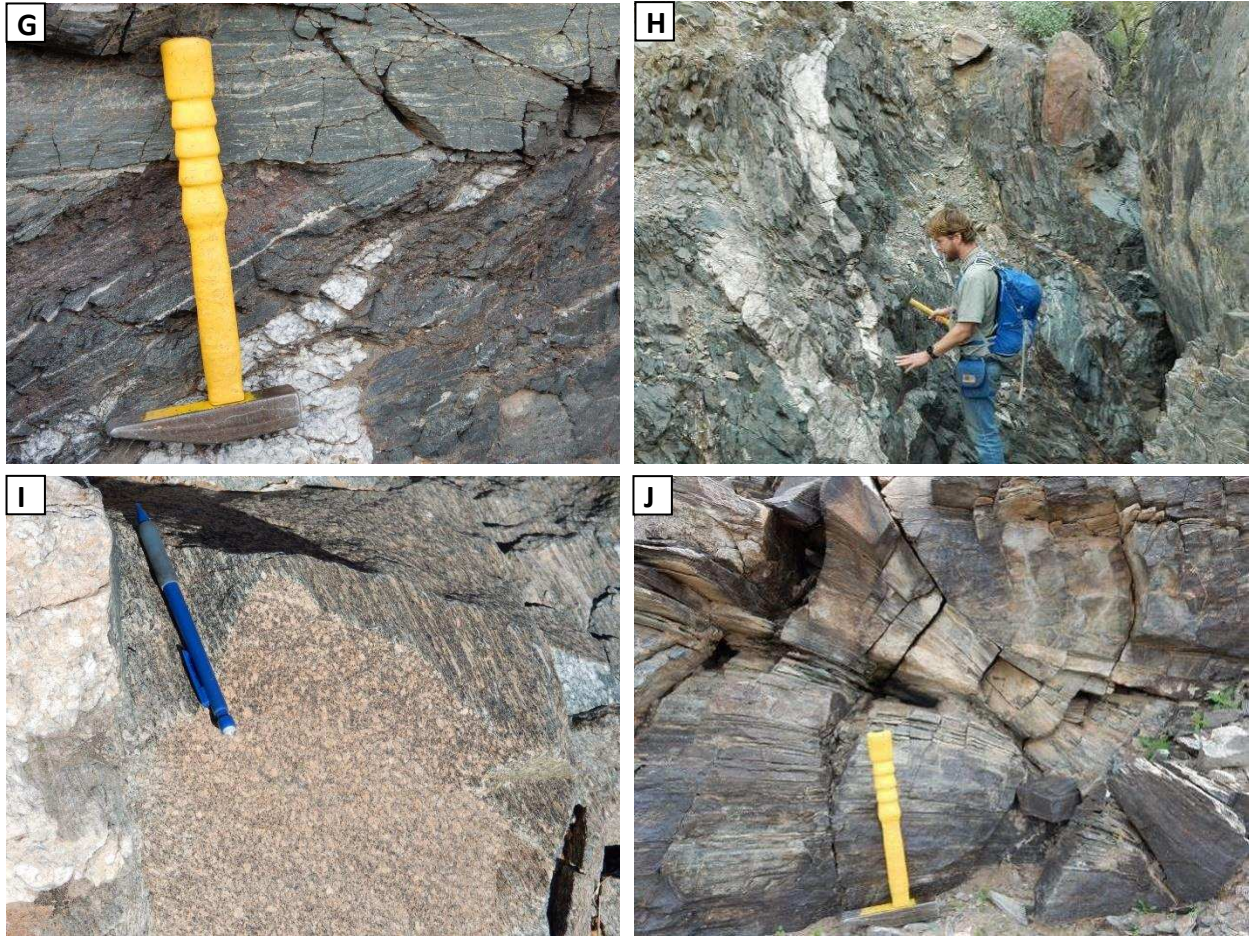
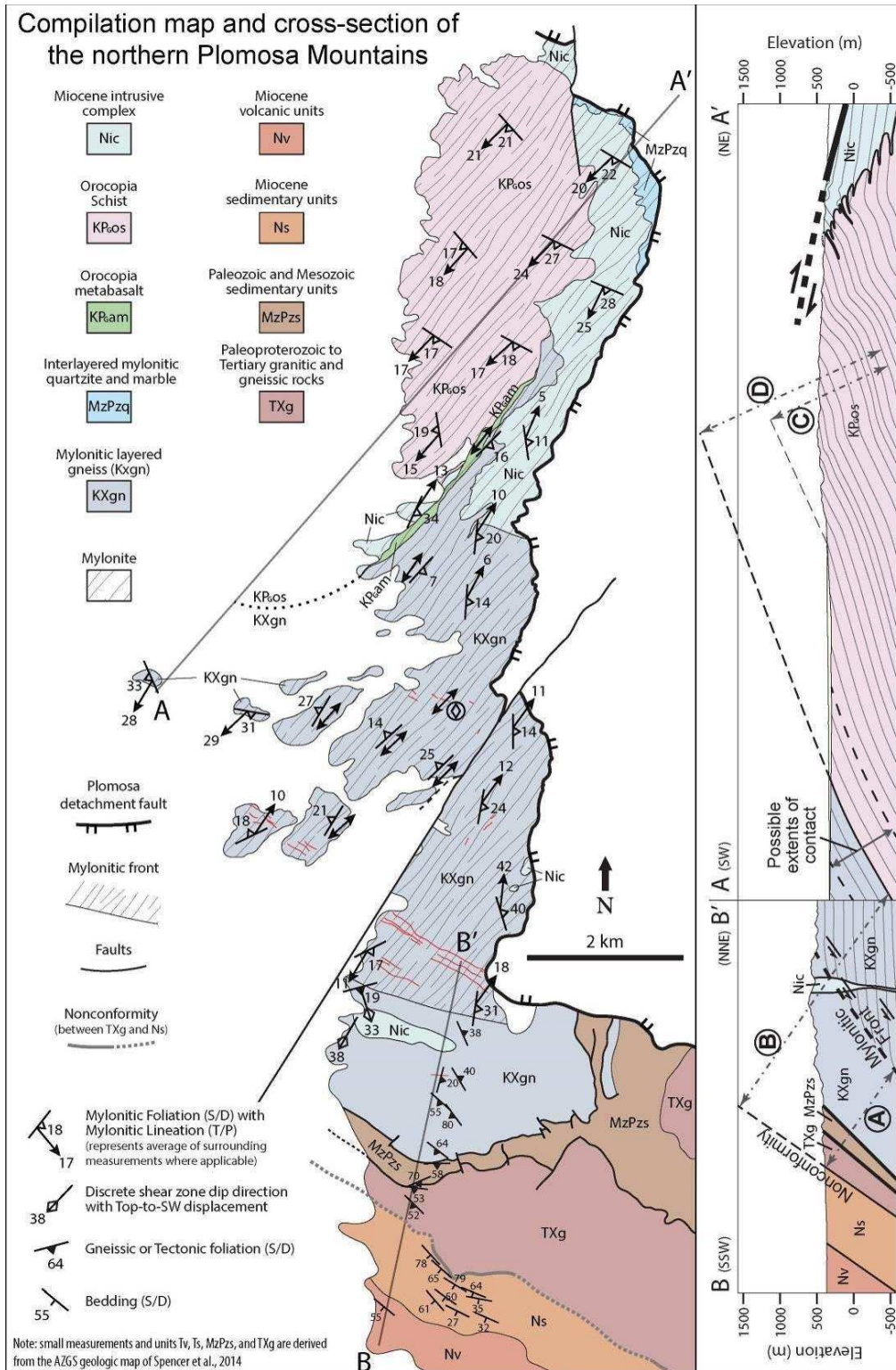


Figure 37: Continued on next page.



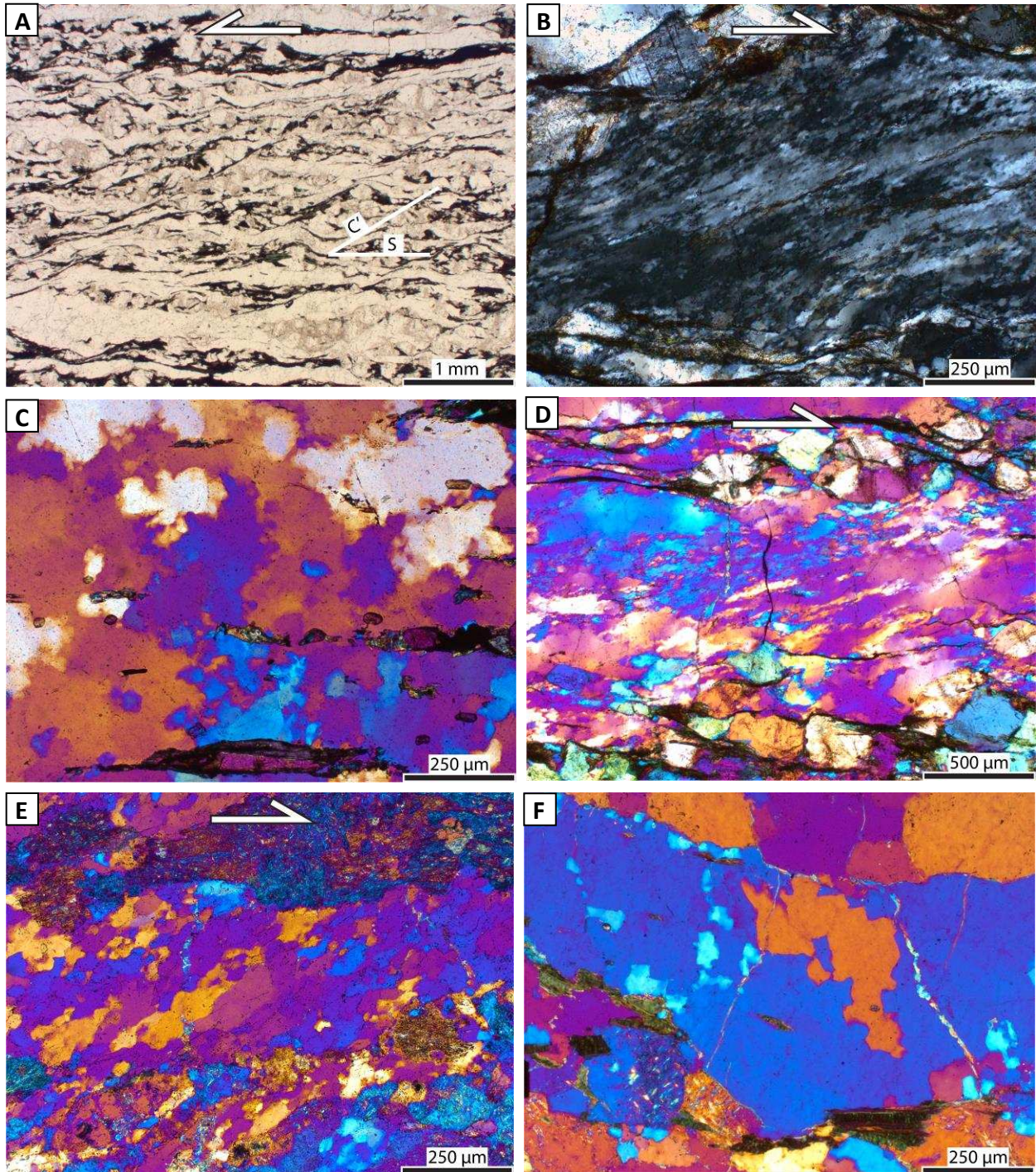
**Figure 37 continued:** Photographs of foliation and lineation fabrics from the northern Plomosa Mountains. **A)** Example of an L-S tectonite, with very planar mylonitic foliation. Pencil is on the mylonitic foliation plane, set parallel to the mylonitic lineation. **B)** Example of an L>S tectonites, viewed perpendicular to the mylonitic lineations. Pencil is set on a mylonitic foliation plane, and is parallel to the mylonitic lineations. **C)** Block diagram illustrating the relationship between isoclinally-folded coherent layers and the mylonitic foliation within the Orocopia Schist, as shown in the photographs D–F, and illustrates how fold axes are parallel to the stretching lineations. **D)** Isoclinally folded leucocratic intrusion of the unit Nic within Orocopia Schist. Pencil is not oriented. **E)** Open/tight fold within Orocopia Schist. Pencil is parallel to the fold axis. **F)** Isoclinally folded meta-arkose layers within the Orocopia Schist. **G)** Gneissic foliation (bottom) cut by mylonitic foliation (top) within the gneiss. **H)** Subvertical undulatory foliation of Orocopia metabasalt (unit KPGam), with a subvertical leucocratic sill left of John Singleton. **I)** Example of an L-tectonite as found in the zone adjacent to unit KPGam. Pencil is set parallel to the mylonitic lineations. **J)** SW-dipping discrete shear zone with top-to-the-SW displacement, south of the map area near the mylonitic front.



**Figure 38:** Compilation map and cross-section of the northern Plomosa Mountains. Units in the left column are the results of this study. Units in the right column are from Spencer et al. 2015. Labels A–D in the cross-section are projections of paleodepths and structural thicknesses, the values for which are reported in the Discussion section.

## 7.2. Mylonitic fabric microstructural observations

Microstructural shear sense indicators include S-C and S-C' fabrics (Figures 11 A & B and 39 A), oblique grain shape orientation in dynamically recrystallized quartz (Figure 39 B), mica-fish (Figure 11 A & B), and sigma-clasts (Figure 26 E & F), all of which consistently record top-to-the-NE shear throughout the footwall in the map area (Plate 1, inset map of mylonitic lineations). Dynamically recrystallized quartz grains commonly form interconnected equant, somewhat irregular polygons, ~10-100  $\mu\text{m}$  in diameter (Figure 39 B), or larger very irregular amoeboid shapes often >200  $\mu\text{m}$  across (Figure 39 C). Large amoeboid grains are often rimmed with the smaller polygonal grains, and the two sizes are often intermixed (Figure 39 D & E). The smaller polygonal and larger amoeboid dynamically recrystallized quartz grains are indicative of the quartz having undergone subgrain rotation (SGR) and grain boundary migration (GBR), respectively (Stipp et al., 2002). The amoeboid grains rimmed by smaller equant grains suggest grains formed from GBM have been overprinted by grains formed from SGR (Figure 39 D). In the gneiss, dynamically recrystallized quartz grains locally have grain boundaries with ~90 degree angles (Figure 39 F), referred to as chessboard quartz.



**Figure 39:** Photomicrographs of mylonitic fabrics in the footwall of the Plomosa detachment fault. **A)** S-C' fabric records top-NE shear sense (PPL) [0316-P156]. **B)** Grain-shape preferred orientation in dynamically recrystallized quartz records top-NE shear sense (XPL) [1116-P4]. Fabric is comprised of masses of rounded polygonal quartz grains  $\sim 10\text{--}50\ \mu\text{m}$  in size. **C)** Example of irregular amoeboid shapes of dynamically recrystallized quartz grains, some of which are  $>200\ \mu\text{m}$  in size ( $1\lambda$  plate) [1016-P274]. Sparse polygonal grains are also present. **D)** A large amoeboid dynamically recrystallized quartz grain (largest blue grain in upper-left) rimmed by smaller polygonal grains ( $1\lambda$  plate) [1116-P4]. **E)** A mixture of larger amoeboid dynamically recrystallized quartz grains and smaller polygonal grains ( $1\lambda$  plate) [0316-P80b]. **F)** Dynamically recrystallized quartz grains with grain boundaries comprised of  $\sim 90$  degree angles, particularly apparent along the boundary of the orange grain right of center ( $1\lambda$  plate) [0316-P94].

### 7.3. Mylonitization conditions

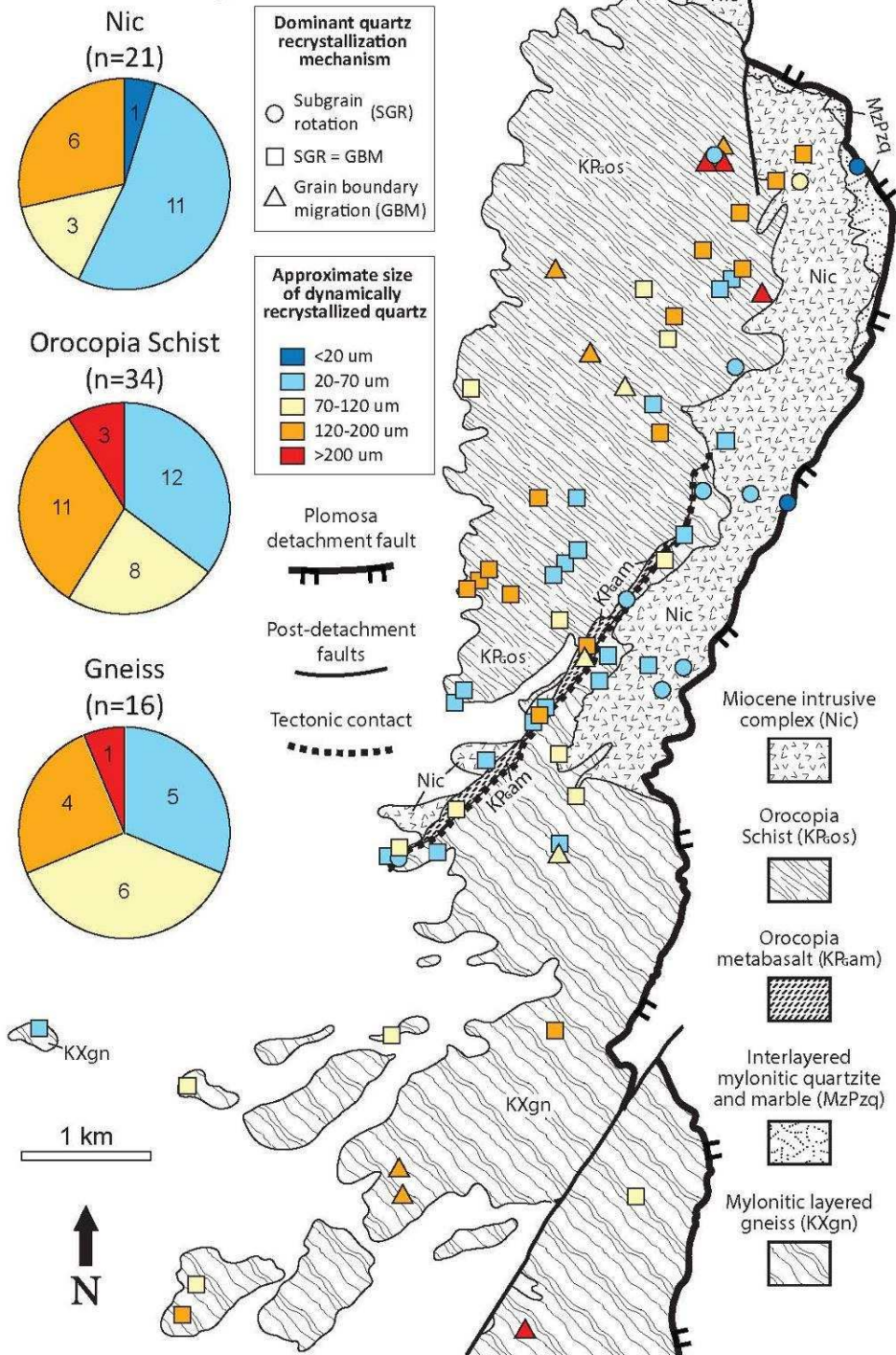
The sizes and recrystallization mechanisms of dynamically recrystallized quartz were recorded for 73 samples of mylonitic rocks in order to document the conditions of mylonitization throughout the footwall of the Plomosa detachment fault (Figure 40). Observed recrystallization mechanisms of quartz include grain boundary migration (GBM) and subgrain rotation (SGR) (fabrics described in previous section), and it was recorded whether one mechanism is dominant or if they are relatively equal in volume (Figure 40). The size of dynamically recrystallized quartz grains correlates to the differential stress present during mylonitization, as well as to the temperature. Higher temperatures promote grain boundary migration which creates larger amoeboid grains (often  $>100\ \mu\text{m}$ ), whereas lower temperatures favors subgrain rotation which creates smaller equant grains ( $\sim 10\text{--}70\ \mu\text{m}$ ). In addition, higher differential stress during SGR consistently yields smaller grains (Stipp et al., 2002).

In the northern Plomosa Mountains, dynamically recrystallized quartz grain sizes range from  $\sim 10\ \mu\text{m}$  to as large as  $300\ \mu\text{m}$ , and there is no clear spatial relationship between grain size and the location of the Plomosa detachment fault, except that the only two samples with recrystallized quartz  $<20\ \mu\text{m}$  occur right along the detachment fault. The Orocochia Schist and gneiss commonly have recrystallized quartz grains averaging  $>120\ \mu\text{m}$  regardless of the distance to the detachment fault and locally have very large recrystallized quartz grains averaging  $>200\ \mu\text{m}$ . Unit Nic on average has the smallest dynamically recrystallized quartz grain sizes, and it was investigated whether lithology of the units was a factor for the sizes of dynamic recrystallized quartz. For example, unit Nic generally has relatively little mica (average of  $\sim 8\%$ ), so quartz would act as the dominant weak phase

during deformation, absorbing strain at relatively high strain rates and differential stresses. On the other hand, the Orocopia Schist has much more mica (average of ~22%) so quartz would act as the dominant strong phase compared to the mica, and thus would expect to deform at lower strain rates and lower differential stresses. Surprisingly, no clear correlation is observed from plotting the modal percent of mica and quartz, or their ratio to one another, versus the size of dynamically recrystallized quartz (Figure 41), suggesting lithology was not an important factor. Another reason why the unit Nic may generally have smaller recrystallized grain sizes than the Orocopia Schist and gneiss is unit Nic may have intruded into the footwall after it was exhumed below temperatures of grain boundary migration (~500°C), while the Orocopia Schist and gneiss were originally at deeper levels to have undergone GBM.

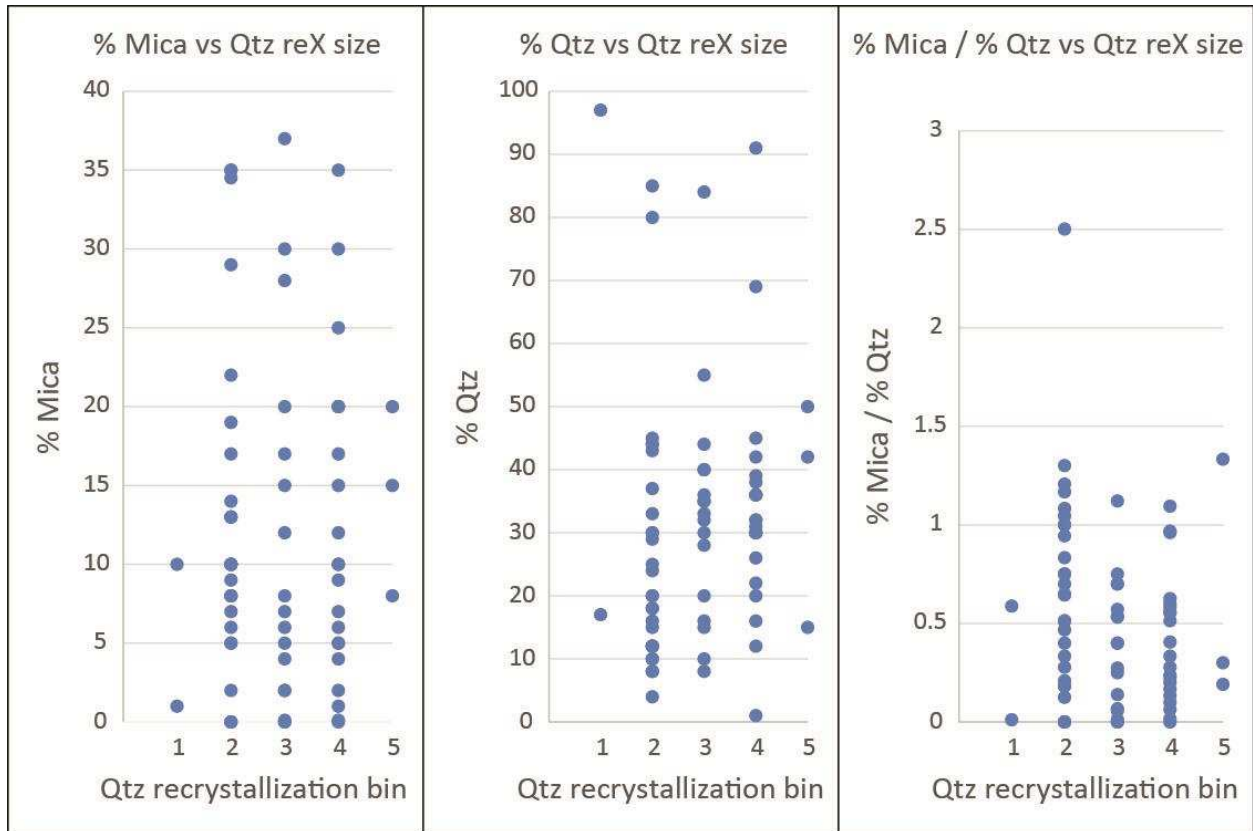
A higher concentration of dynamically recrystallized quartz grains 20–70  $\mu\text{m}$  and 70–120  $\mu\text{m}$  in size occur within one kilometer of either side of the tectonic contact between the Orocopia Schist and gneiss, in contrast to the large percentage of >120  $\mu\text{m}$  grains within the main bodies of the Orocopia Schist and gneiss (Figure 40). Perhaps the smaller grain sizes near the tectonic contact records a concentration of differential stress along the contact, produced by the conditions that created the localized L-tectonites. Alternatively, more intrusions may have been sampled there, which generally have smaller grain sizes as discussed.

## Dynamically recrystallized quartz grain sizes and recrystallization mechanisms



**Figure 40:** Average sizes of dynamically recrystallized quartz and dominant recrystallization mechanism recorded in the footwall of the Plomosa detachment fault. Pie charts display the average sizes as separated by the three main units. Samples dominated by GBM (triangles) with average dynamically recrystallized quartz grains >120  $\mu\text{m}$  (orange and red) suggest temperatures > $\sim$ 500 $^{\circ}\text{C}$  (amphibolite facies). Recrystallized quartz grain sizes 20–70  $\mu\text{m}$  suggest upper- to middle-greenschist facies.





**Figure 41:** Modal % mica, quartz, and ratio of mica/quartz plotted against the average size of dynamically recrystallized quartz as defined by the bins in Figure 40 (bin 1 is <20  $\mu\text{m}$ , bin 2 is 20–70  $\mu\text{m}$ , bin 3 is 70–120  $\mu\text{m}$ , bin 4 is 120–200  $\mu\text{m}$ , and bin 5 is >200  $\mu\text{m}$ ). No pattern is observed, suggesting little to no relationship between lithology of a unit and the size of dynamically recrystallized quartz.

#### 7.4. Metamorphic conditions

The prograde mineral assemblages of the metamorphic units are as follows:

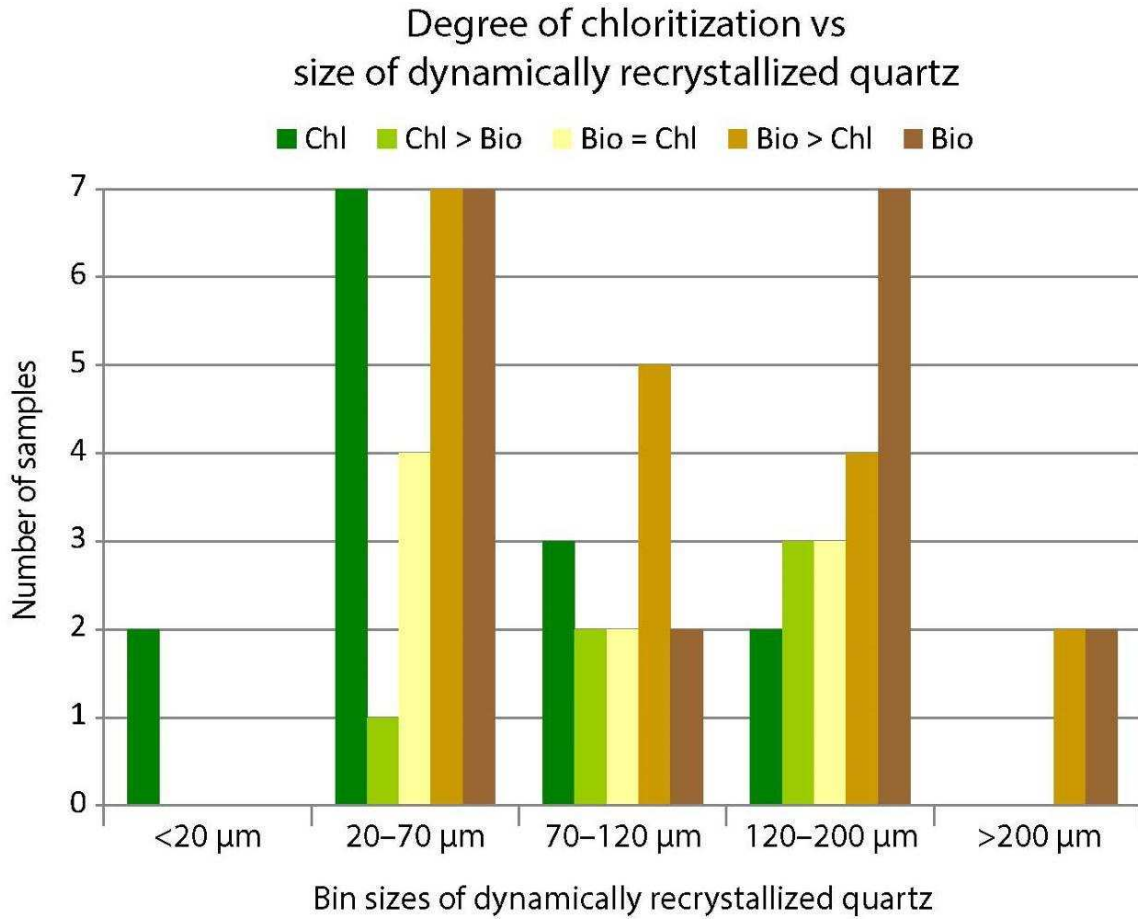
- **Gneiss:** hornblende + biotite + feldspar + quartz
- **Orocopia Schist:** quartz + biotite + feldspar ± muscovite ± actinolite ± garnet
- **Orocopia metabasalt (KPGam):** hornblende + feldspar + quartz ± biotite ± garnet
- **Metachert:** quartz + garnet + hornblende ± actinolite ± biotite
- **Interlayered quartzite and marble:** quartz + calcite + tremolite ± muscovite ± biotite

Evidence for retrograde alteration includes chlorite after biotite and hornblende, which occurs to some degree in every unit these minerals are present, though this alteration is most prevalent in unit Nic, particularly within the alteration zone Nic<sub>a</sub> as discussed. Also, the garnets observed in a sample of Orocopia amphibolite have been replaced by plagioclase + biotite + epidote (Figure 14 B & C), and a nonmylonitic dike has a relic euhedral grain entirely replaced by calcite in the center and chlorite on the rims (Figure 28 E & F). Metamorphic accessory minerals throughout the footwall units include tourmaline, epidote, allanite, and clinozoisite. In addition, the radiating white mica in a sample of unit Nic is likely secondary (Figure 20 D). The prograde mineral assemblages are consistent with amphibolite-grade metamorphism, while the alteration and metamorphic minerals are indicative of partial overprinting by greenschist-grade metamorphism.

The dynamic recrystallization mechanisms of quartz also provide information on metamorphic grade: The presence of GBM suggests deformation under amphibolite-grade metamorphic conditions (~500°C), whereas SGR is typically indicative a deformation under upper greenschist-grade metamorphic conditions (~400-500°C) (Stipp et al., 2002).

One sample of gneiss [0316-P94] from the southern mapping area exhibits dynamically recrystallized chessboard quartz (Figure 39 F), indicative of very high-temperature metamorphic conditions ( $>600^{\circ}\text{C}$ ) (Passchier and Trouw, 2005). SGR is commonly observed to have overprinted GBM (Figure 39 D), consistent with a transition from amphibolite-grade to greenschist-grade metamorphism, as recorded in the mineral assemblages and alteration. In addition, larger dynamically recrystallized quartz grain sizes associated with GBM correlate to fresh biotite, whereas smaller grain sizes associated with SGR correlate to higher degrees of chloritization (Figure 42), bolstering the interpretation that both chloritization and overprinting of GBM by SGR record the same transition from amphibolite- to greenschist-grade metamorphism.

Ti-in-quartz analysis of sample 1015-P57 of Orocopia Schist from the northern Plomosa mountains yielded deformation temperatures of  $531\text{--}572 \pm 4^{\circ}\text{C}$  (Seymour et al., 2016), further evidence the schist was deformed under amphibolite-grade metamorphism.



**Figure 42:** Samples from the footwall of the Plomosa detachment fault categorized by degree of chloritization and separated into dynamically recrystallized quartz grain size bins. This plot illustrates that smaller sizes of dynamically recrystallized quartz are associated with a higher degree of chloritization, and larger sizes are associated with a lesser degree chloritization.

## 8. Structural Data

### 8.1. Metamorphic fabrics

As mentioned, within the mapping area mylonitic foliations and lineations are pervasive throughout the footwall of the Plomosa detachment fault (Figure 43), and commonly form L-S and L>S tectonites. In areas where L>S tectonites dominate, foliation commonly reverses dip-direction over m-scale wavelengths, so a single foliation representing the overall dip of the fabric would be recorded. The orientations of mylonitic and gneissic fabrics are summarized in the following subsections. All reported mean orientations are based on the maximum eigenvector ( $e_1$ ), unless otherwise noted.

#### 8.1.1. Mylonitic foliations

Mylonitic foliations ( $n = 620$ ) were measured throughout the footwall with an average orientation of: strike/dip (S/D) [116, 10 SW] (Figures 43 A and 44 A; Plate 1). Mylonitic foliations were selected within each unit polygon for the three major units (Nic, KPGos, and KXgn) and plotted separately yielding three unique patterns (Figure 44 B–D):

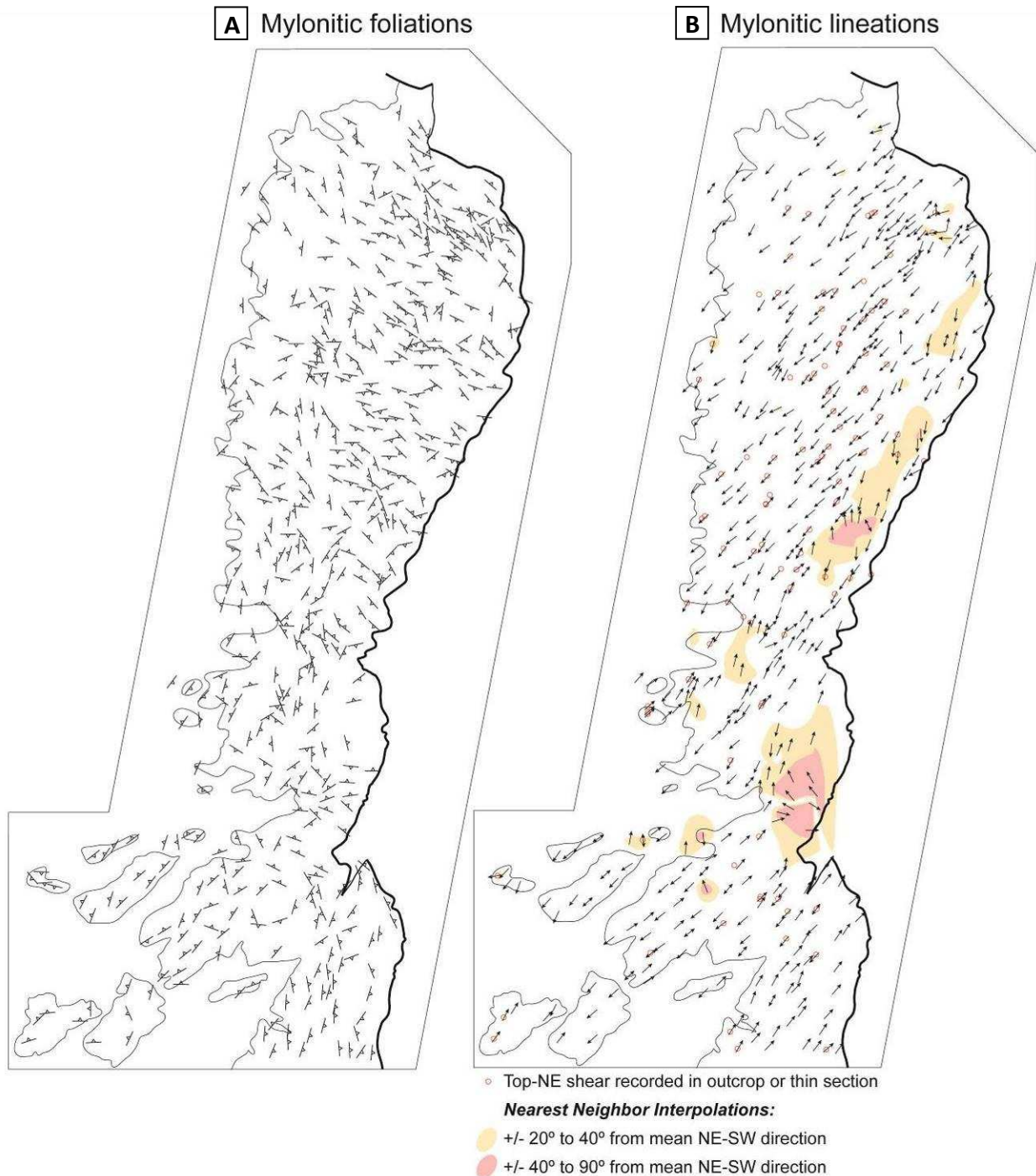
- Unit KPGos has an average mylonitic foliation plane of: S/D [130, 19 SW]. The clustered poles to mylonitic foliations form a poorly-defined girdle distribution with a fold axis of: trend/plunge (T/P) [228, 19].
- Unit KXgn has an average mylonitic foliation plane of: S/D [334, 05 NE]. Mylonitic foliations are a bit more variable and are on average more horizontal than in the other footwall units, and the poles define a girdle with a fold axis of: T/P [028, 05], which is 20° counterclockwise from the fold axis of unit KPGos

- Unit Nic has an average mylonitic foliation plane of: S/D [099, 13 S]. The poles to mylonitic foliations define a girdle that is nearly perpendicular to the other two units with a rotation axis of: T/P [139, 08].

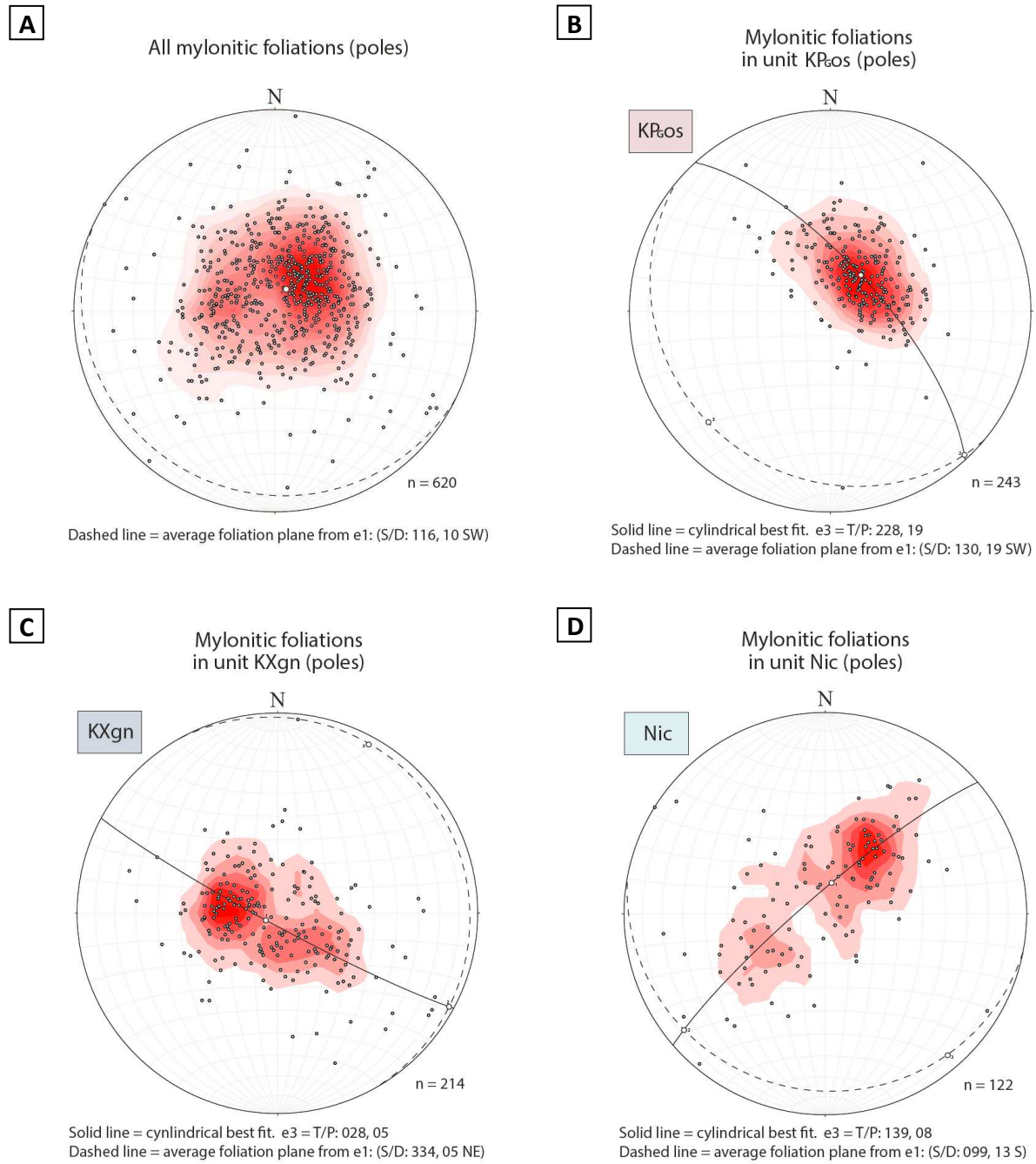
### ***8.1.2. Mylonitic lineations***

Mylonitic lineations (n = 566) were measured throughout the footwall with an average orientation of: T/P [220, 09], which are consistently associated with mylonitic fabrics that record top-to-the-NE sense of shear (Figures 43 B and 45 A; Plate 1). The mylonitic lineations for the three major units were separated in the same way as the mylonitic foliations yielding three unique patterns (Figure 45 B–D):

- Unit KPGos has very tightly clustered mylonitic lineations with an average orientation of: T/P [224, 19].
- Unit KXgn has less tightly clustered mylonitic lineations with an average orientation of: T/P [038, 05].
- Unit Nic has the least tightly clustered lineations with an average orientation of: T/P [211, 11], which is  $\sim 10^\circ$  counterclockwise from the units KPGos and KXgn.

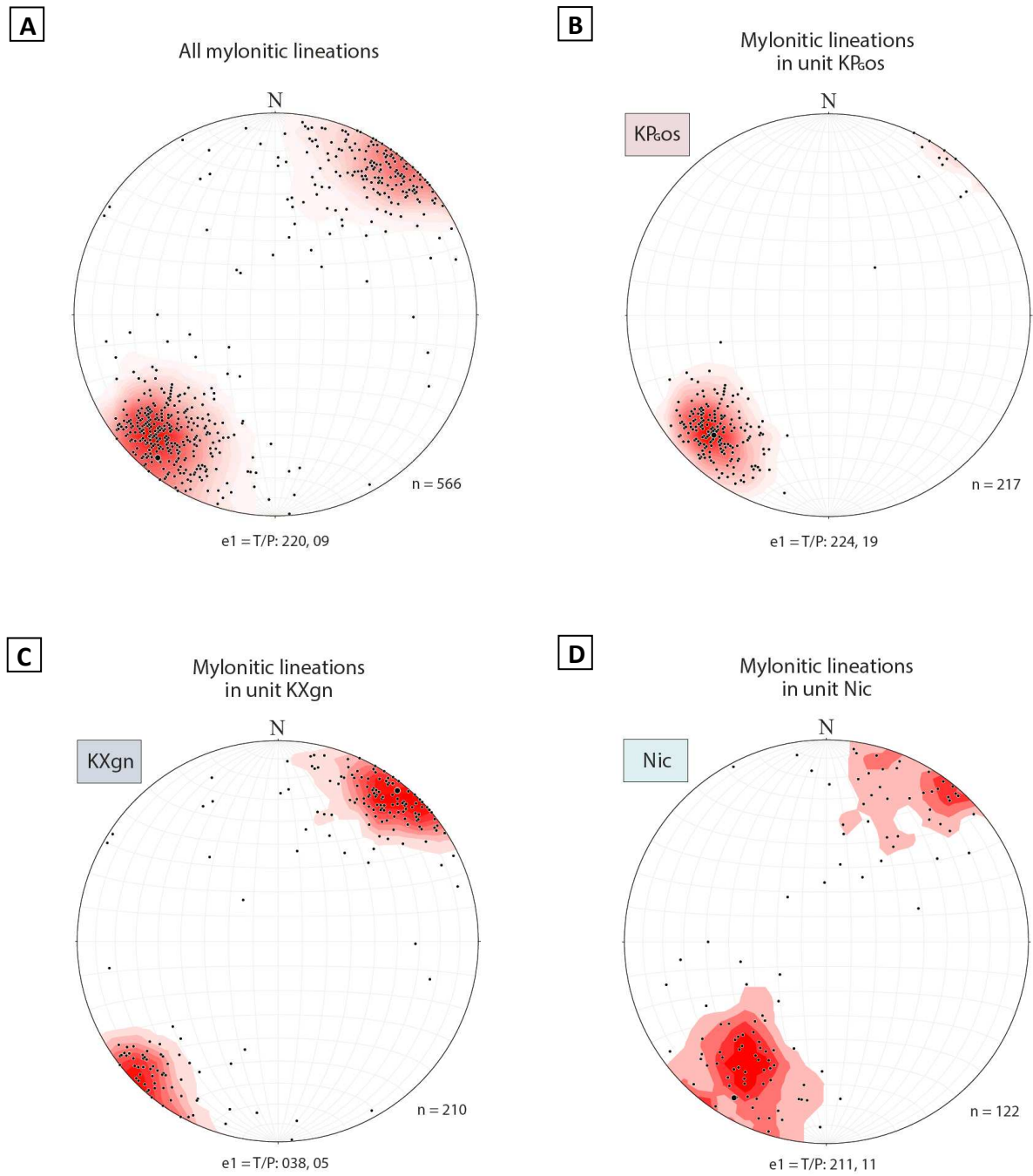


**Figure 43: A)** Distribution of mylonitic foliations illustrating strike and dip direction throughout the footwall of the Plomosa detachment fault (bold line). **B)** Distribution of mylonitic lineations illustrating trend and plunge direction throughout the footwall of the Plomosa detachment fault. Includes distribution of top-to-the NE shear indicators recorded in outcrop or thin section (red circles), and nearest neighbor interpolations of the trend of lineations highlighting deviations from the average NE-SW trend (orange and red polygons). The bulls-eye of highly deviant lineations in the southern half is in an area which is highly faulted and fractured, and is likely the result of brittle rotation. The belt of more northerly trends in the NE is associated with the unit Nic. Figure outlines are equivalent to the map outline in Plate 1.



**Figure 44:** Stereoplots of poles to mylonitic foliations from the footwall of the Plomosa detachment fault. All stereoplots were created with Stereonet 9.9.5 for Windows (Allmendinger, 2017).





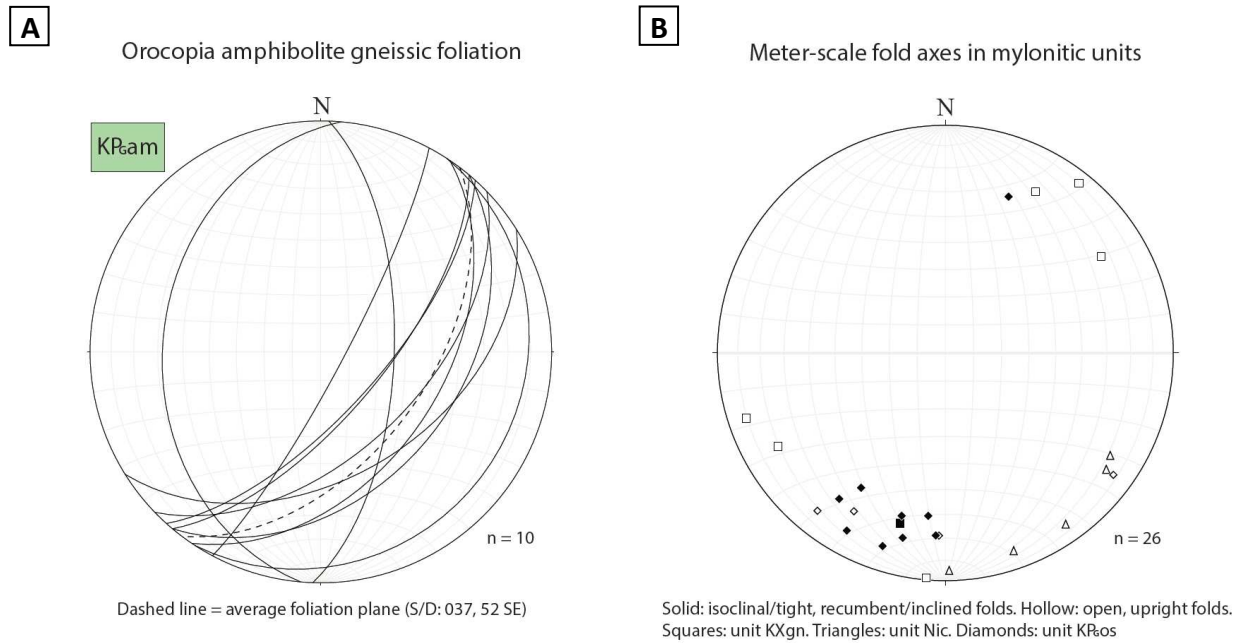
**Figure 45:** Stereoplots of mylonitic lineations from the footwall of the Plomosa detachment fault.

### ***8.1.3. Gneissic foliation in Orocopia metabasalt***

Ten orientations of gneissic foliation were collected across the unit KPGam. The foliation of this unit is undulating with fold axes parallel to the strike of the unit, and orientations generally vary from subvertical to gently SE dipping (Figures 37 H and 46 A). The average orientation is: S/D [037, 52 SE], the dip of which was used to represent the dip of the unit in cross-section D–D' on the geologic map (Plate 1; Figures 8 & 9).

### ***8.1.4. Folded mylonitic fabric***

Fold axes of 26 cm- to m-scale folds, which vary from recumbent/inclined isoclinal/tight to upright open, were measured for the units KPGos, KXgn, and Nic (Figure 46 B). The recumbent/inclined-isoclinal/tight folds have thickened hinges and attenuated limbs, suggesting they formed in the ductile regime (Figure 37 D & E). Some upright-open folds likely formed during brittle deformation as they show evidence of brittle flexural slip along foliation planes. Apparent folds in the unit Nic appear to be associated with heterogeneous brittle rotation that has occurred along fracture planes that sole into foliation planes, and thus measured and mapped folds in the unit may be the product of extensional deformation rather than horizontal shortening. This observation likely explains the girdle distribution of poles to mylonitic foliation of unit Nic (Figure 44 D), which could be produced by rotation along NW-striking normal faults.



**Figure 46:** Stereoplots of **A)** gneissic foliation of unit KPam, and **B)** fold axes of meter-scale folds from the footwall of the Plomosa detachment fault.

## 8.2. Faults, joints, and dikes

### 8.2.1. Plomosa detachment fault

Structural data from the Plomosa detachment fault includes measurements of the principal slip plane (n=8) and slickenline sets (n=11) (Figure 47 A). In addition, the orientation of the Plomosa detachment fault was determined from three-point solutions where the detachment is clearly projected down a hillslope (n=5). Poles to the measured and calculated principal fault planes form a poorly-defined girdle distribution, yielding a corrugation axis of T/P [047, 11.5], which is the same trend as the average of NE-trending slickenlines (n=8): T/P [047, 16]. A second set of SE-trending slickenlines (n=3) have an average orientation of T/P [116, 26], ~70 degrees clockwise from the NE-trending set. The NE-trending slickenlines record top-to-the-NE normal displacement, whereas it is

unknown whether the SE-trending slickenlines record top-to-the NW reverse displacement, or top-to-the SE normal displacement.

### **8.2.2. All other faults**

Excluding principle slip planes of the Plomosa detachment fault, a total of 191 fault planes and 167 slickenlines were measured in the footwall of the Plomosa detachment fault (Figure 47 B). The average trend of their slickenlines is T/P [048, 41], and the average trend of their poles is T/P [227, 41]. A sense of slip was determined for 79 faults, and their shortening and extension axes were determined (Figure 47 C).

### **8.2.3. Normal faults**

53 normal faults were separated from the faults with a known slip sense by the criteria they have a dip  $<80^\circ$  and rake between  $45\text{--}90^\circ$ . These normal faults are mostly NW-striking with NE-plunging lineations. Their average shortening axis is T/P [108, 83], and their average extension axis is T/P [220, 03], which is identical to the average trend of all mylonitic lineations (Figure 47 D).

### **8.2.4. Joints**

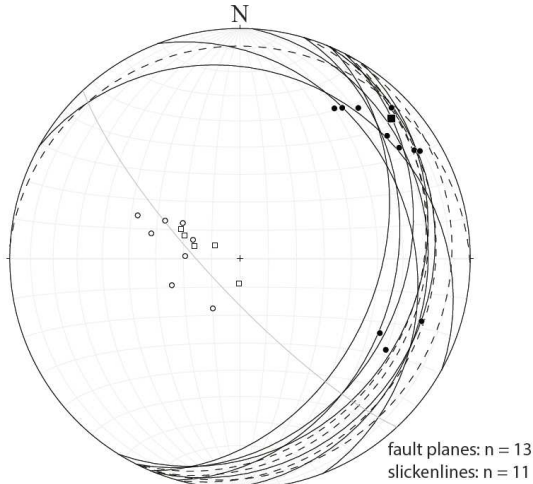
The average orientations of systematic joint sets at 42 localities were measured (Figure 48 A), mostly from within the Orocopia Schist where joint sets are most prevalent. The average orientation of their poles is: T/P [228, 13].

### **8.2.5. Dikes**

32 dikes were measured within the footwall, mostly in the southern half of the map area. Most measured dikes are nonmylonitic and generally subvertical (Figure 48 B), and where only a trend of a dike could be measured the dip was usually reported as vertical.

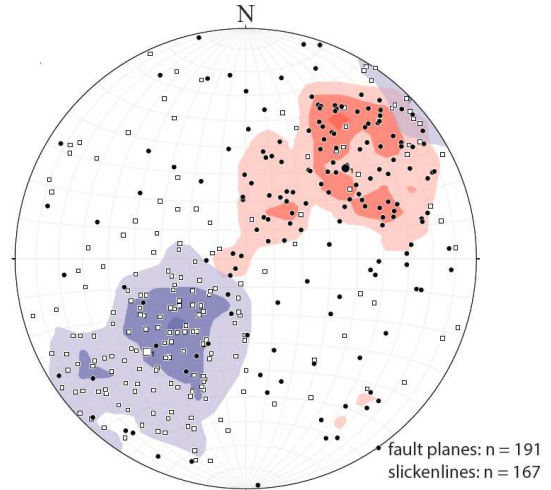
Some dikes are mylonitic but are oblique to the mylonitic foliation, and may be subhorizontal or shallow. The poles to the dikes define a girdle with a rotation axis determined from e3 of: T/P [132, 02], similar to the rotation axis for mylonitic foliations of the unit Nic. The average horizontal extension direction indicated by the dikes is 222/042, consistent with the inferred regional extension direction.

**A** Plomosa detachment fault principal slip planes, poles, and slickenlines



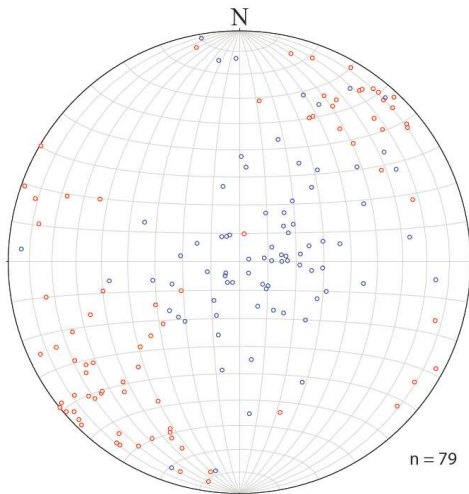
Solid lines = measured fault planes (poles = hollow circles)  
Dashed lines = planes from 3-point solution (poles = hollow squares)  
Gray line = cylindrical best fit to all poles (S/D: 137, 78.5 SW)  
Black square = calculated corrugation axis (e3 = T/P: 047, 11.5)

**B** All footwall faults (poles) and slickenlines



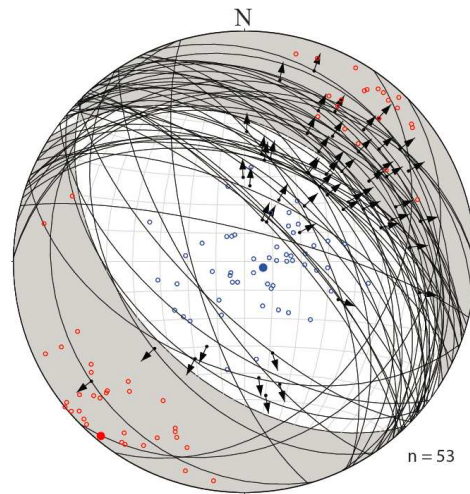
Squares = poles to fault planes (with blue contour). e1 = T/P: 227, 41  
Circles = slickenlines (with red contour). e1 = T/P: 048, 41

**C** Shortening axes (P) and extension axes (T) of all footwall faults with a known slip sense



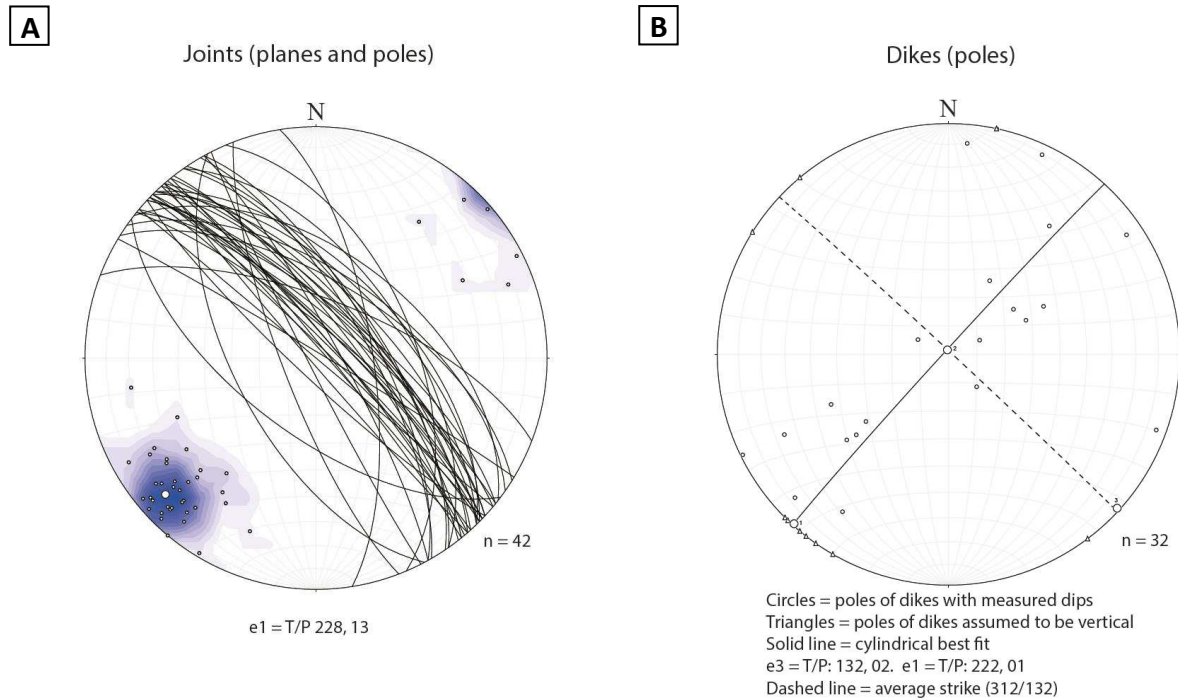
Blue circles = shortening axes (P)  
Red circles = extension axes (T)

**D** Fault planes, slickenlines, shortening axes (P) and extension axes (T) of normal faults



Average extension axis (e1) = 220, 03  
Average shortening axis (e3) = 108, 83  
Arrows indicate direction of hanging-wall movement

**Figure 47:** Stereoplots of faults from the northern Plomosa Mountains.



**Figure 48:** Stereoplots of **A)** joints and **B)** poles to dikes from the footwall of the Plomosa detachment fault.

### 8.3. Barite and carbonate veins, and kinematically-related post-detachment faults

#### 8.3.1. Barite veins

95 barite veins were measured, which overall have very systematic orientation (Figure 49 A). The average orientation of the barite veins determined by e1 is: S/D [030, 80 SE], and their average orientation determined from the 1% contour maximum is: S/D [033, 83 SE], which may be more representative of the unique orientation of barite veining by excluding the influence of barite-mineralized pre-existing features that may have been measured.

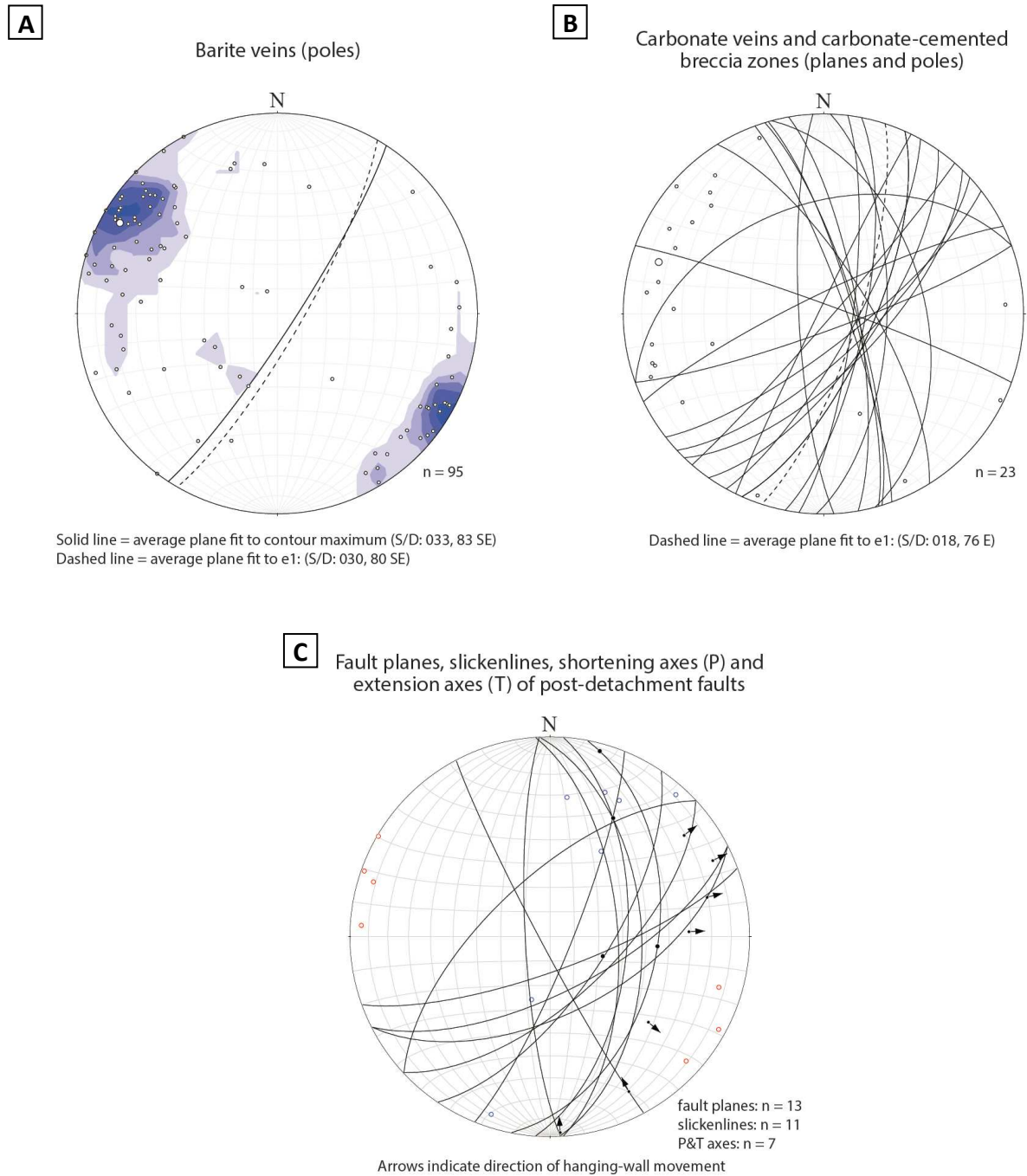
### **8.3.2. Carbonate veins**

Though there is significantly more scatter in the carbonate veins than the barite veins, their overall orientations are similar (Figure 49 B). 23 carbonate veins/carbonate-cemented breccia zones were measured, and their average orientation is: S/D [018, 76 E].

### **8.3.3. Post-detachment faults**

Post-detachment faults include the N- and NE-striking faults that cut the detachment, and other faults that cut across extensional faults or features, have orientations and kinematics similar to the N- and NE-striking faults, or have orientations and mineralization consistent with the late-stage barite and carbonate veining. 13 fault planes with 11 slickenlines met these criteria, seven of which had a known sense of slip (Figure 49 C). The average shortening axis is T/P [023, 21], and the average extension axis is T/P [113, 01]. These young faults are crudely made up of two types: ~N-striking dextral-normal faults, and ~NE-striking sinistral-normal faults, which are kinematically compatible with WNW-ESE extension.



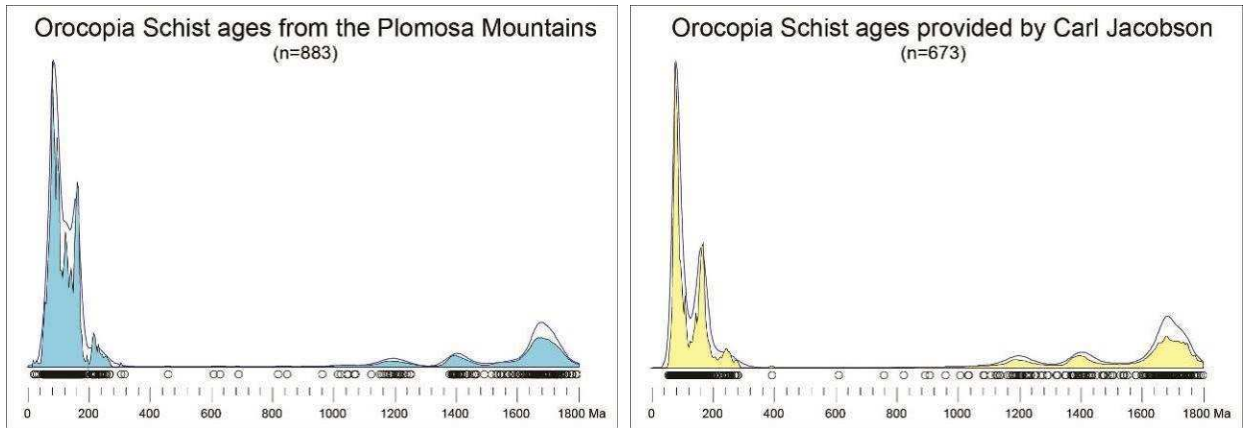


**Figure 49:** Stereoplots of **A)** poles to barite veins, **B)** carbonate veins and carbonate-cemented breccia zones, and **C)** post-detachment faults from the northern Plomosa Mountains.

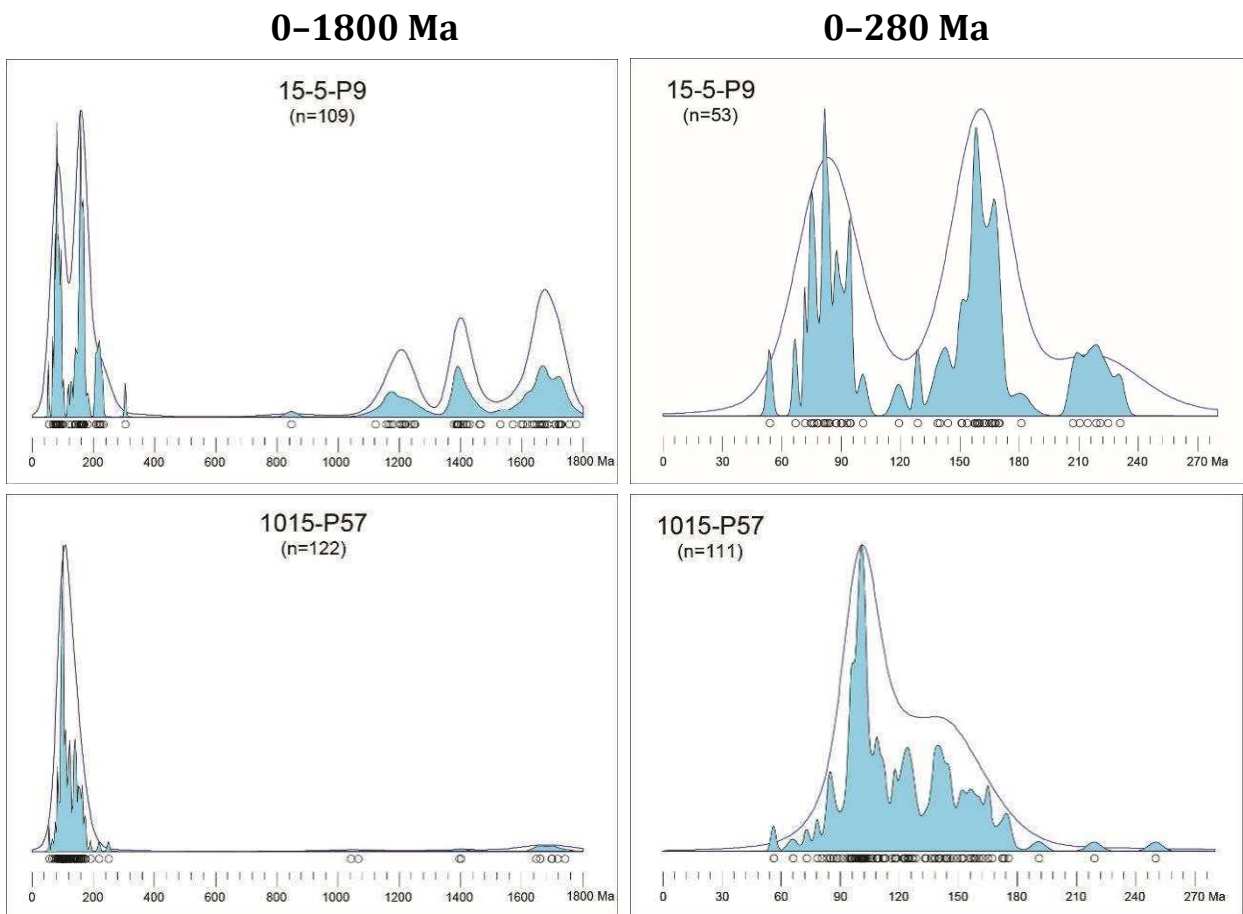
## 9. U-Pb Zircon Geochronology

### 9.1. Orocopia Schist

Figure 50 is a density plot of all ages from six samples of the quartzofeldspathic schist from the northern Plomosa Mountains (Appendix 8) compared to a density plot of ages of Orocopia Schist at other localities produced from data provided by Carl Jacobson (Jacobson 2000). The excellent match in the two age distributions is the most compelling evidence that the schist of the northern Plomosa Mountains is indeed the Orocopia Schist. Interestingly, there is great variability of age distributions between individual samples (Figure 51). Plotting the ratio of Th/U concentration vs age reveals a high density of low Th/U ratios ( $<0.1$ ) between  $\sim 75$ – $50$  Ma (Figure 52, blue circles are from samples of Orocopia Schist), and a sudden drop-off of higher Th/U ratios at  $\sim 68$  Ma. Low Th/U ratios of  $<0.1$  in zircons have been demonstrated to record metamorphic zircon growth, whereas Th/U ratios  $>0.1$  record igneous zircon growth in a typical felsic igneous rock (e.g. Williams and Claesson, 1987). Though some studies caution that Th/U ratios of  $<0.1$  also have been observed for zircon growths that resulted from magmatic crystallization (Lopez-Sanchez et al., 2015), I interpret the low ( $<0.1$ ) Th/U ratios from samples in this study to record metamorphic growth, which is discussed later.



**Figure 50:** Zircon U-Pb age density plot of all samples of Orocopia Schist from the northern Plomosa Mountains (left) compared to samples of Orocopia Schist collected from other localities (data provided courtesy of Carl Jacobson). Solid filled areas are probability density plots (PDP), and the blue lines are kernel density estimates (KDE). The Proterozoic peaks as well as the Mesozoic and Cenozoic populations and peaks of the ages match very well, providing the best evidence that the schist of the northern Plomosa Mountains is the Orocopia Schist.



**Figure 51:** Continued on next two pages.

**0-1800 Ma**

**0-280 Ma**

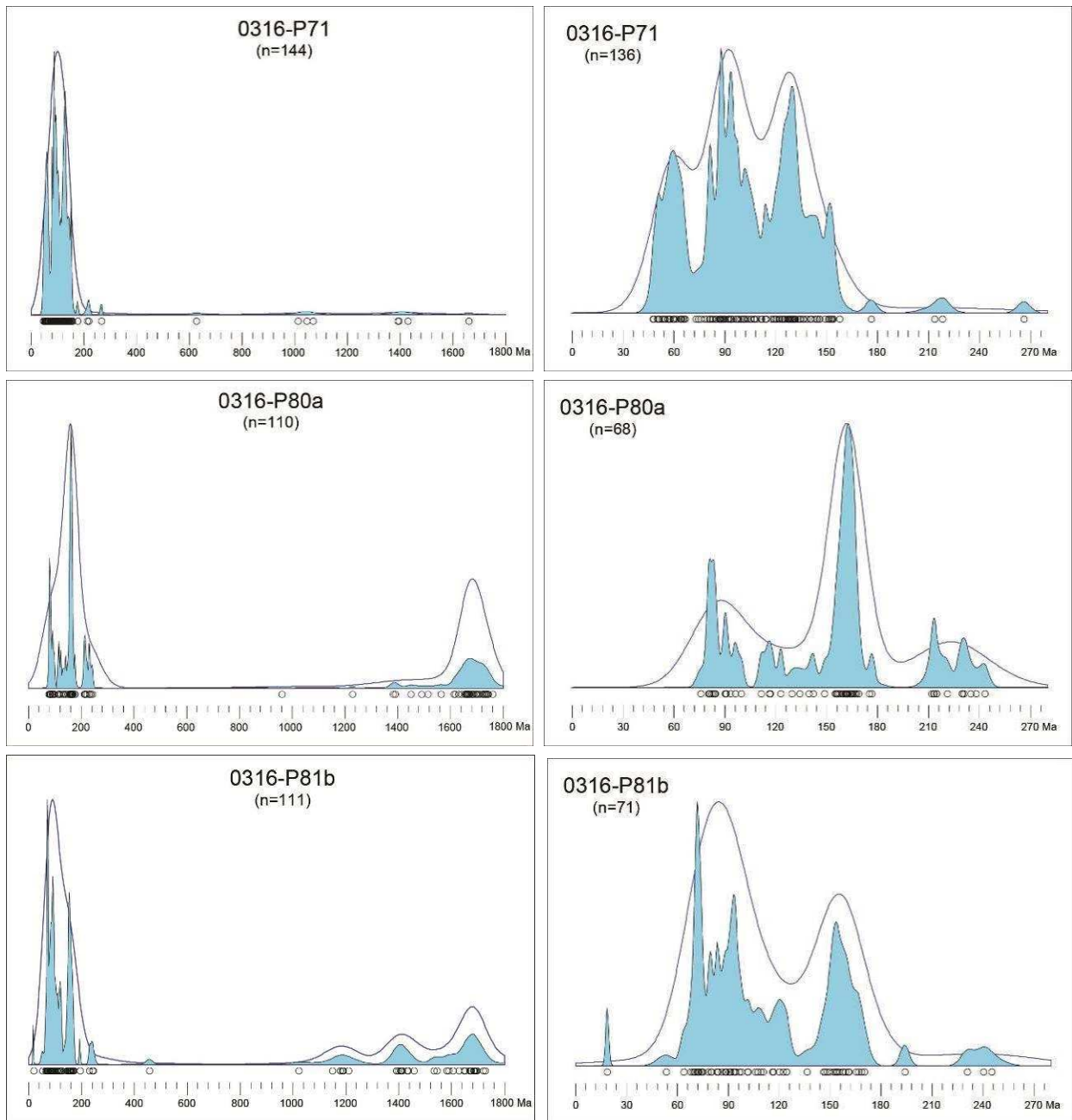
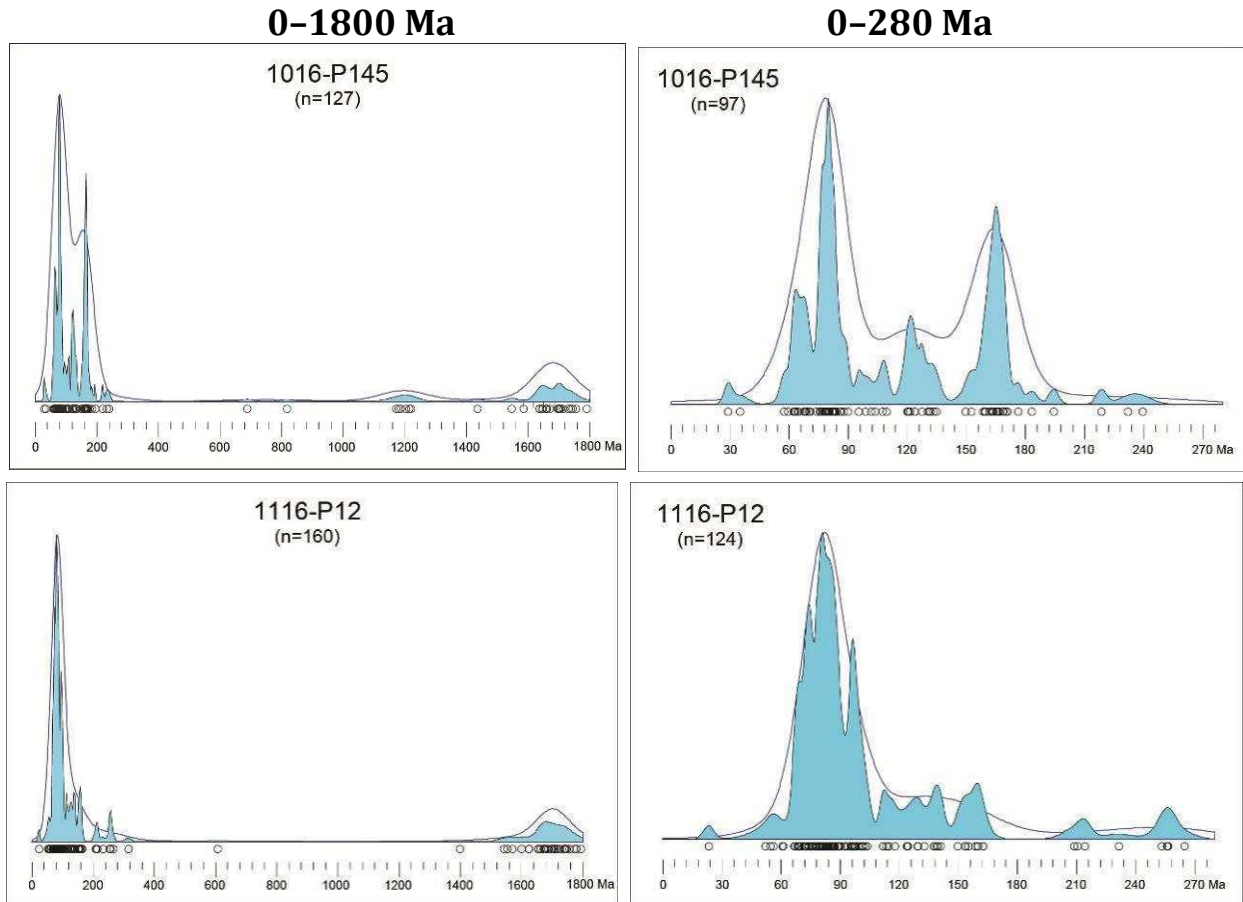
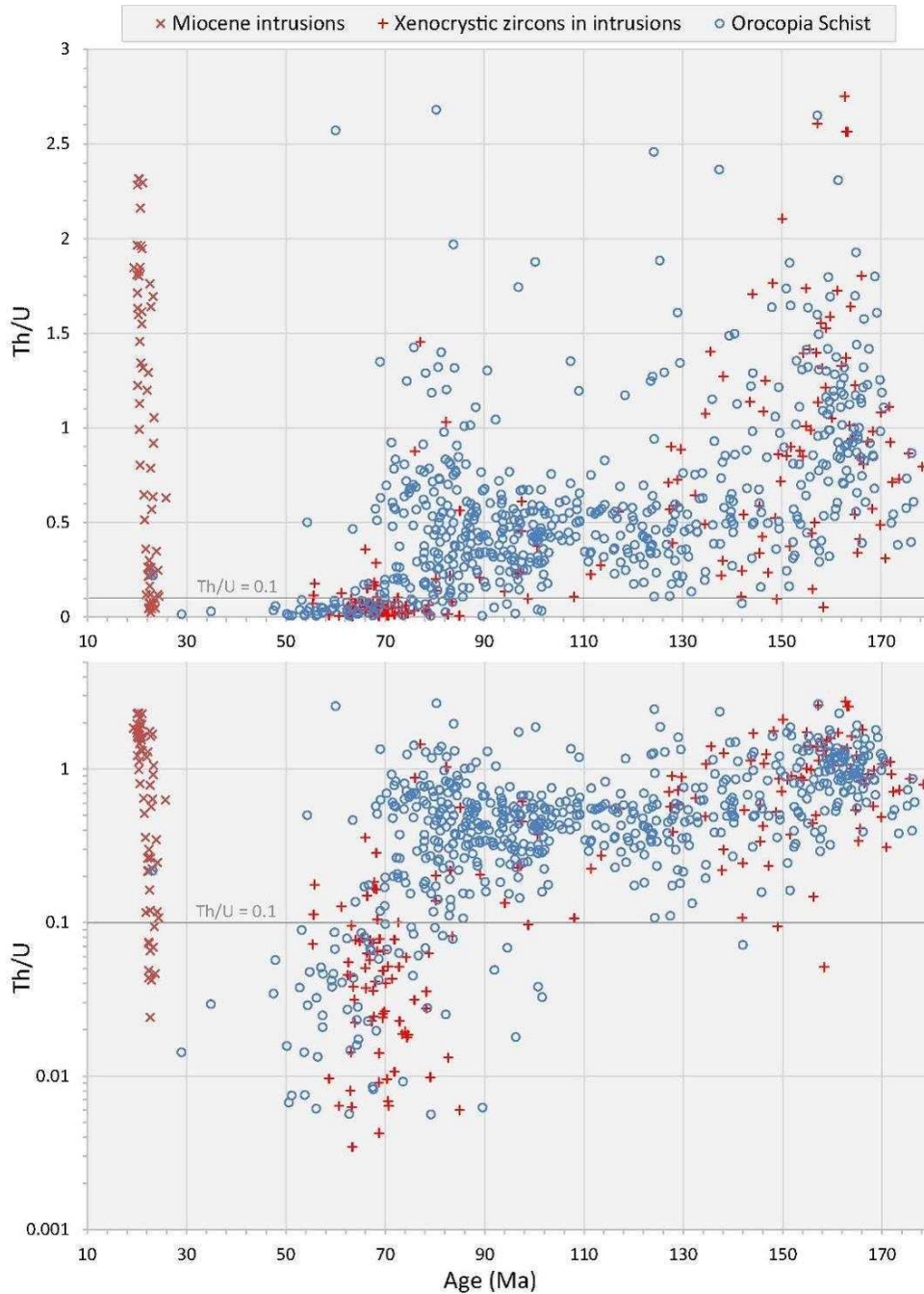


Figure 51 continued.

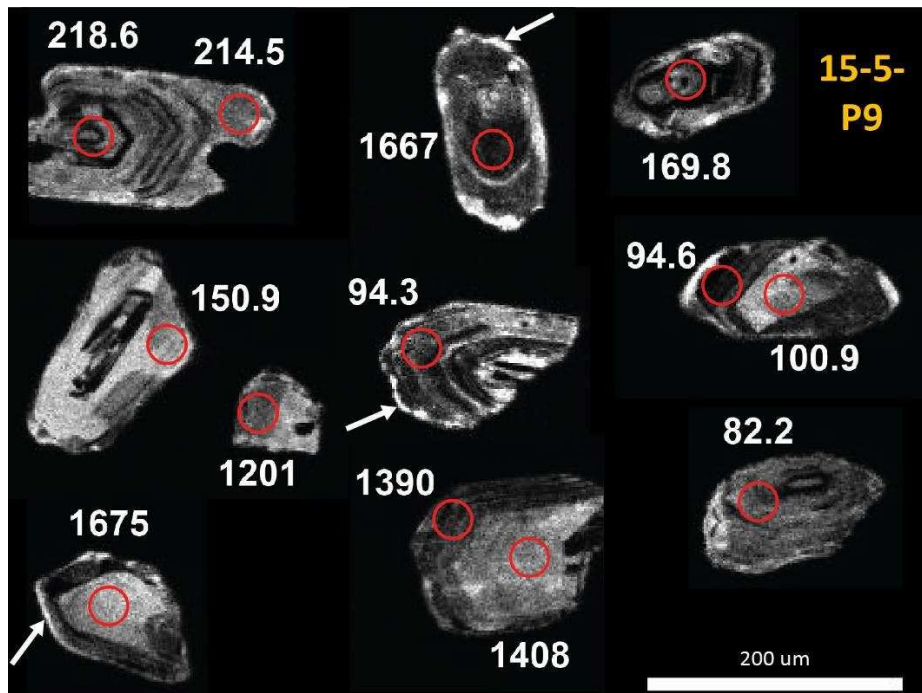


**Figure 51 continued:** Zircon U-Pb age density plots for each of the seven samples of Orocopia Schist collected from the northern Plomosa Mountains. Left-hand column is from 0–1800 Ma, and the right-hand column is zoomed in to 0–280 Ma. There is significant variability to the number of Proterozoic grains, and great variability in the distribution of Cenozoic and Mesozoic peaks, though the overall age range is quite similar.

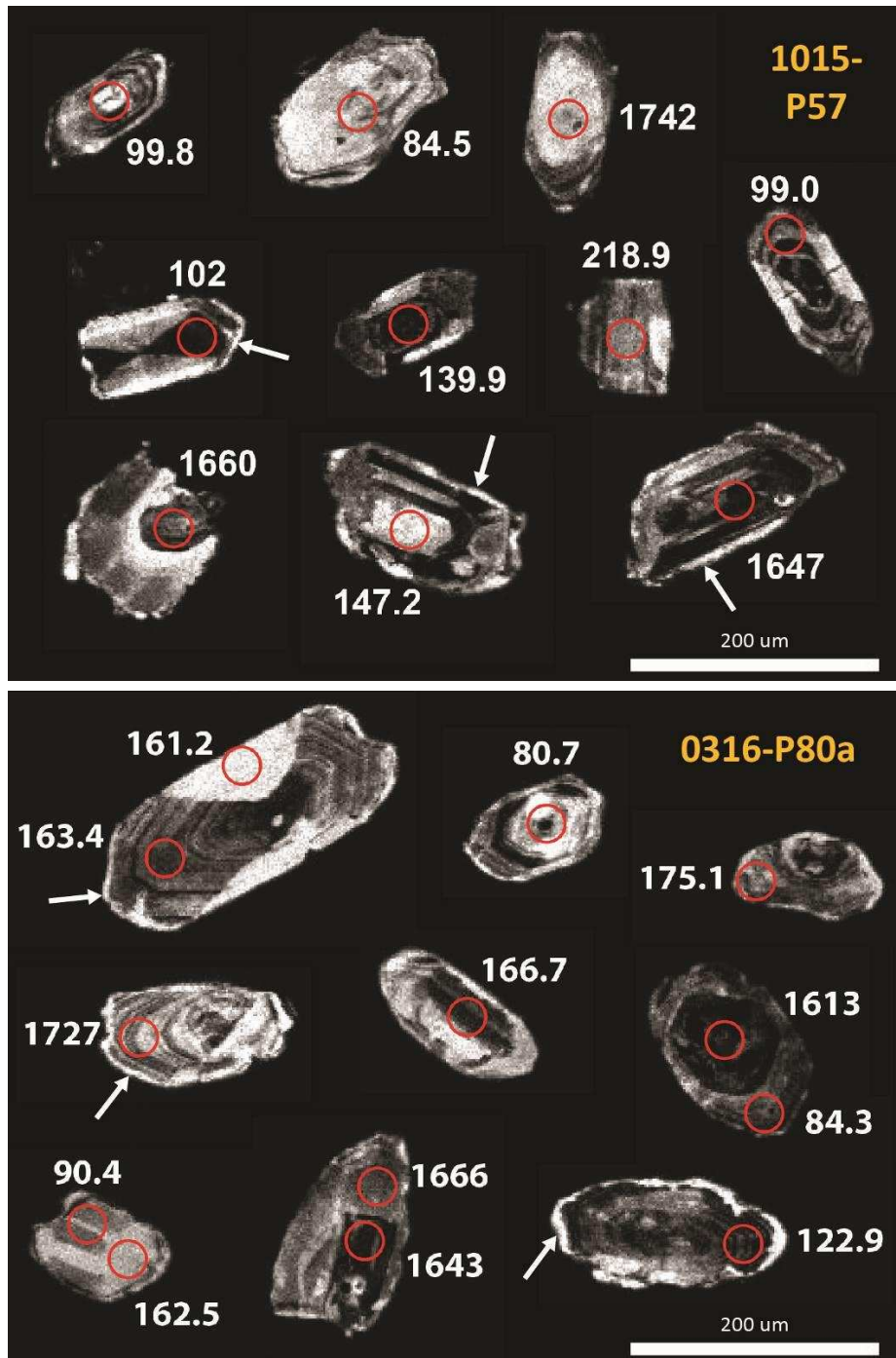


**Figure 52:** Plots of Th/U ratio vs Age (Top: linear scale, Bottom: logarithmic scale, displaying the same data) determined from U-Pb analysis of zircons for samples of Orocopia Schist (blue circles) and Miocene intrusions of unit Nic (orange x's and red +'s). Low Th/U values (<0.1) emerge at ~102 Ma, and continue to as late as ~29 Ma, with a high density between ~75–50 Ma. A sharp drop-off of higher Th/U ratios occurs at ~68 Ma. Low Th/U ratios (<0.1) are thought to be associated with metamorphic growth of zircons, whereas higher Th/U ratios would be associated with igneous growth. Interestingly, the Miocene ages of mylonitic intrusions have a population of low Th/U ratios at ~22–23 Ma, whereas the nonmylonitic diorite south of the map area has a range of higher Th/U ratios at ~20 Ma. The age distribution and range of Th/U ratios of xenocrystic zircons within Miocene intrusions matches the Orocopia Schist very well.

Figure 53 are examples of CL-images taken of the three polished mounts of zircons from Orocopia Schist. Most grains have an oscillatory zoned core, and some have thick metamorphic overgrows. The ages from the polished mounts range from Proterozoic to Late Cretaceous, and a few are Paleocene. The depth profiling technique applied to the remaining four samples yielded abundant latest Cretaceous to Paleogene ages from rims <5  $\mu\text{m}$  thick which have low Th/U ratios (Figure 54). It is suspected that the thin bright metamorphic rims observed in the CL-images (Figure 50, white arrows point to examples) are the source of these latest Cretaceous to Paleogene ages. The discovery of these thin metamorphic rims demonstrates the benefits of utilizing CL-imagery in conjunction with depth profiling, as anything <20  $\mu\text{m}$  cannot currently be targeted in polished samples, yet can be resolved via depth profiling and identified via the CL-imagery.

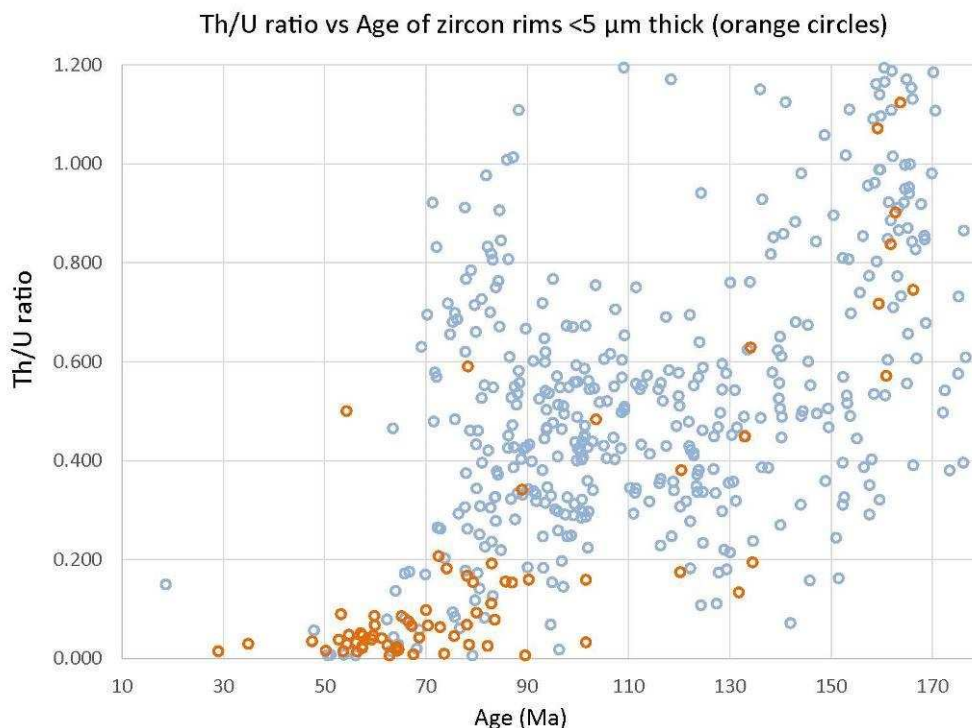


**Figure 53:** Continued on next page.



**Figure 53 continued.** CL-images of a selection of polished zircon grains for samples of Orocopia Schist (Appendix 9). Red circles indicate the area the zircon was ablated, and the resulting age (Ma) is indicated adjacent to each spot. White arrows point to possible examples of thin metamorphic rims, the ages of which were dated in other samples utilizing the depth profiling technique.





**Figure 54:** Plot of Th/U ratio vs age for samples of Orocopia Schist. Orange circles are ages from zircon rims <5  $\mu\text{m}$  thick. Blue circles are from all other ages. There is a high concentration of low Th/U ratios for the <5  $\mu\text{m}$ -thick zircon rims, which could only be dated utilizing the depth profiling technique.

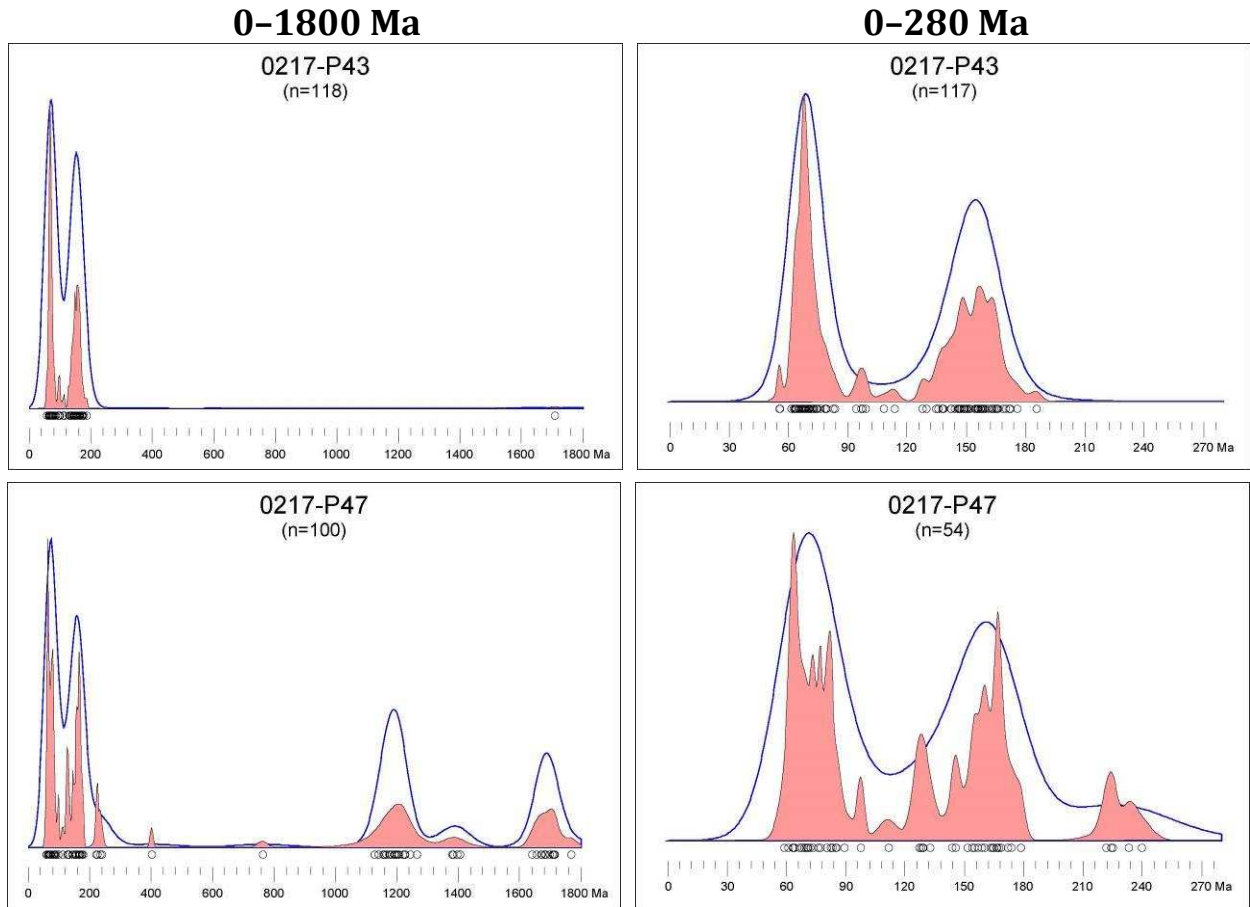
## 9.2. Miocene intrusive complex

U-Pb zircon ages were determined for six samples of intrusions (Table 2). Sample 0316-P71x is a protomylonitic granodiorite sill intruded into the Orocopia Schist directly below a 1.5 m-wide pod of actinolite (Figure 23 E & F). Eight Miocene ages of zircons were determined, yielding a weighted mean age of  $22.58 \pm 0.55$  Ma, whereas the rest of the zircon ages are inherited, having likely incorporated xenocrystic zircons from the Orocopia Schist. Samples 0316-P80b and 0316-P81a are mylonitic granodiorite dikes within the Orocopia Schist, which have similar weighted mean ages of  $22.68 \pm 0.27$  Ma and  $22.81 \pm 0.49$  Ma, respectively, and have only a few xenocrystic ages. Sample 0217-P16 is a nonmylonitic diorite collected  $\sim 2.3$  km south of the field area and structurally above a

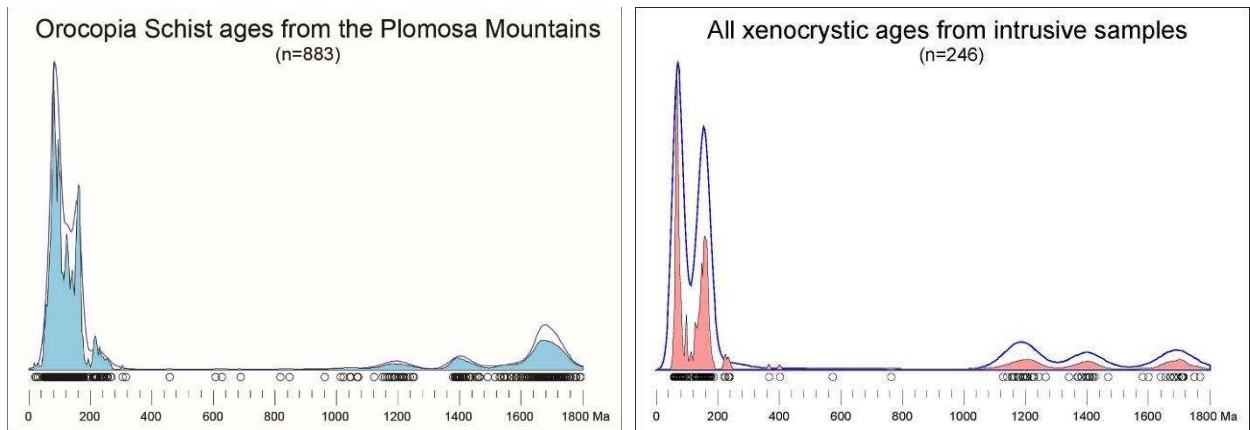
mylonitic front in the footwall (Figures 21 A & B and 38). This diorite has entirely Miocene ages, yielding a weighted mean age of  $20.46 \pm 0.15$  Ma. Sample 0217-P43 is a protomylonitic granodiorite collected to represent the “core” of this unit (Figure 20 A), and sample 0217-P47 is a high-strain mylonitic granodiorite intruded into the Orocopia Schist at its SW extent. Surprisingly, both samples have entirely xenocrystic ages. They yielded no Miocene ages, and their age distribution and concentrations of Th and U with age match that of the Orocopia Schist (Figures 55 and 56).

**Table 2:** Zircon U-Pb ages of intrusive samples (Appendices 6 and 7)

Sample name	Unit	Rock type	UTM coordinates (zone 11 N)	<sup>206</sup> Pb/ <sup>238</sup> U ages (<10% discordant)	
				Weighted mean age	Tuff-Zirc age
0316-P71x	Nic	Granodiorite mylonitic sill	N 325069 E 182316	$22.58 \pm 0.55$ Ma 1 of 8 rejected MSWD = 2.5	$22.49 +0.81/-0.31$ Ma 2 of 8 rejected
0316-P80b	Nic	Granodiorite mylonitic dike	N 324048 E 182428	$22.68 \pm 0.27$ Ma 1 of 18 rejected MSWD = 1.8	$22.71 +0.25/-0.25$ Ma 1 of 18 rejected
0316-P81a	Nic	Granodiorite mylonitic dike	N 324280 E 182190	$22.81 \pm 0.49$ Ma 0 of 10 rejected MSWD = 2.4	$23.10 +0.28/-0.73$ Ma 1 of 10 rejected
0217-P16	Nic	Diorite nonmylonitic	N 312971 E 180478 (2.3 km south of map area)	$20.46 \pm 0.15$ Ma 2 of 26 rejected MSWD = 1.6	$20.45 +0.29/-0.20$ Ma 2 of 26 rejected
0217-P43	Nica	Granodiorite protomylonitic	N 320696 E 181858	All xenocrystic (Paleogene through Proterozoic ages)	
0217-P47	Nic	Granodiorite mylonitic	N 319412 E 179713	All xenocrystic (Paleogene through Proterozoic ages)	



**Figure 55:** Zircon U-Pb age density plots of the two intrusive samples with entirely xenocrystic zircons. Left: 0–1800 Ma; Right: 0–280 Ma.



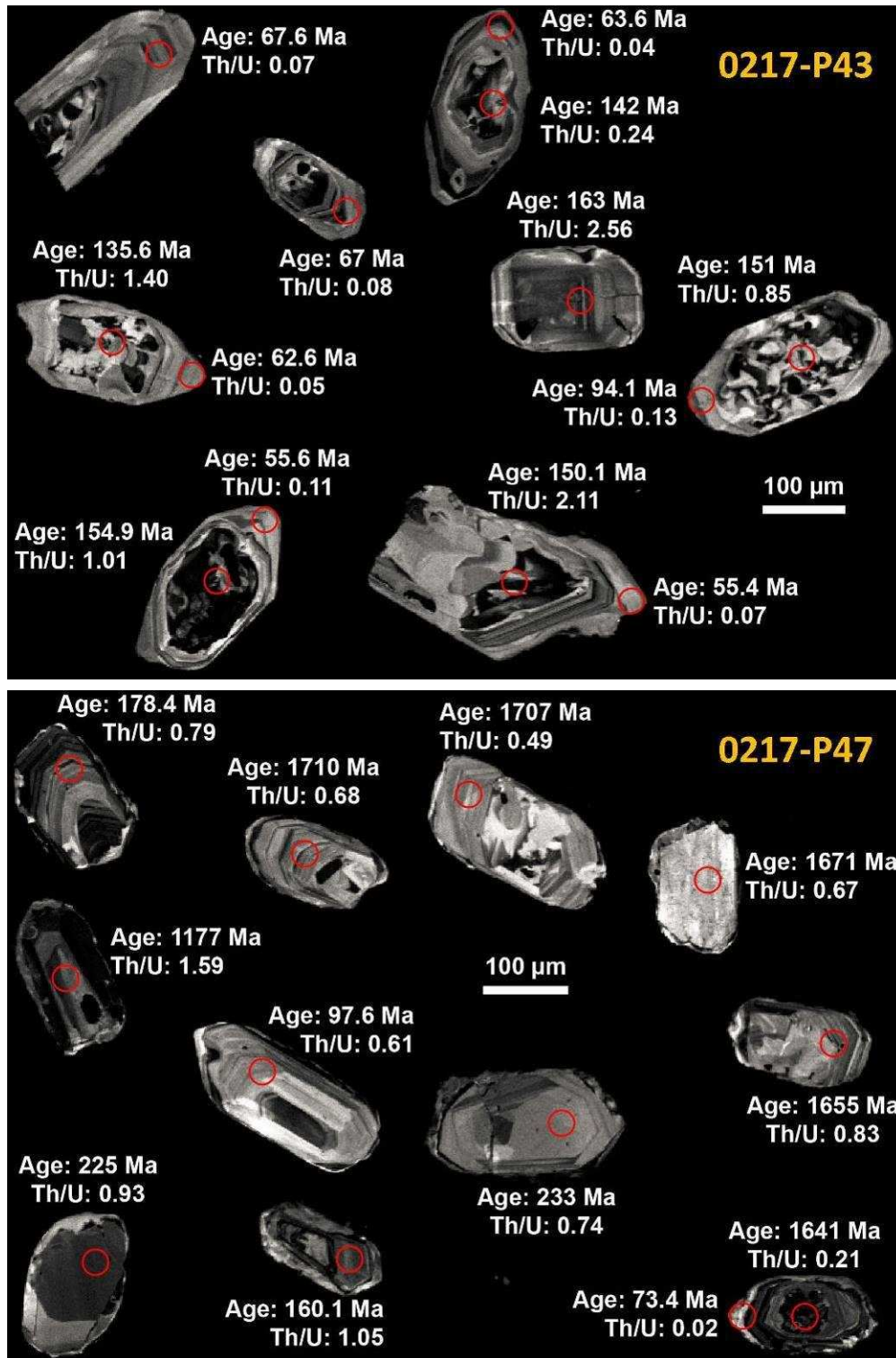
**Figure 56:** Zircon U-Pb age density plots of Orocopia Schist from the northern Plomosa Mountains compared to xenocrystic zircons from the Miocene intrusions of unit Nic.

Figure 57 are CL-images of polished zircons from the intrusive samples 0217-P43 and 0217-P47. Approximately 50 ages each were obtained by ablating polished zircons, and an additional ~50 ages were obtained utilizing depth profiling due to the polished zircons yielding entirely xenocrystic ages. However, the additional ages obtained via depth profiling were also entirely xenocrystic.

Sample 0217-P43 has a preponderance of zircons with “chaotic” or “abstract” patterns (Figure 57), with ages dominantly ranging from 126–186 Ma centered around a well-defined peak at 155 Ma (Figure 55, top). Only one Proterozoic age was determined for sample 0217-P43 out of 118 concordant ages, and Triassic ages are also notably absent. Sample 0217-P47 has only a few cores that resemble the chaotic/abstract patterns (Figure 57), has abundant Proterozoic ages, a small spike of Triassic ages centered at ~228 Ma, and has a broad distribution of Cretaceous to Jurassic ages ranging from 126–180 Ma (Figure 55, bottom). For sample 0217-P43, a possible explanation for the lack of ages prior to the 155 Ma peak could be that the zircons in the assimilated protolith recrystallized during a high-temperature or high-pressure event in the Jurassic, consistent with the intense magmatism and subduction zone geometry of the region at that time. High temperatures and/or high pressures are suggested by the chaotic/abstract cores of the zircons, which resemble high-temperature or high-pressure recrystallization of zircons observed elsewhere (e.g. Corfu et al., 2003).

A second age spike for samples 0217-P43 and 0217-47 is centered around 68 Ma, with ages ranging from 60–90 Ma. These ages overlap the ages of the thin metamorphic rims described in the samples of Orocochia Schist, and have the same low Th/U ratios (Figure 52). The Paleogene metamorphic rims in sample 0217-P43 have weak zoning

patterns which resemble igneous zonation, and are ten times as thick as those in the Orocopia Schist – thick enough to be targeted directly in polished samples with 30  $\mu\text{m}$ -wide beams. The unusually thick metamorphic rims also suggest a unique history for the protolith of sample 0217-P43, as its inherited zircons must have experienced special metamorphic conditions (perhaps saturated with water, or a protracted heating event?) to have grown such uniquely thick metamorphic rims. The metamorphic rims for sample 0217-P47 are more like the Orocopia Schist, as ablating polished zircons yielded only a few 60–90 Ma ages, whereas depth profiling yielded many ages in that range.



**Figure 57:** CL-images of a selection of polished zircons of two intrusive samples. Red circles indicate the location the zircon was ablated, with the resulting age (Ma) and Th/U ratio indicated adjacent to the spot. Note the chaotic/abstract cores in many of the zircons for sample 0217-P43, which yield Jurassic ages, and are consistently overgrown by thick latest Cretaceous to Paleogene rims with low Th/U ratios (<0.1).

## Discussion

### 10. The Northern Plomosa Mountains Metamorphic Core Complex

#### 10.1. Geometry and kinematics of extension

Throughout the map area, extension-related ductile and brittle features record an extremely consistent direction of extension, with top-to-the-NE shear recorded by ductile fabrics, and top-to-the-NE displacement recorded by normal faults. The average trends of mylonitic lineations of the three main units (Nic, KPGos, and KXgn) are nearly parallel, though the lineations of unit Nic trend  $\sim 10^\circ$  more NNE (Figure 45). The average ductile extension direction given by the average trend of all mylonitic lineations is T/P [220, 09], consistent with the fold axis for Orocopia Schist (T/P: 228, 19), and the corrugation axis of the Plomosa detachment fault (T/P: 047, 11.5). 62/63 mylonitic samples with a sense of shear record top-to-the NE shear, and the single sample that records top-to-the SW shear is from within  $\sim 500$  m of the mylonitic front, where antithetic top-to-the SW shears have been described in several other Arizona metamorphic core complexes (Reynolds and Lister, 1990). Several types of brittle structures also record a very consistent NE-SW extension direction, including the average NE-trending slickenlines of the principal slip plane of the Plomosa Detachment fault (T/P: 047, 16), the average extension axis determined from normal faults (T/P: 220, 03), the average pole of joints (T/P: 228, 13), and the average opening-direction of late-stage dikes (T/P: 222, 01). Because the extension direction recorded by ductile and brittle structures in the footwall of the Plomosa detachment fault are nearly identical, it can be inferred that there was no change in

extension direction between the ductile and brittle regime during development of the core complex.

A nonconformity between early Miocene(?) sedimentary units and pre-Cenozoic granitic, gneissic, and metasedimentary rocks in the footwall of the Plomosa Detachment fault dips  $\sim 55^\circ$  to the SW (Figure 38) due to tilting of the footwall during Miocene exhumation. The footwall of the Plomosa detachment fault likely rotated as a large tilt-block between the Plomosa detachment fault and a single, structurally-lower break-away fault to the SW (Spencer and Reynolds, 1991). Rotation of the Plomosa detachment fault must have also occurred during exhumation and tilting of the footwall, resulting in its' current NE-dip of  $\sim 12^\circ$ . Rotating the footwall by  $55^\circ$  to the NE restores the nonconformity to horizontal, and rotating the detachment fault by the same amount yields an initial NE dip of  $77^\circ$ , which is undoubtedly too steep for a fault which has accommodated 15–30 km of displacement (Spencer and Reynolds 1991). Perhaps the SW portion of the footwall at the nonconformity has undergone more tilting than the NE portion in the mapping area, which would be consistent with models of metamorphic core complex development involving listric faults (Lister and Davis, 1989). Rather than restoring the nonconformity to horizontal, it is likely more reasonable to restore the detachment fault to a NE dip of  $60^\circ$ , consistent with Andersonian theory. This would yield a NE rotation of the detachment fault and footwall of  $48^\circ$ , which is applied to the mylonitic foliations in a later section to investigate the implications of their initial orientations.



## **10.2. Timing of mylonitization and extension**

### ***10.2.1. Early Miocene mylonitic fabrics***

The footwall of the Plomosa detachment fault was exhumed between 23–15 Ma based on apatite and zircon fission-track ages (Foster and Spencer, 1992), and three synmylonitic leucocratic intrusions have very consistent ages of between 22.58–22.81 - 0.55 +0.49 Ma. Mylonitic fabrics are widespread in the footwall of the northern Plomosa Mountains, exposed across  $\geq 20$  km<sup>2</sup> in the mapping area, and  $\sim 6$  km<sup>2</sup> of the exposed mylonitic fabrics are early Miocene plutonic rocks. The ages of the intrusions are nearly synchronous with the initiation of the Plomosa detachment fault, suggesting that plutonism and detachment faulting were linked. Synmylonitic plutonic rocks are documented in other nearby core complexes, where they may have triggered large-magnitude extension (e.g. Buckskin-Rawhide Mountains, Singleton et al., 2014; Whipple Mountains, Gans and Gentry, 2016). This study is the first to document syndetachment mylonitic fabrics in the footwall of the Plomosa detachment fault, and to identify a Miocene plutonic suite in the area, revealing the northern Plomosa Mountains is a metamorphic core complex analogous to the other core complexes in the LCREC.

### ***10.2.2. Synkinematic intrusions***

Diorites and quartz diorites of unit Nic mostly likely intruded  $\sim 20.5$  Ma because they are petrographically similar to the  $20.46 \pm 0.15$  Ma nonmylonitic diorite south of the map area, and they cut across mylonitic leucocratic layers that are likely 22–23 Ma (Figure 21 A–D). These dioritic bodies therefore intruded during exhumation of the Plomosa detachment fault footwall, and most likely after most footwall mylonitization had ended.

However, because they are rheologically stronger than the quartz-rich lithologies that dominate the footwall, it is possible that they intruded during the late stages of mylonitization and resisted penetrative deformation. Late-stage non-mylonitic rhyo-dacite dikes (unit Nd in Plate 1) are interpreted to be syndetachment because of their NW-striking orientations, which are consistent with opening resulting from NE-SW extension (Figure 48 B). They are likely fairly shallow intrusions indicated by their very fine-grained ground mass (Figure 28 C & D), and probably intruded after mylonitization ceased in the footwall of the Plomosa detachment fault, though these intrusions were not dated.

### ***10.2.3. Pre-Miocene mylonitic fabrics***

The compilation map of the northern Plomosa Mountains in Figure 38 shows that the mylonitic front (the top of the zone of mylonitic fabrics) in the footwall of the Plomosa detachment fault is only 2.5–3.5 km north of a SW dipping nonconformity between early Miocene(?) sedimentary units and pre-Cenozoic granitic, gneissic, and metasedimentary rocks. The cross-section in Figure 38 (projection A) demonstrates that prior to tilting of the footwall during extension, the mylonitic front would have been only 1.5–2 km below the surface at the initiation of the Plomosa detachment fault in the early Miocene. With a very high geothermal gradient of 100° C/km (possibly reasonable for a highly-extended terrain undergoing magmatic activity), the temperature at 2 km depth could have been at most ~225° C. In both the gneiss and the Orocopia Schist, dynamically recrystallized quartz has undergone grain boundary migration (GBM) (Figure 40) suggesting deformation temperatures of >~500°C (Stipp et al., 2002), and these fabrics record top-to-the NE shear. In addition, the gneiss locally has chessboard patterns within dynamically recrystallized quartz, indicative of mylonitization temperatures >600° C (e.g. Passchier and Trouw,

2005), which was observed within ~3 km north of the mylonitic front, only ~3 km below the presumed Miocene surface (Figure 58). The high-temperature fabrics of the gneiss are therefore too shallow to be the result of Miocene mylonitization, whereas the high-temperature fabrics of the Orocopia Schist are from a structural depth of 9–12 km (northernmost Orocopia Schist, Figure 58), where it was likely hot enough to undergo mylonitization in the early Miocene.

### **10.3. Relationships of amphibolite- and greenschist-facies deformation fabrics**

The higher-temperature fabrics of the Orocopia Schist are in the structurally deeper northern section (9–12 km paleo-depth, Figure 58) and Ti-in-quartz analysis of Orocopia Schist indicates deformation temperatures of  $531\text{--}572^\circ \pm 4^\circ \text{C}$  (Seymour et al., 2016), confirming the fabric in the sample is the result of amphibolite-facies dynamic recrystallization. The Orocopia Schist almost certainly was deformed at much greater depths at an earlier period (discussed later), and the high-temperature fabrics in the Orocopia Schist may record the earlier deformation event. However, an elevated geothermal gradient of  $60^\circ \text{C}/\text{km}$  would yield amphibolite-facies temperatures at depths of 9–12 km ( $\sim 565^\circ \text{C}$  at 9 km), which may be plausible given the association with synmylonitic plutonism. Thus, it is possible the high-temperature fabrics in the Orocopia Schist record Miocene mylonitization. The structurally-higher southwestern exposures of the Orocopia Schist (6–9 km depth) typically record smaller dynamically recrystallized quartz grain sizes (Figure 58), and no sample is dominated by high-temperature GBM except for a sample of metachert interlayered in the metabasalt.

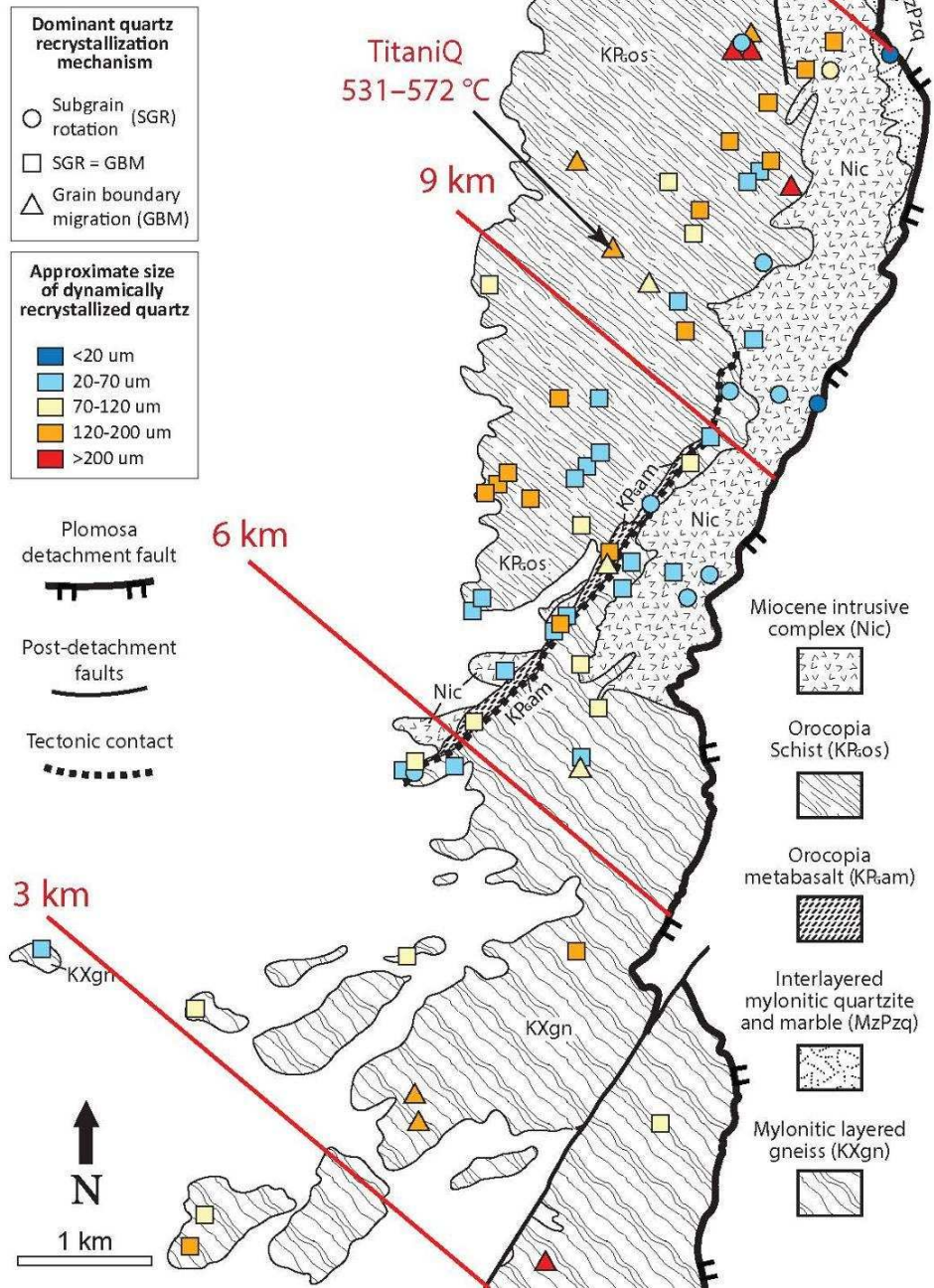
Unit Nic has on average the smallest sizes of dynamically recrystallized quartz grains, and is more often dominated by SGR than any other unit (Figures 40 and 58). The

southern half of unit Nic has dynamically recrystallized quartz grains that are no larger than 70  $\mu\text{m}$ , and several samples are dominated by SGR, which suggests the southern half underwent greenschist-facies dynamic recrystallization. The structurally deeper northern portion of unit Nic on average records higher-temperature fabrics, which is consistent with the Orocopia Schist (Figure 58).

As previously mentioned, the gneiss typically records high-temperature deformation fabrics consistent with amphibolite-facies metamorphic deformation at depths of only  $\sim 3$  km (Figure 58). Interestingly, quartz grain sizes and dynamic recrystallization mechanisms in the gneiss record lower temperatures to the N and NW, in the structurally deeper portions of the footwall. These lower-temperature deformation fabrics are adjacent to, and on trend with, the tectonic contact between the gneiss and the Orocopia Schist (Figure 58).

Most mylonites in the footwall of the Plomosa detachment fault record a combination of GBM + SGR. GBM is often observed to be overprinted by SGR (Figure 39 D), suggesting the mylonites underwent dynamic recrystallization at high temperatures (amphibolite-facies) followed by lower temperatures (upper- to middle-greenschist facies).

Approximate paleo-depths of the footwall of the Plomosa detachment fault including dynamically recrystallized quartz grain sizes and mechanisms



**Figure 58:** Approximate early Miocene pre-detachment paleo-depths of the footwall of the Plomosa detachment fault. Includes dynamically recrystallized quartz grain sizes and mechanisms (see caption in Figure 40 for more information), and a titanium-in-quartz deformation temperature ( $531\text{--}572^\circ \pm 4^\circ \text{C}$ ) of the Orocopia Schist (Seymour et al., 2016).

#### **10.4. Possible origins of mylonitic fabrics**

The mylonitic front as mapped could belong to a shear zone resulting from latest Cretaceous to Early Paleogene extension as suggested to have occurred in the nearby Dome Rock Mountains, Harcuvar Mountains, and Buckskin-Rawhide Mountains (Boettcher and Mosher, 1989; Wong et al., 2013; Singleton and Wong, 2016). The interpretation of a pre-Miocene shear zone is consistent with other localities of Orocochia Schist in SW Arizona and SE California, where mylonitic lineations associated with Paleogene exhumation of the Orocochia Schist trend ENE to NE (Jacobson et al., 2002; Haxel et al., 2002), and are often difficult to separate ~NE-trending lineations associated with Miocene exhumation. Additional evidence for pre-Miocene top-to-the-NE shearing of Orocochia Schist in the Plomosa Mountains include the asymmetry of actinolite pods within the schist. Several pods have  $\sigma$ -clast-shapes that record top-to-the-NE shear (Figure 18 C). However, actinolite within these pods does not show evidence of deformation or recrystallization, and in one thin section, actinolite appears to have grown across a previously folded ultramafic protolith (Figure 18 D). Therefore, formation of actinolite must have occurred after the ultramafic pods within the Orocochia Schist were sheared, which likely occurred before Miocene exhumation. Because the Miocene intrusive complex has mylonitic foliations and lineations that are nearly identical to that of the gneiss and Orocochia Schist (Figures 44 and 45), and all units record top-to-the-NE shear, a pre-existing shear zone may have significantly influenced the geometry and kinematics of mid-crustal extension in the Miocene.

Another possibility for the shallow depth of the mapped mylonitic front is that the nonconformity in the footwall of the Plomosa detachment fault (as illustrated in Spencer et

al., 2015) may actually be in the hanging wall due to a cryptic arch of the Plomosa detachment fault, which in this scenario would reverse dip just north of the Plomosa Pass area and dip SW beneath the nonconformity (as illustrated by Scarborough and Meader, 1983). Thus, the mylonitic shear zone may have been active at greater depths (10–15 km) in the early Miocene, and was arched upwards along with the Plomosa detachment fault in response to unroofing and isostatic rebound (Figure 3). Evidence that the mylonitic fabric in the footwall of the Plomosa detachment fault may be an arched Miocene shear zone are SW-dipping discrete shear zones with top-to-the-SW displacement, and top-to-the-SW sense of shear recorded in mylonitic fabric, which are documented within ~500 m of the mylonitic front. These shear zones with oppositely-directed displacement are identical to the antithetic shears described near the mylonitic fronts of other core complexes in the region, and are interpreted to record folding of the mylonitic shear zone as it is arched during unroofing and isostatic rebound (Figure 5) (Reynolds and Lister, 1990). If the SW-dipping discrete shear zones with top-to-the-SW displacement are Miocene, cutting the ~20.5 Ma diorite (Figure 38), then the mylonitic front would also likely be Miocene. However, to account for the high-temperature fabrics in the gneiss, the paleo-depth of the mylonitic front must be misrepresented in the cross section in Figure 38, opening the possibility that the high-temperature shear zone was active at greater depths. This scenario is unlikely, as the most recent mapping does not support a SW-dipping segment of the Plomosa detachment fault (Spencer et al., 2015).

The Miocene intrusive complex on average has relatively small dynamically recrystallized quartz grain sizes (>50% are 20–70  $\mu\text{m}$ ) formed via subgrain rotation (Figure 40), and it has undergone a greater degree of chloritization than other footwall

units (Figure 31), suggesting mylonitization of unit Nic occurred primarily in the greenschist-facies. In contrast, the shear fabrics in the gneiss and Orocopia Schist record a mix of amphibolite-facies and greenschist-facies mylonitization. However, the preponderance of mylonitic to protomylonitic Miocene intrusions within the Orocopia Schist in the northern Plomosa Mountains demonstrates that the Orocopia Schist was at least partially mylonitized in the Miocene, and some (if not all) of the mylonitic lineations in the Orocopia Schist must record NE-SW extension associated with Miocene detachment faulting. Though there is compelling evidence that the mylonitic fabrics of the gneiss are pre-Miocene, the Orocopia Schist is more likely to have been entirely mylonitized during Miocene detachment faulting because it is richer in mica and quartz, and thus is more easily mylonitized at greenschist-facies conditions than the crystalline gneiss. Also, the Orocopia Schist seems to have hosted more Miocene intrusions than the gneiss, which would locally increase the temperature and allow for mylonitization at shallower depths (Plate 1; cross-section A-A' in Figure 9). Finally, the Orocopia Schist was at a greater structural depth overall compared to the gneiss, suitable for the development of high-temperature fabrics (Figure 58).

#### **10.5. Geometric relationship of mylonitic fabrics and the Plomosa detachment fault**

Mylonitic foliations of the Orocopia Schist as well as unit Nic on average dip moderately to the SW, whereas mylonitic foliations of the gneiss are corrugated, and thus dip moderately to shallowly NW and E, or are near horizontal (Figure 44 B, C & D). Previously discussed was the possibility that some mylonitic fabrics may record latest Cretaceous to early Paleogene exhumation, and though mylonitic Miocene intrusions record Miocene mylonitization, they could have reactivated an older shear zone. The trends



of mylonitic lineations are overall the same throughout the footwall of the Plomosa Detachment fault, but the mylonitic foliation of the gneiss is overall discordant to the mylonitic foliation of the Orocopia Schist and unit Nic (Figure 38). The moderately SE-dipping mylonitic foliations along the tectonic contact between the Orocopia Schist and the gneiss are also discordant to the overall mylonitic fabrics of both units (Plate 1; Figures 9 and 38). The Miocene intrusions along the tectonic contact between the Orocopia Schist and the gneiss, and the gneiss adjacent to the tectonic contact, have mylonitic foliations that locally parallel the SE-dipping contact.

The gently E- to NE-dipping Plomosa detachment fault is discordant to the majority of mylonitic foliations throughout the footwall (Plate 1; Figure 9). This discordance suggests the Plomosa detachment fault captured a mylonitic shear zone at greater depth, and that the mylonitic fabric is not the downward continuation of the detachment fault. The average orientation of mylonitic foliations in unit Nic is S/D [124, 30 SW] based on the contour maximum to its poles, which is similar to the average orientation of the Orocopia Schist, which is S/D [130, 19 SW]. Because the Orocopia Schist has been at least partially reworked by Miocene mylonitization, the mylonitic foliations of unit Nic and the Orocopia Schist may represent the orientation of the Miocene shear zone, and their average orientation is S/D [127, 25 SW]. Restoring the footwall to its original orientation prior to tilting along the Plomosa detachment fault (as described earlier) rotates the average mylonitic foliation of the Orocopia Schist and unit Nic by  $48^\circ$  to a NE-dip of  $\sim 23^\circ$ . Mylonitic fabrics within this Miocene shear zone record top-to-the-NE shear, therefore normal displacement would have been accommodated along the shallowly NE-dipping shear zone prior to capture by and rotation along the Plomosa detachment fault. This initial geometry

has similarities with the Buckskin-Rawhide metamorphic core complex to the NE, where footwall mylonites are interpreted to have initiated as a subhorizontal shear zone that was captured by a moderately-NE-dipping detachment fault (Singleton and Mosher, 2012).

Conducting the same rotation on the gneiss (48° rotation to the NE) reorients the mylonitic fabric to an average dip of ~53° to the NE, considerably steeper than the Orocochia Schist and unit Nic. Because the gneiss has high-temperature fabrics just 2–3 km below the Miocene paleo-surface, it likely records mylonitization during a pre-Miocene deformation period, and its mylonitic fabrics may have formed in a moderately-dipping latest Cretaceous to early Paleogene normal-displacement shear zone.

A zone of mylonitic foliations that are adjacent and subparallel to the Plomosa detachment fault occupies the central map area (Labeled III in Figure 58), and unit Nic in that area is locally intensely chloritized and brecciated (Figure 20 E & F). Mylonitic foliations subparallel to the detachment fault suggests it is a shear zone that was active along the fault rather than one that was captured, and brecciation within the zone suggests it transitioned to localized brittle deformation immediately below the detachment fault during exhumation.

### **10.6. Three mylonitic shear zones**

Based on the geometric relationships between the mylonitic foliations, their discordance or subparallelism to the Plomosa detachment fault, and their relationship to deformation temperatures recorded by microstructures (Figure 58), I propose there are three distinct mylonitic shear zones in the footwall of the Plomosa detachment fault (Figure 59). The oldest shear zone (labeled I in Figure 59) was active prior to the Miocene, and is comprised of the mylonitic corrugated gneiss. This top-NE, normal-sense shear zone is

interpreted to have had a moderate NE-dip prior to detachment faulting. A pre-Miocene age is supported by the high-temperature fabrics recorded in the gneiss at a very shallow depth below the Miocene paleo-surface (Figures 58). The northern extent of the corrugated mylonitic fabric of the gneiss demarcates the Miocene mylonitic front (Figure 59). The second oldest shear zone (labeled II in Figure 59) initiated in the Miocene with a shallow NE dip, and is comprised mostly of Orocopia Schist and unit Nic. Shear zone II was captured and exhumed by the more steeply-dipping Plomosa detachment fault. Miocene dikes and sills throughout the Orocopia Schist and a majority of the Miocene intrusive complex were mylonitized by this shear zone, supporting a Miocene age. The tectonic contact (marked by unit KPGam; Plate 1, Figure 59) is likely the contact between shear zone II and the pre-Miocene shear zone (shear zone I). The mylonitic gneiss was locally re-mylonitized in the Miocene by shear zone II immediately adjacent to the tectonic contact, as suggested by mylonitic foliations of the gneiss that parallel the tectonic contact, and lower temperature fabrics in the gneiss immediately adjacent to the tectonic contact (Figures 58 and 59). Because the Orocopia Schist underwent a greater magnitude of Miocene shear than the adjacent gneiss, the SE-dipping contact between the Orocopia Schist and the gneiss developed into a dextral shear zone, which resulted in a lateral strain-gradient that likely yielding the L-tectonites observed at the contact (Plate 1). The youngest shear zone (labeled III in Figure 59) lies immediately below the Plomosa detachment fault and has moderately to gently E- to NE-dipping mylonitic fabrics that are subparallel to the E-dipping limb of the corrugated detachment fault, suggesting this shear zone is the direct result of mylonitization along the detachment fault. Shear zone III and the brecciated rock associated with it are not present along the northern half of the detachment fault, and was

likely incised into the hanging wall. Incisement of detachment-parallel mylonite zones has been inferred for other core complexes in the region (Lister and Davis, 1989; Singleton and Mosher, 2012). An interpretation for the development of the three shear zones is illustrated in Figure 60.

The highest temperature fabrics (dynamically recrystallized quartz  $>200\ \mu\text{m}$ , dominated by GBM) of the Orocopia Schist are in the structurally deepest (northernmost) position in the footwall, which indicate temperatures of  $>500^\circ\text{C}$ , and Ti-in-quartz analysis from a sample in the northern Orocopia Schist indicate temperatures of  $\sim 550^\circ\text{C}$  (Figure 58) (Seymour et al., 2016). I had suggested that these high-temperature deformation fabrics could have formed from mylonitization at their pre-detachment paleo-depth of 9–12 km due to a high geothermal gradient ( $60^\circ\text{C}/\text{km}$ ). However, the pre-detachment paleo-depths projected from the nonconformity (Figure 58) do not take into account exhumation along shear zone II prior to initiation and capture by the Plomosa detachment fault. Therefore, the pre-extensional paleo-depth of these rocks may have been significantly deeper when shear zone II was active, and thus a less exaggerated geothermal gradient would be necessary to account for high-temperature Miocene fabrics.

## Shear-zone domains in the footwall of the Plomosa detachment fault

Note: each shear zone records top-to-the NE displacement, and only represents the shear zone with the dominant influence

### Detachment-subparallel Miocene shear zone



This Miocene mylonitic shear zone is subparallel to, and is interpreted to be the result of shear from, the Plomosa detachment fault.

### Detachment-discordant Miocene shear zone

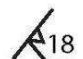



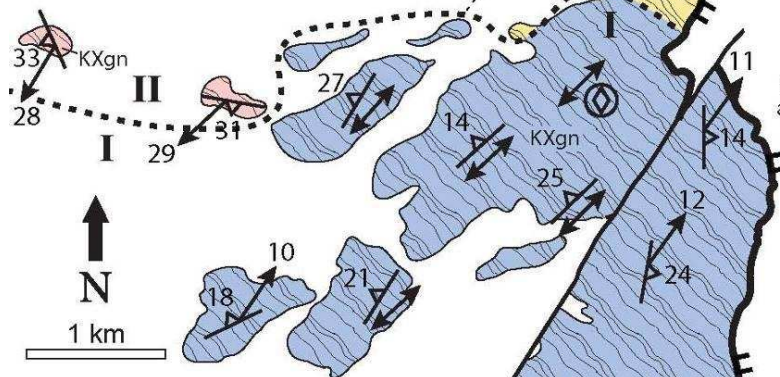
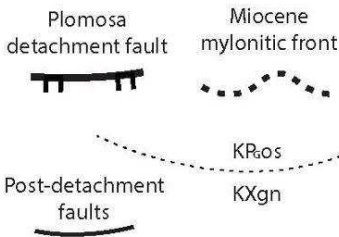
Interpreted to have initiated with a shallow NE-dip, this Miocene mylonitic shear zone was captured and exhumed by the Plomosa detachment fault.




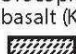

### Pre-Miocene shear zone



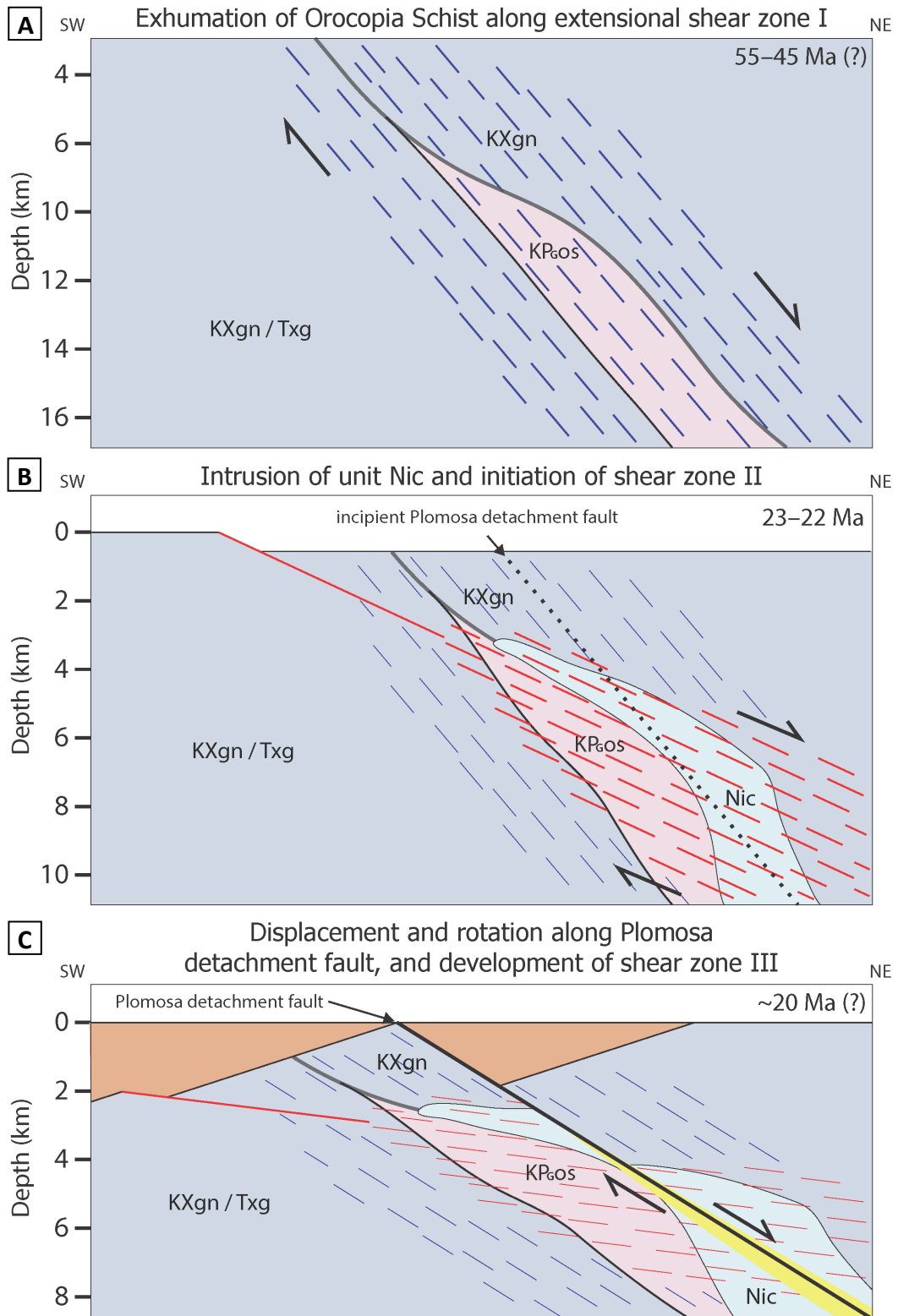
Interpreted to have had a moderate NE-dip prior to Miocene exhumation, this pre-Miocene shear zone is suspected to be latest Cretaceous to Paleogene in age, and is likely responsible for the exhumation of the Orocopa Schist to the near surface prior to Miocene core complex development.

 Mylonitic Foliation (S/D) with Mylonitic Lineation (T/P) (represents average of surrounding measurements where applicable)  


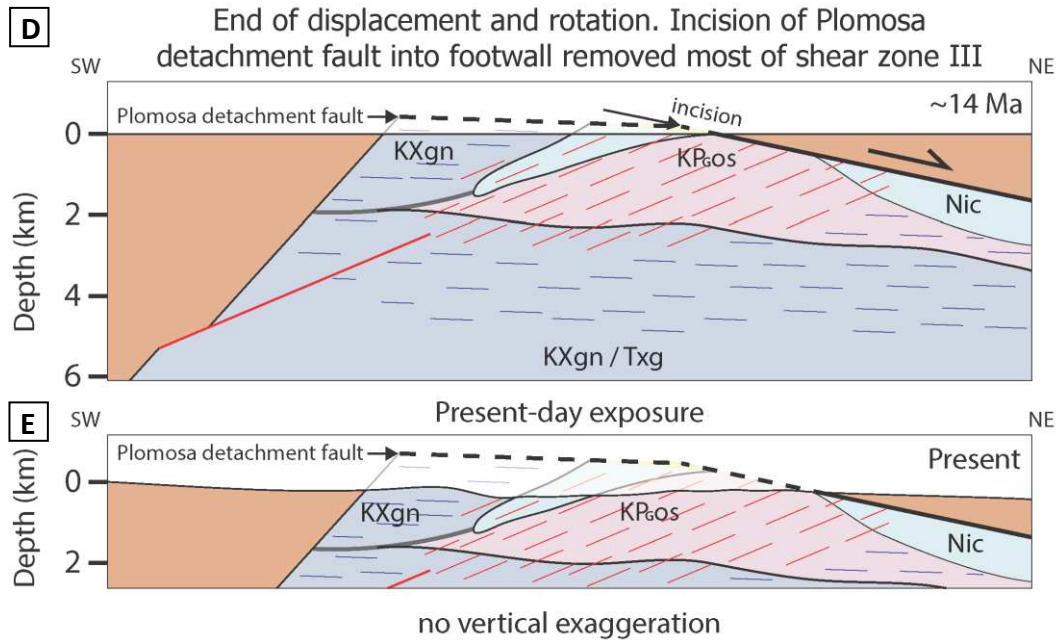


- Miocene intrusive complex (Nic) 
- Orocopa Schist (KR.os) 
- Orocopa metabasalt (KR.am) 
- Interlayered mylonitic quartzite and marble (MzPzq) 
- Mylonitic layered gneiss (KXgn) 

**Figure 59:** Three shear-zone domains interpreted in the footwall of the Plomosa detachment fault, described in the figure and text. Shear zone III may have been incised into the hanging wall to the north, and thus is not continuous along the detachment fault.



**Figure 60:** continued on next page.



**Figure 60 continued:** Interpretation for the structural evolution of the three mylonitic shear zones. **A)** Development of shear zone I, possibly during the Paleogene, accommodating exhumation of the Orocopia Schist. **B)** Initiation of shear zone II during intrusion of unit Nic, overprinting older fabrics in the Orocopia Schist and mylonitizing unit Nic. **C)** Capture and exhumation of shear zone II by the Plomosa detachment fault which initiated at a high angle, and development of shear zone III locally along the Plomosa detachment fault. Rotation of the footwall and the Plomosa detachment fault occurred during displacement along the detachment fault. **D)** End of displacement and rotation of the footwall and Plomosa detachment Fault. Incision of the Plomosa detachment into the footwall near the end of displacement removed most of shear zone III. **E)** Present-day topography and exposure of the subhorizontal mylonitic foliation of the corrugated gneiss, and SW-dipping mylonitic foliation of the Orocopia Schist and unit Nic.

### **10.7. Relationship of Miocene intrusive complex to the Plomosa detachment fault**

The NNE- to NW-trending main body of the Miocene intrusive complex borders the broadly corrugated Plomosa detachment fault as a consistent 0.5–1 km-wide belt (Plate 1), which strongly suggests a relationship between the two. The northern approximately two-thirds of unit Nic was mylonitized in the originally shallowly NE-dipping shear zone (shear zone II), which was later captured by the detachment fault, and therefore unit Nic must have intruded into shear zone II prior to initiation of the detachment fault. Thus, it is unlikely unit Nic localized along the detachment fault; rather, several other structures were present along which unit Nic could have localized to form its arc-shaped distribution. Prior to core complex development, the corrugated foliation of the gneiss dipped  $\sim 50^\circ$  NE, along which unit Nic could have intruded yielding its arcuate distribution (Plate 1; Figures 59 and 60). The pre-detachment boundary between the Orocopia Schist and the gneiss is another weakness that unit Nic could have localized along. Unit Nic is observed to have localized along active shear zones such as the tectonic contact between the Orocopia Schist and gneiss (Plate 1), though if active shear zones were the main control, unit Nic may be expected to have intruded over a wider area within shear zone II rather than confined mostly to a 0.5–1 km-wide belt (Figure 59). Unit Nic within the detachment-subparallel shear zone (shear zone III, Figure 59) likely had already intruded into the location of shear zone III prior to initiation of the Plomosa detachment fault, and was mylonitized in shear zone III after capture by the detachment fault.

Exhumation along the Plomosa detachment fault is thought to have initiated as early as  $23 \pm 2$  Ma (Foster and Spencer, 1992), and intrusions of unit Nic are as earlier as  $22.81 \pm 0.49$  Ma. The overlap in error is consistent with initiation of the Plomosa detachment fault



in response to intrusion of unit Nic, consistent with the conclusion that the Buckskin-Rawhide detachment fault to the NE initiated following intrusion of the Swansea Plutonic Suite into the footwall (Singleton et al., 2014). Intrusion of unit Nic into either the moderately-dipping corrugated geometry of the gneiss, or a moderately-dipping contact between the gneiss and the Orocopia Schist, would have yielded thermal weakening and a favorable geometry to trigger a major high-angle normal fault. Low-temperature thermochronology of the structurally highest portion of the footwall could be used to reveal when rapid cooling began, which would resolve whether the detachment fault was active before or after intrusion of unit Nic.

The relationship of unit Nic<sub>a</sub> to unit Nic (which greatly overlap) and to the Plomosa detachment fault is clear. As described in the section “Mineralization and Alteration”, unit Nic appears to have been the focus of hydrothermal fluids, and it was concluded that the alteration zone borders the Plomosa detachment fault not because the detachment fault caused a localization of alteration there, but because that is where the intrusive complex localized, which was likely the source and conduit of magmatically-derived hydrothermal fluids.

### **10.8. Implications of the Miocene intrusive complex**

As discussed, it seems likely that the Plomosa detachment fault localized along unit Nic, after intrusion of unit Nic along the corrugated foliation of the gneiss and/or the contact between the Orocopia Schist and the gneiss. It also seems likely that the originally shallowly NE-dipping shear zone involving the Orocopia Schist (shear zone II) initiated in response to intrusion of unit Nic due to thermal weakening of already rheologically weak schist. Synmylonitic intrusions have been documented in numerous metamorphic core

complexes of SE California and SW Arizona (e.g. in the South Mountains, Reynolds, 1995, the Buckskin-Rawhide Mountains, Bryant and Wooden, 2008, Whipple Mountains, Gans and Gentry, 2016), and the addition of the Plomosa Mountains as a core complex with synmylonitic intrusions (as documented in this study) bolsters the idea that metamorphic core complexes are intrinsically tied to magmatism. Perhaps the most significant implication of unit Nic is that it was most likely the trigger for the initiation of large-magnitude extension in the northern Plomosa Mountains metamorphic core complex.

Ductile deformation along the tectonic contact between the Orocopia Schist and the gneiss may have been more protracted than throughout the main body of the Orocopia Schist due to localization of intrusions along it. Protracted deformation is suggested by the lower-temperature fabrics of dynamically recrystallized quartz recorded within ~1 km of either side of the contact relative to the main body of Orocopia Schist, which generally has higher-temperature fabrics (Figure 58).

Documentation of the Miocene intrusive complex (unit Nic) in the northern Plomosa Mountains provides an explanation for two observations made in previous studies. Duncan (1990) documented mineralization within the hanging wall of the Plomosa detachment fault, and stated that a late-stage rejuvenation of mineralizing fluids and increase in temperature were possibly due to an igneous source. I had inferred that unit Nic was likely the focus of magmatically-derived hydrothermal fluids, and conclude that is likely the source of the mineralizing fluids and increase in temperature that Duncan (1990) had documented. Knapp and Heizler (1990) inferred from  $^{40}\text{Ar}/^{39}\text{Ar}$  thermochronologic data that the partial resetting of K-feldspar in the Plomosa Pass area of the northern Plomosa Mountains may have been caused by a renewed heating event during Miocene detachment

faulting. This too is explained by the presence of unit Nic documented in this study, which includes a large body of synkinematic diorite near the Plomosa pass area (Figure 38).

### **10.9. Topographic trends**

Several topographic features of the northern Plomosa Mountains can be explained by the orientations of structures documented in this study. The range has an anomalous N-S orientation as compared to the Buckskin-Rawhide and Harcuvar Mountains to the northeast (Figure 2), which is due to the corrugation of the Plomosa Detachment fault plunging to the NE with unequal preservation of its limbs. The eastern limb of the corrugated detachment fault is well preserved, as there are many kilometers of exposure, whereas the northwestern limb is hardly preserved at all. If there was equal preservation of the two, and assuming they were the same length, the Plomosa detachment fault would have a ~10 km-long WSW-striking segment to the northwest. To explain why the western side of the range is not exposed and instead buried by alluvium/colluvium, it was hypothesized that a N-striking fault may have down-dropped the western side of the range, and that a graben lies beneath the N-S La Posa Plain west of the northern Plomosa Mountains. No evidence for such a fault was found, though why there is such unequal preservation of the limbs of the detachment fault is not known. Finally, the N-S orientation of the range was exaggerated by offset along the N- and NE-striking post-detachment faults (Figure 38).

Numerous NE-SW trending ridges and valleys trend nearly parallel to the mylonitic lineations in the footwall of the Plomosa detachment fault (Plate 1). It was hypothesized that these NE-trending ridges and valleys may have formed within folds in the mylonitic foliation, with fold axes parallel to the mylonitic lineation direction. However, folding of

the mylonitic foliation was not observed to be coincident with the ridges and valleys (Plate 1). Several of the NE-trending ridges in the footwall of the Plomosa detachment fault are capped by mylonitic intrusions of the Miocene intrusive complex, which are likely more resistant to erosion. Also, relatively coherent rock interlayered in Orocopia Schist sometimes form elongated ridges parallel to mylonitic lineations and are an expression of L>S mylonitic fabrics. I propose that the NE-trending ridges and valleys simply formed due to erosion of the anisotropic footwall of the Plomosa detachment fault, which includes resistant, elongated, lineation-parallel outcrops of resistant rock. Alternatively, Spencer (2000) concluded that similar extension-parallel drainages documented in the other metamorphic core complexes of SW Arizona likely initiated along surface exposures of the detachment fault scarps, forming down-dip (extension-parallel) drainages that lengthened as the footwall was exhumed.

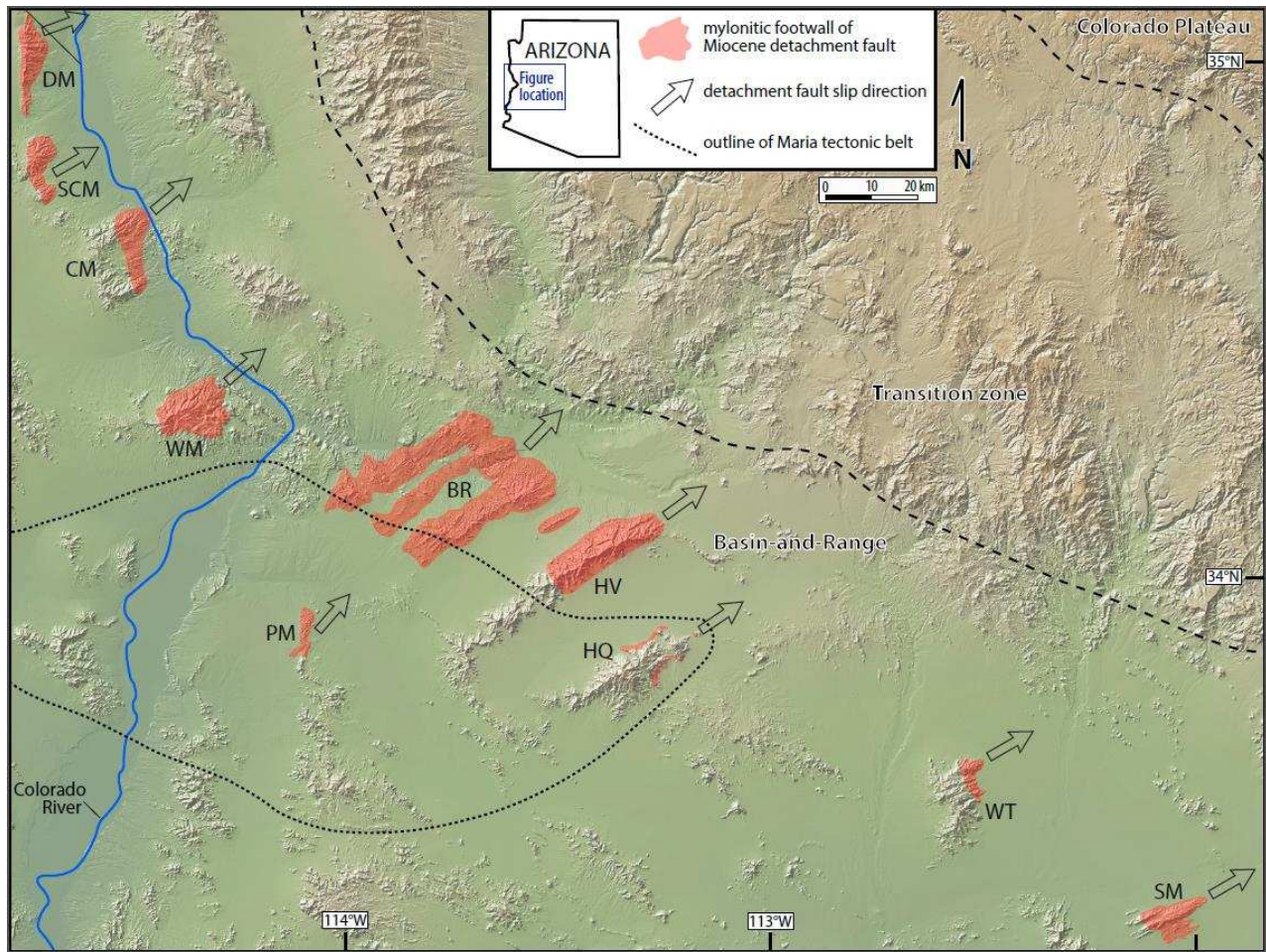
E- and NW-dipping limbs of the prominent corrugation in the gneiss form ridges that 'V' to the NE (Plate 1). Interestingly, the NE-striking fault that separates the limbs is nearly parallel to, and occupies the exact space that the corrugation-axis for the corrugation could be drawn. Lastly, the NNE-trending eastern ridge of the corrugated gneiss is elevated relative to the NE-trending western ridges due to E-side-up displacement along the NE-striking fault.

#### **10.10. Comparison of northern Plomosa Mountains to other core complexes in the LCREC**

The northern Plomosa Mountains metamorphic core complex has many similarities to the other core complexes within the LCREC and only minor differences: 1) Slip accommodated by the Plomosa detachment fault is nearly identical to the direction of slip

of nearby core complexes (Figure 61). 2) The Plomosa detachment fault is corrugated about a NE-trending axis, as is the Whipple-Buckskin-Rawhide-Bullard detachment fault system. A key difference is that Plomosa detachment fault dips  $\sim 12^\circ$  to the NE on average, whereas the detachment faults of the Buckskin-Rawhide Mountains and Harcuvar mountains to the NE are subhorizontal in their dip-direction. The Plomosa detachment fault may have a steeper dip either because it initiated at a steeper angle, or underwent less rotation, having accommodated less displacement. 3) The Plomosa Mountains metamorphic core complex has Miocene age mylonitic fabrics as documented by presence of mylonitic Miocene intrusions. 4) Much of the footwall of the Plomosa detachment is comprised of L>S tectonites in the more homogenous layers, and the compositionally layered gneiss is corrugated, as described for homogenous and layered units in the Buckskin-Rawhide Mountains (Singleton, 2013). Because the corrugated gneiss is interpreted as a pre-Miocene normal-displacement shear zone, it may suggest that constriction is commonly associated with large-magnitude extension, and that the pre-Miocene shear zone was analogous to a core complex shear zone. 5) L>S fabrics are associated with inclined tight/recumbent isoclinal folds with fold axes parallel to the lineation direction, as described in the central Mojave metamorphic core complex (Fletcher and Bartley 1994). 6) The footwall of the Plomosa detachment fault is intruded by synmylonitic intrusions as are the nearby South Mountains (Reynolds, 1986), Buckskin-Rawhide Mountains (Bryant and Wooden, 2008), and Whipple Mountains (Gans and Gentry, 2016), and much of the mylonitic Miocene intrusive complex is compositionally and texturally similar to the Swansea Plutonic suite in Buckskin-Rawhide Mountains to the NE (Figure 20 A) (Bryant and Wooden, 2008; Singleton and Mosher, 2012).

Two notable differences between the northern Plomosa Mountains metamorphic core complex and neighboring core complexes are: 1) the relatively isolated position of the northern Plomosa Mountains off of the trend of the other core complexes of the LCREC (Figure 61), and 2) that the northern Plomosa Mountains contains the Orocopia Schist, which has not been documented in other LCREC core complexes.



**Figure 61:** Mylonitic footwalls (areas in red) of metamorphic core complexes in the LCREC, with the average slip direction of the detachment fault indicated by an arrow. DM: Dead Mountains, SCM: Sacramento Mountains, CM: Chemehuevi Mountains, WM: Whipple Mountains, PM: Plomosa Mountains, BR: Buckskin-Rawhide Mountains, HV: Harcuvar Mountains, HQ: Harquahala Mountains: WT: White Tank Mountains, SM: South Mountains. Figure from Singleton et al. in review.

## **11. Orocopia Schist at the Northern Plomosa Mountains**

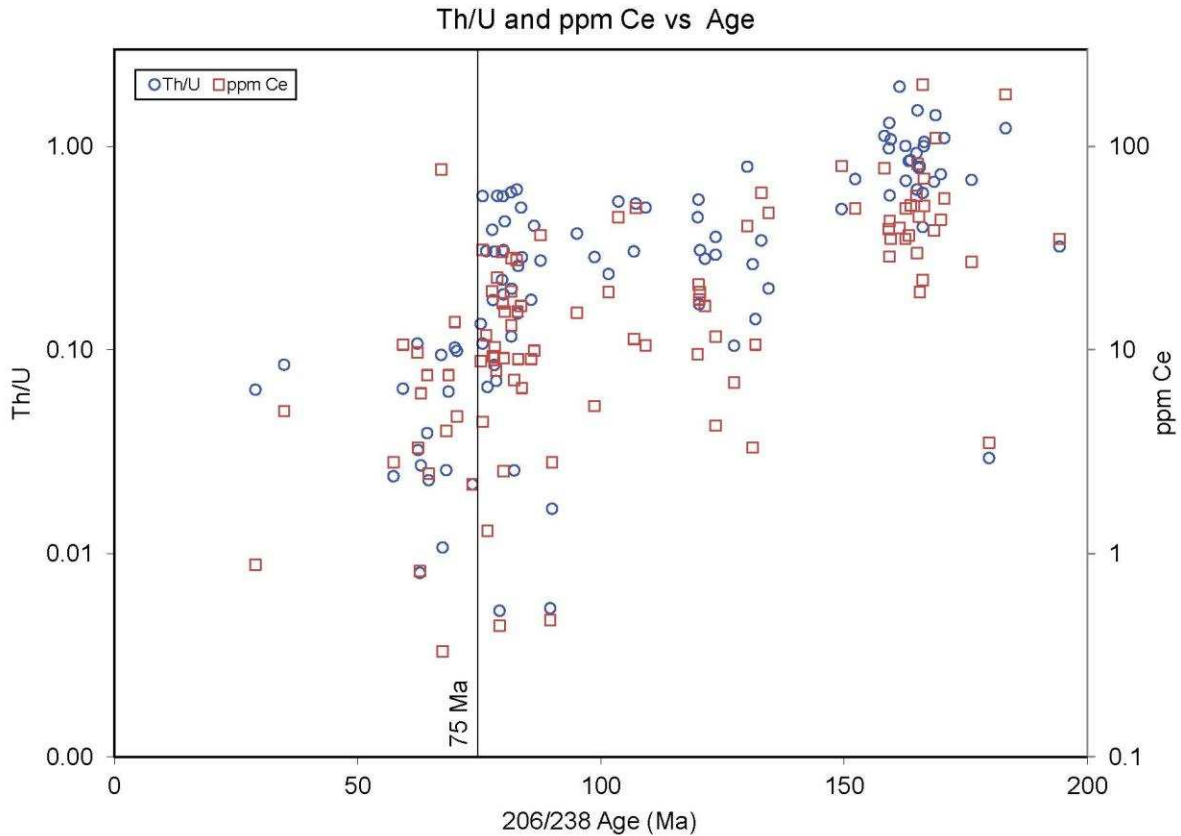
### **11.1. Deposition, subduction, and metamorphism of the Orocopia Schist**

The history of deposition, subduction, and metamorphism of the Orocopia Schist can be inferred by the plot of Th/U ratios versus the age of zircons (Figure 52). High Th/U values for Orocopia Schist ranging from  $>0.1$  to  $\sim 3$  are interpreted to record igneous growth of zircons that were later eroded, transported, and deposited as detrital zircons. A Jurassic-Cretaceous magmatic arc was active along California (e.g. Decelles, 2004), providing a plentiful source of volcanic zircons that could be incorporated into the trench sediments shortly after eruption. A sharp drop-off in Th/U ratios  $>0.1$  occurs at  $\sim 68$ – $70$  Ma, which represents the maximum depositional age of the Orocopia Schist (the youngest age of detrital zircons in the sedimentary protolith of the Orocopia Schist). The maximum depositional age of  $68$ – $70$  Ma for the Orocopia Schist at the northern Plomosa Mountains is similar to the maximum depositional age of zircons for Orocopia Schist at Cemetery Ridge, which is  $\sim 65$  Ma (Jacobson et al., 2017). Though it has been cautioned that interpreting low Th/U ratios of  $<0.1$  as a cutoff for metamorphic zircon growth can be misleading in some instances (Lopez-Sanchez et al., 2015), this cutoff works remarkably well for the Orocopia Schist at the Plomosa Mountains. It was demonstrated that thin metamorphic rims of zircons in the Orocopia Schist correspond to Th/U ratios  $<0.1$ , and the age range of the high density of Th/U ratios  $<0.1$  is consistent with the time frame the Orocopia Schist would have been metamorphosed after it was subducted.

Trace element analysis during zircon split-stream laser ablation was conducted for sample 1016-P145, yielding a concentration of a variety of elements for each age, including cerium (Ce). Ce concentrations for this sample drop-off at the exact age the Th/U ratios do



(~75 Ma, Figure 62), suggesting that the low Th/U ratios formed from metamorphism in the presence of ocean water (e.g. Aranovich et al., 2017), evidence that latest Cretaceous to Paleogene metamorphism was the result of subduction of the Orocopia Schist. I propose that Th/U ratios  $<0.1$  for Orocopia Schist ages between ~75–50 Ma record metamorphism of the Orocopia Schist as it was subducted (Figure 52), and that Th/U ratios  $<0.1$  prior to ~75 Ma likely record regional metamorphism associated with pluton emplacement in the Sierra Nevada magmatic arc, which would have overprinted older metamorphic rims that are mostly absent from zircons older than the Late Cretaceous. It is interesting to note that there is no time gap between the drop-off of Th/U ratios  $>0.1$ , and the maximum density of Th/U ratios  $<0.1$ , but rather they appear to occur simultaneously, suggesting the drop-off of Th/U ratios  $>0.1$  at 68–70 Ma represents not just the maximum depositional age, but the age of subduction of the Orocopia Schist as well (Figure 52). This is not surprising given the very high subduction rates of up to 120 km/Myr active during the early Paleogene (Engebretson et al., 1985; Stock and Molnar, 1988; Doubrovine and Tarduno, 2008), which would result in rapid initiation of metamorphism following subduction. The Th/U ratios and Ce concentration of sample 1016-P145 suggest it was subducted ~75 Ma (Figure 62), implying the Orocopia Schist may have been subducted over a protracted period of time as slivers that were accreted beneath the crust. The range of post-~70 Ma zircon ages with Th/U ratios  $<0.1$  suggests that subduction-related metamorphism continued to at least 50 Ma when the majority of ages disappear, a time-span of ~20 Myr.



**Figure 62:** Th/U ratios (left axis) and ppm Ce (right axis) vs. age for sample 1016-P145 of Orocopia Schist. Note logarithmic Y-axes. A sharp drop-off for both the Th/U ratios and ppm Ce occurs at ~75 Ma.

## 11.2. Implications for emplacement of the Orocopia Schist

In the northern Plomosa Mountains, the paleo-depth of the Orocopia Schist prior to initiation of the early Miocene Plomosa detachment fault was determined to be 3–4 km (Figure 38, projection B), and the structurally deepest (northernmost) exposed portion of the Orocopia Schist had a paleo-depth of 9–12 km. The exposed portion of the Orocopia Schist has a structural thickness of ~1.8 km (Figure 38, projection C), but a minimum structural thickness as projected in cross-section is ~2.7 km (Figure 38, projection D).

As discussed, an originally moderately NE-dipping pre-Miocene mylonitic shear zone (shear zone I, Figure 59) comprised of the corrugated gneiss is cut by an originally

shallowly NE-dipping Miocene shear zone (shear zone II, Figure 59) comprised of the Orocopia Schist and unit Nic. Both shear zones record top-to-the-NE shear, indicating they accommodated normal displacement in their originally NE-dipping orientations. The Orocopia Schist was exhumed to a depth of 3–4 km prior to Miocene exhumation, and the pre-Miocene shear zone of the corrugated gneiss is a likely structure to have accommodated this exhumation.

The isolated location of the Plomosa Mountains metamorphic core complex relative to other core complexes in the region, and the presence of Orocopia Schist at the Plomosa Mountains which is not documented in other core complexes, suggests that the Orocopia Schist may be linked to the development of the Plomosa Mountains core complex. The rheological contrast between the Orocopia Schist and surround gneiss would potentially localize strain near their contact, and it may have been favorable for the Plomosa detachment fault to initiate above the rheologically weak Orocopia Schist that extended from a paleo-depth of 3–4 km to at least 10–12 km. However, exhumation of the Orocopia Schist to a within 3–4 km of the surface prior to early Miocene detachment faulting is a greater puzzle. The northern Plomosa Mountains is located within the Maria fold-and-thrust belt (Figure 7), an area presumed to have formed a crustal welt as thick as 50 km in the Cretaceous (Spencer and Reynolds, 1990), prior to subduction of the Orocopia Schist at 68–70 Ma. If subducted below the crustal welt, the Orocopia Schist at the northern Plomosa Mountains would have needed to be exhumed ~45 km through the crust sometime in the Paleogene. However, there is no evidence that the Orocopia metabasalt (unit KPGam) underwent eclogite-facies metamorphism, which would be expected if subducted below 50 km of crust (>14 kilobars), and thus it is unlikely the Orocopia Schist was ever subducted

below a 50 km crustal welt. Explanations for why the Orocopia Schist was not subducted to depths >50 km include 1) the Maria fold-and-thrust belt was never 50 km thick, 2) the bottom of the 50 km-thick crustal welt of the Maria fold-and-thrust belt was sheared off by the shallowly-subducting Farallon slab, or 3) the Orocopia Schist relaminated from the top of the Farallon slab (Chapman et al., 2013; Chapman 2016), and was extruded into the middle crust before reaching the crustal welt. Even if the Orocopia Schist was only 20–30 km depth after subduction, significant Paleogene exhumation of the Orocopia Schist would have been necessary for the Orocopia Schist to have reached 3–4 km depth prior to the Miocene.

As just described, the 3–4 km early Miocene paleo-depth of the Orocopia Schist in the northern Plomosa Mountains necessitates a period of Paleogene exhumation, which is documented to have occurred in other locations of POR schists and metamorphic core complexes in the region. Detailed thermochronologic studies of Orocopia Schist at the Gavilan Hills (Picacho area in Figure 7) and Orocopia Mountains revealed a Paleogene period of rapid cooling between ~52–43 Ma (Jacobson et al., 2002, 2007), consistent with movement on the Paleogene Chocolate Mountains fault of the Chocolate Mountains anticlinorium, SW of the Plomosa Mountains (Figure 7) (Haxel et al., 2002). Also, Latest Cretaceous to Early Paleogene NE-SW extension is suggested to have occurred in the nearby Dome Rock Mountains, Harcuvar Mountains, and Buckskin-Rawhide Mountains (Boettcher and Mosher, 1989; Wong et al., 2013; Singleton and Wong, 2016). The pre-Miocene shear zone recorded by the corrugated gneiss likely accommodated Paleogene exhumation of the Orocopia Schist in the northern Plomosa Mountains. Because the mylonitic lineation direction of the pre-Miocene shear zone is identical to that of the

Miocene shear zones (Figure 59), it is possible that the specific Miocene extension direction of the Plomosa Mountains metamorphic core complex was influenced by pre-existing NE-SW lineated fabric.

Paleogene extension following subduction of the Orocopia Schist could have been triggered by rheological weakening of the crust from: 1) hydration associated with shallow subduction, and/or 2) from emplacement of rheologically weak schist in the lower crust, leading to gravitational collapse of the overthickened crust. Therefore, the Orocopia Schist not only seems to control the location of the northern Plomosa Mountains metamorphic core complex, but regionally may also have been responsible for latest Cretaceous to Paleogene extension documented in the area.

Documentation of Orocopia Schist at the northern Plomosa Mountains provides additional constraint on the geometry and extent of the subducted POR schists. It has been debated whether the POR schists form a continuous layer sandwiched between the subducting plate and overlying crust, or whether the linear exposure along the Chocolate Mountains anticlinorium implies that the Orocopia Schist is continuous in the subsurface only along strike, and not parallel to the direction of subduction (Haxel et al., 2002). The location of Orocopia Schist at both Cemetery Ridge and the northern Plomosa Mountains confirm that the Orocopia Schist was transported far inland, and it is likely that a continuous layer extends from these locations to the Chocolate Mountains anticlinorium (Figure 7).

### **11.3. Xenocrystic zircons: Melting of Orocopia Schist?**

Xenocrystic zircons in the leucocratic intrusions of the Miocene intrusive complex (unit Nic) have age distributions and Th/U ratios that appear identical to the Orocopia

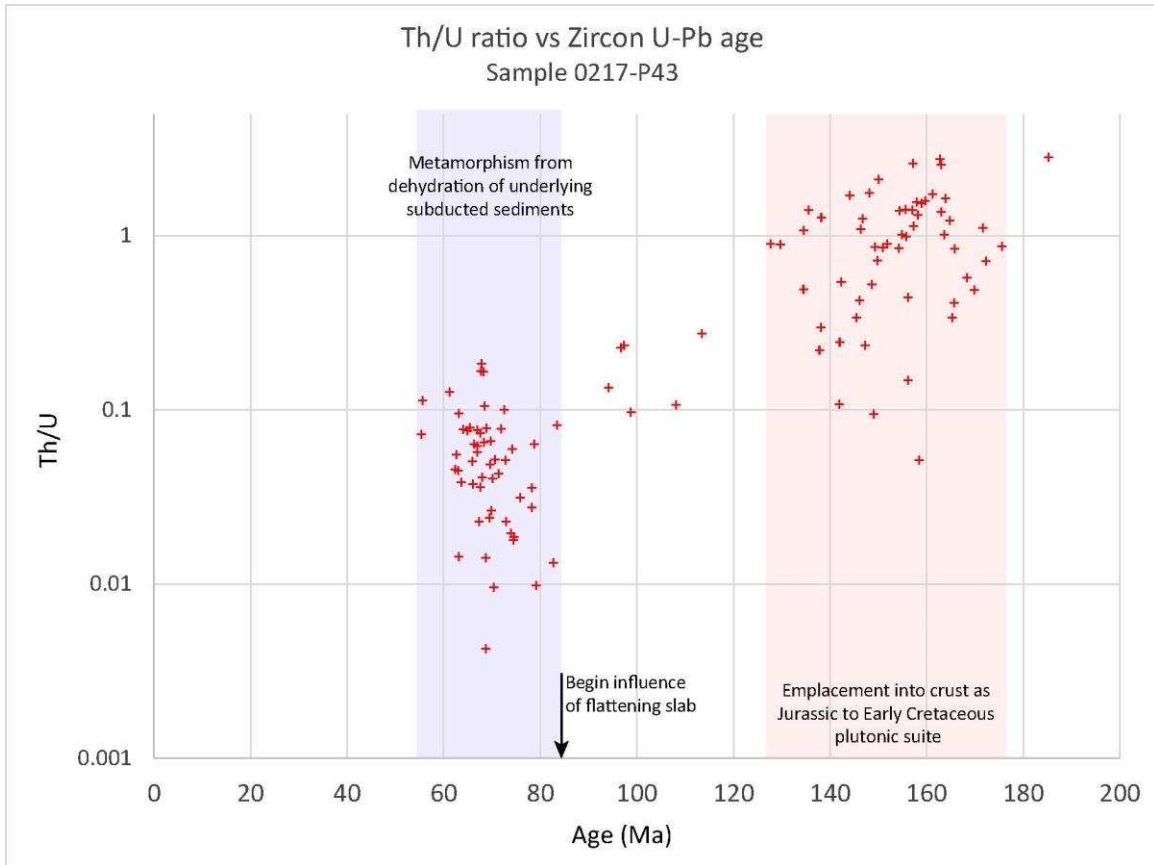
Schist (Figure 52), and two intrusive samples [0217-P43 and 0217-P47] have entirely xenocrystic zircons, one of which [0127-P43] was collected to represent the core of the intrusive complex. These two samples with entirely xenocrystic zircons suggest that melting or assimilation of Orocopia Schist at a deeper structural level was the source of these leucocratic intrusions. However, an age distribution that mimics that of the Orocopia Schist could also be produced from melting and assimilation the continental crust, directly assimilating zircons from the same sources that had eroded and shed their zircons into the oceanic trench. Zircon textures may discriminate zircons inherited from sedimentary rock versus zircons inherited directly from continental crust, as a detrital zircon should appear rounded, while zircons inherited directly from melted or assimilated plutonic rocks should have euhedral and/or unrounded textures.

Many xenocrystic zircons from the intrusion 0217-P47 are rounded, consistent with derivation from sediment, whereas sample 0217-P43 has dominantly euhedral and unrounded zircons (Appendix 10). Sample 0217-P43 also has a very unique population of zircons, with a Jurassic peak at ~155 Ma, and a lack of Triassic and Proterozoic zircons (Figure 55). The euhedral, unrounded zircons of this sample and the Jurassic peak suggest that sample 0217-P43 may have formed from the melting or assimilation of a Jurassic to early Cretaceous plutonic suite comprised of intrusions with ages ranging from ~180–130 Ma, which is the distribution of ages defining the 155 Ma peak (Figure 55). If the protolith for sample 0217-P43 is indeed plutonic rocks which were intruded into the crust in the Jurassic and Early Cretaceous, then the thick metamorphic rims with low Th/U ratios (<0.1) do not record metamorphism from subduction of this unit, but likely still record metamorphism related to subduction of the Orocopia Schist. The unusual thickness of the

metamorphic rims for sample 0217-P43 (~10x as thick as that of the Orocopia Schist) further argues for having undergone metamorphic conditions unique to the subducting Orocopia Schist. If the protolith of sample 0217-P43 occupied the lower crust above the subducting plate, then dehydration of trench sediments as they were subducted would be expected to result in metamorphism of the overlying protolith of sample 0217-P43. If the subduction geometry remained stable for a protracted period of time, this would result in a conveyor-belt style configuration where hydrated schist would be continually subducted and undergo dehydration, leading to protracted metamorphism of the overlying crust (Figure 63), which could have produced the unusually thick metamorphic rims of sample 0217-P43 (Figure 57). Alternatively, this intrusion could have assimilated Orocopia Schist that was derived exclusively from Jurassic to Early Cretaceous sediments, and that was at a deeper structural level, therefore producing thicker metamorphic rims.

Several characteristics of sample 0217-P47 and its zircons indicate it is likely the product of melting or assimilation of Orocopia Schist. 1) Many zircons in this sample are rounded, suggesting they are detrital. 2) The metamorphic rims of the zircons are thin like those of the Orocopia Schist, and its zircon age distribution matches the Orocopia Schist very well; it has three Proterozoic peaks, and several peaks through the Triassic to the Cretaceous (Figure 55). 3) It is petrographically very similar to the Orocopia Schist, as this sample was collected from an area where intrusions were very hard to distinguish from Orocopia Schist (e.g. Figure 24 E & F). No evidence was observed to suggest that the Orocopia Schist within the map area had melted or partially melted, as there was no evidence for migmatization of the Orocopia Schist. I suggest instead that structurally deeper Orocopia Schist had been melted by or assimilated into magma pooling in the mid-

crust, which then intruded into the footwall of the Plomosa detachment fault. This interpretation is supported by leucocratic intrusions which locally have magmatic garnet (e.g. samples 0316-P24 and 0316-P81a), suggested assimilation of Al-rich crustal rocks.



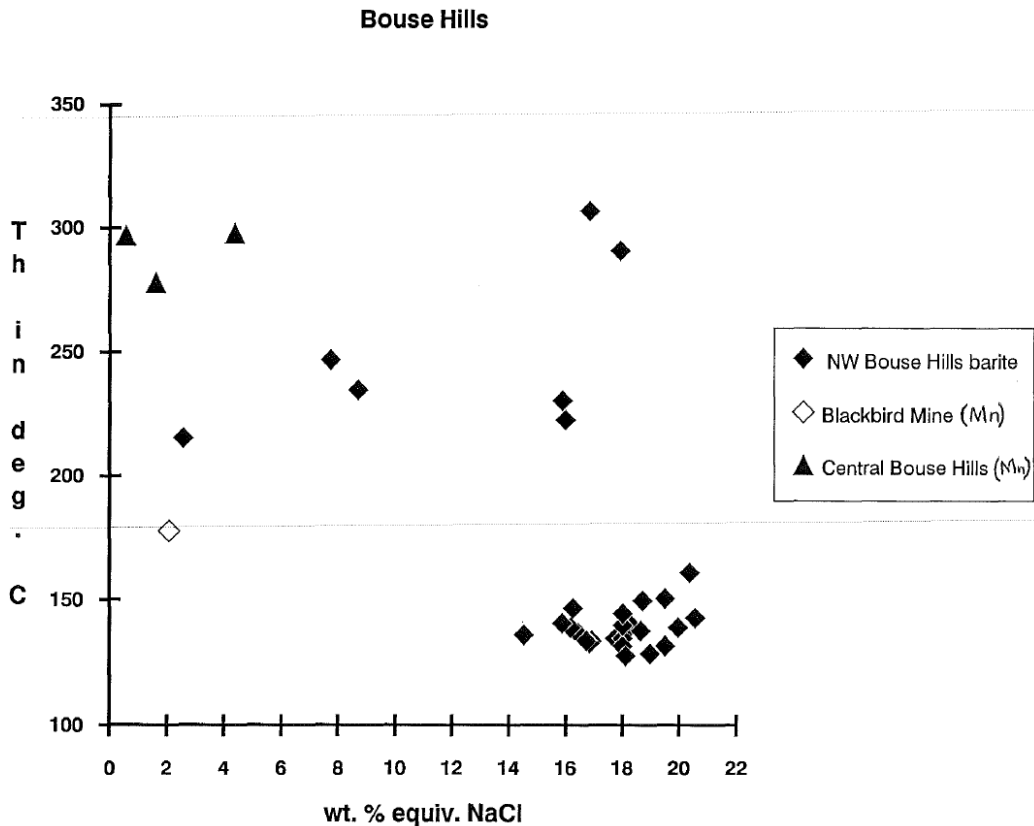
**Figure 63:** Th/U ratio vs zircon U-Pb age for sample 0217-P43. Note logarithmic scaling of Y-axis. Hypothetical tectonic events for this sample are annotated based on the clusters of Th/U ratios.



## **12. Post-detachment Faulting and Barite Mineralization**

### **12.1. Barite mineralization**

According to Duncan (1990), barite in the hanging wall of the Plomosa detachment precipitated into NW-striking brittle features during NE-SW detachment-related extension, and has different sulfur isotope values than barite in the footwall (orientations were not reported), suggesting two different sources. I have noted a wide-spread episode of barite mineralization that postdates structures related to NE-SW core complex extension, and thus is a barite mineralization event that post-dates the detachment-related barite documented by Duncan (1990). I suggest the barite veins Duncan (1990) had sampled in the footwall of the Plomosa detachment fault are the NE-striking veins documented in this thesis, and that his conclusion of a differing source of barite applies to the barite veins in this study. Additionally, based on fluid inclusions within barite veins in the Bouse Hills immediately to the NE of the map area, roughly two populations of barite mineralization were identified: a higher-temperature population that formed between 200–300 °C, and a lower-temperature population that formed between ~125–150 °C (Figure 64) (Spencer and Reynolds, 1990b). Unfortunately, the orientations of the barite veins were not reported, but I speculate that the high-temperature barite precipitated during detachment faulting into NW-SE-striking faults and veins, and that the low-temperature barite may be related to the post-detachment barite mineralization documented in this study.



**Figure 64:** Temperature vs. wt. % equiv. NaCl determined by fluid inclusion analysis for barite (black diamonds) from the Bouse Hills immediately NE of the map area. The tight cluster of data points for barite in the lower-right corner likely represents temperatures for the barite veins documented in the northern Plomosa Mountains. From Spencer and Reynolds, 1990b.

## 12.2. Causes for post-detachment faulting and veining

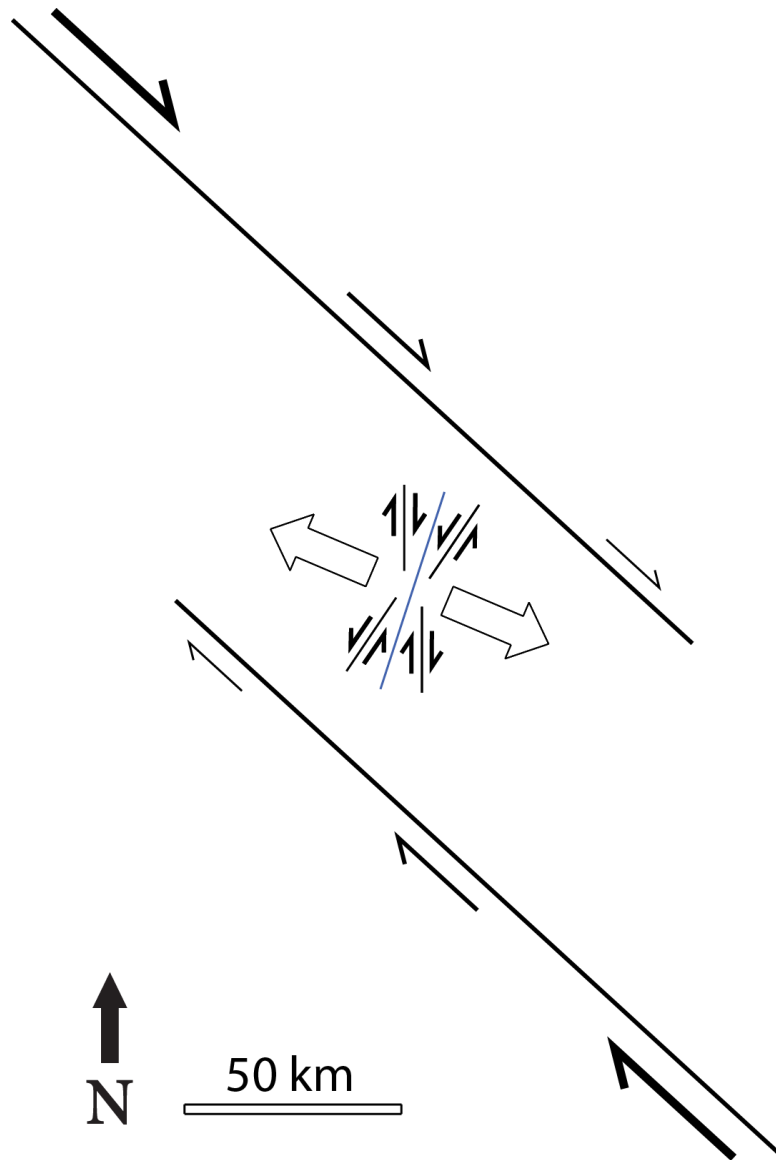
The average extension axis of post-detachment faulting is T/P [113, 01], nearly parallel to the average opening direction of barite veins (120/300) and carbonate veins (108/288), indicating a period of post-detachment extension oriented WNW-ESE (Figure 49). A zone of NW-striking post-detachment dextral faults occurs throughout the core complex belt NE of the northern Plomosa Mountains, which is attributed to the superposition of the San Andreas fault system onto the Basin and Range Province in SW Arizona and SE California (Singleton 2015; Singleton et al., 2016). The magnitude of dextral

displacement decreases from the NW to the SE, with ~7–8 km of dextral displacement having occurred across the Buckskin-Rawhide Mountains, and ~2–4 km of dextral displacement having occurred across the Harquahala Mountains (Singleton, 2015; Singleton et al., 2016). Dextral faulting along NW-striking faults has also been documented in the southern Plomosa Mountains, which has accommodated at least 6 km of total dextral displacement (Miller, 1970; Miller and Mckee, 1971).

Both north and south of the northern Plomosa Mountains, dextral faulting along NW-striking faults is the most recent deformation event of significance to have been documented. However, dextral faulting along NW-striking faults was not documented in the northern Plomosa Mountains. Rather, the most recent deformation event in the northern Plomosa Mountains is the WNW-ESE-directed extension accommodated by N-striking dextral-normal faults, NE-striking sinistral-normal faults, and NNE- to NE-striking barite and carbonate veins. Dextral faulting north and south of the northern Plomosa Mountains and WNW-ESE-directed extension within the northern Plomosa Mountains are compatible with transtension, with the northern Plomosa Mountains occupying a transtensional step between the two zones of dextral faulting (Figure 65). While a clockwise shift in extension direction from NE-SW to ENE-WSW and E-W occurred in the Buckskin-Rawhide Mountains (Singleton, 2015), there is no evidence that the northern Plomosa Mountains underwent a change in extension direction during detachment-related extension, suggesting that the distributed dextral-shear system was not superimposed onto the northern Plomosa Mountains during core complex development. Thus, it is inferred that extension in the northern Plomosa Mountains had ceased as extension in the core complexes to the NE continued, and that the northern Plomosa Mountains were

tectonically stable until WNW-ESE extension initiated from the influence of the San Andreas fault system onto the region. Low-temperature thermochronology of the northern Plomosa Mountains supports an early cessation of extension (15–14 Ma; Foster and Spencer, 1992) relative to the Buckskin Mountains to the NE (12–11 Ma, Singleton et al., 2014).

Along a WNW-ESE trend, The NE-striking post-detachment fault accommodated ~140 m of apparent displacement, and the N-striking post-detachment fault accommodated ~180 m of apparent displacement, totaling ~320 m of total apparent WNW-ESE extension. Barite veins typically are 1–4 cm wide, and are typically spaced tens of meters apart. Carbonate veins are commonly 0.3–1 m wide, but are spaced at even greater distances, perhaps hundreds of meters apart. Because the apparent displacement of the faults yields a minimum value for extension, and extension along barite veins and carbonate veins is small, the total WNW-ESE extension in the northern Plomosa Mountains accommodated by the N- and NE-striking faults and veins is estimated to be on the order of ~350–600 m.



**Figure 65:** Schematic illustration of the orientations of faults and veins resulting from transtension at the northern Plomosa Mountains (centered) between two dextral fault zones, creating N-striking dextral faults, NE-striking sinistral faults, and NNE-striking veins (blue line in center). White arrows indicate the direction of transensional extension.

## Conclusions

Based on 1:10,000-scale geologic mapping, structural and microstructural analysis, and U-Pb zircon geochronology, this study has documented the Orocopia Schist and a newly identified Miocene intrusive complex in the footwall of the Plomosa detachment fault, and has demonstrated that the northern Plomosa Mountains is a metamorphic core complex with Miocene mylonitic fabrics.

Mylonitic fabrics are pervasive throughout the mapping area, and the mylonitic lineations are very consistent with an average T/P of [220, 09]. Synmylonitic early Miocene intrusions demonstrate that the footwall of the Plomosa detachment fault records penetrative mid-crustal strain coeval with detachment fault slip. Normal faults throughout the footwall of the Plomosa detachment fault have an average extension axis of T/P [220, 03], the same trend as the mylonitic lineations, which indicates there was no change in the extension direction between the ductile and brittle regimes.

The Plomosa detachment fault is corrugated with an average NE dip of  $\sim 12^\circ$ , and is discordant to the majority of subhorizontal to SW-dipping mylonitic foliations in its footwall. Based on this discordance, and the geometric differences between the mylonitic foliations of the Orocopia Schist, Miocene intrusive complex, and the gneiss, three distinct mylonitic shear zones were identified: I) A pre-Miocene originally moderately NE-dipping ( $\sim 50^\circ$ ) normal-displacement shear zone that deformed the corrugated gneiss. A pre-Miocene age is inferred based on high-temperature deformation fabrics in the gneiss located at a pre-detachment paleo-depth of  $\sim 3$  km – too cold for Miocene mylonitization. II) An originally shallowly NE-dipping ( $\sim 25^\circ$ ) normal-displacement shear zone that

deformed the Orocopia Schist and Miocene intrusive complex, and locally the gneiss at the boundary with the Orocopia Schist. This shear zone likely initiated during 23–22 Ma emplacement of the footwall granitoids, approximately coeval with or shortly before capture by the Plomosa detachment fault. III) A detachment-subparallel shear zone that is the result of mylonitization along the Plomosa detachment fault, which is capped by brecciated and intensely chloritized rock, recording a transition from ductile to brittle deformation. The subparallel shear zone is not continuous along the Plomosa detachment fault, and was likely incised into the hanging wall at its northern end.

The Orocopia Schist of the northern Plomosa Mountains contains five of the hallmarks of the Orocopia Schist described elsewhere: 1) the quartzofeldspathic nature of the schist, 2) poikiloblastic graphitic plagioclase throughout the schist, 3) layers of amphibolite interlayered with the schist, interpreted as metabasalt, 4) layers of metachert common throughout the metabasalt, and 5) pods of coarse-grained green actinolite scattered throughout the schist, which are rich in Mg, Ni, and Cr, and are likely derived from an ultramafic protolith. The zircon U-Pb age distribution for the Orocopia Schist at the northern Plomosa Mountains matches the age distribution of other localities of Orocopia Schist, which is the most compelling evidence they are the same. Th/U ratios vs age (derived from U-Pb zircon geochronology) for samples of Orocopia Schist reveal a sudden drop-off at 68–70 Ma of Th/U ratios  $>0.1$  to Th/U ratios  $<0.1$ , which demarcates the maximum depositional age of the Orocopia Schist. Th/U ratios of  $<0.1$  between ~75–50 Ma are interpreted to record subduction-related metamorphism of the Orocopia Schist, which is supported by Th/U ratios of  $<0.1$  for thin metamorphic rims imaged using cathodoluminescence. Xenocrystic zircons from igneous intrusions have age distributions

that are identical to the Orocopia Schist, suggesting the Orocopia Schist was melted or assimilated during Miocene plutonism. The top of the Orocopia Schist was 3–4 km below the surface at the initiation of the Plomosa detachment fault in the early Miocene, and therefore must have been exhumed from lower-crustal depths in the Paleogene after it was subducted. Paleogene exhumation of the Orocopia Schist may have occurred along the pre-Miocene moderately NE-dipping normal-displacement shear zone that deformed the corrugated gneiss.

Post-detachment WNW-ESE extension was accommodated by ~N-striking dextral faults, ~NE-striking sinistral faults, and NNE- to NE-striking barite and carbonate veins. This deformation may have occurred in the Pliocene or early Pleistocene, as a prominent NE-striking fault offsets a young, weakly- to moderately-consolidated sedimentary breccia, similar in appearance to older alluvium/colluvium. The WNW-ESE period of extension is attributed to transtension, with the northern Plomosa Mountains occupying a transtensional step between post-detachment dextral strike-slip zones documented to the north and south.

The documentation of Orocopia Schist in the northern Plomosa Mountains provides important insight for the spatial and temporal emplacement of the Orocopia Schist in SW Arizona and SE California. As a result of this study, it can be concluded that the Orocopia Schist likely forms a continuous layer extending from the Chocolate Mountains anticlinorium northeast to the northern Plomosa Mountains and Cemetery Ridge (located ~70 km SE of the northern Plomosa Mountains), providing compelling evidence that the subducted Orocopia Schist was emplaced above a shallow Farallon slab. The pre-detachment paleo-depth of 3–4 km for the Orocopia Schist at the northern Plomosa



Mountains necessitates a Paleogene exhumation event, supporting major Paleogene exhumation documented by thermochronological studies of Orocopia Schist at other localities, as well as studies of nearby core complexes. Mylonitic lineations recorded during Paleogene exhumation have a near-identical trend as lineations recorded during Miocene exhumation, as is documented in studies of Paleogene exhumation in nearby core complexes. Furthermore, the association of Orocopia Schist with Paleogene exhumation, as concluded by this study, suggests that the subduction of rheologically weak schist beneath previously thickened crust may have been the trigger for major Paleogene exhumation in SW Arizona.

The documentation of magmatism as shortly preceding or coeval with inception of the Plomosa detachment fault supports findings in nearby core complexes, and bolsters the idea that core complexes are inherently tied to magmatism. The isolated position of the northern Plomosa Mountains metamorphic core complex with respect to main core complex belt in the region may be due to the presence of the Orocopia Schist, which has not been documented in other core complexes. The major structural boundary between the Orocopia Schist and the gneiss may have provided a pathway for Miocene intrusions, leading to thermal weakening of the crust, and combined with the low rheological strength of the schist, provided the ideal conditions for the development of the shallowly NE-dipping shear zone and initiation of the Plomosa detachment fault.

## References

- Allmendinger, R.W., (2017), Stereonet 9.9.5, for Windows:  
<http://www.geo.cornell.edu/geology/faculty/RWA/programs/stereonet.html>
- Aranovich, L.Y., Bortnikov, N.S., Zinger, T.F., Borisovskiy, S.E., Matrenichev, V.A., Pertsev, A.N., Sharkov, E.V., and Skolotnev, S.G., (2017), Morphology and Impurity Elements of Zircon in the Oceanic Lithosphere at the Mid-Atlantic Ridge Axial Zone (6°–13° N): Evidence of Specifics of Magmatic Crystallization and Postmagmatic Transformations: *Petrology*, v. 25, no. 4, p. 339-364.
- Barth, A.P., Wooden, J.L., Grove, M.G., Jacobson, C.E., and Pedrick, J.N., (2003), U-Pb zircon geochronology of rocks in the Salinas Valley region of California: A reevaluation of the crustal structure and origin of the Salinian block: *Geology*, v. 31, p. 517–520.
- Bryant, B., and J. L. Wooden, (2008), Geology of the northern part of the Harcuvar complex, west-central Arizona: U.S. Geol. Surv. Prof. Pap. 1752, 52.
- Boettcher, S.S., and Mosher, S., (1998), Mid- to Late Cretaceous ductile deformation and thermal evolution of the crust in the northern Dome Rock Mountains, Arizona: *Journal of Structural Geology*, v. 20, no. 6, p. 745-764.
- Chapman, A.D., Kidder, S., Saleeby, J.B., and Ducea, M.N., (2010), Role of extrusion of the Rand and Sierra de Salinas schists in Late Cretaceous extension and rotation of the southern Sierra Nevada and vicinity: *Tectonics*, v. 29, p. TC5006.
- Chapman, A.D., Saleeby, J.B., and Eiler, J., (2013), Slab flattening trigger for isotopic disturbance and magmatic flare-up in the southernmost Sierra Nevada batholith, California: *Geology*, v. 41, p. 1007–1010.
- Chapman, A.D., (2016), The Pelona-Orocopia-Rand and related schists of southern California: a review of the best-known archive of shallow subduction on the planet: *International Geology Review*, p. 1-38.
- Chapman, A.D., Jacobson, C.E., Ernst, W.G., Grove, W., Dumitru, T., Hourigan, J., Ducea, M.N., (2016), Assembling the world's type shallow subduction complex: Detrital zircon geochronologic constraints on the origin of the Nacimiento block, central California Coast Ranges: *Geosphere*, v. 12, no. 2, p. 533–557.
- Cloos, M., (1982), Flow mélanges: Numerical modeling and geologic constraints on their origin in the Franciscan subduction complex, California: *Geological Society of America Bulletin*, v. 93, p. 330–345.

- Coney, P.J., (1978), Mesozoic-Cenozoic Cordilleran plate tectonics: in Smith, R.B., and Eaton, G.P., eds., Cenozoic tectonics and regional geophysics of the western Cordillera: Geological Society of America Memoir 152, p. 33-50.
- Coney, P.J., (1980), Cordilleran metamorphic core complexes: An overview, in Crittenden, M.D., Coney, P.J., and Davis, G.H., eds., Cordilleran metamorphic core complexes: Geological Society of America Memoir 153, p. 7-34.
- Coney, P.J., Harms, T.K., (1984), Cordilleran metamorphic core complexes: Cenozoic extensional relics of Mesozoic compression: *Geology* 12, 550-554.
- Corfu, F., Hanchar, J.M., Hoskin, P.W.O., and Kinny, P., (2003), Atlas of Zircon Textures: Reviews in Mineralogy and Geochemistry, 53, p. 16-32, January.
- Crowell, J.C., (1968), Movement histories of faults in the Transverse Ranges and speculations on the tectonic history of California, in Dickinson, W.R., and Grantz, A., eds., Proceedings of Conference on Geologic Problems of San Andreas Fault System: Stanford, California, Stanford University Publications in the Geological Sciences, v. 11, p. 323-341.
- Davis, G.A., Lister, G.S., Reynolds, S.J., (1986). Structural evolution of the Whipple and South Mountains shear zones, southwestern United States: *Geology*, 14, p. 7-10.
- Dawson, M.R., and Jacobson, C.E., (1989), Geochemistry and origin of Mafic Rocks from the Pelona, Orocoipa, and Rand Schists, Southern-California: *Earth and Planetary Science Letters*, v. 92, p. 371-385.
- Decelles, P.G., (2004), Late Jurassic to Eocene evolution of the Cordilleran thrust belt and foreland basin system, western U.S.A: *American Journal of Science*, v. 304, p. 105-168.
- Dickinson, W.R., and Lawton, T.F., (2001), Tectonic setting and sandstone petrofacies of the Bisbee basin (USA-Mexico): *Journal of South American Earth Sciences*, v. 14, p. 475-504.
- Dobrovine, P.V., and Tarduno, J.A., (2008), A revised kinematic model for the relative motion between Pacific oceanic plates and North America since the Late Cretaceous: *Journal of Geophysical Research*, v. 113, 20 p.
- Dumitru, T.A., Elder, W.P., Hourigan, J.K., Chapman, A.D., Graham, S.A., and Wakabayashi, J., (2016), Four Cordilleran paleorivers that connected Sevier thrust zones in Idaho to depocenters in California, Washington, Wyoming, and, indirectly, Alaska: *Geology*, v. 44, p. 75-78.

- Duncan, J. T., (1990), The geology and mineral deposits of the northern Plomosa District, La Paz County, Arizona: Arizona Geological Survey Open-File Report 90-10, p. 5-53, December.
- Engebretson, D.C., Cox, A., and Gordon, R.G., (1985), Relative Motions between Oceanic and Continental Plates in the Pacific Basin: Geological Society of America Special Paper 206, 59 p.
- Ernst, W.G., (1970), Tectonic contact between the Franciscan mélangé and the Great Valley sequence – Crustal expression of a Late Mesozoic Benioff zone: Journal of Geophysical Research, v. 75, no. 5, p. 886-901, February.
- Fletcher, J.M., and Bartley, J.M., (1994), Constrictional strain in a non-coaxial shear zone: implications for fold and rock fabric development, central Mojave metamorphic core complex, California: Journal of Structural Geology, v. 16, no. 4, p. 555-570.
- Foster, D.A., and Spencer, J.E., (1992), Apatite and zircon fission-track dates from the northern Plomosa Mountains, La Paz county, west-central Arizona: Arizona Geological Survey Open-File Report 92-9.
- Gans, P.B., and Gentry, B.J., (2016), Dike emplacement, footwall rotation, and the transition from magmatic to tectonic extension in the Whipple Mountains metamorphic core complex, southeastern California: Tectonics, v. 34, p. 2564-2608.
- Graham D.J. and Midgley N.G. (2000), Graphical representation of particle shape using triangular diagrams: an Excel spreadsheet method. Earth Surface Processes and Landforms 25(13): 1473-1477.
- Grove, M., Jacobson, C.E., Barth, A.P., and Vucic, A., (2003), Temporal and spatial trends of Late Cretaceous-early Tertiary underplating Pelona and related schist beneath Southern California and southwestern Arizona: Special Papers Geological Society of America, v. 374, p. 381–406.
- Grove, M., Bebout, G.E., Jacobson, C.E., Barth, A.P., Kimbrough, D.L., King, R.L., Zou, H., Lovera, O.M., Mahoney, B.J., and Gehrels, G.G., (2008), The Catalina schist: Evidence for middle Cretaceous subduction erosion of southwestern North America, in Draut, A.E., Clift, P.D., and Scholl, D.W., eds., Formation and Applications of the Sedimentary Record in Arc Collision Zones: Geological Society of America Special Paper, v. 436, p. 335–362.
- Harlow, G.E., and Sorensen, S.S., (2005), Jade (nephrite and jadeitite) and serpentinite: Metasomatic connections: International Geology Review, v. 47, p. 113–146.

- Haxel, G., and Dillon, J., (1978), The Pelona-Orocopia Schist and Vincent-Chocolate Mountain thrust system, southern California: in Howell, D.G., and McDougall, K.A., eds., Mesozoic paleogeography of the western United States: Pacific Section, Society of Economic Paleontologists and Mineralogists Pacific Coast Paleogeography Symposium 2, p. 453-469.
- Haxel, G.B., Budahn, J.R., Fries, T.L., King, B.W., White, L.D., and Aruscavage, P.J., (1987), Geochemistry of the Orocopia Schist, southeastern California: Summary, in Dickinson, W.R., and Klute, M.A., editors, Mesozoic rocks of southern Arizona and adjacent areas: Arizona Geological Society Digest, v. 18, p. 49-64.
- Haxel, G.B., Jacobson, C.E., Richard, S.M., Tosdal, R.M., and Grubensky, M.J., (2002), The Orocopia Schist in southwest Arizona: Early Tertiary oceanic rocks trapped or transported far inland, in Barth, A., ed., Contributions to crustal evolution of the southwestern United States: Geological Society of America Special Paper, v. 365, p. 99-128.
- Haxel, G.B., Jacobson, C.E., Wittke, J.H., (2014), Mantle peridotite in newly discovered far-inland subduction complex, southwest Arizona: initial report: International Geology Review, <http://dx.doi.org/10.1080/00206814.2014.928916>
- Howard, K. A., and John, B. E., (1987), Crustal extension along a rooted system of imbricate low-angle faults' Colorado River extensional corridor, California and Arizona: Continental Extensional Tectonics, Spec. Publ. Geol. Soc. London, 28, 299-312.
- Jacobson, C.E., Oyarzabal, F.R., and Haxel, G.B., (1996), Subduction and exhumation of the Pelona-Orocopia-Rand schists, southern California: Geology, v. 24, no. 6, p. 547-550, June.
- Jacobson, C. E., Barth, A. P., and Grove, M., (2000), Late Cretaceous protolith age and provenance of the Pelona and Orocopia Schists, southern California: Implications for evolution of the Cordilleran margin: Geology, v. 28, no. 3, p. 219-222, March.
- Jacobson, C.E., Grove, M., Stamp, M.M., Vucic, A., Oyarzabal, F.R., Haxel, G.B., Tosdal, R.M., and Sherrod, D.R., (2002), Exhumation history of the Orocopia Schist and related rocks in the Gavilan Hills area of southeasternmost California, in Barth, A., ed., Contributions to crustal evolution of the southwestern United States: Geological Society of America Special Paper, v. 365, p. 129-154.

- Jacobson, C. E., Grove, M., Vučić, A., Pedrick, J.N., and Ebert, K.A., (2007), Exhumation of the Orocochia Schist and associated rocks of southeastern California: Relative roles of erosion, synsubduction tectonic denudation, and middle Cenozoic extension: in Cloos, M., Carlson, W.D., Gilbert, M.C., Liou, J.G., and Sorensen, S.S., eds., *Convergent Margin Terranes and Associated Regions: A Tribute to W.G. Ernst: Geological Society of America Special Paper 419*, p. 1-37.
- Jacobson, C.E., Grove, M., Pedrick, J.N., Barth, A.P., Marsaglia, K. M., Gehrels, G.E., and Nourse, J.A., (2011), Late Cretaceous to early Cenozoic tectonic evolution of the southern California margin inferred from provenance of trench and forearc sediments: *Geological Society of America Bulletin*, v. 123, no. 3-4, p. 485-506.
- Jemmett, J. P., (1966), *Geology of the northern Plomosa Mountain range, Yuma County, Arizona*: Tuscon, University of Arizona, unpublished Ph.D. dissertation, 128 p.
- Knapp, J. H., and Heizler, M. T., (1990), Thermal History of Crystalline Nappes of the Maria Fold and Thrust Belt, West Central Arizona: *Journal of Geophysical Research*, vol. 95, no. B12, p. 20,049-20,073, November.
- Laubach, S.E., Reynolds, S.J., Spencer, J.E., and Marshak, S., (1989), Progressive deformation and superposed fabrics related to Cretaceous crustal underthrusting in western Arizona, U.S.A: *Journal of Structural Geology*, v. 11, p 735-749.
- Lister, G.S., and Baldwin, S.L., (1993), Plutonism and the origin of metamorphic core complexes: *Geology*, v. 21, p. 607-610.
- Lister, G.S., Davis, G.A., (1989). The origin of metamorphic core complexes and detachment faults formed during tertiary continental extension in the northern Colorado River region, U.S.A. *Journal of Structural Geology* 11, 65e94.
- Lopez-Sanchez, M.A., Aleinikoff, J.N., Marcos, A., Martínez, F.J., and Llana-Fúnez, Sergio, (2015), An example of low-Th/U zircon overgrowths of magmatic origin in a late orogenic Variscan intrusion: the San Ciprián massif (NW Spain): *Journal of the Geological Society*, v. 173, p. 282-291.
- Ludwig, K., (2003), *User's Manual for Isoplot 3.00: A Geochronological Toolkit for Microsoft Excel*, Geochronology Center, vol. 4, Spec. Publ., Berkeley.
- Miller, F. K., (1970), *Geologic map of the Quartzite quadrangle, Yuma County, Arizona*: U.S. Geol. Surv., Geol. Quad. Map GQ-841.
- Miller, F. K., and Mckee, E. H., (1971), Thrust and Strike-Slip Faulting in the Plomosa Mountains, Southwestern Arizona: *Geological Society of America Bulletin*, v. 82, p. 717-722, March.

- Moran, A.E., (1993), The effect of metamorphism on the trace element composition of subducted oceanic crust and sediment: Rice University, Ph.D. dissertation, 378 p.
- Oze, C., Fendorf, S., Bird, D.K., and Coleman, R.G., (2004), Chromium geochemistry in serpentized ultramafic rocks and serpentine soils from the Franciscan complex of California: *American Journal of Science*, v. 304, p. 67–101, January.
- Passchier, C.W., Trouw, R.A.J., (2005), *Microtectonics*: Springer, p. 366.
- Prior, M.G., Stockli, D.F., Singleton, J.S., (2016), Miocene slip history of the Eagle Eye detachment fault, Harquahala Mountains metamorphic core complex, west-central Arizona: *Tectonics*, v. 35, no. 8, p. 1913-1934.
- Reynolds, S.J., (1986), *Geology of the South Mountains, central Arizona*: Arizona Bureau of Geology and Mineral Technology Bulletin, 195, 61 p.
- Reynolds, S.J., and Lister, G.S., (1990), Folding of mylonitic zones in Cordilleran metamorphic core complexes: Evidence from near the mylonitic front: *Geology*, v. 18, p. 216–219, March.
- Reynolds, S. J., Spencer, J. E., Richard, S. M., and Laubach, S. E., (1986), Mesozoic structures in west-central Arizona, *Frontiers in Geology and Ore Deposits of Arizona and the Southwest*: *Ariz. Geol. Soc. Dig.*, 16 35-51.
- Saleeby, J., (2003), Segmentation of the Laramide Slab – evidence from the southern Sierra Nevada region: *GSA Bulletin*; v. 115, no. 6, p. 655-668.
- Seymour, N.M., Wong, M., and Singleton, J.S., (2016), TitanQ analyses of mylonites from metamorphic core complexes in west-central Arizona: Implications for two phases of extension in the lower Colorado River Extensional Corridor: Abstract T21A-2796 presented at 2016 Fall Meeting, AGU, San Francisco, Calif., 11-15 Dec.
- Scarborough, R., and Meader, N., (1983), Reconnaissance geology of the northern Plomosa Mountains: Arizona Bureau of Geology and Mineral Technology Open-File Report 83–24, 35 p.
- Scarborough, R. B., Menges, C. M. and Pearthree, P. A. , (1983), Map of Basin and Range (post 15 mya) exposed faults, grabens, and basaltic dominated volcanism in Arizona, Arizona Bureau of Geology and Mineral Technology Open-File Rep. 82–21, scale 1: 500,000, text 7 p.
- Singleton, J.S., (2013), Development of extension-parallel corrugations in the Buckskin-Rawhide metamorphic core complex, west-central Arizona: *GSA Bulletin*, v. 125, no. 3/4, p. 453–472, March/April.

- Singleton, J.S., (2015), The transition from large-magnitude extension to distributed dextral faulting in the Buckskin-Rawhide metamorphic core complex, west-central Arizona: *Tectonics*, 34, p. 1685–1708.
- Singleton, J.S., and Mosher, S., (2012), Mylonitization in the lower plate of the Buckskin-Rawhide detachment fault, west-central Arizona: Implications for the geometric evolution of metamorphic core complexes: *Journal of Structural Geology*, 39, p. 180–198.
- Singleton, J.S., and Wong, M.S., (2016), Polyphase mylonitization in the Harcuvar and Buckskin-Rawhide metamorphic core complexes, west-central Arizona: *Geological Society of America Abstracts with Programs*. Vol. 48, No. 4
- Singleton J.S., Stockli, D.F., Gans, P.B., and Prior, M.G., (2014), Timing, rate, and magnitude of slip on the Buckskin-Rawhide detachment fault, west central Arizona: *Tectonics*, 33, 1596–1615.
- Singleton J.S., Wong, M.S., and Johnston, S.M., in review, The role of calcite-rich metasedimentary mylonites in localizing detachment fault strain and influencing the structural evolution of the Buckskin-Rawhide metamorphic core complex, west-central Arizona: *Lithosphere*
- Spencer, J. E., (1999), Geologic continuous casting below continental and deep-sea detachment faults and at the striated extrusion of Sacsayhuamán, Peru: *Geology*, v. 27, no. 4, p. 327–330.
- Spencer, J.E., and Reynolds, S.J., (1989), Middle Tertiary tectonics of Arizona and adjacent areas: in Jenny, J.P., and Reynolds, S.J., 1989, *Geologic evolution of Arizona*: Tuscon, Arizona Geological Society Digest 17, p. 539-574.
- Spencer, J.E., and Reynolds, S.J., (1990a), Relationship between Mesozoic and Cenozoic tectonic features in west-central Arizona and adjacent southeastern California: *Journal of Geophysical Research* 95, 539-555.
- Spencer, J.E., and Reynolds, S.J., (1990b), *The Geology and Mineral Resources of the Bouse Hills, West-central Arizona*: Arizona Geological Survey. Open-File Report 90-9, scale: 1:24,000.
- Spencer, J. E., and Reynolds, S. J., (1991), Tectonics of mid-Tertiary extension along a transect through west central Arizona: *Tectonics*, vol. 10, no. 6, p. 1204-1221, December.



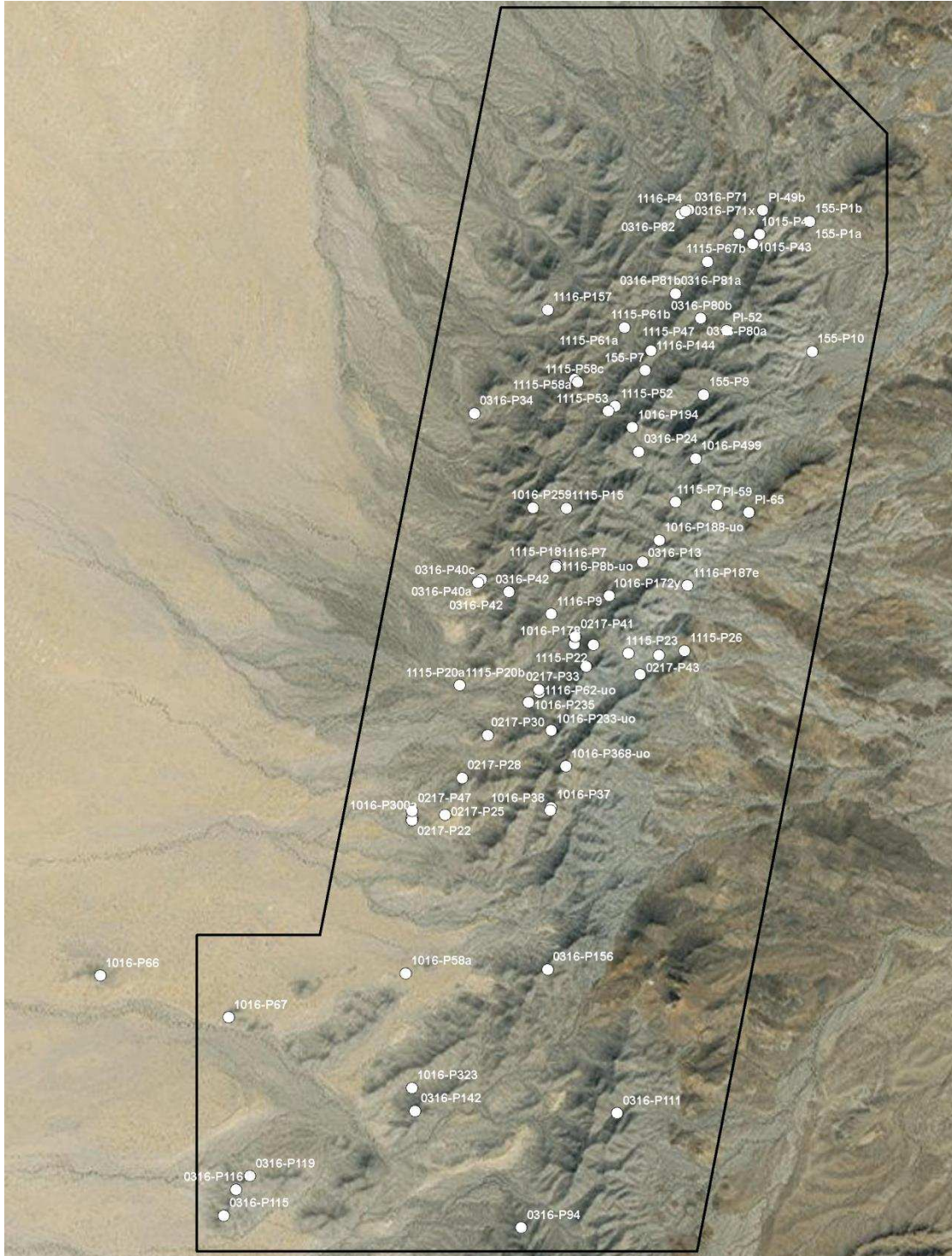
- Spencer, J.E., Richard, S.M., Reynolds, S.J., Miller, R.J., Shafiqullah, M., Gilbert, W.G., Grubensky, M.J., (1995): Spatial and temporal relationships between mid-Tertiary magmatism and extension in southwestern Arizona.
- Spencer, J.E., Youberg, A., Love, D., Pearthree, P.A., Steinke, T.R., and Reynolds, S.J., (2015), Geologic map of the Bouse and Ibex Peak 7 ½' Quadrangles, La Paz County, Arizona: Arizona Geological Survey Digital Geologic Map DGM-107, version 2.0, scale 1:24,000.
- Steinke, T. R., (1997), Geologic map of the eastern Plomosa Pass area: Arizona Geological Survey Contributed Map CM-97-A, scale 1:3,570.
- Stipp, M., Stunitz, H., Heilbronner, R., and Schmid, S.M., (2002). The eastern Tonale fault zone: a 'natural laboratory' for crystal plastic deformation of quartz over a temperature range from 250 to 700 °C.: *Journal of Structural Geology* 24, 1861-1884.
- Stock, J., and Molnar, P., (1988), Uncertainties and implications of the Late Cretaceous and Tertiary position of North America relative to the Farallon, Kula, and Pacific plates: *Tectonics*, v. 7, p. 1339-1384.
- Taliaferro, N. L., (1943). Franciscan-Knoxville problem: *Bull. Amer. Ass. Petrol. Geol.*, 27, 109-219.
- Vermeesch, P., (2012). On the visualisation of detrital age distributions. *Chemical Geology*, v.312 313, 190-194, doi: 10.1016/j.chemgeo.2012.04.021 0
- Williams, I.S., and Claesson, S., (1987), Isotopic evidence for the Precambrian provenance and Caledonian metamorphism of high grade paragneisses from the Seve Napped, Scandinavian Caledonides: *Contrib. Mineral Petrol.*, 97, p 205-217.
- Wong, M.S., and Gans, P.B., (2008). Geologic, structural, and thermochronologic constraints on the tectonic evolution of the Sierra Mazatán core complex, Sonora, Mexico: new insights into metamorphic core complex formation. *Tectonics* 27. doi:10.1029/2007TC002173.
- Wong, M.S., Singleton, J.S., Baughman, J., Bunting, K.C., (2013), Evidence for Miocene reactivation of a Late Cretaceous to Early Tertiary shear zone in the Harcuvar and Buckskin-Rawhide metamorphic core complexes, Arizona: *Geological Society of America Abstracts with Programs*. Vol. 45, No. 7, p.523.
- Yeats, R.S., (1968), Southern California structure, seafloor spreading, and history of the Pacific basin: *Geological Society of America Bulletin*, v. 79, p. 1693-1702.

Yin, A., (2002), Passive-roof thrust model for the emplacement of the Pelona-Orocopia Schist in southern California, United States: *Geology*, v. 30, p. 183–186.

Zoback, M.L., Anderson, R.E., and Thompson, G.A., (1981), Cenozoic evolution of the state of stress and style of tectonism of the Basin and Range province of the western United States: *Philosophical Transactions of the Royal Society of London, series A*, v. 300, p. 189-216.

# Appendices

## Appendix 1: Locations of thin section samples



## Appendix 2: Thin section analysis spreadsheet

**NOTES: Unique ID:** Year, month, and station number. **Coordinate system:** UTMNAD83 11N. **Mineral abbreviations:** Fld = unidentified feldspar, Plg = plagioclase, Ksp = potassium feldspar, Qtz = Quartz, Hbl = hornblende, Chl = Chlorite, Bio = biotite, Msc = muscovite, Opq = opaque minerals, Gph = graphite, Tit = titanite, Calc = calcite, Apt = apatite, Grt = Garnet, Rut = Rutile, Epi = epidote, Zrc = zircon, sauss = saussurite. **Modal mineralogy:** (X) = X%, none stated = accessory mineral. **Microstructures:** Assym Qtz = grain shape preferred orientation in quartz.

Unique_ID	Sample_Name	Map_Unit	Rock_Type	UTM_X	UTM_Y	Modal Mineralogy	Mylon_Type	Sense_of_Shear	Supporting Microstructures	Quartz recrystallization	Approx quartz re-X bins (um)	Chlorite_bronite	Seritization (intense, strong, moderate, weak, none)	Comments
2007May_49	PI-49b	Nic	Hornblende granodiorite	183011	325064	Fld(48), Qtz(20), Hbl(13), Chl(12), Ser(2), Epi(2), fibrous pale amphibole(2), Apt, Tit, Opq	mylonite	Top NE	asym Qtz, C'	SGR + GBM	4	Chl	strong	Fibrous pale amphibole and and around epidote. Also fibrous pale amphibole(?) in fractures.
2007May_52	PI-52	Orocopia	Schisty Biotite Orocopia	182673	323934	Qtz(50), Fld(35), Biot(15), Apt, Rut, Zrc	mylonite	Top NE	asym Qtz	GBM > SGR	5	Bio	weak	Biotite is dark redish brown. Long rutiles in quartz
2007May_59	PI-59	Nic	Granodiorite	182580	322293	Fld(80), Qtz(25), Chl(10), Opq(3), Tit, Allantite, Apt, Zrc	mylonite	Top NE	asym Qtz, sigma clasts,	SGR	2	Chl	strong	Relatively large apatites.
2007May_65	PI-65	Nic	Quartz Monzodiorite	182881	322220	Fld(62), Qtz(17), Chl(10), Ser(10), Opq(1), Allantite, Calcite, Apt,	mylonite	Top NE	sigma clasts,	SGR	1	Chl	strong	calcite + saussurite + chl in fractures
2015May_1	155-P1a	Marble/Qtzite	Quartzite mylonite	183451	324961	Qtz(97), Chl(1), Opq(1), Plg, Saus	mylonite	N/A	N/A	SGR	1	Chl	moderate	
2015May_1	155-P1b	Marble/Qtzite	Marble mylonite	183451	324961	Calc(98), Opq(1), Msc, Bio		unknown	N/A	N/A	-	Bio > Chl	N/A	
2015May_7	155-P7	Orocopia	Muscovite Biotite Orocopia	181906	323558	Fld(50), Qtz(32), Bio(15), Msc(2), Opq, Epi	mylonite	Top NE	S-C, Mca fish, assym Qtz	SGR+GBM	3	Bio > Chl	moderate	Poikiloblastic plagioclase
2015May_9	155-P9	Orocopia	Muscovite Biotite Orocopia	182455	323327	Qtz(45), Fld(25), Bio(19), Msc(10), Opq/graphite(1)	mylonite	Top NE	S-C, Mca fish, assym Qtz	SGR > GBM	2	Bio	moderate	graphitic albite
2015May_10	155-P10	Marble/Qtzite	Marble mylonite	183475	323735	Calc(79), Trm(20), Opq(1), other?	mylonite	unknown	N/A	N/A	-	N/A	N/A	
2015May_15	115-P15	Marble/Qtzite	Marble mylonite	182459	311690	Calc(98), Opq(4)	mylonite	unknown	N/A	N/A	-	N/A	N/A	From south of field area.
2015May_18	115-P18		Granitoid	181898	311358									From south of field area.
2015May_19	115-P19		-	181895	311385									From south of field area.
2015May_21	115-P21		Granitoid	181857	311776									From south of field area.
2015May_23	115-P23		Detachment fault plane	181884	314534									From south of field area.
2015May_24	115-P24		Granitoid	181885	314565									From south of field area.
2015Oct_41	1015-P41	Nic	Granitoid	182981	324837	Fld(65), Qtz(30), Chl(2), Opq(2), Clinozoisite, Epi	mylonite	Top NE	asym Qtz,	SGR > GBM	3	Chl	strong	
2015Oct_43	1015-P43	Gneiss	Hnbl Amphibolite	182916	324746	Hbl(90), Fld(4), Bio(3), Chl(3)		unknown	N/A	N/A	-	Bio = Chl	moderate	

2015Nov_7	1115-P7	Orocopia	Granitoid	182191	322318	Fld(33), Qtz(29), Bio(20), Chl(15), Opq(3),	mylonite	Top NE	S-C, assym qtz,	SGR > GBM	2	Chl = Bio	strong	
2015Nov_15	1115-P15	Nic	Granitoid	181162	322261	Fld(60), Qtz(30), Biot(7), Chl(3), Apt	mylonite	Top NE	S-C	SGR + GBM	2	Bio > Chl	strong	has zoning in feldspars, + myrmekite
2015Nov_18	1115-P18	Nic	Hnbl-Qtz diorite intrusion	181067	321728	Plg(47), Hbl(30), Qtz(10), Bio(10), Ksp(3), Tit, Apt	mylonite	Top NE	sigma clasts,	SGR + GBM	2	Bio	moderate/weak	feldspars clearly zoned
2015Nov_20	1115-P20a	Orocopia	Schistly Orocopia	180163	320594	Bio(34), Qtz(33), Fld(28), Opq-Gph(4) Msc(0.5), Zrc	mylonite	Top NE	S-C, Mica fish, assym qtz	SGR + GBM	2	Bio	moderate	biotite rich in Ti (is red)
2015Nov_20	1115-P20b	Orocopia	Schistly Orocopia	180163	320594	Fld(31), Qtz(30), Bio(30), Chl(5), Opq-Gph(3), Msc, Zrc	mylonite	Top NE	S-C, Mica fish, assym qtz	SGR + GBM	2	Bio > Chl	moderate/weak	biotite more re-crystallized than 20a
2015Nov_22	1115-P22	Nic	Hnbl-Qtz monzodiorite	181418	320976	Plg(45), Hbl(20), Qtz(10), Bio(10), Ksp(10), Chl(3), Opq(1) Allantite, Epi, Tit, Apt, Zrc	mylonite	Top NE	assym clasts & qtz	SGR + GBM	2	Bio > Chl	moderate/weak	
2015Nov_23	1115-P23	Nic	Tonalite	181747	320894	Fld(62), Qtz(20), Chl(13), Opq(3), Allantite(1), Clinozoisite, Tit, Epi	mylonite	Top NE	sigma clasts,	SGR + GBM	2	Chl	strong	completely chloritized besides perhaps very FG re-cr'd biotite
2015Nov_25	1115-P25a (1)	Nic	Non-mylon dike	182032	320878	Plg-phenos(10), Plg-laths/GM(50), Chl(20), Calc(12), Sauss(3), Allantite?(3), Opq(1), Apt	non-mylon	none	N/A	N/A	-	Chl	Intense/strong	Looks like amphiboles have been pseudomorphed into calcite (core), chl (rims), and allantite.
2015Nov_25	1115-P25a (2)	Nic	Non-mylon dike	182032	320878	"	non-mylon	none	N/A	N/A	-	-	-	
2015Nov_25	1115-P25b	Unknown	Hnbl-tonalite	182032	320878	Fld(46), Qtz(18), Hbl(15), Bio(10), Chl(7), Opq(2), Tit(1), Apt	mylonite	Top NE	sigma clasts, assym qtz	SGR > GBM	2	Chl = Bio	moderate	
2015Nov_26	1115-P26	Marble/Qtzite	Marble mylon	182276	320919	Calc(97), Qtz(2), Hbl	mylonite	Top NE	sigma clasts	N/A	-	N/A	N/A	
2015Nov_47	1115-P47	Orocopia	Schistly Orocopia	182426	324046	Qtz(43), Fld(30), Bio(15), Msc(7), Opq(4), Epi	mylonite	Top NE	S-C-C', mica fish, assym qtz	SGR + GBM	2	Bio	moderate/weak	high Ti-biotite
2015Nov_52	1115-P52	-	-	181622	323220	-	-	-	-	-	-	-	-	was broken for Ti-Hn-Qtz analysis
2015Nov_53	1115-P53	Orocopia	Biot-Tonalite	181555	323173	Fld(42), Qtz(35), Bio(10), Chl(10), Opq(2), Rut, Epi, Msc, Apt, Zrc	mylonite	Top NE	assym qtz,	GBM > SGR	3	Chl = Bio	strong	Sagenitic biotite
2015Nov_57	1115-P57T1	Orocopia	Actinolite schist	181243	323477	Act(98), Tlc(1), Opq	non-mylon	none	N/A	N/A	-	N/A	N/A	
2015Nov_57	1115-P57a	-	-	181243	323477	-	-	-	-	-	-	-	-	Don't think this was ever cut
2015Nov_57	1115-P57c	-	-	181243	323477	-	-	-	-	-	-	-	-	was broken for Ti-Hn-Qtz analysis
2015Nov_58	1115-P58a	Orocopia	Actinolite schist	181271	323448	Act(97), Tlc(1), Qtz(1), Chl, Plg	mylonite	unsure	N/A	GBM	4	N/A	weak	
2015Nov_58	1115-P58c	Orocopia	Talc-Actinolite schist	181271	323448	Act(97), Opq(2) Tlc, Plg	non-mylon	unsure	N/A	N/A	-	N/A	N/A	
2015Nov_61	1115-P61a	Orocopia	Schistly Orocopia	181708	323961	Qtz(40), Plg(24), Msc(20), Bio(3), Chl(7), Hem+Opq(5), Clinozoisite,	mylonite	Top NE	Mica fish, S-C, assym qtz	SGR+GBM	3	Chl > Bio	moderate	lots of hematite staining. Plagioclases are poikiloblastic

2015Nov_61	1115-P61b	Nic	Quartz-diorite	181708	323961	Plg(70), Qtz(15), Bio(8), Ksp(6), Allanite, Opq, Chl, Apt	mylonite	Top NE	S-C-C'	N/A	-	Bio > Chl	weak	
2015Nov_67	1115-P67b	Orocopia	Schisty Orocopia	182492	324582	Qtz(39), Fld(38), Bio(12), Chl(8), Opq-Gph(2), Apt, Epi, Rut	mylonite	Top NE	assym Qtz,	GBM + SGR	4	Chl = Bio	moderate	Sagenitic biotite. Graph-albite. Epidote mineralized along fractures
2016Mar_13	0316-P13	Gneiss	Hnbl-Qtz-diorite	181880	321755	Fld(64), Qtz(10), Hbl(15), Chl(6), Bio(2), Opq(3), Tit(0.5), Calc, Allanite, Clinozoisite, Apt, Grt, Rut	mylonite	Top NE	assym Qtz, sigma clast	SGR + GBM	3	Chl > Bio	strong/moderate	calcite in fracture. Some feldspars have undergone exsolution
2016Mar_24	0316-P24	Nic	Tonalite/granodiorite	181842	322792	Fld(65), Qtz(30), Msc(3), Chl(1), Grt(0.5), Opq, Tit, Epi	mylonite	Top NE	Mca fish	SGR + GBM	4	Chl	strong	Muscovite is chloritized and sericitized. Some garnets are chloritized, and also turned to epidote?
2016Mar_34	0316-P34	Orocopia	Schisty Orocopia	180299	323153	Qtz(40), Fld(30), Bio(20), Msc(8), Opq-Gph(1), Epi, Apt, Rut, Zrc	mylonite	Top NE	Mca fish,	SGR + GBM	3	Bio	weak	
2016Mar_39	0316-P39a	Orocopia	Schisty Orocopia	180366	321587	Fld(34), Qtz(31), Bio(30), Opq/Gph(1), Calc/Sauss(3),	mylonite	Top NE	Mca fish, S-C-C', assym Qtz	SGR + GBM	4	Bio	weak	Pokiloblastic + Graphitic albite. Calcite in fractures
2016Mar_39	0316-P39b	Orocopia	Schisty Orocopia	180366	321587	Qtz(32), Fld(31), Bio(20), Msc(15), Opq/Gph(1), Tourmaline, Grt, Apt, Rut	mylonite	Top NE	Mca fish, S-C-C', assym Qtz & folds	SGR + GBM	4	Bio > Chl	moderate/weak	Sagenitic biotite (Chl).
2016Mar_40	0316-P40a	Orocopia	Schisty Orocopia	180331	321560	Qtz(45), Fld(38), Bio(15), Opq(1), Epi	mylonite	Top NE	assym Qtz	SGR + GBM	4	Bio	weak	
2016Mar_40	0316-P40a	Nic	Quartz-diorite	180331	321560	Plg(81), Qtz(10), Bio(6), Ksp(2), Clc, Rut, Apt	mylonite	unsure	N/A	N/A	-	Bio	moderate/weak	Sagenitic biotite (Chl).
2016Mar_40	0316-P40c	Nic	Biot Qtz-Diorite	180331	321560	Plg(76), Qtz(10), Bio(10), Ksp(2), Clc(1), Opq, Rut, Apt	mylonite	Top NE	S-C-C', mica fish	N/A	-	Bio	moderate	calcite in veins.
2016Mar_42	0316-P42	Orocopia	Schisty Orocopia	180624	321472	Qtz(36), Fld(42), Chl(12), Bio(8), Opq-Gph(1), Apt, Rut	mylonite	unsure	N/A	SGR + GBM	4	Chl > Bio	moderate	Sagenitic biotite (Chl). Graphitic albite
2016Mar_42	0316-P42	Nic	Tonalite/granodiorite	180624	321472	Fld(65), Qtz(34), Chl, Opq, Epi	mylonite	unsure	N/A	SGR + GBM	-	N/A	intense	Chlorite veins
2016Mar_71	0316-P71	Orocopia	Schist	182316	325069					GBM	5	Bio	weak	
2016Mar_80	0316-P80a	Orocopia	Schistly Orocopia	182428	324048	Qtz(42), Fld(37), Bio(12), Msc(5), Opq(3), Clinozoisite, Grt, Epi, Rut?, Zrc	mylonite	Top NE	Mca fish, S-C, assym Qtz	SGR + GBM	4	Bio	moderate/weak	
2016Mar_80	0316-P80b	Nic	Msc-Chl Tonalite	182428	324048	Fld(70), Qtz(24), Chl(4), Msc(1) Rut, Apt, Zrc	mylonite	Top NE	Mca fish, assym Qtz	SGR + GBM	2	Chl	intense / strong	Sagenitic Biotite (Chl). These rutile needles are shorter than normal.
2016Mar_81	0316-P81b	Orocopia	Orocopia meta-arkose	182190	324280	Fld(69), Qtz(15), Bio(13), Chl(2), Opq, Apt, Zrc	mylonite	Top NE	Weak S-C	N/A	-	Bio > Chl	weak	
2016Mar_81	0316-P81a	Nic	Granite	182190	324280	Ksp(52), Qtz(32), Plg(13), Bio(1), Chl(1), Grt, Opq, Epi, Zrc	mylonite	N/A	N/A	SGR + GBM	4	Bio = Chl	Strong / Moderate	Myrmekite
2016Mar_81	0316-P81ab	-	Contact of dike and orocopia schist	182190	324280	-	mylonite	N/A	N/A	SGR + GBM	-	Chl > Bio		Sagenitic Biotite (Chl) (very sparse)

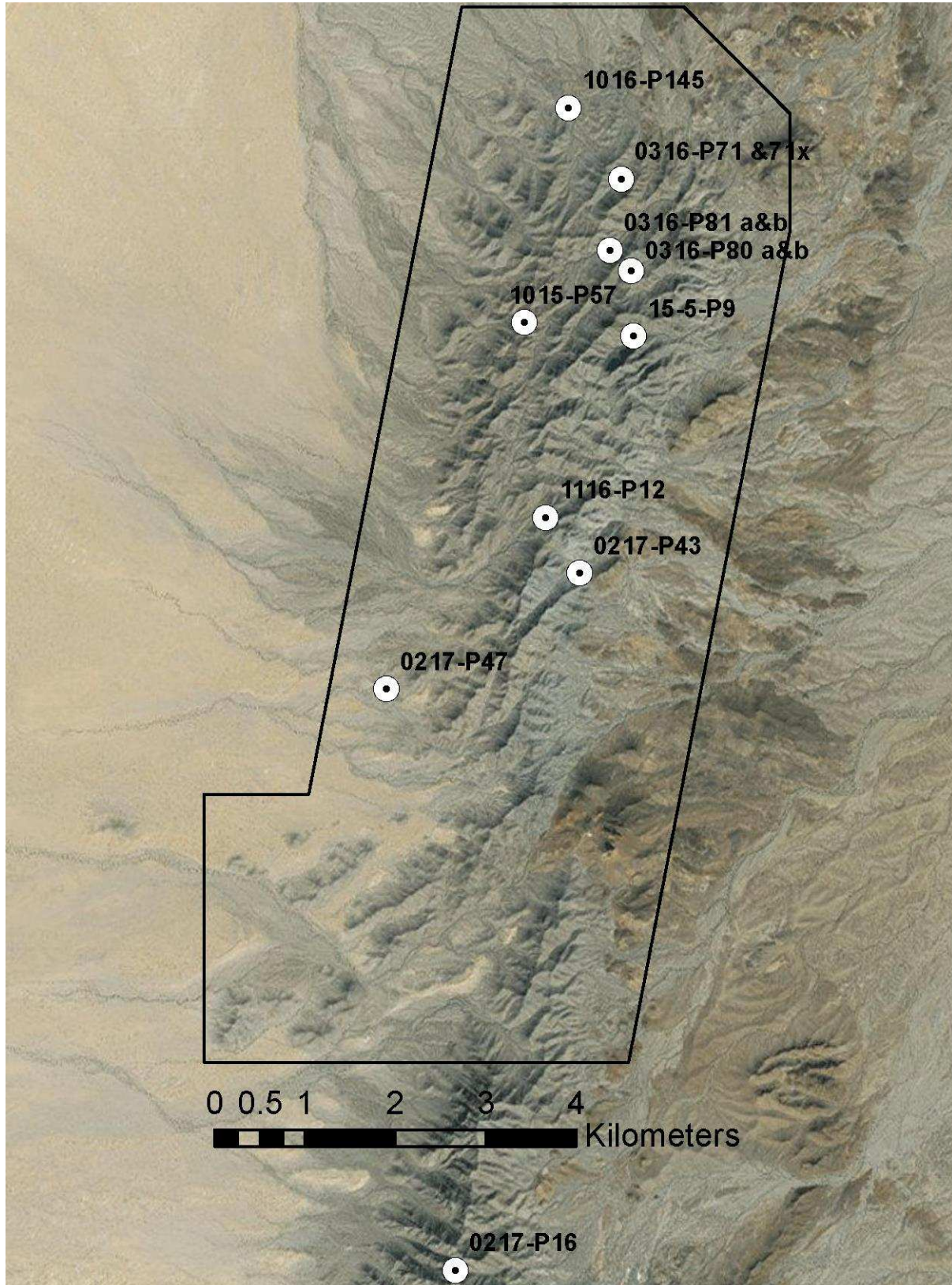
2016Mar_82	0316-P82	Orocopia	Schisty Orocopia	182241	325029	Fld(61), Bio(16), Qtz(15), Chl(4), Opq-Gph(3), Grt(0.5), Apt	mylonite	Top NE	S-C-C', sigma clasts	GBM > SGR	5	Bio > Chl	weak	Poikiloblastic, Graphitic albite. Minor Sagenitic Biotite (Chl)
2016Mar_94	0316-P94	Gneiss	Biotite Tonalite gneiss	180741	315490	Fld(47), Qtz(42), Bio(7), Opq(2), Chl(1), Epi, sauss	mylonite	Top NE	Weak S-C	GBM > SGR	5	Bio > Chl	moderate	Dark brown biotite. Checker-board quartz recrystallization
2016Mar_111	0316-P111	Gneiss	Hnbl-Biotite Tonalite gneiss	181642	316666	Fld(40), Qtz(28), Hbl(10), Bio(14), Chl(1), Opq(4), Tit(2), Apt.	mylonite	Top NE	assym qtz	SGR + GBM	3	Bio > Chl	moderate / weak	
2016Mar_115	0316-P115	Gneiss	Biot Qtz-Dionite gneiss	177944	315603	Fld(78), Qtz(12), Bio(6), Opq(2), Chl(1), Tit(0.5), Allanite, Epi, Apt	mylonite	Top NE	S-C-C', sigma clasts, assym qtz	SGR + GBM	4	Bio > Chl	moderate / weak	Sagenitic Chl (Very minor. Small needles)
2016Mar_116	0316-P116	Gneiss	Hnbl-Qtz dionite gneiss	178058	315848	Fld(82), Qtz(8), Hbl(8), Opq(0.5), Tit(1), Epi, Chl, Apt	mylonite	Top NE	S-C-C', sigma clasts, assym qtz	SGR + GBM	3	N/A	weak	Epidote + Calcite in a fracture.
2016Mar_118	0316-P119	Dike	Biotite Rhyo- dacite dike	178188	315975	Phenocrysts: Plg(14), Kspar(6), Bio(7), Qtz(7), Opq(2), Hbl(0.5), Epi, Rut, Groundmass: 62% Plg-laths()	non-mylon	N/A	N/A	N/A	-	Bio > Chl	Strong	Embayed qtz and plag. Myrmekite (qtz in plag).
2016Mar_142	0316-P142	Gneiss	Biot-Tonalite gneiss	179742	316588	Fld(62), Qtz(30), Bio(5), Chl(1), Opq(1), Apt(0.5), Epi,	mylonite	Top NE	Sigma clasts	GBM > SGR	4	Bio > Chl	weak	relatively lots of Apatite.
2016Mar_156	0316-P156	Gneiss	Biot-Tonalite gneiss	180987	317919	Fld(64), Qtz(30), Bio(3), Chl(2), Opq(0.5), Epi, Tic?, Apt	mylonite	Top NE	S-C-C', sigma clasts, assym qtz	SGR + GBM	4	Bio = Chl	strong	Chlorite + Calcite + Epidote + Allanite in veins
2016Mar_71	0316-P71x	Nic	Granodiorite	182316	325069	Plg(63), Qtz(22), Ksp(9), Bio(6), Epi, Chl, Opq, Apt, Tit, Rut, Zrc	mylonite	unsure	N/A	GBM > SGR	4	Bio	weak	
2016Oct_37	1016-P37	Gneiss	Tonalite // Hnbl- Biot Tonalite Gneiss	181022	319444	Leuco layer: Fld(77), Qtz(20), Chl(1), Opq(1), Tit, Allanite. Mafic Layer: Fld(44), Hbl(23), Bio(12), Qtz(15), Opq(3), Tit(2)	mylonite	Top NE	S-C-C'	SGR + GBM	2	Bio = Chl	moderate	Myrmekite. Chl + calcite in fractures. Poikiloblastic plag
2016Oct_38	1016-P38	Gneiss	Hnbl-Biotite Tonalite gneiss	181011	319415	Fld(50), Qtz(36), Opq(6), Bio(4), Hbl(3), Chl(1), Tit, Apt	mylonite	Top NE	S-C-C'	GBM > SGR	3	Bio > Chl	weak	Poikiloblastic plag.
2016Oct_58	1016-P58a	Gneiss	Biotite Hnbl Tonalite Gneiss	179653	317881	Fld(57), Qtz(15), Hbl(15), Bio(4), Opq(3), Epi(2), Chl(2), Tit(1), Tourmaline, Fibrous Pale Amphibole, Apt, Zrc,	mylonite	Top NE	S-C-C', assym qtz,	SGR + GBM	3	Bio > Chl	moderate	Has abundant pale fibrous amphibole in epidote and chlorite, concentrated in fractures. Hornblende has also altered to this fibrous amphibole (photo)
2016Oct_66	1016-P66	Gneiss	Biotite Hnbl Qtz- Dionite Gneiss	176780	317860	Fld(62), Hbl(18), Qtz(8), Bio(8), Opq(3), Tit(0.5), Apt, Chl, Epi,	mylonite	Top NE	S-C, sigma clasts, assym clasts	SGR + GBM	2	Bio	weak	Myrmekite. Hornblende has altered to biotite.
2016Oct_67	1016-P67	Gneiss	Biotite Tonalite gneiss	177987	317468	Fld(67), Qtz(20), Bio(6), Chl(2), Opq(4), Tit, Tourmaline, Apt, Allanite, Zrc	mylonite	Top NE	assym qtz, S-C-C', sigma clasts.	SGR + GBM	3	Bio = Chl	Strong / Moderate	High strained. Relatively abundant and euhedral zircon

2016Oct_172	1016-P172y	Nic	Minor Hnbl, Biotite Tonalite	181568	321434	Plg(59), Qtz(20), Bio(12), Ksp(5), Chl(2), Hbl(1), tourmaline, Tit, Opq, Apt, Zrc, sauss,	mylonite	Top NE	S-C-C', sigma clasts, assym qtz	SGR > GBM	2	Bio > Chl	moderate/weak	
2016Oct_178	1016-P178	Orocopia	Metachert	181239	320984	Qtz(55), Grt(40), Actinolite, Opq(4), Apt, Epi	mylonite	Top NE	assym clasts	GBM > SGR	3	N/A	N/A	Calcite + Allanite(?) + Opaques in fractures. Most garnets are zoned and have inclusions in the center.
2016Oct_188	1016-P188-uo	Orocopia	Metachert	182036	321959	Qtz(65), Opq(10), Grt(2), Allanite?(2),	mylonite	N/A		SGR + GBM	2	N/A	N/A	Calcite + saussurite + Allanite(?) (radiating fibers, brown pleochroism) + Epidote in fractures.
2016Oct_194	1016-P194	Orocopia	Shisty orocopia	181784	323021	Fld(42), Qtz(37), Bio(12), Chl(4), Msc(3), Opq(1), Zrc	mylonite	Top NE	S-C-C', mica fish, assym qtz, simga clasts	SGR + GBM	2	Bio > Chl	moderate	Calcite + sericitized plagioclase in fractures. Minor sagenitic chlorite.
2016Oct_233	1016-P233-uo	Orocopia	Schistly Muscovite Orocopia	181019	320171	Qtz(33), Fld(29), Bio(18), Msc(15), Chl(4), Opq, Apt, Zrc	mylonite	N/A	Mca fish, assym qtz, S-C-C'	SGR + GBM	3	Bio > Chl	weak	Numerous plagioclase porphyroclasts with masses of apatite within. There is some K-Spar
2016Oct_235	1016-P235	Orocopia	Quartz & Plagrich Orocopia	180810	320435	Qtz(44), Fld(44), Chl(8), Opq(2), Epi(1), Bio, Apt, Rut, Zrc	mylonite	Top NE	assym qtz	SGR + GBM	2	Chl	Strong / Moderate	Sagenitic chlorite.
2016Oct_259	1016-P259	Orocopia	Schistly tremolite Orocopia	180849	322264	Qtz(26), Bio(25), Fld(25), TrmAct(20), Opq(2), Rut, Apt, Zrc	mylonite	Top NE	S-C-C', assym qtz,	SGR + GBM	4	Bio	weak	Sagenitic biotite. Poikiloblastic plagioclase.
2016Oct_274	1016-P274-uo	Orocopia	Metachert	181243	321053	Qtz(69), Grt(15), TrmAct(9), Opq(4), Bio(1), Apt(1)	mylonite	N/A	N/A	SGR + GBM	4	Bio	N/A	
2016Oct_278	1016-P278a-uo	Nic	Brecciated & Cataclastic granodiorite	181347	320770	Fld(-), Qtz(-), Allanite(-), Epi(-), Zrc	Cataclastic & brecciated mylonite	N/A	N/A	SGR > GBM	-	Chl	moderate / weak	
2016Oct_278	1016-P278b	Gneiss	Homblende granodiorite gneiss	181347	320770	Fld(47), Hbl(24), Qtz(12), Bio(11), Opq(3), Chl(2), Tit, Apt	mylonite	Top NE	assym qtz, S-C-C', sigma clasts.	SGR + GBM	2	Bio > Chl	weak	
2016Oct_300	1016-P300a	Orocopia	Quartz & Plagrich Orocopia	179714	319344	Qtz(44), Fld(46), Chl(7), Bio(1), Opq(1), Epi, Sauss, Apt, Rut,	mylonite	Top NE	S-C-C', sigma clasts	SGR + GBM	2	Chl	moderate	Sagenitic Chlorite. Calcite in a vein.
2016Oct_323	1016-P323	Gneiss	Minor Hnbl, Biotite Granodiorite Gneiss	179712	316804	Fld(50), Qtz(38), Bio(8), Chl(1), Opq(2), Hbl, Apt, Epi, Zrc	mylonite	unsure	N/A	GBM > SGR	4	Bio > Chl	weak	myrmekite
2016Oct_368	1016-P368-uo	Nic	Granodiorite	181158	319830	Fld(57), Qtz(35), Opq(5), Chl(2), Tit, Tourmaline, Apt, Epi	mylonite	N/A	N/A	SGR + GBM	3	Chl	intense	
2016Oct_499	1016-P499	Nic	Quartz-monzodiorite	182378	322726	Plg(53), Ksp(18), Qtz(12), Bio(7), Hbl(3), Chl(3), Opq(3), Apt, Zrc,	mylonite	Top NE	S-C-C', sigma clasts	SGR + GBM	2	Chl = Bio	weak	Sagenitic Chlorite + Biotite. Relatively lots of zircons.
2016Nov_4	1116-P4	Orocopia	Garnet Porphyroblasts meta-arkose	182284	325056	Fld(69), Qtz(12), Bio(9), Grt(5), Opq(3), Apt(1), Epi	mylonite	Top NE	assym qtz, S-C-C', sigma clasts.	SGR > GBM	2	Bio	moderate / weak	Lots of Apatite disseminated throughout.
2016Nov_7	1116-P7	Nic	Homblende Quartz Diorite	181067	321721	Plg(44), Hbl(35), Ksp(6), Qtz(4), Bio(10), Tit(0.5), Opq, Chl, Sauss, Apt,	mylonite	Top NE	S-C-C'	SGR + GBM	2	Bio	moderate	Well zoned and twinned poikiloblastic feldspars.



2016Nov_8	1116-P8b-uo	Nic	Hornblende Biotite Quartz monzodiorite	181063	321702	Plg(47), Ksp(24), Qtz(15), Hbl(5), Bio(5), Chl(2), Tit(1), Tourmaline, Opq, Sauss, Apt,	mylonite	N/A	N/A	SGR + GBM	2	Bio > Chl	weak	Well zoned and twinned feldspars.
2016Nov_9	1116-P9	Orocopia	Quartz & Plag nch Orocopia	181022	321263	Qtz(44), Plg(42), Bio(12), Opq- Gph(1), Chl, Epi, Tit, tourmaline, Apt, Zrc	mylonite	Top NE	assym qtz, S-C-C', sigma clasts.	SGR + GBM	3	Bio	moderate/weak	Zircon grain looks detrital (rounded).
2016Nov_62	1116-P62-uo	Orocopia	Metachert	180908	320525	Qtz(91), Hbl(3), Opq(3), Grt(2), Apt(0.5),	mylonite	N/A	assym qtz	SGR + GBM	4	N/A	N/A	
2016Nov_144	1116-P144	Nic	Biotite Tonalite / Granodiorite	181958	323743	Fld(52), Qtz(36), Chl(7), Bio(3), Opq(1), Epi, Zrc,	mylonite	Top NE	assym qtz,	SGR + GBM	4	Chl > Bio	intense / strong	
2016Nov_157	1116-P157	Orocopia	Schistly Biotite Orocopia	180988	324127	Fld(40), Qtz(36), Bio(20), Opq- Gph(3), Grt, Apt, Zrc,	mylonite	Top NE	S-C-C', sigmal clasts	GBM > SGR	4	Bio	weak	Poikiloblastic and Graphitic plagioclase. Orangish-red biotite.
2016Nov_185	1116-P185- uo	Nic	Biotite Quartz Mondodiorite	182785	324845	Plg(39), Ksp(34), Qtz(16) ,Chl(8), Bio(2), Opq, Tourmaline, Zrc,	protomylonite	N/A	N/A	SGR + GBM	4	Chl > Bio	moderate / weak	Sagenitic Chlorite + Biotite
2016Nov_187	1116-P187e	Nic	Diorite	182303	321533		non-mylon	N/A	N/A	N/A	-	Chl	strong	Pale fibrous amphibole
2017Feb_8	0217-P8		gneiss	179806	314188						3			myrmekite. South of map area.
2017Feb_13	0217-P13		Hnbl-bearing protomylonite	179804	313704			Top SW			3			South of map area.
2017Feb_16	0217-P16		Med-grained diorite	180478	312971									South of map area.
2017Feb_20	0217-P20		High-strain S- tectonite	181432	313224			Top NE			4			South of map area.
2017Feb_22	0217-P22	Gneiss	Leucocratic gneiss	179711	319322	Fld(70), Hnbl(18), Qtz(12), Tit, Tourm, Apt	Mylon	Top NE	all listed	SGR	2	N/A	moderate / strong	
2017Feb_25	0217-P25	Gneiss	gneiss	180024	319373	Fld(70), Hnbl(12), Chl(4), Apt, Qtz(8), Opq(2), Bio(2), Tit(1)	Proto	unsure	-	SGR + GBM	2	Chl > Bio	moderate	
2017Feb_28	0217-P28	Orocopia	Metachert	180182	319721	Qtz(84), Hnbl(5), Grt (5), Opq (5), Apt,	Mylon	Top NE	assym clasts	SGR + GBM	3	N/A	N/A	
2017Feb_30	0217-P30	Orocopia	Mica-poor schist	180424	320124	Fld(76), Qtz(18), Chl(5), Opq, Msc, Apt, Tit	Mylon	Top NE	all listed	SGR + GBM	2	Chl	moderate / weak	sagenitic.
2017Feb_33	0217-P33	Orocopia	Metachert	180906	320555	Qtz(80), Hnbl(8), Grt(6), Opq(6)	Mylon	unoriented	N/A	SGR + GBM	2	N/A	N/A	
2017Feb_41	0217-P41	Orocopia	Metabasalt	181247	321051	Hnbl(77), Plg(15), Qtz(6), Tit(2), Biot, Chl, Grt, Epi, sauss,	not mylonitic	N/A	N/A	static?	-	N/A	moderate / weak	Plagioclase generally has well defined twinning. Quartz has undulose extinction. Has relict garnets that have turned into Plag + Biot + Epi + Hnbl(?).
2017Feb_43	0217-P43	Nic	Leucocratic intrusion	181868	320696	Fld(80), Qtz(16), Opq(1), Chl(2), Tourm, Sauss, Zrc	Proto	Top NE	all listed	SGR > GBM	2	Chl	Intense	plagioclases are destroyed with saussurite in fractures.
2017Feb_47	0217-P47	Nic	L-tectonite leucocratic intrusion	179713	319412	Fld(76), Qtz(16), Chl(4), Opq(3), Zrc, Apt	Mylon	Top NE	S-C	SGR + GBM	3	Chl	Strong	
blank	0217-PM4	Orocopia	Meta basalt	-	-	Hnbl(62), Plg(29), Qtz(5), Tit(3), Cpx?, Opq, Epi, Apt	not mylonitic	N/A	N/A	SGR then static?	-	N/A	moderate / weak	Plagioclase generally has well defined twinning. Quartz has undulose extinction.

### Appendix 3: Locations of geochronology samples



## Appendix 4: Actinolite geochemical data

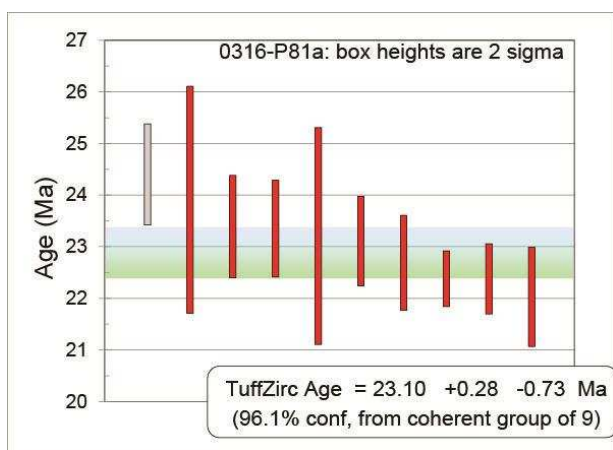
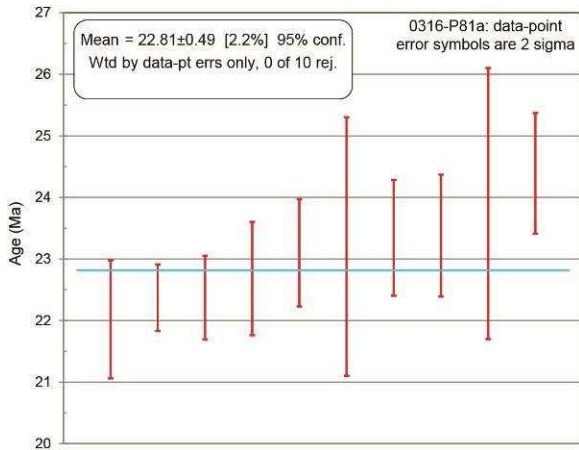
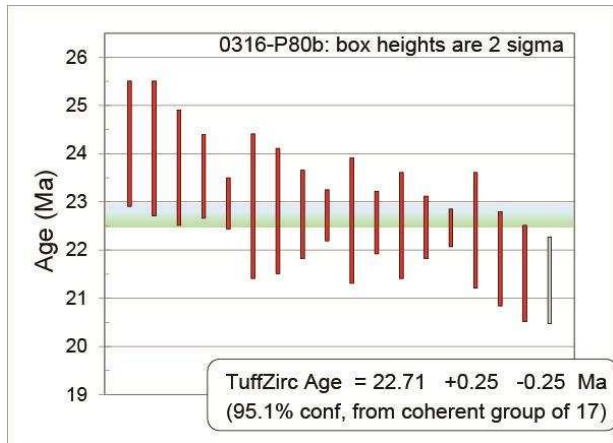
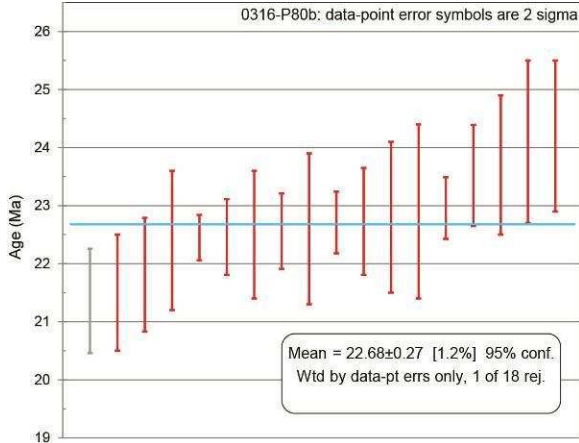
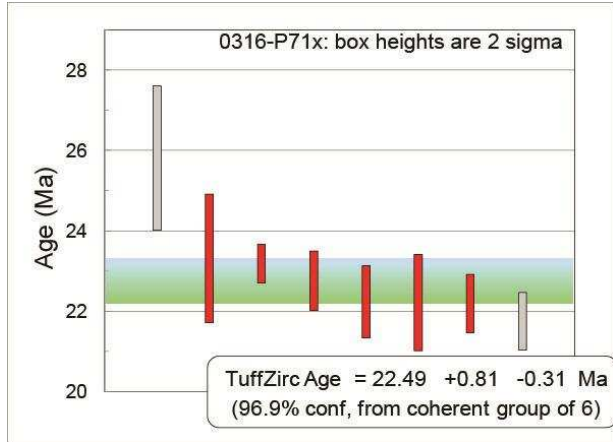
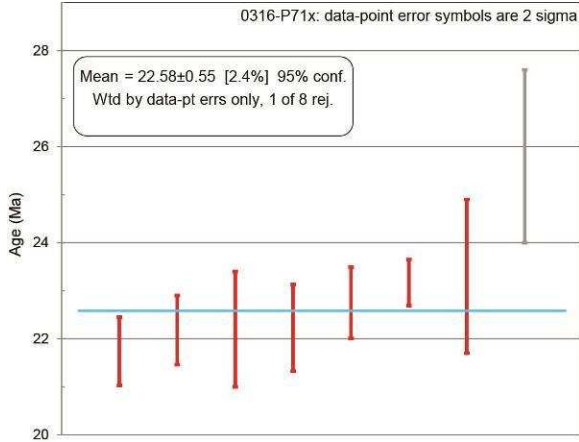
SAMPLE	Ba	Ce	Cr	Cs	Dy	Er	Eu	Ga	Gd	Hf	Ho	La	Lu	Nb	Nd
DESCRIPTION	ppm	ppm	ppm	ppm	ppm	ppm	ppm	ppm	ppm	ppm	ppm	ppm	ppm	ppm	ppm
P57 - actinolite	59.5	2.6	1700	0.01	0.96	0.59	0.32	5.3	0.72	0.2	0.19	1	0.1	0.5	2.2
P71 - actinolite	12.9	1.8	2330	0.13	0.69	0.6	0.32	5.2	0.38	<0.2	0.19	1.1	0.1	0.7	0.8
P-421 - actinolite	19.7	1.2	1580	0.53	0.43	0.35	0.32	5.9	0.36	<0.2	0.1	0.8	0.06	<0.2	0.9
	Pr	Rb	Sm	Sn	Sr	Ta	Tb	Th	Tm	U	V	W	Y	Yb	Zr
continued	ppm	ppm	ppm	ppm	ppm	ppm	ppm	ppm	ppm	ppm	ppm	ppm	ppm	ppm	ppm
P57 - actinolite	0.48	0.8	0.82	1	21.7	0.1	0.14	0.09	0.09	0.11	50	<1	5.9	0.64	9
P71 - actinolite	0.19	0.9	0.3	1	26.4	<0.1	0.09	0.08	0.1	0.11	96	1	6.3	0.95	3
P-421 - actinolite	0.2	0.4	0.28	2	51.2	<0.1	0.07	0.05	0.06	0.06	25	2	3.2	0.43	<2
	SiO2	Al2O3	Fe2O3	CaO	MgO	Na2O	K2O	Cr2O3	TiO2	MnO	P2O5	SrO	BaO	LOI	Total
continued	%	%	%	%	%	%	%	%	%	%	%	%	%	%	%
P57 - actinolite	56.5	2.94	7.1	10.95	19.2	0.32	0.07	0.24	0.06	0.25	<0.01	<0.01	0.01	2.07	99.71
P71 - actinolite	59.7	3.07	6.5	10.1	18.85	0.31	0.07	0.33	0.08	0.19	<0.01	<0.01	<0.01	1.87	101.07
P-421 - actinolite	55.2	3.61	5.62	11.15	20.3	0.26	0.04	0.22	0.03	0.23	<0.01	0.01	<0.01	2.04	98.71
	Ag	As	Cd	Co	Cu	Li	Mo	Ni	Pb	Sc	Tl	Zn			
continued	ppm	ppm	ppm	ppm	ppm	ppm	ppm	ppm	ppm	ppm	ppm	ppm			
P57 - actinolite	<0.5	<5	<0.5	44	3	10	1	1290	<2	6	<10	80			
P71 - actinolite	<0.5	<5	<0.5	43	3	<10	1	413	3	19	<10	78			
P-421 - actinolite	<0.5	<5	0.6	52	4	10	<1	1080	4	2	<10	72			

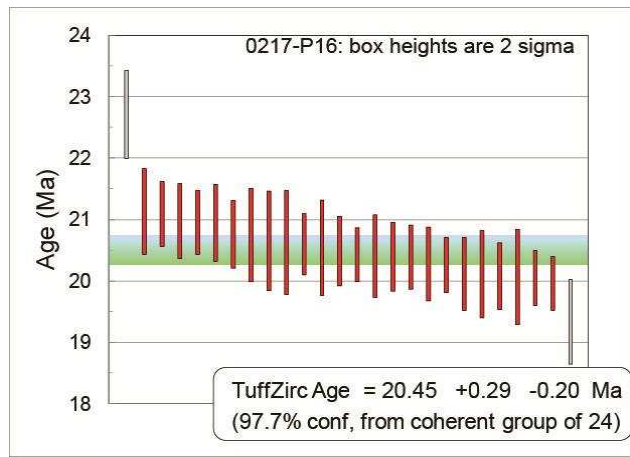
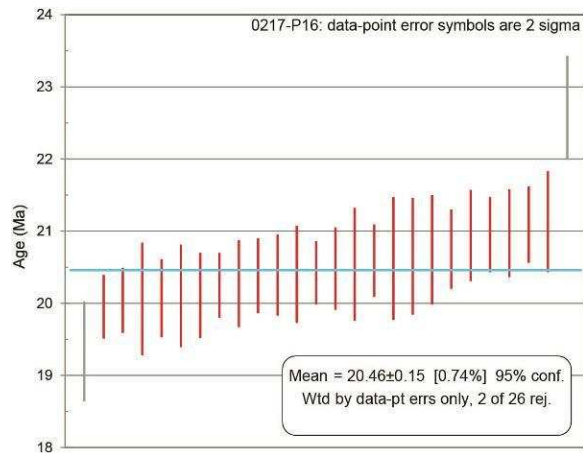
## Appendix 5: Metabasalt and metachert geochemical data

Major Elements																						
Lab No.	Field No.	Sample Description	xrf SiO <sub>2</sub> %	xrf TiO <sub>2</sub> %	xrf Al <sub>2</sub> O <sub>3</sub> %	xrf Fe <sub>2</sub> O <sub>3</sub> * %	calc FeO* %	calc Fe <sub>2</sub> O <sub>3</sub> %	titr FeO %	xrf MnO %	xrf MgO %	xrf CaO %	acid BaO %	xrf Na <sub>2</sub> O %	xrf K <sub>2</sub> O %	xrf P <sub>2</sub> O <sub>5</sub> %	H <sub>2</sub> O+	CO <sub>2</sub> %	S %	F %	Cl %	Σ
C-437866	P188	amphibolite schist; metabasalt	49.8	1.34	13.2	11.8	10.6	3.86	7.14	0.17	6.40	10.3		2.82	0.80	0.14	1.7	1.6	0.019	0.07	0.04	99.3
C-437867	PM4	amphibolite schist; metabasalt	48.3	1.63	13.8	13.8	12.4	4.43	8.43	0.18	7.08	9.87		2.99	0.91	0.18	1.3	0.1	0.017	0.04	0.02	99.2
C-437868	PM5/P41	amphibolite schist; metabasalt	49.2	1.86	13.8	14.8	13.3	4.49	9.28	0.23	6.38	10.1		2.18	1.00	0.18	1.5	0.2	0.015	0.04	0.03	100.4
C-437869	PM9	amphibolite schist; metabasalt	51.0	2.80	13.8	9.75	8.77	2.99	6.08	0.10	4.06	9.8		3.39	0.37	0.29	1.9	2.6	0.025	0.06	0.02	99.2
C-437871	P274	quartzite; metachert	80.6	0.19	3.06	10.3	9.27	7.23	2.76	1.80	1.03	1.84	0.18	0.09	0.16	0.65	0.6	0.2	0.037	0.05	<0.01	100.4
C-437872	PM1	quartzite; metachert	85.6	0.14	3.16	3.67	3.30	2.23	1.30	0.43	1.01	3.61	0.01	0.31	0.08	0.25	0.6	1.1	0.019	0.02	<0.01	99.8
C-437873	PM2	quartzite; metachert	83.3	0.14	2.51	7.11	6.40	4.88	2.01	1.34	1.19	1.69	0.28	0.30	0.45	0.39	0.5	0.2	0.027	0.04	<0.01	99.2
C-437874	PM3	quartzite; metachert	86.7	0.10	1.54	4.95	4.45	2.75	1.98	0.61	0.92	1.65	0.30	0.22	0.09	0.31	0.3	0.5	0.030	0.03	<0.01	98.0
C-437875	PM6	quartzite; metachert	84.4	0.13	2.52	6.06	5.45	5.36	0.63	2.40	0.28	1.96	0.08	0.08	0.05	0.39	0.4	0.7	0.031	0.03	<0.01	99.4
Trace Elements (except REE) — Preferred Data																						
Field No.	Sample Description	acid Ag ppm	acid As ppm	fa Au ppb	sinter B ppm	acid Ba ppm	acid Be ppm	acid Bi ppm	C %	acid Cd ppm	acid Co ppm	sinter Cr ppm	acid Cs ppm	sinter Cu ppm	sinter Ga ppm	sinter Ge ppm	sinter Hf ppm	acid In ppm	acid Li ppm	acid Mo ppm		
P188	amphibolite schist; metabasalt	0.18	0.6	<1	31	256	0.97	0.07	0.44	0.08	40.2	140	0.75	11	18.8	2	2	0.137	11.5	1.28		
PM4	amphibolite schist; metabasalt	0.12	1.0	<1	35	112	0.72	0.01	0.02	0.18	49.5	120	0.28	31	19.1	2	3	0.095	8.5	0.64		
PM5/P41	amphibolite schist; metabasalt	0.16	2.7	<1	39	114	0.89	0.09	0.05	0.13	51.1	120	0.27	35	19.9	2	3	0.108	9.2	0.73		
PM9	amphibolite schist; metabasalt	0.47	3.8	1	20	87	1.58	0.02	0.71	0.10	36.5	65	0.04	10	19.2	2	6	0.123	9.3	1.47		
P274	quartzite; metachert	0.17	3.0	<1	27	1570	1.87	0.07	0.05	0.13	11.5	42	0.57	130	8.60	2	1	0.114	2.7	9.67		
PM1	quartzite; metachert	0.10	<0.2	4	<10	92	0.37	0.09	0.29	0.09	8.7	30	0.06	186	6.52	1	1	0.142	4.6	3.55		
PM2	quartzite; metachert	0.13	1.7	<1	14	2540	1.22	0.06	0.06	0.10	11.3	31	0.76	85	6.35	2	1	0.085	5.4	4.79		
PM3	quartzite; metachert	0.10	4.5	1	<10	2660	0.58	0.06	0.14	0.13	4.0	40	0.16	31	4.03	1	<1	0.108	3.9	5.25		
PM6	quartzite; metachert	0.07	4.3	<1	11	704	0.77	0.07	0.20	0.11	10.6	43	0.11	84	6.44	2	<1	0.058	3.0	7.94		

Trace Elements (except REE) — Preferred Data — continued																					
Field No.	Sample Description	acid Nb ppm	sinter Ni ppm	acid Pb ppm	fa Pd ppb	fa Pt ppb	sinter Rb ppm	acid Sb ppm	acid Sc ppm	acid Se ppm	acid Sn ppm	acid Sr ppm	acid Ta ppm	acid Te ppm	sinter Th ppm	acid Tl ppm	sinter U ppm	acid V ppm	acid W ppm	acid Zn ppm	sinter Zr ppm
P188	amphibolite schist, me	5.9	61	3.6	<1	<5	19.5	0.32	44.7	1.0	1.9	288.	0.80	0.03	0.9	0.06	0.69	340.	0.8	76.4	89.6
PM4	amphibolite schist, me	4.8	62	1.6	<1	<5	14.2	0.41	47.4	1.1	1.2	180.	0.91	0.01	0.3	0.07	0.28	362.	0.5	107.	100.
PM5/P41	amphibolite schist, me	5.7	61	7.1	<1	<5	17.2	0.32	47.0	1.3	1.4	168.	0.86	0.05	0.4	0.10	0.25	441.	0.7	117.	108.
PM9	amphibolite schist, me	16.9	37	1.8	<1	<5	3.1	0.41	47.4	1.7	2.8	409.	1.29	0.05	1.1	0.01	0.59	379.	0.9	52.0	218.
P274	quartzite; metachert	4.4	60	3.0	7	<5	8.0	0.09	7.7	0.6	<0.2	76.8	0.25	0.25	4.1	0.09	1.67	164.	0.3	119.	74.0
PM1	quartzite; metachert	2.4	27	2.6	11	6	1.7	0.10	5.1	0.5	0.5	196.	0.22	0.09	3.1	<0.01	1.34	87.7	0.4	26.5	52.2
PM2	quartzite; metachert	3.7	66	6.4	8	<5	18.3	0.08	6.0	1.2	0.7	137.	0.16	0.15	2.9	0.21	0.90	88.4	0.1	97.2	51.8
PM3	quartzite; metachert	1.7	34	12.7	6	8	3.9	0.17	4.0	0.6	0.4	97.1	0.17	0.12	1.8	0.02	0.56	98.8	0.2	74.1	38.7
PM6	quartzite; metachert	2.0	50	3.7	11	<5	2.3	<0.05	4.8	1.7	0.4	93.6	0.16	0.19	2.2	0.02	0.76	97.5	0.3	45.5	48.7
REE																					
Field No.	Sample Description	sinter La ppm	sinter Ce ppm	sinter Pr ppm	sinter Nd ppm	sinter Sm ppm	sinter Eu ppm	sinter Gd ppm	sinter Tb ppm	sinter Dy ppm	sinter Ho ppm	sinter Er ppm	sinter Tm ppm	sinter Yb ppm	sinter Lu ppm	sinter Y ppm					
P188	amphibolite schist, me	5.9	13.5	2.31	11.3	3.6	1.29	4.93	0.87	5.77	1.23	3.55	0.56	3.6	0.55	35.1					
PM4	amphibolite schist, me	5.2	13.4	2.37	12.5	4.0	1.51	6.12	1.05	7.06	1.51	4.25	0.65	4.4	0.68	39.6					
PM5/P41	amphibolite schist, me	5.5	14.5	2.52	13.0	4.3	1.51	5.99	0.99	7.15	1.55	4.17	0.66	4.4	0.64	38.1					
PM9	amphibolite schist, me	12.3	34.4	4.77	22.6	6.4	2.21	8.59	1.37	9.77	2.06	5.74	0.92	5.7	0.90	54.7					
P274	quartzite; metachert	76.6	43.6	20.9	86.7	17.2	4.17	17.7	2.18	12.7	2.59	6.70	0.96	5.9	0.90	70.6					
PM1	quartzite; metachert	36.0	24.5	10.2	40.7	8.4	2.10	9.28	1.32	7.59	1.57	3.96	0.60	4.0	0.60	39.7					
PM2	quartzite; metachert	53.7	28.6	14.4	58.7	12.2	3.21	12.9	1.85	10.7	2.12	5.52	0.74	4.9	0.71	59.5					
PM3	quartzite; metachert	36.1	19.2	10.4	43.3	9.3	2.50	9.61	1.33	7.38	1.44	3.78	0.56	3.3	0.51	39.6					
PM6	quartzite; metachert	44.3	25.0	12.7	52.5	11.3	2.75	12.9	1.83	11.4	2.26	6.06	0.86	5.0	0.76	59.7					

# Appendix 6: Zircon U-Pb weighted mean and tuff-zircon ages for igneous intrusions





## Appendix 7: Raw zircon U-Pb ages for intrusions

Sample	Duration(s)	FinalAge207_235	FinalAge207_235_Int2SE	FinalAge206_238	FinalAge206_238_Int2SE	FinalAge207_206	FinalAge207_206_Int2SE	Final_U_Th_ratio
P80b_1	27.8	86	13	28.3	1.2	1860	260	0.91
P80b_2	16.7	24.2	1.2	22.96	0.53	130	100	23.7
P80b_3	17.1	25.1	4.7	22.8	1.3	150	330	0.61
P80b_4	6.7	26.5	2	23.69	0.74	290	140	6.75
P80b_5	28.8	23.1	3.1	21.5	1	140	240	1.95
P80b_6	3.7	24.2	1.3	24.2	1.3	110	130	4.06
P80b_7	13.1	23.83	0.9	22.71	0.53	144	68	41.5
P80b_8	21.2	21.6	3	21.81	0.98	-50	220	8.6
P80b_9	7.4	22	1.2	22.56	0.65	60	120	6.14
P80b_10	13.2	22.3	1.7	24.1	1.4	20	150	8.5
P80b_11	3.9	26	2	23.7	1.2	270	190	21.5
P80b_12	8.8	24	1.6	23.52	0.87	100	100	10.6
P80b_13	24.8	22.95	0.86	22.45	0.39	60	75	3.34
P80b_14	6.5	31	6.1	24.7	2.1	520	420	2.05
P80b_15	15.8	21	3	22.4	1.2	-50	250	13.4
P80b_16	9	57	16	27.7	3.3	1110	580	2.51
P80b_17	16.4	22.9	1	22.46	0.65	144	99	13.7
P80b_18	24.9	22.8	2.5	21.36	0.9	120	200	1.55
P80b_19	23.9	21.7	4.1	22.9	1.5	-260	280	1.76
P80b_20	5.2	24.2	1.3	22.73	0.92	270	100	15.3
P80b_21	28.7	1066	91	928	89	1604	24	13.3
P80b_22	16.5	22.5	2.7	22.5	1.1	-60	190	4.6
P80b_23	28.7	1202	38	1101	47	1407	30	10.5
P80b_24	22.3	22.5	3.7	22.6	1.3	-40	260	0.568
Sample	Duration(s)	FinalAge207_235	FinalAge207_235_Int2SE	FinalAge206_238	FinalAge206_238_Int2SE	FinalAge207_206	FinalAge207_206_Int2SE	Final_U_Th_ratio
P81a_1	11.4	22.7	6.2	23.2	2.1	-70	410	0.591
P81a_2	6.2	23.9	2.8	24.39	0.98	-10	200	9.3
P81a_3	11.9	44	12	25.4	3.8	-1800	4800	1.44
P81a_4	4.5	23.5	6.2	23.9	2.2	40	470	2.89
P81a_5	19.4	26.2	5.4	23.1	1.5	50	340	0.648
P81a_6	15.2	21.4	2.2	22.02	0.96	90	210	0.835
P81a_7	5.5	24.5	2.8	23.38	0.99	230	250	0.95
P81a_8	3.2	34.8	5.8	23.5	2.1	880	310	35
P81a_9	9.5	79	17	24.8	1.5	2160	330	6.7
P81a_10	28.7	1060	110	1010	120	1463	35	9.9



P81a_11	28.8	23.3	2.6	23.1	0.87	50	200	4.47
P81a_12	14.2	22.82	0.95	22.37	0.54	114	82	20.53
P81a_13	4.1	23.5	2.4	22.2	2.4	260	190	53.3
P81a_14	13	22.4	1.1	22.37	0.68	80	87	22.9
P81a_15	20.6	700	110	573	89	1090	150	11
P81a_16	28.8	168.7	4.5	170	2.8	148	60	0.926
P81a_17	7.3	324	18	215	11	1310	71	15.5
P81a_18	4.6	22.8	2.3	23.34	0.94	40	180	14.5
P81a_19	15	111.6	5	117.1	2.8	10	100	1.797
P81a_20	18.2	1495	12	1423	17	1599	26	2.56
P81a_21	12.1	22.3	1.4	22.68	0.92	30	110	8.36
Sample	Duratio n_(s)	FinalAge20 7_235	FinalAge 207_235 _Int2SE	FinalAge206 _238	FinalAge206_23 8_Int2SE	FinalAge20 7_206	FinalAge207_ 206_Int2SE	Final_U_ Th_ratio
X0217_P16_1	36.7	19.2	3	20.74	0.76	-170	230	0.745
X0217_P16_2	36.7	20.4	1.8	20.38	0.52	30	150	0.548
X0217_P16_3	36.7	21.2	2	20.48	0.57	50	160	0.887
X0217_P16_4	36.7	21.9	2.6	20.11	0.59	60	180	0.817
X0217_P16_5	36.7	24.6	2.6	20.68	0.62	250	190	0.539
X0217_P16_6	36.7	23.2	2.2	20.94	0.63	160	170	0.62
X0217_P16_7	36.7	21.1	2.5	19.33	0.69	90	200	0.542
X0217_P16_8	36.7	20.2	1.6	19.95	0.44	40	140	0.553
X0217_P16_9	36.7	20.7	2.9	20.1	0.71	-60	230	0.613
X0217_P16_10	37.5	34.7	2.9	22.88	0.65	680	170	1.41
X0217_P16_11	36.7	23.8	2.6	22.71	0.72	50	180	1.273
X0217_P16_12	36.7	21.7	1.8	20.04	0.45	110	150	0.509
X0217_P16_13	36.7	16.3	4.6	21.3	1	-620	330	1.38
X0217_P16_14	36.7	20.2	1.6	20.75	0.55	0	150	0.51
X0217_P16_15	36.7	19.8	1.7	20.59	0.5	-50	150	0.541
X0217_P16_16	36.7	21.4	2	20.07	0.54	70	160	0.438
X0217_P16_17	27.2	35	3.6	20.02	0.74	920	230	0.661
X0217_P16_18	35.1	17.1	2.7	20.25	0.76	-310	230	0.67
X0217_P16_19	22.5	20.4	2.5	20.06	0.78	30	210	0.584
X0217_P16_20	36.7	21.2	1.6	20.25	0.45	100	140	0.432
X0217_P16_21	36.7	19.7	2.8	20.65	0.81	-90	220	0.463
X0217_P16_22	36.7	20.6	2	20.95	0.52	-30	160	0.646
X0217_P16_23	36.7	20.3	3	20.62	0.85	-50	240	1.246
X0217_P16_24	36.7	25.2	3.5	21.52	0.8	80	230	0.732
X0217_P16_25	36.7	20.6	2.2	20.27	0.6	40	180	0.626
X0217_P16_26	36.7	22	1.6	20.42	0.44	150	130	0.432

X0217_P16_27	36.7	19.5	3.2	20.54	0.78	-100	240	0.687
X0217_P16_28	36.7	20.1	2.2	21.13	0.7	-60	180	0.76
X0217_P16_29	18.2	211	25	32	1.9	3380	190	0.547
X0217_P16_30	26.1	89.2	7.6	24.79	0.9	2430	160	1.32
X0217_P16_31	36.7	29.6	3.2	20.4	0.66	560	200	0.813
X0217_P16_32	36.7	21.8	2.7	20.4	0.67	20	210	1.009
X0217_P16_33	36.7	20.3	2.3	20.39	0.56	-30	180	0.555
X0217_P16_34	36.7	20.2	1.8	20.97	0.61	-30	150	0.514
X0217_P16_35	36.7	21.4	1.9	21.09	0.53	20	150	0.436
X0217_P16_36	36.7	29	2.1	20.94	0.47	590	150	0.81
X0217_P16_37	16.3	159	21	29.4	1.9	2880	280	0.689
Sample	Duratio n_(s)	FinalAge20 7_235	FinalAge 207_235 _Int2SE	FinalAge206 _238	FinalAge206_23 8_Int2SE	FinalAge20 7_206	FinalAge207_ 206_Int2SE	Final_U_ Th_ratio
X0316_P71x_1	36.7	25.2	1.6	23.17	0.48	210	120	1.574
X0316_P71x_2	19.2	1323	12	1269	14	1400	26	1.101
X0316_P71x_3	4.4	31.2	3.9	25.3	1.1	440	260	38.1
X0316_P71x_4	28.1	104	4.7	97.5	1.5	224	93	2.209
X0316_P71x_5	2.6	26	11	24.6	3.4	70	720	1.88
X0316_P71x_6	22.3	1416	20	1296	19	1581	35	46.1
X0316_P71x_7	6.1	23.9	3.7	22.2	1.2	110	270	4.63
X0316_P71x_8	21	1289	21	1176	25	1468	41	0.888
X0316_P71x_9	3	33	14	20.6	2.3	580	740	1.49
X0316_P71x_10	29.1	132.3	3.9	127.4	2.8	202	53	1.761
X0316_P71x_11	28.2	1752	9.7	1737	14	1750	15	1.464
X0316_P71x_12	36.7	26	1.5	23.18	0.48	230	110	2.42
X0316_P71x_13	19	1334	15	1305	18	1368	35	1.16
X0316_P71x_14	18.8	373.3	9.1	366.7	4.2	378	64	5.03
X0316_P71x_15	21.6	90	10	71.4	3.7	500	180	37.5
X0316_P71x_16	12.9	24	12	20.9	2.2	-1200	1200	1.55
X0316_P71x_17	20.2	1379	15	1343	15	1418	37	0.729
X0316_P71x_18	18.4	27	3.3	22.03	0.92	300	240	1.076
X0316_P71x_19	9.5	293.9	7	199.9	4.2	1111	37	5.2
X0316_P71x_20	9.1	67	18	24.9	1.9	1480	430	0.945
X0316_P71x_21	36.3	30.2	1.9	23.38	0.55	510	130	1.135
X0316_P71x_22	33.3	25.4	1.6	20.64	0.41	410	120	1.839
X0316_P71x_23	36.7	21.4	4.2	22.23	0.9	-280	270	0.7739
X0316_P71x_24	5.4	26.4	2.6	23.6	1.2	270	230	6.55
X0316_P71x_25	22.1	115	13	76	3.1	800	250	0.985
X0316_P71x_26	36.7	22.4	2.5	21.74	0.71	70	190	2.79

X0316_P71x_27	25	21.2	2.3	22.75	0.74	-70	180	3.81
X0316_P71x_28	3.1	33.5	9.2	36.5	4.2	-130	470	4.43
X0316_P71x_29	27.1	160.9	5.7	170.9	3.3	53	72	3.23
X0316_P71x_30	6.6	24.7	4.7	23.3	1.6	90	330	1.09
X0316_P71x_31	18.7	1380	12	1356	16	1425	25	1.09
X0316_P71x_32	32.4	33.7	5.8	22.5	1.1	360	340	2.39
X0316_P71x_33	15.4	48	5	24.9	1.3	1250	240	4.28
X0316_P71x_34	11	251	10	235.6	5.5	410	100	1.817
X0316_P71x_35	5.7	482	34	55.2	3.6	4280	130	0.746
X0316_P71x_36	26.7	1798	31	1428	24	2258	43	0.893
X0316_P71x_37	6.5	57.5	6.8	55.8	5.3	150	200	5.67
X0316_P71x_38	25.1	158.1	6.9	162	2.9	114	96	0.754
X0316_P71x_39	17.8	1457	26	1110	19	2015	44	4.56
X0316_P71x_40	15.3	25.6	4.9	25.8	1.8	-50	310	1.59
X0316_P71x_41	13.4	1270	17	1222	18	1371	35	0.953
X0316_P71x_42	21.2	1293	13	1235	14	1401	30	1.185
X0316_P71x_43	22.5	1363	11	1341	14	1409	23	4.17
X0316_P71x_44	37.8	27.1	3.5	22.68	0.84	160	220	1.283
X0316_P71x_45	6.3	23.4	3.7	20.8	1.2	330	320	20.9
X0316_P71x_46	22.3	103.2	3.3	100.7	2.2	199	68	2.67
X0316_P71x_47	3.2	28.2	9.8	26.4	2.8	90	560	1.26
X0316_P71x_48	19.1	807	21	689	19	1164	41	1.413
X0316_P71x_49	10.6	26.9	4.7	22.1	1.4	300	350	2.32
X0316_P71x_50	13.7	1156	26	1166	20	1140	75	2.16
X0316_P71x_51	36.7	1387	10	1371	12	1417	25	0.807
X0316_P71x_52	37.8	69.3	3.5	66	2	169	71	2.8
X0316_P71x_53	9	23.4	2.5	22.18	0.72	80	170	3.81
X0316_P71x_54	21.4	1337	14	1341	17	1341	34	0.973
X0316_P71x_55	37.1	63.5	3.5	68.2	2.3	3	94	3.52
Sample	Duratio n(s)	FinalAge20 7_235	FinalAge 207_235 _Int2SE	FinalAge206 _238	FinalAge206_23 8_Int2SE	FinalAge20 7_206	FinalAge207_ 206_Int2SE	Final_U_ Th_ratio
X0217_P43_1	37.7	155.2	3.1	151	1.9	209	43	1.175
X0217_P43_2	37.7	97.6	5.1	94.1	2.3	190	100	7.48
X0217_P43_3	37.7	163	4.4	163	2.3	160	60	0.39
X0217_P43_4	37.7	71	3.9	67.6	1.4	180	110	13.63
X0217_P43_5	34.3	162.3	3.6	150.1	2	329	47	0.475
X0217_P43_6	35.9	59.4	2.3	55.41	0.91	214	83	13.89
X0217_P43_7	35.7	168.9	4.5	154.9	1.5	356	57	0.991
X0217_P43_8	37.7	61.4	9.8	55.6	2.6	150	270	8.9

X0217_P43_9	37.7	69.4	3.5	67	1.2	145	99	13.06
X0217_P43_10	37.7	66.9	3.3	67.8	1.1	57	93	5.46
X0217_P43_11	37.7	160.4	6.2	159.7	2.6	172	82	0.63
X0217_P43_12	37.7	168.8	5.4	164.8	2.2	221	70	0.817
X0217_P43_13	37.7	70.2	2.7	67.98	0.97	145	77	24.4
X0217_P43_14	37.7	162.7	6.5	157	2.8	238	86	0.716
X0217_P43_15	37.5	69	6.8	63.3	2	190	180	-2.2
X0217_P43_16	37.7	98.2	3.6	97.4	2.4	118	63	4.26
X0217_P43_17	37.7	139.2	3.4	135.6	2	209	53	0.713
X0217_P43_18	37.7	64.9	3.9	62.6	1.3	130	110	18.2
X0217_P43_19	33	141.5	4.1	127.7	1.9	355	55	1.112
X0217_P43_20	37.7	80.1	4.9	67.6	1.3	370	130	13.83
X0217_P43_21	37.7	149.4	3	146.7	1.8	195	47	0.801
X0217_P43_22	32.6	38.2	3.1	30.68	0.79	370	150	30.2
X0217_P43_23	37.7	68.9	2.3	68.44	0.97	110	71	9.56
X0217_P43_24	37.7	111.7	2.8	96.3	1.3	419	54	0.543
X0217_P43_25	37.7	167.2	4.9	165.8	2.5	197	66	1.193
X0217_P43_26	37.7	77.7	3.2	78.3	1.8	82	76	36.4
X0217_P43_27	37.7	165.8	4.8	161.2	2.3	215	66	0.58
X0217_P43_28	37.7	73.4	4.5	66.3	1.4	280	130	15.8
X0217_P43_29	37.7	160.4	2.1	158.4	1.6	187	30	19.56
X0217_P43_30	37.7	72	3.3	70.1	1.2	147	91	-1
X0217_P43_31	37.7	70.5	4.2	66.9	1.4	170	120	17.6
X0217_P43_32	37.7	171.9	3.8	165.3	2.4	256	48	2.95
X0217_P43_33	11.5	74.6	7.6	69.6	2.5	230	200	20.7
X0217_P43_34	20.4	141.9	3.6	138.2	1.9	207	60	0.787
X0217_P43_35	31	155.3	3.4	157.2	2.3	138	47	0.3836
X0217_P43_36	8.8	154.4	7.2	144.1	3.1	305	99	0.586
X0217_P43_37	25.3	184.7	5.7	185.3	2.6	169	66	0.3546
X0217_P43_38	38.3	144.6	7.2	103.6	1.7	756	97	5.32
X0217_P43_39	29.9	178	6.9	119.9	2.2	971	91	0.446
X0217_P43_40	37.7	73.4	4	65	1.2	330	120	12.08
X0217_P43_41	37.7	73.2	3.6	70.6	1.2	160	98	19.33
X0217_P43_42	37.7	144.4	4.3	142	2.2	188	62	4.1
X0217_P43_43	37.7	66.6	3	63.6	1	169	91	26.2
X0217_P43_44	37.7	165.9	5.8	165.7	2.7	170	74	2.438
X0217_P43_45	37.7	150.9	3.8	148.2	1.7	187	55	0.567
X0217_P43_46	37.7	1618.2	8.9	1550	14	1708	19	1.484
X0217_P43_47	37.7	75.3	3.2	71.9	1.2	175	86	12.93

X0217_P43_48	36.3	83.7	3.9	73.1	1.2	334	95	21.8
X0217_P43_49	37.7	164.6	2.2	162.7	1.6	200	33	0.3636
X0217_P43_50	20.8	115.3	6.4	113.5	2.5	160	120	3.67
X0217_P43_51	18.4	104.1	5	98.8	2.2	218	93	10.38
X0217_P43_52	37.7	148.7	3.9	145.5	2.5	207	56	2.964
X0217_P43_53	36.6	153.8	3.9	156.1	2.2	132	53	2.26
X0217_P43_54	37.7	159.8	3.9	147.2	2	343	60	4.28
X0217_P43_55	37.7	70.4	2.7	69.9	1.1	107	75	38.1
X0217_P43_56	37.7	166	11	163.7	3.8	180	130	0.99
X0217_P43_57	37.7	140.4	2.8	141.9	1.9	133	43	9.33
X0217_P43_58	21.9	136.8	4.7	137.8	3.2	152	78	4.57
X0217_P43_59	36.1	69.5	6	68.4	1.9	90	160	15.4
X0217_P43_60	37.7	74.5	3.1	72.8	1.3	133	79	19.5
X0217_P43_61	27	73.7	2.6	74.4	1.4	81	72	56
X0217_P43_62	37.7	67.9	2.6	68.2	1.2	64	67	6.07
X0217_P43_63	37.7	157.9	4.3	155.6	2.1	209	60	0.707
X0217_P43_64	37.7	67.6	2.4	67.7	1.7	108	73	5.99
X0217_P43_65	19.2	165.4	8.1	158.9	4.3	260	110	0.655
X0217_P43_66	37.7	62.1	4.9	61.2	1.4	100	150	7.9
X0217_P43_1	17.1	71.3	4.1	66.1	1.9	250	110	26.8
X0217_P43_2	17.5	84.6	4.8	74.2	2.2	360	110	16.9
X0217_P43_3	22.5	90.9	4.4	96.7	2.2	5	90	4.41
X0217_P43_4	14.5	179.7	7.8	142.6	4.4	697	90	0.763
X0217_P43_5	3.6	87	18	71.4	4.8	390	350	23.3
X0217_P43_6	17.8	154.6	6.9	154.4	3.7	162	82	0.717
X0217_P43_7	27.7	65.4	4	63.2	1.5	130	110	10.49
X0217_P43_8	22.7	84.1	6.1	65.8	1.9	520	150	12.73
X0217_P43_9	14.4	150.4	4.5	149.8	3.1	160	56	1.395
X0217_P43_10	6.7	76	8	78.8	5.9	40	180	15.8
X0217_P43_11	19.4	148.8	4.5	149.3	3.4	148	62	1.164
X0217_P43_12	8.8	70.4	6.5	69.7	2.9	100	170	15.2
X0217_P43_13	13.6	150.1	5.6	146.3	3.6	220	78	0.921
X0217_P43_14	7.9	73.8	6.7	72.6	4	120	180	10
X0217_P43_15	17.5	151	6.5	149	4.6	151	72	10.6
X0217_P43_16	27.7	88.4	5.7	68.4	1.8	570	140	12.8
X0217_P43_17	20.3	222	17	156.5	4.3	830	160	0.674
X0217_P43_18	10.9	65.2	5.4	67.6	3.6	10	140	27.9
X0217_P43_19	19.5	70.7	4.3	68.8	2.5	160	120	71
X0217_P43_20	28.7	140.6	5	134.5	3.7	266	73	2.04

X0217_P43_21	27.7	65.4	3.7	64	1.4	120	110	13
X0217_P43_22	27.7	64.4	3.7	65.4	1.6	50	110	12.72
X0217_P43_23	9	71.1	4.1	68.8	2.2	140	110	236
X0217_P43_24	12.2	164.6	8.3	158.2	6	258	99	0.761
X0217_P43_25	14	75	7.6	66.9	2.5	240	180	16.19
X0217_P43_26	11.7	146	6.9	146.1	6.8	151	79	2.36
X0217_P43_27	24.4	82.5	3.1	79.1	2.2	194	63	102
X0217_P43_28	24.9	74.8	4.3	66	1.8	320	120	19.8
X0217_P43_29	9.3	166.8	6.3	157.3	3.7	263	84	0.881
X0217_P43_30	8.3	111.7	8.1	108.1	3.8	160	130	9.4
X0217_P43_31	17.6	156.8	6.6	157.9	3.5	133	83	0.644
X0217_P43_32	16	135.9	7.1	134.6	5.4	170	100	0.93
X0217_P43_33	18.6	155.7	7.1	151.8	3.9	230	100	1.113
X0217_P43_34	27.7	156	6.2	156.2	4.6	162	56	6.8
X0217_P43_35	27.7	80.8	5.1	78.3	3.7	160	110	28.2
X0217_P43_36	6.8	73.4	7.3	70.4	5	180	190	105
X0217_P43_37	16.2	133.4	5.1	129.7	3.4	197	89	1.13
X0217_P43_38	27.7	66.3	4.2	64.9	1.7	120	120	13.23
X0217_P43_39	27.7	59	4.1	62.4	2	-50	120	22
X0217_P43_40	16.1	66.4	5	69.5	2.5	-30	120	41.8
X0217_P43_41	9.3	170	6.4	171.7	6.8	147	73	0.901
X0217_P43_42	24	1229	27	152.9	5.4	4802	83	0.579
X0217_P43_43	6.9	76.3	6.9	74.6	4.9	230	190	54
X0217_P43_44	11.1	156	15	155.8	7.1	160	200	1.012
X0217_P43_45	27.7	77.5	4.2	74	2	171	99	51.5
X0217_P43_46	12.8	67.1	7	67.3	3.2	80	180	44
X0217_P43_47	10.4	176.1	6	175.6	3.8	184	69	1.157
X0217_P43_48	27.7	135.2	4.8	138.1	3.1	110	65	3.36
X0217_P43_49	22.8	87.1	3.7	83.5	2.2	199	90	12.3
X0217_P43_50	9.3	72.3	4.6	75.9	4.6	60	120	32
X0217_P43_51	10.9	184	10	172.3	4.9	310	120	1.406
X0217_P43_52	15.9	153.9	7	148.7	4.4	243	97	1.911
X0217_P43_53	24.3	74.8	4.5	70.1	1.9	200	110	24.9
X0217_P43_54	19.9	163.2	5.7	168.3	4.8	102	51	1.75
X0217_P43_55	21.8	161.2	5.4	163	3.8	164	68	0.73
X0217_P43_56	11.4	66	4.5	63	3	170	120	22.4
X0217_P43_57	14.6	163.3	7.8	154.2	5.7	284	93	1.18
X0217_P43_58	3.8	96	10	82.7	4.7	380	200	76
X0217_P43_59	10.9	179	11	163.9	5.2	350	130	0.61

X0217_P43_60	27.7	71.4	4.7	68.9	2.1	140	120	12.8
X0217_P43_61	9.4	63.9	5.2	63.1	3.5	100	140	70
X0217_P43_62	15.7	171.9	9.7	169.9	4.2	180	120	2.06
X0217_P43_63	17	222	17	154.9	4.7	860	140	0.81
X0217_P43_64	3.5	78	15	72.9	4.9	160	330	44
X0217_P43_65	12.4	142.5	4.9	142.3	4	135	61	1.85
Sample	Duration(s)	FinalAge207_235	FinalAge207_235_Int2SE	FinalAge206_238	FinalAge206_238_Int2SE	FinalAge207_206	FinalAge207_206_Int2SE	Final_U_Th_ratio
0217-P47_1.FIN2	37.7	128.9	7.6	127.1	2.9	140	110	1.408
0217-P47_2.FIN2	37.7	1200	29	1205	25	1158	86	1.62
0217-P47_3.FIN2	37.7	97.5	4.1	97.6	1.7	115	86	1.636
0217-P47_5.FIN2	37.7	228.8	4.2	225	2.4	259	47	1.072
0217-P47_6.FIN2	37.7	1790	8.4	1806	16	1767	17	1.665
0217-P47_7.FIN2	37.7	169.4	3.5	166.5	1.6	203	47	1.24
0217-P47_8.FIN2	37.7	80.4	1.9	77.1	1	194	52	0.688
0217-P47_9.FIN2	37.7	1708.7	7.5	1712	13	1707	15	2.025
0217-P47_10.FIN2	37.7	1626.5	8.1	1590	15	1672	16	3.57
0217-P47_11.FIN2	37.7	176.1	5.2	178.4	2.3	149	63	1.259
0217-P47_12.FIN2	37.7	1199.7	7.8	1186	11	1226	21	1.07
0217-P47_13.FIN2	37.7	125.7	5	128.8	4.3	108	60	1.7
0217-P47_14.FIN2	37.7	1211.9	7.7	1207.4	9.8	1220	20	2.023
0217-P47_15.FIN2	37.7	218.6	5.6	221.5	2.9	193	62	2.772
0217-P47_16.FIN2	37.7	1682.8	7.1	1657	12	1710	14	1.469
0217-P47_17.FIN2	37.7	148.9	3	145.5	1.9	205	45	1.71
0217-P47_18.FIN2	37.7	1717.1	8.5	1715	14	1714	19	1.656
0217-P47_19.FIN2	37.7	1700	11	1703	16	1697	23	2.25
0217-P47_20.FIN2	37.7	1391.3	9.7	1396	11	1380	26	1.063
0217-P47_21.FIN2	4.7	546	26	269	14	1980	110	3.08
0217-P47_22.FIN2	26.1	1099	15	1012	14	1265	42	1.017
0217-P47_23.FIN2	37.7	81.4	2.8	80.2	1.2	131	69	4.945
0217-P47_24.FIN2	37.7	157.9	2.7	154.9	1.8	192	40	0.576
0217-P47_25.FIN2	37.7	412.5	6.8	401.5	4.7	462	45	1.653
0217-P47_26.FIN2	37.7	1228	12	1222	11	1224	33	1.687
0217-P47_27.FIN2	37.7	1204	17	1204	16	1191	49	1.32
0217-P47_28.FIN2	21	150	11	143.6	3.6	230	140	0.88
0217-P47_29.FIN2	37.7	1207.4	7.9	1205	10	1204	23	1.9
0217-P47_30.FIN2	37.7	1200	11	1205.6	9.7	1183	34	1.441
0217-P47_31.FIN2	37.7	1200	12	1201	12	1194	31	1.138
0217-P47_32.FIN2	36.7	168.1	3.7	160.1	1.9	261	46	0.952

0217-P47_33.FIN2	36.7	165.4	3.7	168.4	2.2	136	50	1.02
0217-P47_34.FIN2	36.7	168.8	3.1	167.3	1.7	197	37	1.079
0217-P47_34.FIN2	36.7	1185.6	8.7	1189.3	9.3	1177	25	0.627
0217-P47_35.FIN2	36.7	1729	12	1778	19	1671	25	1.491
0217-P47_36.FIN2	36.7	82.9	3	82.3	1	120	75	0.971
0217-P47_37.FIN2	36.7	224.4	9.6	233	3.8	153	93	1.344
0217-P47_38.FIN2	36.7	1657.3	8.1	1644	12	1671	19	1.539
0217-P47_39.FIN2	36.7	1655.6	8.6	1652	14	1655	20	1.202
0217-P47_40.FIN2	25.5	1560.8	7.7	1499	12	1641	15	4.69
0217-P47_41.FIN2	36.7	76.5	3	73.4	1.2	194	84	53.4
0217-P47_42.FIN2	21	1123	29	1109	20	1140	85	1.006
0217-P47_43.FIN2	33.8	1410	14	1427	15	1384	35	0.952
0217-P47_1.FIN2	15.883	1120	13	1081	16	1175	30	1.966
0217-P47_3.FIN2	17.629	245	7.8	239.7	5.4	271	60	3.47
0217-P47_4.FIN2	24.508	173.9	6.1	164.7	5.3	298	78	1.848
0217-P47_5.FIN2	27.674	99.3	3.4	80.2	2	562	75	7.22
0217-P47_6.FIN2	27.674	no value	NAN	no value	NAN	no value	NAN	no value
0217-P47_8.FIN2	19.486	1660	17	1651	28	1670	24	1.585
0217-P47_9.FIN2	27.674	1395	15	1387	20	1405	33	1.121
0217-P47_10.FIN2	24.836	1207	15	1204	23	1220	28	1.488
0217-P47_11.FIN2	18.502	1660	18	1612	30	1712	23	9.34
0217-P47_12.FIN2	5.1319	68.2	4.7	66.4	3.4	130	130	6.7
0217-P47_12.FIN2	16.319	167	10	166.1	4.2	160	130	0.5547
0217-P47_13.FIN2	6.1146	126.8	6.4	128	4.1	130	110	2.57
0217-P47_13.FIN2	17.629	173	4	173.6	2.4	159	50	1.373
0217-P47_14.FIN2	18.72	1665	22	1617	36	1713	20	6.94
0217-P47_15.FIN2	12.278	82.3	6.9	70.7	4	357	86	157
0217-P47_16.FIN2	8.8443	87.9	6.5	89.1	4.8	80	120	4.86
0217-P47_16.FIN2	16.756	163.4	8.8	164.2	4.7	140	110	1.062
0217-P47_17.FIN2	27.674	153.3	6.8	153.7	6.7	154	53	1.14
0217-P47_18.FIN2	20.14	1168	20	1143	19	1198	58	1.519
0217-P47_19.FIN2	2.293	89	13	66.7	6.2	640	290	56
0217-P47_19.FIN2	9.4404	1151	25	1120	32	1201	46	1.427
0217-P47_20.FIN2	21.123	1707	19	1654	34	1767	30	3.1
0217-P47_21.FIN2	18.285	1667	17	1648	30	1685	35	1.506
0217-P47_22.FIN2	2.4022	93	13	85	12	250	140	167
0217-P47_22.FIN2	17.083	1145	20	1077	25	1243	49	1.456
0217-P47_23.FIN2	4.04	69.9	8.8	58.7	3.7	380	200	104
0217-P47_23.FIN2	19.703	161.8	5.3	158.8	2.9	197	68	0.825



0217-P47_24.FIN2	21.232	1272	21	1293	30	1226	39	0.498
0217-P47_25.FIN2	17.629	1161	15	1152	15	1160	37	1.629
0217-P47_27.FIN2	12.387	156	10	112.2	6.7	830	130	17.9
0217-P47_28.FIN2	27.675	65.8	2.4	63.3	1.5	143	65	160
0217-P47_29.FIN2	6.2729	61.6	3.7	63.9	2.9	10	110	45
0217-P47_30.FIN2	22.76	153.5	4	151.6	3.5	181	51	2.68
0217-P47_31.FIN2	7.9708	72	4	69.5	2.2	150	110	39.1
0217-P47_31.FIN2	14.571	152.9	8	156.7	4.6	120	110	2.01
0217-P47_32.FIN2	22.106	85.7	5	85.1	2.2	120	110	1.781
0217-P47_33.FIN2	27.674	1952	25	342.5	9.6	4956	63	1.1
0217-P47_34.FIN2	14.025	87.5	6.6	69.6	3.7	540	160	37.1
0217-P47_34.FIN2	7.9708	218	14	224	10	170	130	5.88
0217-P47_35.FIN2	18.831	66.9	3	63.4	2.2	209	67	290
0217-P47_36.FIN2	7.6933	73.9	7.4	68.7	4.4	250	120	110
0217-P47_36.FIN2	17.252	1038	29	964	22	1206	80	1.343
0217-P47_37.FIN2	17.192	869	18	763	16	1168	30	19.3
0217-P47_38.FIN2	5.9453	58.8	7.3	60.7	3.5	100	150	157
0217-P47_38.FIN2	18.344	1589	16	1539	28	1680	23	3
0217-P47_39.FIN2	4.3676	75.2	9.9	70.6	6.5	250	230	146
0217-P47_39.FIN2	18.831	1100	28	1094	27	1127	74	1.682
0217-P47_40.FIN2	12.824	1134	20	1139	23	1160	50	1.885
0217-P47_41.FIN2	7.3157	63.4	3.1	63.8	2	100	82	31.9
0217-P47_41.FIN2	19.594	75.1	2.8	76	1.7	105	67	1.143
0217-P47_43.FIN2	10.81	66.3	3.6	63	2.5	208	98	125
0217-P47_43.FIN2	10.969	1065	43	1038	41	1140	120	1.327
0217-P47_44.FIN2	10.701	82.3	3.3	83.1	2.7	113	80	4.61
0217-P47_44.FIN2	13.152	129.9	7.5	132.5	4.6	128	96	1.551
0217-P47_45.FIN2	4.4768	67	7.2	67.7	5.1	90	210	41
0217-P47_45.FIN2	13.916	126.4	7.6	129	4.7	130	110	1.38
0217-P47_46.FIN2	19.485	1126	24	1121	28	1165	59	1.222
0217-P47_47.FIN2	18.94	1179	16	1205	23	1155	38	1.46
0217-P47_48.FIN2	14.68	1162	30	1049	27	1396	87	1.24
0217-P47_49.FIN2	6.4422	109.1	5.6	111.5	4.6	90	110	4.46
0217-P47_49.FIN2	18.502	191	13	171.9	4.7	430	140	1.084
0217-P47_50.FIN2	8.626	71.1	5	71.9	4.1	90	110	94
0217-P47_50.FIN2	14.026	161	3.9	163.3	3.9	160	42	0.39

## Appendix 8: Raw zircon U-Pb ages for Orocopia Schist

sample	Duration(s)	FinalAge207_235	FinalAge207_235_Int2SE	FinalAge206_238	FinalAge206_238_Int2SE	FinalAge207_206	FinalAge207_206_Int2SE	Final_U_Th_Ratio
P9_1	27.03	1551	22	1382	36	1776	28	21.90
P9_2	9.33	956	18	847	18	1192	53	2.86
P9_3	28.00	185.1	8.7	180.7	4.8	201	95	4.08
P9_4	27.03	144	3.9	143.8	2.4	177	60	0.82
P9_5	23.92	137	11	119	2.9	420	170	2.95
P9_6	27.42	58.8	2.1	53.8	1.4	242	77	133.00
P9_7	27.42	1500	12	1423	20	1603	30	31.90
P9_8	27.03	1120	14	1060	19	1247	42	4.23
P9_9	27.81	154.5	4.9	153.5	3	185	70	1.24
P9_10	22.36	1317	19	1118	27	1643	29	46.40
P9_1	27.29	162.9	2.9	157.5	1.3	239	46	0.77
P9_2	19.13	81.1	8.3	87.5	2.2	-10	160	1.82
P9_3	27.29	1415.1	9.5	1389	11	1461	22	1.77
P9_4	27.03	1361.1	6.9	1326.4	8.7	1421	16	3.70
P9_5	27.03	1166.4	5.7	1159.7	7.1	1172	16	2.22
P9_6	12.24	1662.7	8.7	1646	11	1683	20	4.14
P9_7	27.29	173.6	7.8	169.2	2.9	240	100	0.62
P9_8	11.22	1654.5	7.4	1635	13	1661	18	1.00
P9_9	27.03	221.1	4.4	218.6	2.5	237	46	1.61
P9_10	27.29	211.2	6.8	214.5	2.3	163	73	9.70
P9_11	27.03	150	8.2	150.9	2.9	150	110	0.58
P9_12	22.70	1699.2	9.7	1707	11	1675	21	1.89
P9_13	27.03	1671	10	1672	13	1671	21	1.87
P9_14	24.74	1409.5	6.2	1421.4	9.3	1385	14	1.65
P9_15	27.03	1316.7	4.7	1273.8	7.5	1391	12	2.17
P9_16	27.03	1165	13	1140	12	1201	39	1.14
P9_17	13.26	169.2	8.1	157.5	3	310	120	0.67
P9_18	13.01	1092	15	1074	17	1122	35	2.29
P9_19	14.79	1597.2	5.8	1592	11	1598	15	15.41
P9_20	27.29	178.5	6.7	167.3	2	318	78	0.82
P9_21	27.03	97	8.1	89.7	2.3	250	170	1.50
P9_22	27.03	81.5	3.1	81	1.4	123	85	1.90
P9_23	27.03	307.6	4	304.2	2.6	332	37	1.80
P9_24	27.03	86.4	1.9	87.2	1.1	101	47	0.99
P9_25	16.83	1167.6	7.6	1176	12	1164	19	2.01
P9_26	11.99	1645.5	7.9	1662	14	1632	15	27.60

P9_27	27.03	212.1	5.7	210.4	2.3	231	67	1.69
P9_28	27.03	163.7	4	158.5	2	266	56	1.87
P9_29	26.52	1689.7	9.4	1733	16	1665	20	1.41
P9_30	19.64	1375	11	1361	14	1418	30	1.50
P9_31	17.85	1417	11	1429	13	1412	30	2.44
P9_32	27.03	1658.2	8.2	1659	12	1672	19	2.41
P9_33	27.03	81.7	2.7	82.2	1.1	108	73	1.20
P9_34	12.50	158.9	5.1	150.5	1.9	269	73	1.12
P9_35	16.07	1493.2	8	1472	12	1529	18	16.30
P9_36	27.03	1197	18	1190	14	1219	50	1.69
P9_37	27.03	1190	17	1198	15	1156	49	1.46
P9_38	27.03	1316.2	7.4	1280	11	1390	16	3.41
P9_39	27.03	1381.8	8.7	1375	11	1408	23	1.97
P9_40	27.03	1216	12	1220	12	1216	35	1.08
P9_41	27.03	164.4	3.4	167.8	1.8	120	46	1.09
P9_42	27.29	102.5	2.6	94.3	1.1	296	58	1.87
P9_43	27.29	128.5	2.7	128.5	1.4	133	51	1.68
P9_44	27.03	163.2	4.1	159.7	2	217	53	1.01
P9_45	27.03	145.8	9.7	139.8	3.3	190	140	1.80
P9_46	27.29	81.3	2.1	81.33	0.79	112	55	0.72
P9_47	21.42	1602	11	1509	15	1726	25	1.81
P9_48	26.52	1406.3	6.9	1397	10	1401	20	1.04
P9_49	27.29	1176	21	1161	19	1178	58	1.73
P9_50	13.52	1235	27	1205	25	1251	75	1.48
P9_51	27.29	1216	18	1216	15	1207	45	1.37
P9_52	25.76	1644	7.9	1613	12	1667	12	2.05
P9_53	20.15	1236	19	1223	18	1237	52	1.32
P9_54	27.03	169.2	6.6	165.9	2.7	189	87	0.87
P9_55	27.03	173.2	4	159.4	2.9	326	54	0.56
P9_56	6.37	191.6	9	161.8	4.4	460	130	1.19
P9_57	8.92	161	40	166	11	190	440	1.19
P9_58	27.29	212	4.2	207	2.3	247	46	1.21
P9_59	16.07	1390	11	1384	16	1392	27	2.38
P9_60	8.41	1390	17	1363	24	1465	44	2.27
P9_61	27.03	85.3	8	77.7	2.4	230	180	1.10
P9_62	27.03	78.3	2.2	74.39	0.95	158	60	0.80
P9_63	27.29	76	2.4	66.7	1.2	374	74	5.70
P9_64	27.03	164	7	157.2	3.4	230	100	0.63
P9_65	27.29	176.8	7.9	159	3.3	379	96	0.77

P9_66	27.29	84.8	2.1	84.01	0.9	102	54	2.64
P9_67	27.03	1720.9	7.5	1718	13	1722	19	1.94
P9_68	27.29	72.4	1.6	71.54	0.75	76	51	2.09
P9_69	27.03	238.3	5.9	230.8	2.5	287	60	2.03
P9_70	14.79	173.6	3.1	169.8	1.9	211	44	0.80
P9_71	27.03	1563.6	8	1555	14	1571	19	2.35
P9_72	27.29	1647	13	1633	17	1656	26	1.42
P9_73	19.89	1716	14	1713	24	1707	28	2.07
P9_74	19.89	1730	13	1724	19	1727	27	2.31
P9_75	20.66	1647.9	7.6	1639	14	1648	14	3.28
P9_76	27.03	76.8	3	75.3	1.4	83	88	1.47
P9_77	27.03	167.1	4	164.6	2.1	202	53	1.05
P9_78	17.09	1229	17	1228	17	1211	45	0.81
P9_79	16.83	1699	18	1737	27	1641	42	1.41
P9_80	14.28	1638.4	9.6	1577	18	1720	19	1.70
P9_81	7.90	84	11	78.3	3.7	220	260	1.69
P9_82	27.29	96.3	6.5	100.9	2.2	20	130	2.28
P9_83	27.29	94.7	1.9	94.6	1.4	90	40	14.62
P9_84	15.81	1774	8.2	1828	18	1720	21	3.30
P9_85	27.29	227.5	7.4	220.6	3.4	329	78	2.01
P9_86	21.68	98.8	5.7	93	1.8	220	120	1.39
P9_87	27.03	91	4.8	90.2	1.7	180	100	2.92
P9_88	27.03	1734	12	1729	19	1755	23	1.94
P9_89	28.31	1749.5	6.5	1771	14	1728	14	0.94
P9_90	27.03	1379.3	9.8	1355	13	1430	24	2.53
P9_91	27.29	220.1	7.7	224.7	2.9	166	79	1.22
P9_92	27.03	77.8	3.1	76.2	1.3	125	81	1.46
P9_93	25.50	1637.4	5.6	1647.7	9.3	1617	11	2.09
P9_94	27.03	1725	11	1735	14	1711	25	0.82
P9_95	18.11	1357.7	7.1	1341	10	1388	15	2.01
P9_96	27.03	199	11	131	2.2	1070	120	2.65
P9_97	27.03	169.5	4.7	163.1	2.1	247	60	1.29
P9_98	28.31	153	10	138.6	4.2	380	130	1.17
P9_99	15.05	1621	10	1574	14	1682	21	8.87
P9_100	27.15	no value	NAN	no value	NAN	no value	NAN	no value
P9_101	27.29	92.8	4.8	83.2	1.4	290	110	1.24
P9_102	20.66	1202.3	7.3	1116	10	1378	18	1.35
P9_103	27.15	no value	NAN	no value	NAN	no value	NAN	no value
P9_104	27.15	no value	NAN	no value	NAN	no value	NAN	no value

sample	Duratio n(s)	FinalAge20 7_235	FinalAge207_ 235_Int2SE	FinalAge20 6_238	FinalAge206_ 238_Int2SE	FinalAge20 7_206	FinalAge207_2 06_Int2SE	Final_U_ Th_Ratio
P57_1	27.81	1540.2	9.4	1433	13	1699	17	7.09
P57_2	27.22	92.1	5.1	96.1	2.3	61	96	3.37
P57_3	27.81	121.6	3.7	118.4	3.2	184	46	0.85
P57_4	17.31	1341	12	1305	15	1396	29	2.12
P57_5	27.22	175	11	173.4	5.2	190	120	2.63
P57_6	27.22	107.8	8	100.8	3	290	150	3.11
P57_7	20.22	1558	15	1431	27	1717	30	5.16
P57_8	27.22	145	8.2	144	3.9	140	110	3.22
P57_9	27.22	89.7	2.4	88.1	1.6	144	56	3.00
P57_10	27.22	101.6	3.3	100.7	2	122	69	3.52
P57_11	27.03	63	11	65.8	2.5	60	260	5.83
P57_12	27.22	125.4	8.3	123.8	3.8	140	130	2.63
P57_13	27.22	98.1	5.1	97.9	2.4	120	100	3.07
P57_1	27.03	100.7	3.9	102.1	1.3	102	81	1.78
P57_2	27.54	1112	13	1128.9	9.8	1067	41	1.45
P57_3	23.72	144.1	3.7	144.2	2.2	166	49	0.78
P57_4	27.03	119.9	8.3	122	3.2	140	130	2.33
P57_5	27.03	119	2.5	99.87	0.98	516	50	2.05
P57_6	27.29	99.5	3.3	99.9	1.3	115	71	1.79
P57_7	27.03	162.7	3.8	162.3	1.7	186	62	1.41
P57_8	16.83	1639	11	1578	16	1742	24	1.32
P57_9	27.03	165.2	2.5	165	1.1	182	41	0.52
P57_10	27.29	104.7	4.3	103.5	1.5	138	88	1.33
P57_11	27.29	132	8.8	136	3.3	90	120	0.87
P57_12	27.03	117.5	2.4	117.47	0.98	140	47	2.33
P57_13	27.03	78.5	3.6	78.2	1.2	125	90	0.78
P57_14	27.29	142.4	2	145.4	1.2	123	34	1.48
P57_15	27.03	144.7	4.6	142.9	1.7	184	72	1.13
P57_16	27.29	138.8	3.3	137.6	1.3	152	59	2.60
P57_17	27.29	108.4	2	108.7	1	109	43	1.76
P57_18	24.74	1066.8	8.1	1088.8	8.7	1042	24	8.73
P57_19	27.29	141.6	3.7	140.3	1.6	172	62	2.05
P57_20	27.03	140.2	3.4	147.2	2.1	78	50	2.02
P57_21	27.03	173.3	7.2	172.1	2.5	203	90	2.01
P57_22	27.29	108.5	5	108.5	2	129	99	2.36
P57_23	27.29	115.2	4.1	111.5	1.4	186	83	1.80
P57_24	21.68	111.8	5.4	112.3	2.2	114	99	1.84

P57_25	27.29	231	10	218.9	3.4	365	96	3.55
P57_26	27.03	176.1	5.4	166.9	2.2	268	74	1.65
P57_27	18.36	108.1	6.5	102.1	2.8	290	130	3.37
P57_28	27.03	89.1	5.4	84.5	1.6	240	130	1.49
P57_29	27.29	163.1	3.8	160.5	1.7	189	57	0.84
P57_30	19.38	1642.3	8.7	1627	15	1661	15	1.57
P57_31	27.29	123.2	7.1	118	2.2	230	120	1.72
P57_32	27.03	106.5	3	106.4	1.4	114	67	1.62
P57_33	27.03	123	7	126.3	3.2	140	120	0.77
P57_34	27.29	123.4	5.6	122.9	2.5	139	99	2.41
P57_35	18.62	1622	11	1599	18	1660	22	4.50
P57_36	27.29	102.1	3.4	101.6	2.2	94	54	3.49
P57_37	27.03	98.7	2.7	99	1.3	92	61	1.49
P57_38	27.03	187.6	4.8	190.7	3.2	196	59	2.26
P57_39	27.29	105.5	2.2	103	1.3	170	52	2.94
P57_40	27.29	153	3.6	151.6	1.5	168	51	0.53
P57_41	27.03	109.3	6.2	109.2	2.1	150	110	1.53
P57_42	27.03	99	3.4	100	1.4	114	75	2.36
P57_43	27.03	96	4.1	96.8	2	127	80	5.08
P57_44	27.03	170.1	5.7	152.4	2.3	397	80	1.76
P57_45	27.29	163.9	8.5	172.5	3.2	70	110	1.85
P57_46	27.29	164.2	3.7	165.1	1.6	174	50	1.15
P57_47	15.56	1657	10	1667	17	1647	18	2.39
P57_48	27.29	95	3	95.5	1.5	106	72	3.32
P57_49	27.03	107.1	2.4	102.3	1.1	202	50	1.84
P57_50	27.03	174.1	3.4	175.2	1.7	159	43	1.37
P57_51	27.03	138.9	4.6	140	2.2	153	79	3.71
P57_52	20.66	144.6	5.1	144.1	2.5	157	74	1.02
P57_53	27.29	100.8	2.6	95.1	1.2	229	54	1.30
P57_54	27.03	171.6	5.6	155.1	2.1	381	74	2.25
P57_55	9.43	86	6.5	80.6	3.9	160	190	3.99
P57_56	27.29	123.7	6	97.2	1.9	640	110	2.57
P57_57	27.03	102	2.4	101.5	1.5	128	49	1.49
P57_58	19.64	142	3.7	139.9	2.8	181	55	1.54
P57_59	27.29	103	2.3	102	1.3	109	50	2.34
P57_60	27.03	152.3	5.9	149.4	2.6	218	86	1.98
P57_61	17.85	160.3	3.3	158	3.2	201	52	2.48
P57_62	21.17	177	8.8	152.3	2.7	510	110	3.22
P57_63	27.03	64.6	2.5	56.1	1.2	320	84	163.00

P57_64	27.29	157.6	3.8	157.6	2.5	138	51	3.44
P57_65	27.03	73.7	3.1	72.9	1.5	102	78	3.82
P57_66	27.29	99.6	4.5	100.3	1.6	99	95	0.53
P57_67	27.03	97.4	3	94.7	1.6	153	63	3.04
P57_68	27.29	137.3	8.7	139.7	3.1	130	130	1.90
P57_69	27.03	136.7	3	133.5	2	172	56	1.60
P57_70	27.29	92.1	3.5	90.9	1.6	175	83	2.51
P57_71	27.29	108.9	3.6	105.8	1.7	201	72	1.92
P57_72	27.29	122.5	8.1	122.9	2.9	140	130	2.44
P57_73	27.54	1643	11	1609	18	1698	17	4.52
P57_74	27.29	143.3	6	140.2	3	225	94	1.64
P57_75	17.60	134.7	9.3	116.3	2.9	420	150	2.75
P57_76	27.29	85.8	3.1	86.3	1.3	124	78	1.24
P57_77	27.03	259.2	5.1	250	3.4	323	50	1.83
P57_78	27.03	95.7	3.6	96.1	2.3	148	82	3.87
P57_79	21.68	100	3.7	95.9	1.6	195	82	1.75
P57_80	27.03	101.1	2.3	99.7	1.6	141	50	1.69
P57_81	21.42	101.9	4.5	99.8	1.5	127	88	2.50
P57_82	27.29	125.6	4.4	122.3	2	227	81	2.37
P57_83	27.03	132.5	4.3	128.1	2.4	203	75	2.01
P57_84	14.54	111.6	3.9	112.7	2.4	130	72	1.81
P57_85	27.03	113	3	112.5	1.6	106	57	2.31
P57_86	20.15	127.6	7.5	124	3.3	220	120	1.56
P57_87	27.03	103.4	3.6	101.3	1.3	143	70	2.24
P57_88	27.29	103	2	101.9	1.4	139	44	2.79
P57_89	15.30	161.4	6.8	159	2.6	184	93	1.25
P57_90	14.54	110.6	4.3	104.3	2.3	220	83	1.93
P57_91	27.03	99.9	1.7	97.3	1.4	182	41	2.02
P57_92	27.29	102	5.4	102.9	2.6	70	110	2.28
P57_93	7.39	93.7	8.1	89	3.2	240	200	2.93
P57_94	23.21	114.8	4.9	109.2	1.9	261	96	1.97
P57_95	28.05	146.4	3.5	138.1	2.1	271	45	1.22
P57_96	27.29	1435	11	1451	19	1403	25	1.16
P57_97	10.71	98.7	4	93.4	1.7	249	90	1.55
P57_98	27.03	127	11	124.6	3.8	200	160	2.17
P57_99	11.99	104.9	8.7	100.7	3	230	180	2.49
P57_100	23.72	97.3	2.8	96	1.1	151	61	2.45
P57_101	27.29	127.3	2.3	124.7	1.8	182	39	4.28
P57_102	14.28	143	4.9	132.9	3.1	338	64	2.22

P57_103	24.99	128.8	7.9	139.9	3.2	-10	120	1.98
P57_104	27.29	155.8	3	156.5	1.9	177	40	2.59
P57_105	27.03	83.4	2.7	84.8	1.1	76	66	1.18
P57_106	27.03	108.5	5.9	108.6	2.1	130	110	2.01
P57_107	27.29	98.8	2.5	98.2	1.4	131	54	1.82
P57_108	14.54	124	10	122.2	4.6	120	160	3.61
P57_109	27.29	87.8	3	83.2	1.3	183	72	7.93
P57_110	18.11	128.8	3.2	126.8	1.8	191	59	2.61
sample	Duratio n(s)	FinalAge20 7_235	FinalAge207_ 235_Int2SE	FinalAge20 6_238	FinalAge206_ 238_Int2SE	FinalAge20 7_206	FinalAge207_2 06_Int2SE	Flnal_U_ Th_Ratio
P80_1	15.75	1615	26	1511	35	1743	62	1.67
P80_2	12.06	1260	17	1127	16	1491	47	2.54
P80_3	17.11	257	15	211.8	5.7	590	120	3.35
P80_4	26.64	1539	32	1155	22	2106	68	6.57
P80_5	27.22	94.6	5.2	81.9	1.7	340	110	1.02
P80_6	28.39	349	47	59.2	6	1400	3400	4.30
P80_7	27.22	144.3	7.1	139.5	3.9	179	94	1.61
P80_8	28.20	116	13	93.1	3.7	480	230	4.06
P80_9	28.78	1663	20	1561	32	1818	38	1.23
P80_10	27.22	1514	16	1398	24	1688	34	18.39
P80_11	16.14	313	25	111.4	6.5	2360	170	22.50
P80_12	27.22	264	20	183.8	8	930	170	8.50
P80a_1	27.03	163.9	3.3	162.2	1.8	217	52	0.99
P80a_2	27.29	1380.1	7	1375.8	9	1383	16	1.03
P80a_3	27.03	1667.8	8.1	1649	12	1701	16	1.47
P80a_4	27.29	1630	4.8	1602.9	9.4	1665	13	2.47
P80a_5	27.03	1357.8	5.6	1327.5	9.2	1391	14	2.39
P80a_6	27.03	175	4.2	166.7	1.5	278	57	1.21
P80a_7	27.80	234.6	3.9	213	1.4	433	42	2.11
P80a_8	26.01	1721.1	5.7	1707.3	8.9	1727	14	1.79
P80a_9	9.94	119.9	6.7	111.3	1.6	260	120	2.99
P80a_10	27.80	201	12	158	6.2	580	120	0.77
P80a_11	10.46	188	18	175.1	6.3	290	210	1.74
P80a_12	13.52	95.7	4.8	90.4	1.8	250	100	2.31
P80a_13	29.07	149.3	8.1	162.5	3	-10	110	0.79
P80a_14	20.91	163.2	9	155.3	3.9	290	120	0.76
P80a_15	10.46	1612.5	9.1	1564	14	1671	23	1.99
P80a_16	27.29	1616.3	8.7	1603	14	1631	15	0.96
P80a_17	27.03	1714.1	9.8	1702	12	1732	21	1.44



P80a_18	11.73	1694	17	1721	25	1662	32	1.71
P80a_19	27.03	1651	11	1635	13	1669	25	1.21
P80a_20	27.29	243.6	4.2	243.1	2.6	225	44	1.50
P80a_21	27.29	1666	7.5	1649	12	1696	18	1.17
P80a_22	27.03	167.9	5.5	165.4	1.7	212	72	1.05
P80a_23	27.29	123.5	2.6	122.9	1.3	134	45	1.81
P80a_24	28.31	114.6	7.4	116.8	4.6	130	120	1.92
P80a_25	27.03	151	3.5	148.7	2	188	53	0.95
P80a_26	17.85	1670	14	1667	20	1676	31	6.42
P80a_27	14.03	1708	15	1688	17	1722	37	4.79
P80a_28	21.17	1715.5	7.2	1804	14	1618	14	8.15
P80a_29	18.87	1627.7	9.8	1609	14	1655	23	1.00
P80a_30	27.29	157.8	3.9	155.7	2.5	218	53	1.35
P80a_31	27.29	168.4	4.6	167.6	1.9	182	67	0.71
P80a_32	27.03	234.4	4	230.7	2.6	287	43	1.90
P80a_33	22.19	177.4	8.2	161.4	2.9	450	110	1.08
P80a_34	27.03	177.1	2.8	176.6	1.6	187	39	1.64
P80a_35	16.58	1661	12	1617	23	1729	20	1.99
P80a_36	12.24	209	10	213.3	3.7	170	110	1.61
P80a_37	16.58	257	13	229.7	4.1	480	120	1.64
P80a_38	27.29	81.6	4.8	80.7	1.6	130	110	0.76
P80a_39	26.52	263	20	165.7	3.9	1080	170	0.89
P80a_40	27.29	218	3.9	221.1	2.3	196	42	1.68
P80a_41	27.03	162.5	6.1	164.8	2.2	137	85	0.59
P80a_42	27.29	1691	11	1680	15	1697	24	1.19
P80a_43	27.03	164.9	4	159.5	2	268	55	1.01
P80a_44	27.03	1606.3	9.4	1571	16	1659	21	3.43
P80a_45	27.03	160.7	4.5	158.6	2.8	201	67	1.04
P80a_46	21.93	1731.8	8.9	1716	17	1739	17	1.72
P80a_47	27.03	99.3	4.1	99.5	1.7	144	87	2.29
P80a_48	21.68	173	11	161.9	4.4	300	140	0.90
P80a_49	27.03	1674	11	1664	15	1687	21	1.34
P80a_50	27.03	144.8	2.8	142	1.8	198	45	14.00
P80a_51	21.17	1629.5	7.3	1594	12	1666	17	2.21
P80a_52	15.05	1585.5	7.8	1533	13	1643	14	5.13
P80a_53	27.03	166	12	166.1	3.7	160	150	0.88
P80a_54	20.66	1350	12	1243	19	1515	31	7.72
P80a_55	16.83	91.4	8.4	90.6	3.7	140	190	0.77
P80a_56	27.29	95.9	2.4	96.1	1.4	112	56	1.95

P80a_57	27.03	151	10	157.2	4	80	130	0.38
P80a_58	27.03	165.8	2.9	164.4	1.6	166	42	1.09
P80a_59	7.39	236	8.4	238	5	201	88	30.70
P80a_60	5.35	155	12	134.1	4.1	390	150	1.59
P80a_61	27.29	163.4	9.9	160.7	3.9	270	140	0.78
P80a_62	19.13	1566.7	6.7	1558	13	1565	17	10.10
P80a_63	27.29	1698.7	8.5	1694	15	1707	21	1.43
P80a_64	26.52	1635	18	1607	20	1653	39	1.60
P80a_65	10.97	1510.5	9.3	1436	19	1613	22	1.72
P80a_66	27.03	89.2	3.8	84.3	1.4	193	84	1.31
P80a_67	27.03	166.5	6.5	156.3	2.9	293	93	1.17
P80a_68	18.11	1727	13	1733	24	1736	25	1.62
P80a_69	27.03	162.7	6.9	161	2.6	197	97	0.73
P80a_70	27.03	1679.4	9.6	1673	14	1682	21	1.79
P80a_71	27.03	163	10	161.9	4	180	130	0.81
P80a_72	21.68	1714.9	8.6	1689	15	1760	20	2.07
P80a_73	27.29	217.9	5.4	214.6	3.5	252	59	2.21
P80a_74	25.25	74.8	6.7	84	2.1	-30	150	0.76
P80a_75	27.29	130	11	129.4	3.5	170	160	5.56
P80a_76	27.29	84.1	5.7	83.8	1.7	90	130	1.33
P80a_77	13.52	118	13	54	2.3	1630	260	6.55
P80a_78	17.60	959	19	950	22	960	54	3.03
P80a_79	27.29	161	4.2	163.4	2.1	142	57	1.16
P80a_80	27.29	159.6	4.5	161.2	2.1	131	67	1.66
P80a_81	27.29	232.2	3.8	229.8	2.7	252	40	2.26
P80a_82	27.03	82.6	1.8	80.33	0.95	135	52	0.37
P80a_83	14.03	90.9	6.5	80.6	2.6	290	140	7.08
P80a_84	17.85	1661	16	1608	25	1712	31	2.64
P80a_85	22.44	1641	15	1623	19	1661	31	0.89
P80a_86	26.01	130.8	6.1	116.1	2.1	378	97	2.82
P80a_87	27.03	117.8	4.8	116.3	2.4	125	74	4.38
P80a_88	20.66	1620.8	9.9	1575	17	1680	22	1.25
P80a_89	27.03	236.6	5.2	234.8	4.7	209	49	1.38
P80a_90	17.85	179	14	162	5	340	180	0.84
P80a_91	27.29	1728	12	1732	21	1722	23	2.49
P80a_92	22.19	1378	11	1319	19	1450	19	1.44
P80a_93	27.29	172.4	6.5	163.8	2.7	237	76	1.37
P80a_94	27.03	161.7	6.1	161.2	3.2	149	86	1.18
P80a_95	27.29	158.5	8.4	155	2.7	200	110	0.71

P80a_96	27.03	1748.9	9.6	1754	20	1741	22	1.26
P80a_97	27.03	168.1	7.3	159.8	3.2	268	97	0.91
P80a_98	27.29	216.3	7.1	214.8	3.8	241	75	1.76
P80a_99	19.38	168.3	5	168.7	3.3	158	67	1.47
P80a_100	27.29	164	4.9	164.6	3	175	69	1.00
P80a_101	27.03	86.1	7.1	75.8	2.6	390	170	0.70
P80a_102	27.29	1150	15	1108	15	1228	42	1.46
P80a_103	27.03	86.2	2.7	82.9	1.6	215	63	1.22
P80a_104	27.03	165.8	4.8	161.8	2.1	237	65	1.13
P80a_105	27.15	2759.5	8.5	2396	16	3036	10	4.81
P80a_106	10.97	95.4	1.7	90.1	1.3	227	45	5.44
P80a_107	17.60	1605.8	8.7	1564	16	1663	24	2.76
sample	Duratio n(s)	FinalAge20 7_235	FinalAge207_ 235_Int2SE	FinalAge20 6_238	FinalAge206_ 238_Int2SE	FinalAge20 7_206	FinalAge207_2 06_Int2SE	Final_U_ Th_Ratio
P71_0	24.15	131	8	123.8	3	240	130	1.76
P71_1	25.04	99.9	4	94.9	2.3	208	77	6.50
P71_2	24.15	151.6	3	151	1.7	151	42	4.10
P71_3	24.15	94.9	3.5	93.5	1.8	143	74	3.18
P71_4	20.15	136.1	7.3	140.2	3.1	110	110	2.24
P71_5	24.15	137.5	5.6	134.6	3.5	197	77	4.21
P71_6	15.71	88.3	6.1	84.8	3.5	200	130	4.57
P71_7	2.66	61.3	8.2	54.8	4.7	340	310	21.00
P71_8	14.82	137.5	7.8	131.4	2.6	220	120	2.14
P71_9	20.59	135.6	8.4	132.8	3.1	180	130	2.05
P71_10	20.15	99.7	5.8	103.2	2.1	50	110	1.83
P71_11	6.22	74.5	5	72.8	3.6	150	150	15.80
P71_12	12.16	136	13	127.2	4.3	260	190	2.99
P71_13	3.11	123	14	59	1.8	1600	220	38.80
P71_14	19.71	125.4	6.3	118.8	2.2	220	100	2.80
P71_15	11.71	106.1	8.2	93.2	3.3	380	160	5.46
P71_16	13.77	140	11	136.1	3.5	210	170	2.06
P71_17	24.59	99.5	3.9	93.9	2.1	252	92	2.14
P71_18	5.94	66.4	4	66.6	6.7	10	150	13.40
P71_19	20.87	131.2	5.9	125.4	2.7	230	100	0.53
P71_20	23.26	155.5	4.1	152.3	2.1	204	61	2.53
P71_21	4.44	63	3.9	57.1	1.6	290	110	19.60
P71_22	17.04	100.6	5.7	100.5	2.1	120	120	2.40
P71_23	4.44	73.9	8.5	74.1	3.9	110	220	5.50
P71_24	18.82	138.6	8	119.5	2.5	440	120	2.13

P71_25	24.15	no value	NAN	no value	NAN	no value	NAN	no value
P71_26	25.48	76.8	9.6	52.2	1.3	670	180	18.40
P71_27	25.92	97.4	2.5	96.8	1.2	127	61	2.16
P71_28	27.70	123	4.7	122.2	2.5	159	71	5.49
P71_29	24.59	100.9	7.2	107	3	30	140	2.24
P71_30	10.38	53.7	4.8	51.2	3.7	200	180	134.00
P71_31	20.87	171	15	157.6	4.8	320	190	2.85
P71_32	24.15	94	4.1	93.5	1.8	141	91	1.67
P71_33	23.70	139.7	4.2	127.8	2.7	341	64	5.76
P71_34	21.48	499	24	183.2	3.6	2403	80	0.65
P71_35	13.93	52.1	2.7	50.6	1.2	200	100	149.00
P71_36	23.26	130.7	4.6	130.7	2	130	76	2.80
P71_37	24.15	no value	NAN	no value	NAN	no value	NAN	no value
P71_38	24.15	4520	390	3700	940	5120	160	1.50
P71_39	25.92	123.6	7.2	108.7	1.7	380	120	1.66
P71_40	9.49	68.1	3.4	63.6	2.2	220	110	23.00
P71_41	24.15	no value	NAN	no value	NAN	no value	NAN	no value
P71_42	6.66	62.9	3.8	54.4	1.8	400	130	34.60
P71_43	15.71	97.5	6.8	82.8	2.2	420	140	3.28
P71_44	27.70	136.9	5.7	134	2.6	197	97	1.31
P71_45	28.14	67.5	2.2	65.8	1.8	127	56	12.40
P71_46	12.16	59.1	3.3	47.9	1.5	480	110	17.60
P71_47	27.70	94.8	3.6	86.9	1.2	279	77	1.90
P71_48	5.05	66.4	4.1	61.3	2.9	220	110	24.60
P71_49	18.65	131.2	6.7	123.4	2.4	240	110	2.87
P71_50	4.88	69.4	5	56.4	3.1	510	110	75.00
P71_51	16.15	994	12	950	10	1070	36	2.27
P71_52	29.03	105.6	9	99.3	4	200	150	3.20
P71_53	27.26	111.8	5.7	111.5	3.2	143	87	2.91
P71_54	17.04	120	10	117.4	3.3	170	170	1.45
P71_55	25.48	140.2	7.6	136.3	2.6	180	100	2.59
P71_56	20.15	98.7	3.4	96.5	1.5	135	71	1.83
P71_57	14.82	123.5	9.4	123.9	3.4	120	150	2.62
P71_58	28.14	107	4.1	102	2.4	198	73	4.47
P71_59	26.81	124.9	6.1	114.2	2.3	295	93	2.42
P71_60	23.70	122.2	5.6	118.5	2.7	188	91	4.05
P71_61	27.70	101.9	2.6	101	2	138	53	3.37
P71_62	7.99	85.6	7.7	79.3	3.8	240	130	6.49
P71_63	16.60	146.7	4	140.6	2.2	248	65	1.17

P71_64	25.03	267.8	7.5	266	3.8	278	69	1.94
P71_65	5.94	49.5	4.3	47.5	3.6	190	160	29.00
P71_66	19.54	130	6.5	127.7	2.3	162	97	2.14
P71_67	23.70	132.9	6.5	129.3	2.4	200	100	1.74
P71_68	26.81	192	12	124	2.3	1000	130	7.67
P71_69	24.59	156.4	6	153.1	2.2	208	79	1.88
P71_70	17.93	1185	43	1092	56	1395	53	1.84
P71_71	25.03	1390	15	1368	20	1429	30	0.67
P71_72	24.15	112.6	2.8	113.7	1.4	105	54	1.75
P71_73	23.70	132	3.4	130	2.2	170	52	4.67
P71_74	28.14	85.3	2.6	81	1.7	240	59	1.38
P71_75	27.26	211	17	133	3	990	160	2.42
P71_76	29.48	121.1	4.9	120.2	3.1	166	79	3.26
P71_77	25.03	968	9.8	948	13	1012	33	3.58
P71_78	5.50	67.9	5.5	64.3	3.2	190	120	43.10
P71_79	20.43	156.4	5.7	151.5	3.4	242	69	6.17
P71_80	24.15	152.4	4.3	153.8	2.2	131	63	2.04
P71_81	23.70	94.5	3.4	88.3	1.3	244	84	1.72
P71_82	24.15	1609	12	1564	15	1660	22	1.29
P71_83	27.70	115.4	4.5	111	3.3	195	66	3.42
P71_84	4.61	80.2	7.4	75.6	7.6	230	160	22.20
P71_85	21.32	153.1	5.4	145.5	2	255	66	1.67
P71_86	27.26	127	7.4	121.9	4.1	195	94	2.09
P71_87	17.49	104.1	7	84.2	2.5	520	140	2.69
P71_88	20.59	86.4	2.3	81.1	1	218	52	2.53
P71_89	23.26	94	2.8	88.1	1.2	247	64	1.87
P71_90	28.59	131.1	5.5	130.4	2.3	155	87	2.21
P71_91	8.16	63.5	4.9	59.9	2.2	190	170	14.90
P71_92	17.76	94.9	6.9	91.8	2.2	160	150	3.14
P71_93	28.14	91.8	3.3	89.1	1.7	175	76	3.02
P71_94	25.92	94.5	2.1	93.4	1.4	128	42	2.25
P71_95	20.59	127	10	126.9	4.2	160	160	2.23
P71_96	24.15	964.5	9.3	931	10	1045	26	2.79
P71_97	5.77	90.2	9.6	64.2	3	750	260	7.70
P71_98	9.33	96.5	8.4	87.3	3.7	290	160	2.59
P71_99	12.16	137	10	128.5	3.8	240	160	1.84
P71_100	24.15	94.5	3.6	93.6	1.4	119	79	1.85
P71_101	9.05	78.9	6.6	64	2.6	490	180	7.33
P71_102	16.43	102.2	4.7	89.8	2.1	381	91	2.34

P71_103	27.26	128.9	5.5	128.9	2.4	147	91	4.55
P71_104	28.14	101.9	4	101.3	1.9	107	76	1.71
P71_105	27.26	68.3	3.9	64.5	3.8	275	93	35.50
P71_106	28.14	99	3.8	88.8	1.9	324	77	2.48
P71_107	19.26	170	10	124.8	3.3	760	130	2.50
P71_108	19.71	135	10	128.5	3.4	220	150	3.36
P71_109	24.15	141.1	3.5	124.7	1.5	414	57	1.70
P71_110	29.03	88.1	2.9	87.1	1.8	132	70	2.12
P71_111	23.70	100.3	5.4	93.6	1.9	220	110	1.62
P71_112	12.88	98.2	8.8	58.9	4.3	1140	200	167.00
P71_113	13.04	113.1	8.2	99.2	3.2	360	150	3.46
P71_114	10.38	59.1	2.9	59.2	2.5	110	120	23.90
P71_115	16.88	104.7	7.3	107.4	2.8	80	140	1.42
P71_116	24.15	90.2	3.3	82.3	2.1	277	73	2.38
P71_117	24.59	151.7	4.6	148.9	2.3	195	68	2.79
P71_118	3.72	59.9	6.2	56.2	5.8	230	180	31.00
P71_119	23.09	128	12	90.4	2.1	780	180	2.07
P71_120	6.66	71.1	6.4	57.4	4.7	490	180	48.00
P71_121	20.59	230	11	213.5	7.7	370	75	2.47
P71_122	13.49	150.4	6.5	145.8	4.5	220	110	6.34
P71_123	4.44	61.8	5.9	57.5	4.7	240	170	21.60
P71_124	21.93	80.1	2.9	80.7	1.8	94	77	3.25
P71_125	24.15	98.7	2	97.8	1	129	43	1.49
P71_126	5.49	67.2	5.7	65.2	3.5	130	130	11.70
P71_127	15.54	226.2	8.7	218.2	4	293	88	0.95
P71_128	24.15	145.5	6.5	138.4	2.5	238	92	1.73
P71_129	5.05	95	11	87	8.9	300	170	6.53
P71_130	22.20	128.7	5.2	124.7	2.7	192	82	2.97
P71_131	8.16	310	13	47.6	2	3691	76	18.70
P71_132	16.88	187	30	68.2	2.6	1810	220	4.84
P71_133	27.26	164.1	7.2	144.1	2.2	409	96	2.04
P71_134	8.60	64.3	5.8	59.8	3.9	170	140	11.60
P71_135	21.76	151.2	8.1	140.5	3.6	330	110	0.67
P71_136	25.48	91.6	4.8	92.4	2.7	83	89	1.91
P71_137	7.72	56.4	5.6	53.7	5	178	99	70.00
P71_138	23.54	145.5	7.9	144.4	3.3	170	110	2.00
P71_139	25.92	90.3	4	86.5	1.8	182	87	1.64
P71_140	24.15	1115	55	1009	59	1391	29	1.23
P71_141	24.59	192	14	137.2	2.5	760	140	1.52

P71_142	20.59	140.4	8.1	143	2.8	100	110	1.47
P71_143	7.72	55.5	5.6	52.8	2.1	150	170	26.60
P71_144	18.21	108.4	6.3	105.2	1.8	170	120	1.65
P71_145	21.48	163.4	6.7	152.6	4.1	316	77	3.07
P71_146	21.93	102	4.5	101	2.2	130	86	2.46
P71_147	24.15	134.1	6.3	129.8	3.2	222	87	2.82
P71_148	29.48	113	4	114.1	1.9	97	75	3.15
P71_149	29.03	89.2	2.2	87.4	1.2	132	50	2.34
P71_150	8.44	50.8	3	50.2	2.3	100	110	63.70
P71_151	17.49	93.9	4.1	91.7	2.2	163	92	3.01
P71_152	8.60	66.1	3.3	59.6	2.4	330	120	21.60
P71_153	13.32	104.3	6.1	107.3	2.6	50	110	2.48
P71_154	29.03	742	19	627	22	1127	43	5.19
P71_155	3.27	89.1	5.7	78.1	3.5	370	170	5.98
P71_156	23.98	111	5.6	105.1	1.9	220	110	2.33
P71_157	8.88	68.8	3.1	60	3.1	390	110	0.39
P71_158	18.82	133	4.7	131	2.5	169	76	1.84
P71_159	19.26	188.5	8	176.1	3.3	329	95	2.53
sample	Duratio n(s)	FinalAge20 7_235	FinalAge207_ 235_Int2SE	FinalAge20 6_238	FinalAge206_ 238_Int2SE	FinalAge20 7_206	FinalAge207_2 06_Int2SE	Final_U_ Th_Ratio
P81b_0	6.80	77	8.7	72.5	4.1	270	260	4.84
P81b_1	17.51	162.8	8.5	168.4	3.6	120	110	1.17
P81b_2	27.47	88.2	2.8	79.6	1.2	311	74	1.40
P81b_3	25.41	156.8	3.8	151.8	2.3	235	55	0.61
P81b_4	22.41	1106	14	1054	16	1210	36	1.18
P81b_5	21.74	1162	26	1151	26	1150	80	1.24
P81b_6	27.78	95	12	88.3	5.5	190	240	0.90
P81b_7	28.55	74.7	3.4	74.8	1.5	99	92	1.53
P81b_8	27.50	153.4	6.3	158.9	2.8	111	87	0.86
P81b_9	21.35	1438	11	1367	15	1545	23	12.27
P81b_10	12.77	160.8	5.8	157.3	3.3	215	79	1.05
P81b_11	26.80	161	5.2	157.5	4.4	215	68	1.29
P81b_12	26.02	1147	11	1130	14	1179	26	2.92
P81b_13	27.86	1359	13	1329	18	1413	33	2.68
P81b_14	23.60	109	6.5	109.1	3.2	130	120	0.84
P81b_15	28.34	161.7	4.6	160.6	2.8	191	62	0.86
P81b_16	24.46	1585	15	1517	28	1669	34	3.49
P81b_17	16.23	150.4	8.1	136.4	3.9	340	110	1.08
P81b_18	23.25	1373	14	1354	17	1391	33	2.05

P81b_19	22.21	254.7	8.1	240.2	4.4	362	67	1.32
P81b_20	29.30	132.2	5	115.9	4	429	91	1.84
P81b_21	8.86	70.3	3.1	67.6	2.4	182	70	122.00
P81b_22	15.48	200.7	5.1	193.9	2.6	270	59	1.92
P81b_23	26.69	91.2	2.5	91.2	1.4	135	61	1.66
P81b_24	3.73	94.7	6.1	90.3	7.4	260	170	6.28
P81b_25	6.52	163	14	160.9	5.9	170	160	1.75
P81b_26	11.86	1316	16	1229	15	1457	48	1.95
P81b_27	25.48	1368.3	9.5	1348	11	1391	23	1.22
P81b_28	23.44	170.1	5.5	166.6	2.5	212	72	0.64
P81b_29	21.32	98.2	6.2	86	2	360	130	0.99
P81b_30	24.15	1680.4	9	1678	20	1674	22	2.77
P81b_31	26.98	1373	13	1345	16	1406	23	2.47
P81b_32	19.56	1426	15	1313	20	1589	23	3.04
P81b_33	23.49	82.2	2.8	79.9	1.5	151	70	2.31
P81b_34	20.49	126	6	124.3	4.7	168	92	1.06
P81b_35	23.31	1627	15	1432	24	1889	23	4.90
P81b_36	25.42	1498	14	1437	21	1581	26	3.32
P81b_37	24.31	1336	12	1289	14	1409	27	4.07
P81b_38	27.52	1022	13	1016	11	1021	39	2.71
P81b_39	24.15	no value	NAN	no value	NAN	no value	NAN	no value
P81b_40	24.15	70.6	1.9	70.28	0.93	93	57	1.44
P81b_41	23.47	1458.2	9.1	1405	13	1534	19	5.18
P81b_42	21.95	1522	16	1443	25	1628	33	1.73
P81b_43	27.67	102.2	3.1	101.4	1.7	122	66	2.13
P81b_44	20.19	92.3	3.2	88.5	1.7	183	69	1.79
P81b_45	27.40	1005	22	922	30	1187	59	1.39
P81b_46	9.57	61	14	21.3	2.8	1440	660	37.00
P81b_47	18.98	152.1	4.8	153.9	3	138	69	1.43
P81b_48	27.79	93.6	2.5	93	1.5	110	55	2.63
P81b_49	28.29	170	5.4	165.2	2.7	218	68	1.52
P81b_50	2.30	80	18	73	16	310	350	15.80
P81b_51	23.65	162.8	6.9	154.1	3.1	271	97	0.77
P81b_52	21.02	1539	17	1428	26	1684	30	2.85
P81b_53	24.48	94.5	3.6	91.3	1.9	172	80	2.96
P81b_54	27.73	75.6	2.2	74.3	1.5	124	57	1.39
P81b_55	22.51	151	4.1	148	3.1	193	55	0.61
P81b_56	22.43	68.8	3.2	69.1	1.7	79	97	1.59
P81b_57	23.50	96.3	4.8	97.5	1.9	80	100	3.44



P81b_58	24.15	99.7	5.6	101.3	3.1	100	110	2.22
P81b_59	25.86	1630	14	1580	21	1693	30	1.17
P81b_60	24.15	76.9	2.9	72.1	1	207	75	1.20
P81b_61	27.23	16.7	2.8	18.64	0.94	-170	250	6.69
P81b_62	28.15	77.9	3	72.1	1.2	234	84	1.76
P81b_63	28.60	202	12	158.4	2.9	642	96	1.15
P81b_64	26.89	101.6	3	96.3	1.8	235	63	55.70
P81b_65	18.69	172.8	9.4	170.2	3.4	190	120	0.84
P81b_66	14.75	1643.5	9.8	1668	21	1605	20	14.42
P81b_67	25.48	85.3	2.7	83	1.3	117	59	4.23
P81b_68	26.33	238.2	9	230.7	3.8	281	82	0.75
P81b_69	27.86	75.6	2	73.72	0.88	141	59	4.94
P81b_70	20.88	1600.5	8.4	1561	15	1645	16	1.69
P81b_71	28.46	92.1	2.5	87.9	1.6	183	57	1.95
P81b_72	24.15	149.1	7.1	145.9	4.3	184	98	1.81
P81b_73	25.98	151.6	9.8	149.4	5	190	130	0.82
P81b_74	28.32	1698	11	1680	17	1720	19	1.87
P81b_75	28.22	82.7	4.1	77.9	1.4	230	100	1.30
P81b_76	25.22	1160	21	1140	19	1190	57	0.99
P81b_77	24.15	no value	NAN	no value	NAN	no value	NAN	no value
P81b_78	18.82	1385	15	1351	20	1431	37	2.37
P81b_79	23.70	145.9	5.1	124.2	2.2	477	71	0.41
P81b_80	27.92	165.9	5.5	160.7	2.6	216	67	1.88
P81b_81	24.15	122.7	5.2	105.7	2.5	454	93	2.47
P81b_82	22.76	1684	15	1636	21	1727	27	1.32
P81b_83	24.15	no value	NAN	no value	NAN	no value	NAN	no value
P81b_84	28.85	112.5	5.4	107.4	4.9	210	67	0.74
P81b_85	18.97	156.9	5.6	153	4.6	204	68	0.74
P81b_86	24.30	1660	10	1631	14	1686	24	1.24
P81b_87	24.15	no value	NAN	no value	NAN	no value	NAN	no value
P81b_88	27.88	87.1	5.4	60.8	1.7	800	120	5.57
P81b_89	24.50	1132	22	1103	27	1188	39	3.28
P81b_90	27.17	1519	22	1295	27	1847	46	1.42
P81b_91	24.36	175.9	7.2	147	4	571	90	1.19
P81b_92	24.15	no value	NAN	no value	NAN	no value	NAN	no value
P81b_93	24.15	no value	NAN	no value	NAN	no value	NAN	no value
P81b_94	24.15	no value	NAN	no value	NAN	no value	NAN	no value
P81b_95	24.15	no value	NAN	no value	NAN	no value	NAN	no value
P81b_96	3.59	56	17	37.3	5.3	600	590	23.00

P81b_97	20.55	145.7	7.2	104.7	2.5	840	110	1.97
P81b_98	24.15	no value	NAN	no value	NAN	no value	NAN	no value
P81b_99	24.73	1656.1	7.6	1638	14	1682	17	1.95
P81b_100	25.58	1362	11	1319	14	1436	26	3.10
P81b_101	27.62	95.3	2.5	93.8	2.2	142	49	2.16
P81b_102	5.53	53.9	5.3	53.2	5	140	130	11.20
P81b_103	19.89	156.8	4.6	155.3	2.9	193	67	0.61
P81b_104	22.66	1575	11	1514	16	1651	21	3.65
P81b_105	14.79	1055	32	1002	21	1178	83	1.37
P81b_106	27.51	27.5	5.6	18.8	1.6	300	430	13.40
P81b_107	26.91	80.8	7.6	83.8	2.9	30	170	0.51
P81b_108	24.26	154.1	7.9	152.9	2.2	170	110	0.98
P81b_109	24.48	1537	14	1429	24	1695	26	26.30
P81b_110	17.37	1335	12	1290	18	1408	26	2.31
P81b_111	23.93	154.5	9.6	111.5	2.3	760	150	2.00
P81b_112	26.99	181	11	131.4	4	790	100	0.61
P81b_113	28.18	247.9	7.7	245.2	6.8	265	65	2.80
P81b_114	25.26	78.1	3.3	71.3	1.2	268	90	1.09
P81b_115	26.22	1646	10	1607	14	1691	21	1.38
P81b_116	6.41	85.4	9.7	67.8	2.8	540	230	1.85
P81b_117	17.74	663	19	417	16	1623	26	2.88
P81b_118	24.31	119.6	5.1	116.4	2.1	189	92	1.80
P81b_119	27.79	83.9	3	83.7	1.3	119	77	3.06
P81b_120	19.57	93.5	4.5	94	2.6	95	85	2.89
P81b_121	21.78	74.6	4.2	69.9	2.7	210	100	5.90
P81b_122	8.84	308	22	195	15	1260	190	41.20
P81b_123	16.57	1313	13	1265	19	1398	29	2.56
P81b_124	24.15	no value	NAN	no value	NAN	no value	NAN	no value
P81b_125	29.15	113.3	3	110.3	2.8	178	53	2.90
P81b_126	28.24	132	4.9	122.1	2.9	309	85	1.44
P81b_127	24.45	94.8	2.5	93.8	1.2	120	57	1.99
P81b_128	27.94	1533	20	1411	17	1694	41	2.34
P81b_129	26.34	1600.3	7.8	1547	17	1668	19	12.47
P81b_130	7.50	774	42	509	36	1676	93	7.01
P81b_131	20.37	1582	20	1528	35	1671	30	2.65
P81b_132	27.48	74.5	2.6	71.8	1	167	71	1.73
P81b_133	21.80	138.3	7.2	119.9	2	440	120	1.73
P81b_134	27.25	1531	25	1323	15	1834	59	2.95
P81b_135	7.00	72.4	8.8	40.2	3.7	1280	230	18.10

P81b_136	13.24	506	17	457	13	716	86	1.38
P81b_137	27.37	845	15	595	13	1586	31	4.48
P81b_138	26.18	73.7	5.3	63.5	2	360	130	2.15
sample	Duration(s)	FinalAge207_235	FinalAge207_235_Int2SE	FinalAge206_238	FinalAge206_238_Int2SE	FinalAge207_206	FinalAge207_206_Int2SE	Final_U_Th_Ratio
P145_1	27.67	80.7	2.1	79.99	0.83	98	58	2.91
P145_3	16.33	66.2	2	62.3	1.3	207	63	12.70
P145_4	18.43	1663.3	9.5	1582	19	1754	26	5.50
P145_5	27.68	165.7	3.2	165	2.3	167	40	1.80
P145_7	27.67	159.4	5.7	161.4	2.3	126	76	0.43
P145_8	16.37	1472	12	1342	18	1661	19	2.72
P145_9	3.18	36	4.8	34.9	4.3	140	250	34.00
P145_10	13.80	121	6.1	120.1	4.5	140	100	1.96
P145_11	20.74	165.9	3.7	163.3	2	187	55	1.10
P145_12	24.94	72.5	2.5	68.7	2.2	214	60	17.30
P145_13	6.88	87.4	3.5	85.7	3.8	163	93	6.44
P145_14	6.10	1433	14	1263	25	1701	27	2.14
P145_15	8.17	159.3	4.2	159.4	4.8	155	51	1.40
P145_16	22.80	82	1.6	81.7	1	94	35	4.43
P145_17	2.42	66.8	4.5	62.4	3.5	230	100	36.90
P145_18	24.02	81.6	2.3	83.8	1.2	46	58	3.60
P145_19	12.72	77.5	2.1	75.3	1.9	160	52	10.70
P145_20	17.98	126.7	3.8	123.6	2.9	188	59	2.69
P145_21	3.64	94.4	8.3	82.2	4.3	390	120	39.70
P145_22	11.49	935	21	816	23	1232	52	1.97
P145_23	4.81	67.6	3.1	67.5	2.1	76	68	118.00
P145_24	6.16	731	16	688	19	865	40	1.01
P145_25	23.82	220.8	3.4	218.5	2.6	256	38	3.33
P145_27	25.88	82.8	2.6	79.7	2	176	51	8.50
P145_28	7.96	1694	13	1655	22	1739	20	1.84
P145_29	23.82	196.7	3.1	194.3	2.5	221	38	14.00
P145_30	13.57	94.8	4.8	86.3	2.3	300	120	2.22
P145_31	20.23	176.9	3.6	176.2	1.9	180	46	1.16
P145_32	11.05	82	4	76.7	2.2	230	110	16.40
P145_33	13.55	139.9	9.1	131.2	3.3	250	130	3.14
P145_34	23.31	167.1	2.4	168.8	1.5	145	34	0.56
P145_35	27.67	77.8	2.1	78.7	1.2	70	56	2.17
P145_36	27.67	79.8	2.3	79.87	0.88	85	59	1.52
P145_38	1.71	27.3	4.2	29	2	-70	250	70.00

P145_39	23.05	85.2	2.3	83.6	1.2	133	62	3.07
P145_40	3.34	123.4	8	120.4	2.5	150	120	2.63
P145_41	21.25	160.2	3.9	165.6	2.1	102	55	1.00
P145_42	2.83	105.1	8.6	103.6	3.9	130	140	2.07
P145_43	19.46	164.6	5	165.1	3.1	164	70	0.70
P145_44	23.05	1713	11	1715	21	1713	18	5.47
P145_45	25.36	128.1	1.9	127.4	1.3	148	36	9.04
P145_47	16.12	1576	13	1515	20	1658	19	4.80
P145_48	4.56	84.3	5.6	82.9	3.5	130	120	9.01
P145_49	14.83	161.8	3.5	158.3	3.1	207	48	0.92
P145_50	8.48	133.4	3.9	131.8	3.4	176	65	7.49
P145_51	15.86	166	3.1	166.2	2.8	164	44	2.56
P145_52	14.83	1623	13	1586	28	1670	29	2.40
P145_54	18.42	84.2	2.4	81.6	2.6	156	59	12.20
P145_55	22.80	1209	13	1202	20	1219	33	1.04
P145_56	23.62	78.2	1.8	75.7	1.3	150	45	11.90
P145_57	10.17	64.3	2.1	63	1.8	116	65	68.00
P145_58	8.48	72.8	2.6	67.2	1.8	249	78	15.20
P145_59	5.52	168.7	8.1	166.2	3.6	190	110	1.34
P145_61	27.67	76.7	2.4	77.7	1.6	72	65	3.27
P145_62	26.39	77.7	2.3	77.8	1.3	84	55	5.63
P145_63	6.79	83.9	6.2	83	4.2	70	110	5.22
P145_64	27.67	1666.5	8.2	1645	16	1697	16	1.36
P145_65	7.83	71.6	3.1	70	2.4	135	90	10.23
P145_66	14.78	89.5	3.2	87.6	2	172	79	3.56
P145_67	10.21	1564.4	8	1509	18	1636	19	6.05
P145_68	27.67	82.5	1.8	82.7	0.86	87	45	1.43
P145_69	21.00	1232	11	1239	11	1214	30	1.05
P145_70	14.57	1721	22	1661	46	1790	42	2.45
P145_71	15.86	69.4	2.6	68.2	2.2	127	70	50.70
P145_72	4.75	72.1	2.9	70.4	2.5	124	59	15.00
P145_73	19.59	121.7	3.6	119.9	2.3	156	60	1.89
P145_74	8.15	1154	40	933	42	1597	67	9.40
P145_75	17.66	1684	11	1645	18	1730	20	8.77
P145_76	1.54	502	15	330	13	1382	50	18.82
P145_77	17.66	1661	10	1665	18	1644	16	2.57
P145_78	6.65	61.3	2	57.4	1.9	237	78	40.30
P145_79	5.55	123.9	6.3	120.2	3.9	190	110	5.74
P145_84	12.30	185.5	5.3	183.2	2.9	213	67	0.70

P145_86	2.77	80.3	4.8	80	3.7	88	76	10.80
P145_87	16.43	166.6	2.5	166.5	1.8	175	39	0.76
P145_88	27.67	1642.7	6.4	1598	10	1700.6	9.1	13.59
P145_89	16.12	1720	11	1701	17	1743	21	3.47
P145_90	14.83	1534.9	9.3	1528	17	1546	17	13.40
P145_92	21.00	1798	18	1658	46	1970	47	3.58
P145_93	18.68	1108	14	1069	14	1179	32	2.38
P145_94	13.80	1617	11	1585	21	1657	21	3.33
P145_95	4.39	269	13	179.8	8.2	1123	95	52.90
P145_96	15.60	1388	8.8	1353	13	1436	20	2.77
P145_98	19.32	176.9	6.2	166.4	3	297	77	0.83
P145_101	6.68	144	5.4	134.5	3	278	75	5.15
P145_102	15.50	275.9	7.9	239.3	5.9	575	56	6.17
P145_103	5.65	65.1	2.9	62.8	2.2	138	81	177.00
P145_104	14.58	163.3	4.3	159.6	2.3	205	62	0.88
P145_105	27.67	76.8	1.8	76.43	0.93	102	47	3.42
P145_106	27.67	168.2	2.3	168.5	1.2	153	32	1.18
P145_107	5.93	80.3	2.9	78.1	2.3	130	71	14.70
P145_108	10.82	95.8	4	95.1	1.6	105	93	2.10
P145_109	2.03	123	17	90	11	770	110	72.70
P145_110	14.83	1585	13	1533	19	1647	22	1.20
P145_111	5.22	60.6	5	59.3	4.7	120	110	26.20
P145_112	14.70	142	12	130.1	4.3	280	130	1.32
P145_113	27.68	82.3	1.8	80.27	0.96	136	47	2.17
P145_114	8.99	535	15	410	12	1087	48	14.58
P145_115	13.80	1171	15	1162	21	1171	48	1.80
P145_116	27.67	167.4	2.4	165.4	1.4	187	36	1.06
P145_117	1.36	85.6	8.8	73.6	4.7	410	130	109.00
P145_118	15.35	1153	19	1133	15	1186	52	0.99
P145_119	21.51	169	3.9	170.6	2.3	159	53	0.90
P145_120	3.61	169.5	7.6	159.2	5.6	313	96	0.93
P145_121	18.42	154.1	4.4	149.5	3.5	232	61	2.14
P145_122	18.69	1005	14	910	16	1202	33	1.84
P145_124	18.94	97.8	3.1	98.7	2.4	114	73	4.02
P145_125	2.05	143	20	133	17	300	240	2.23
P145_126	8.67	1522	25	1468	46	1585	49	4.73
P145_127	6.48	149	11	106.8	5.2	840	120	2.93
P145_130	5.84	166.4	5.1	162.7	2.9	208	78	1.11
P145_133	17.66	1704	15	1711	30	1704	23	5.31

P145_134	17.40	106.9	2.9	107.2	1.9	105	51	1.82
P145_135	6.10	90.4	1.6	89.6	1.6	116	41	160.40
P145_136	9.73	80.4	1.9	79.2	1.8	127	53	177.90
P145_137	5.33	81.9	4.3	78.5	2.9	179	77	36.00
P145_138	5.24	178	8.7	163.7	4	360	110	0.89
P145_139	14.58	1564	14	1475	27	1696	18	2.99
P145_141	26.01	110	3.5	109.2	1.8	135	68	1.99
P145_142	2.31	64.3	2.6	64.3	1.7	78	59	63.00
P145_143	17.14	170.2	3	169.9	1.8	176	42	1.02
P145_145	24.59	150.7	3.2	152.3	2.2	135	47	1.24
P145_146	26.65	125.2	2.6	121.4	1.7	207	37	3.15
P145_147	21.25	162.2	3.7	162.6	2	167	52	0.76
P145_148	12.52	1514	13	1432	15	1636	17	2.45
P145_151	11.53	76.3	2.8	78.2	2.1	51	76	3.82
P145_152	27.67	74.7	1.5	75.7	1.3	64	42	2.07
P145_153	6.42	109.2	5.5	101.6	5	268	74	6.30
P145_154	15.16	161.8	4	159.3	2.3	202	63	0.71
P145_155	3.85	66.1	2.5	64.6	2.1	114	82	57.70
P145_156	20.23	124.1	3.8	123.6	1.7	149	71	2.97
P145_157	27.67	82.8	1.9	81.56	0.94	120	46	1.81
P145_158	6.87	237.4	5.7	231.9	6	282	44	6.66
P145_159	5.39	1146	24	918	26	1601	28	6.16
P145_160	11.77	171.1	4.5	164.9	1.8	232	57	0.85
sample	Duratio n(s)	FinalAge20 7_235	FinalAge207_ 235_Int2SE	FinalAge20 6_238	FinalAge206_ 238_Int2SE	FinalAge20 7_206	FinalAge207_2 06_Int2SE	Final_U_ Th_Ratio
1116_P12_1	4.81	107.9	6.5	101.6	3	250	140	30.60
1116_P12_2	28.88	161.2	3.9	159.6	2.5	179	52	3.12
1116_P12_3	14.33	123.9	8.7	124.3	6.8	130	110	9.30
1116_P12_4	20.90	250.8	8.2	255.6	5.2	197	69	1.15
1116_P12_5	2.99	71	13	68.7	6.5	180	340	23.70
1116_P12_6	17.55	278	28	160.5	6.4	1200	220	0.81
1116_P12_7	21.09	112	17	97.9	5	270	260	4.06
1116_P12_8	31.96	1474	18	1352	32	1704	31	5.17
1116_P12_9	38.67	100.2	5.2	97.1	2	170	100	1.96
1116_P12_10	25.35	75.9	5.8	67	2.1	300	150	14.80
1116_P12_11	20.90	261.9	6.7	256.3	3.6	302	62	1.45
1116_P12_12	38.67	80.8	2.2	78.9	1	147	59	1.27
1116_P12_13	4.62	67	16	54.3	7.6	450	540	2.00
1116_P12_14	31.15	110.8	3.5	111.5	1.6	101	68	1.33

1116_P12_15	28.25	1616	11	1563	16	1677	19	3.62
1116_P12_16	3.54	77.9	8.9	83.6	5.3	-10	220	12.80
1116_P12_17	27.98	150	7.7	153.6	2.5	120	100	0.90
1116_P12_18	36.50	81.4	3.8	72.3	1.5	321	93	3.78
1116_P12_19	36.13	106.5	4	100.4	1.9	247	78	2.36
1116_P12_20	23.35	1580.1	8	1543	13	1681	16	33.50
1116_P12_21	12.11	335	10	203.8	6.5	1372	61	17.04
1116_P12_22	38.58	94.5	2.9	97.1	1.5	62	61	6.92
1116_P12_23	28.25	1610	6.5	1567	10	1662	14	4.04
1116_P12_24	7.80	290	24	178	12	1340	120	31.60
1116_P12_25	21.99	1683	21	1700	29	1654	47	1.53
1116_P12_26	18.91	81	1.9	80.2	1.4	142	52	5.80
1116_P12_27	35.50	99.1	3.3	99.3	1.9	105	60	1.79
1116_P12_28	37.49	86.9	3	89.3	1.9	52	59	2.36
1116_P12_29	38.31	84.5	2.5	84.5	1.3	110	58	1.10
1116_P12_1	38.67	80.8	1.9	77.78	0.84	208	54	1.61
1116_P12_2	36.77	89.9	2.9	83.3	1.2	290	76	1.83
1116_P12_3	37.84	83.7	3.1	86.2	2	59	70	2.35
1116_P12_4	27.40	1641	22	1472	27	1859	29	6.81
1116_P12_5	21.19	1524	10	1443	12	1656	17	19.83
1116_P12_6	22.01	1376	12	1159	12	1741	23	2.43
1116_P12_7	5.97	61	17	55.9	3.4	180	510	-22.00
1116_P12_8	22.59	1700	14	1698	20	1717	25	3.85
1116_P12_9	5.55	328	40	202	13	1210	260	9.20
1116_P12_10	20.36	1307	13	1260	19	1399	32	1.01
1116_P12_11	38.67	87.8	4	86.8	3	146	80	3.10
1116_P12_12	24.00	1609	21	1455	30	1707	26	2.24
1116_P12_13	37.10	132	5.1	141	2.6	36	78	0.89
1116_P12_14	22.43	84.1	2.6	82.4	1.5	147	63	0.83
1116_P12_15	26.41	251.6	9.2	256.1	4.3	218	86	1.32
1116_P12_16	19.03	152.2	5.4	153.2	2.9	186	73	1.94
1116_P12_17	38.67	72.1	4	69	1.8	200	110	0.74
1116_P12_18	38.67	75.4	5.4	77.9	2.1	30	130	2.67
1116_P12_19	22.84	78.9	2	75.7	1.1	66	44	1.43
1116_P12_20	38.67	no value	NAN	no value	NAN	no value	NAN	no value
1116_P12_1	27.67	78.9	2.7	77.9	1.9	115	60	2.95
1116_P12_2	14.45	1446	20	1374	29	1553	30	2.11
1116_P12_3	27.68	725	32	607	34	1140	30	4.32
1116_P12_4	18.53	94.8	2.2	93.7	2	125	40	2.42

1116_P12_5	18.61	1452	17	1391	25	1543	20	11.34
1116_P12_6	27.67	94.2	2.3	92	1.9	151	39	20.36
1116_P12_7	25.05	86.5	2.4	88.7	1.8	58	49	2.25
1116_P12_8	13.26	267.7	8.4	264.6	5.8	300	64	2.80
1116_P12_9	16.43	156.7	4.7	158.3	3.3	133	60	1.24
1116_P12_10	12.72	1334	20	1100	23	1738	30	2.57
1116_P12_11	22.76	70.6	2.4	71.5	1.6	68	68	1.65
1116_P12_12	25.38	1620	16	1534	23	1738	25	2.17
1116_P12_13	26.36	70.8	2	71.8	1.4	62	51	1.28
1116_P12_14	15.66	92.4	3.9	69.2	1.9	719	83	12.80
1116_P12_15	21.12	90.9	3.5	81.3	1.7	321	86	1.64
1116_P12_16	27.68	73.6	2.9	68.4	1.3	230	83	1.96
1116_P12_17	22.65	1755	14	1760	25	1741	21	2.79
1116_P12_18	26.15	82.1	2.5	75	1.1	259	66	1.48
1116_P12_19	24.40	98.8	2.1	95.5	1.6	145	44	2.82
1116_P12_20	20.03	1682	24	1713	38	1624	29	4.27
1116_P12_21	28.55	84	2.3	80.9	1.2	132	52	2.01
1116_P12_22	16.21	94.9	4	84.2	2.2	335	98	1.29
1116_P12_23	22.43	154.4	4.5	149.6	2.6	200	59	1.03
1116_P12_24	19.38	1287	19	1070	23	1651	36	2.19
1116_P12_25	26.47	91.9	5.7	92.3	2.3	80	120	0.96
1116_P12_26	21.23	141.6	6.3	137.4	3.5	187	91	0.42
1116_P12_27	17.85	143.6	7.8	137.8	4.3	210	100	1.36
1116_P12_28	13.81	171	12	154.9	4.9	330	150	1.56
1116_P12_29	18.07	134	5	129	3	245	85	0.62
1116_P12_30	17.52	105.5	3.4	100.8	2.1	202	65	3.54
1116_P12_31	12.88	86.6	5.8	78.1	2.8	260	120	5.40
1116_P12_32	13.26	134.6	6.2	129.5	2.8	226	91	0.75
1116_P12_33	27.68	85.8	3.6	86.6	1.9	92	84	2.83
1116_P12_34	27.67	1309	48	1145	66	1674	24	3.08
1116_P12_35	26.91	77.7	2.1	79.4	1.3	60	55	0.84
1116_P12_36	14.68	134.5	5.7	132.5	4.5	196	73	1.33
1116_P12_37	15.72	90	9	83.2	3.9	230	190	7.10
1116_P12_38	11.19	160.9	8.6	162.5	4.9	160	110	1.42
1116_P12_39	24.18	169.6	4.8	162.5	3.1	265	59	0.85
1116_P12_40	26.91	97.2	3.4	96.4	1.9	127	69	4.38
1116_P12_41	27.67	83.9	3.3	77.1	1.5	274	85	1.29
1116_P12_42	18.72	98.3	8	82.6	2.4	380	160	1.70
1116_P12_43	12.28	135.7	8.4	124	3.1	310	130	0.79



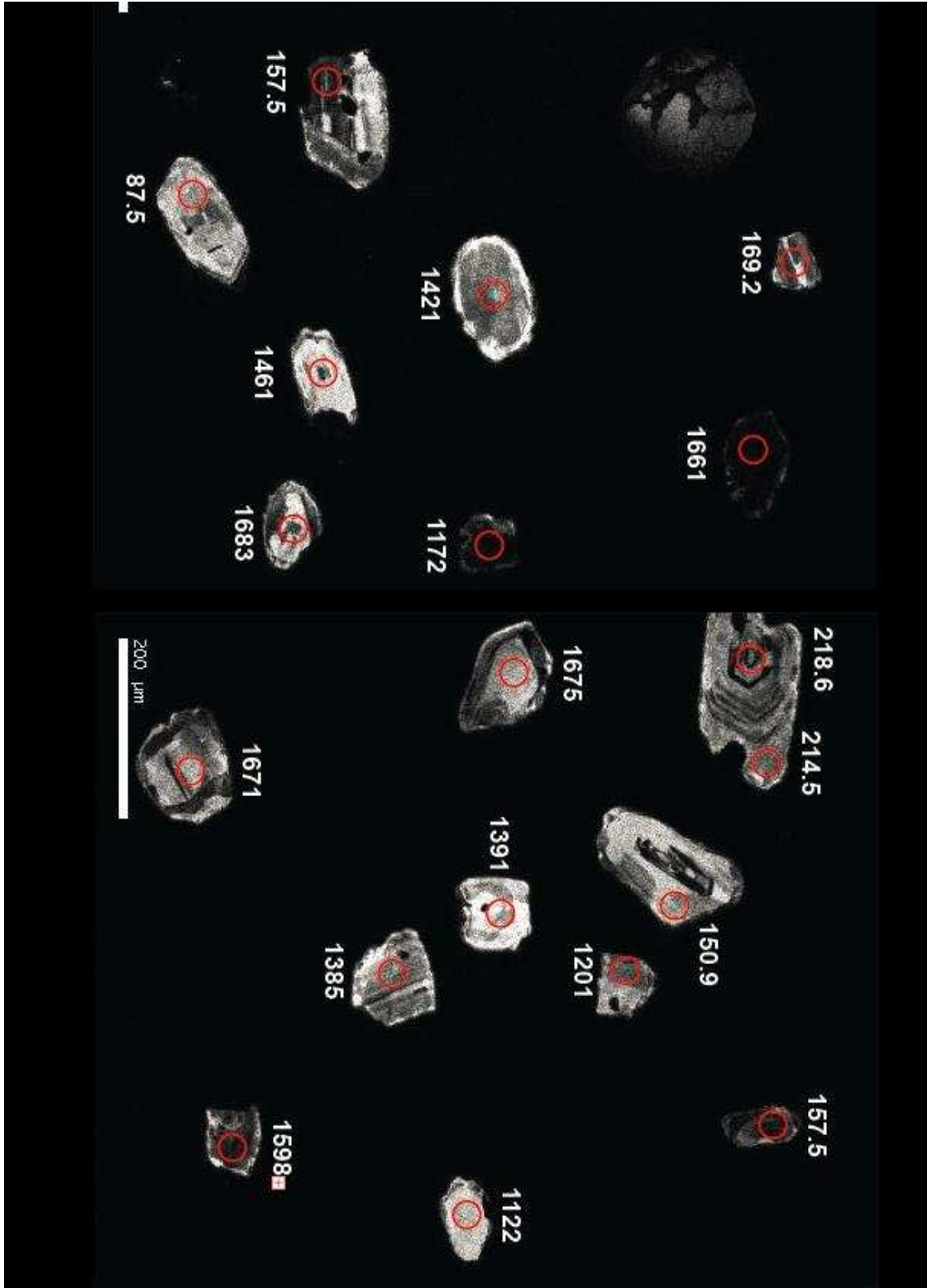
1116_P12_44	26.47	84.8	3.3	80.9	1.8	193	76	3.87
1116_P12_45	23.64	97.8	4.4	80.9	1.5	510	100	1.37
1116_P12_46	17.96	1442	19	1354	19	1571	34	2.52
1116_P12_47	19.16	108.1	5.7	114.3	3.2	50	100	1.69
1116_P12_48	25.27	97.8	2.4	97.3	1.8	131	52	1.50
1116_P12_49	11.73	83.3	6.5	63.6	2.7	680	160	47.80
1116_P12_50	26.69	80.7	1.8	80.7	1.2	101	37	2.99
1116_P12_51	27.13	76.2	1.7	73.9	1.1	152	42	1.24
1116_P12_52	17.08	1736	14	1743	26	1744	21	1.54
1116_P12_53	25.38	103.7	3.4	103.4	2	122	63	2.37
1116_P12_54	9.88	85	13	56.9	2.9	760	290	20.00
1116_P12_55	3.28	92	23	53.1	5.5	1010	640	31.90
1116_P12_56	16.76	261.3	7.6	253.2	6.1	319	65	1.96
1116_P12_57	3.76	69	19	53.6	4.2	350	530	-1.00
1116_P12_58	18.13	1580	30	1507	50	1687	23	0.93
1116_P12_59	28.44	99	3.9	87.3	1.5	376	88	1.67
1116_P12_60	3.06	90	22	57.9	7.5	990	510	-1.00
1116_P12_61	16.10	1675	20	1610	29	1741	24	8.60
1116_P12_62	17.52	92.1	5.2	83.3	2.1	270	110	2.19
1116_P12_63	27.67	87.6	2.9	85.2	1.6	145	64	2.68
1116_P12_64	6.27	69.8	6.2	70	3	70	170	5.09
1116_P12_65	14.96	1642	21	1545	34	1757	33	7.90
1116_P12_66	10.37	70.9	5.1	68.1	2.4	160	150	1.75
1116_P12_67	16.65	104.1	5.7	96.9	2.3	200	110	0.57
1116_P12_68	2.75	101	33	58.1	9.8	980	550	-15.00
1116_P12_69	19.55	1454	17	1347	28	1599	26	52.10
1116_P12_70	26.36	84.5	4	86.6	1.6	43	93	2.02
1116_P12_71	21.12	1638	14	1601	24	1672	19	2.17
1116_P12_72	23.74	89.4	3.4	88.6	2	111	70	4.28
1116_P12_73	28.55	77.5	2.6	72.9	1.4	214	68	2.68
1116_P12_74	27.67	95.9	1.5	96	1.3	95	33	3.19
1116_P12_75	2.95	60	17	51.8	9.6	560	640	-65.00
1116_P12_76	19.38	1579	26	1454	38	1747	39	6.31
1116_P12_77	24.18	85.5	4.1	79.1	2.8	252	88	3.69
1116_P12_78	18.29	1675	19	1646	34	1712	26	3.81
1116_P12_79	24.07	106.9	4.6	100.8	3.7	244	55	26.18
1116_P12_80	25.71	79.5	3.3	76.3	1.6	167	83	1.76
1116_P12_81	28.00	88.2	4	85.5	2.5	164	85	2.42
1116_P12_82	28.11	114.3	6.3	86.1	2.2	660	100	3.39

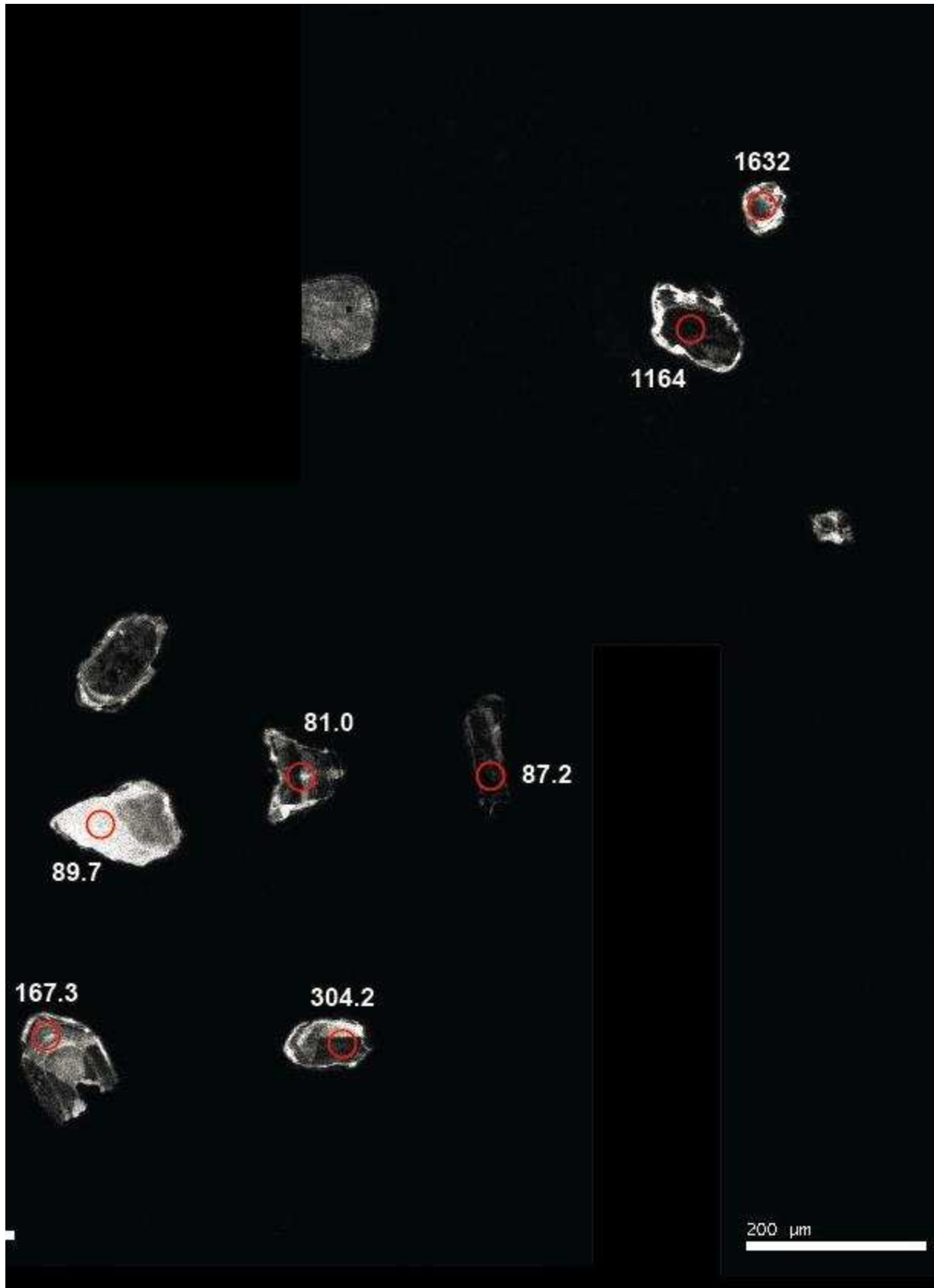
1116_P12_83	18.94	1652	16	1629	25	1676	28	1.10
1116_P12_84	22.22	69	1.7	66.5	1.4	162	55	44.00
1116_P12_85	11.19	212.4	6.8	210.3	5.9	228	61	1.67
1116_P12_86	15.45	96	7.5	88.5	3	240	150	4.04
1116_P12_87	26.37	92.5	2.6	85.9	1.5	270	66	3.80
1116_P12_88	19.27	97.4	3.7	96.9	2.1	119	77	2.27
1116_P12_89	27.57	120.4	7.8	90.8	2.8	660	130	0.72
1116_P12_90	9.17	89.1	3.3	85.7	2.6	186	90	9.40
1116_P12_91	10.97	328.3	9.6	314	10	424	52	2.12
1116_P12_92	5.13	73	17	60.5	9.9	370	500	-33.00
1116_P12_93	19.16	241.7	8.1	231.2	7.2	330	80	5.54
1116_P12_94	20.47	1691	19	1619	27	1778	28	2.54
1116_P12_95	19.05	1406	26	1225	36	1699	18	14.34
1116_P12_96	27.67	78.2	2.6	73.9	1.2	191	67	1.57
1116_P12_97	16.21	112.6	6.6	69.4	1.9	1120	120	5.29
1116_P12_98	27.67	86.8	3.8	75.1	1.9	424	86	6.49
1116_P12_99	26.26	1624	32	1506	56	1794	44	5.95
1116_P12_100	13.92	73.5	3.8	71.7	2.7	170	110	5.00
1116_P12_101	21.67	143.4	6	139.4	3.2	200	80	0.67
1116_P12_102	6.77	122.9	5.5	114.3	2.8	305	97	1.21
1116_P12_103	17.08	170	5.1	159.8	2.7	337	68	0.59
1116_P12_104	17.52	73.5	4	69.9	2.6	221	99	7.80
1116_P12_105	17.52	111.7	5.3	113.2	4.7	140	75	1.79
1116_P12_106	22.11	92	3.4	86.2	1.8	280	79	3.17
1116_P12_107	2.51	23.9	2.4	23.2	2.6	140	200	4.60
1116_P12_108	22.98	100.5	3.2	102.8	3.4	95	59	5.67
1116_P12_109	17.30	88.9	3.6	81.4	1.9	294	82	2.19
1116_P12_110	15.66	1611	26	1557	47	1697	32	7.02
1116_P12_111	24.94	138.8	3.8	138.8	2.6	138	53	2.03
1116_P12_112	28.66	111.7	4.9	95.2	1.7	429	91	4.18
1116_P12_113	28.44	146	14	62.5	2.7	1510	230	5.30
1116_P12_114	2.18	53	25	61	10	-70	790	-19.00
1116_P12_115	19.05	1141	26	979	34	1458	30	2.68
1116_P12_116	15.66	1674	19	1638	31	1706	35	2.14
1116_P12_117	19.59	85.4	4.7	79.6	2.6	240	110	1.88
1116_P12_118	17.96	76	2.8	73.8	1.6	128	77	1.83
1116_P12_119	17.41	1671	21	1627	31	1712	31	1.16
1116_P12_120	22.00	138	11	123.6	4	310	150	0.80
1116_P12_121	17.08	1455	20	1337	28	1623	34	4.16

1116_P12_122	26.80	92.8	3.2	90.1	2	172	69	1.48
1116_P12_123	27.24	178	12	118.1	4.8	990	110	2.18
1116_P12_124	27.68	1618	14	1580	21	1674	19	11.62
1116_P12_125	20.25	1581	19	1481	32	1725	32	5.63
1116_P12_126	20.69	222.9	9.5	208.6	6.3	368	97	2.55
1116_P12_127	27.67	73.1	4	72.6	2.3	110	100	5.10
1116_P12_128	20.25	106.2	3.4	89.4	2	503	76	1.31
1116_P12_129	27.67	85.2	2.1	83.8	1.4	128	48	2.01
1116_P12_130	7.04	72	15	52.7	3.9	600	480	7.00
1116_P12_131	19.16	86.3	4.2	81.7	1.8	210	100	1.81
1116_P12_132	16.21	77.1	3.8	69	1.4	310	100	8.40
1116_P12_133	27.67	220	4	214.1	3.1	262	42	2.37
1116_P12_134	23.09	1645	19	1539	28	1772	22	2.42
1116_P12_135	9.99	95	13	58.1	5.1	1030	270	16.30
1116_P12_136	24.29	124.3	3.8	117.5	3.1	240	69	3.47

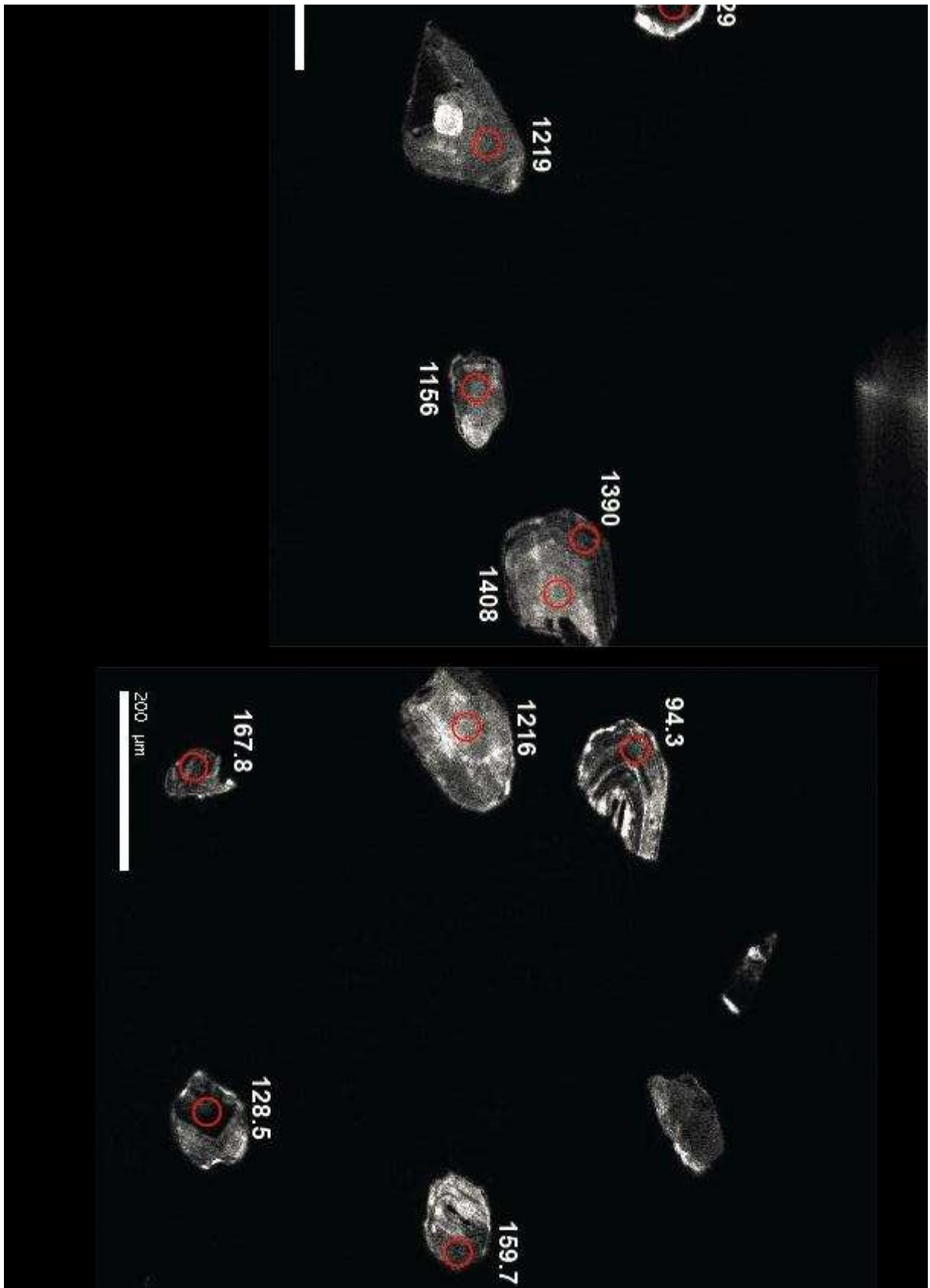
# Appendix 9: CL Imagery of zircons from Orocopia Schist

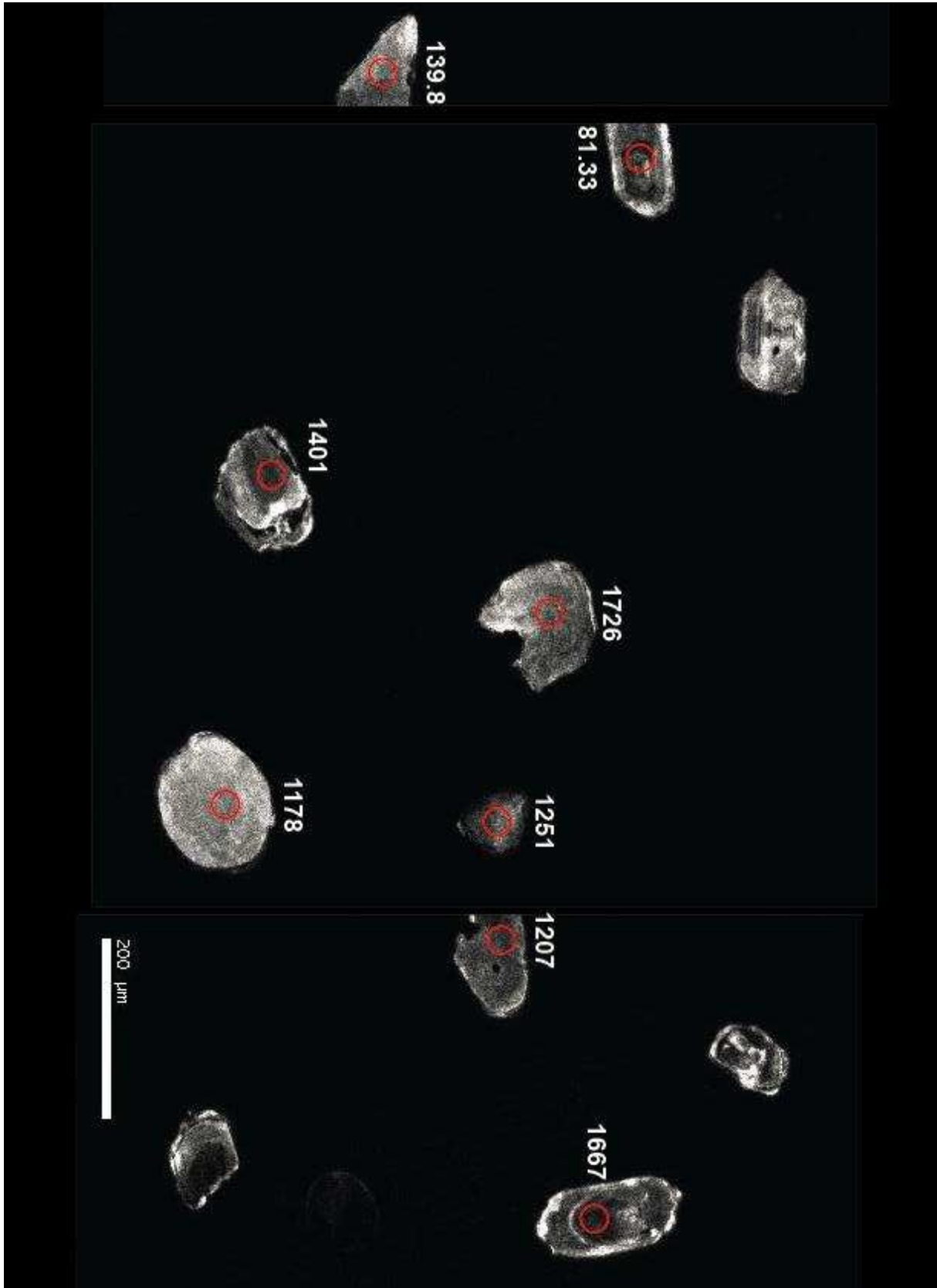
Sample 15-5-P9



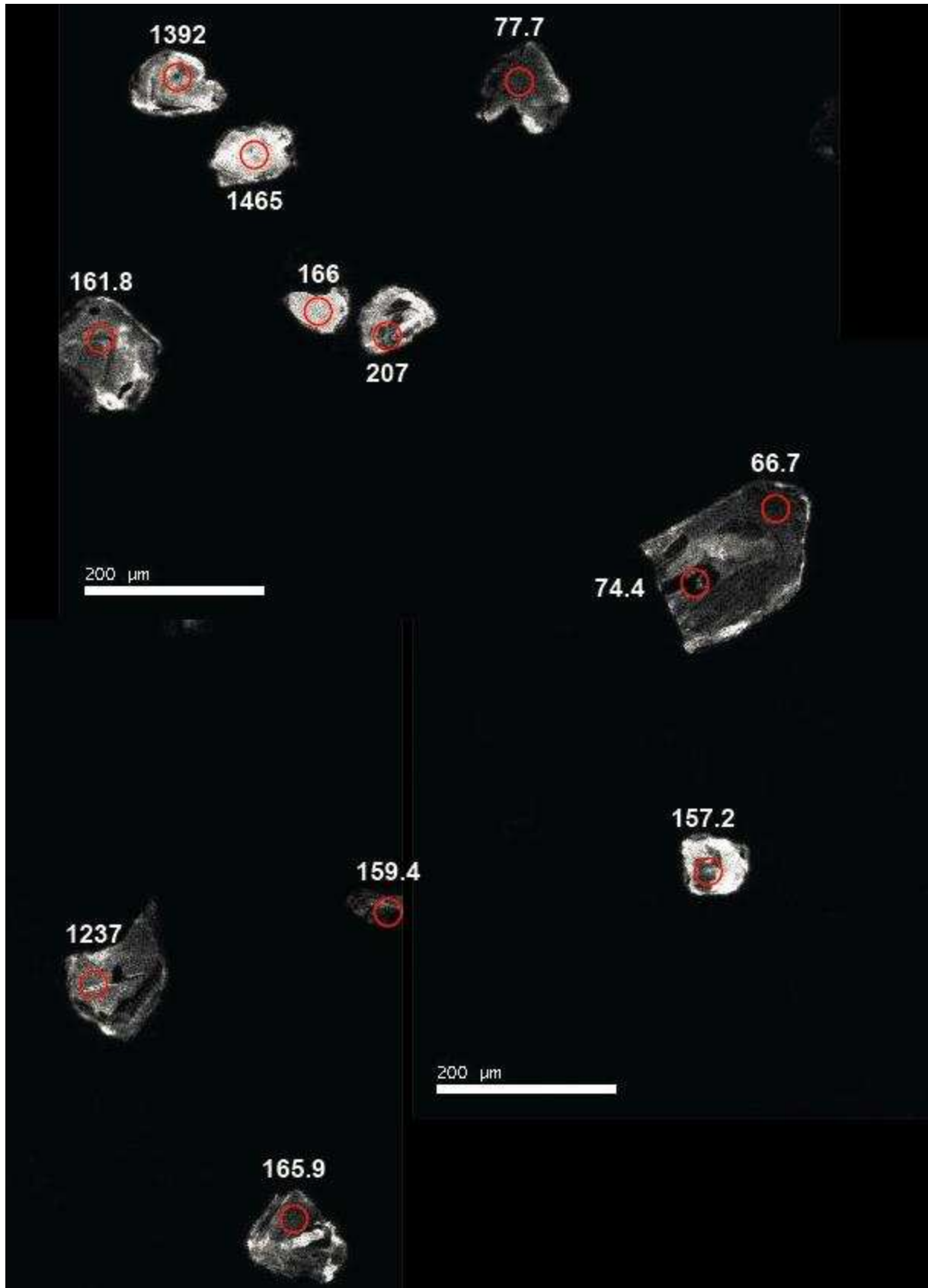


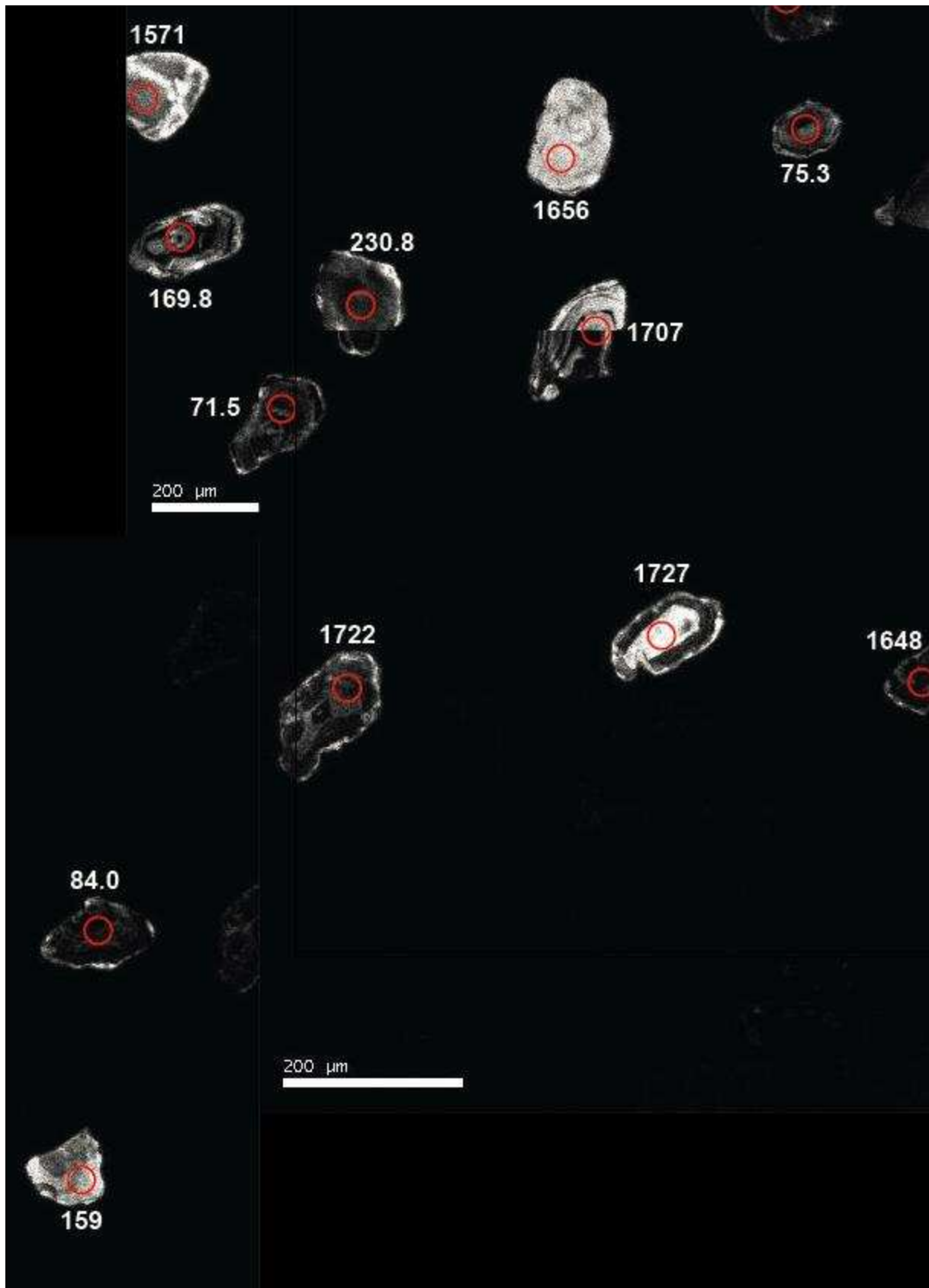


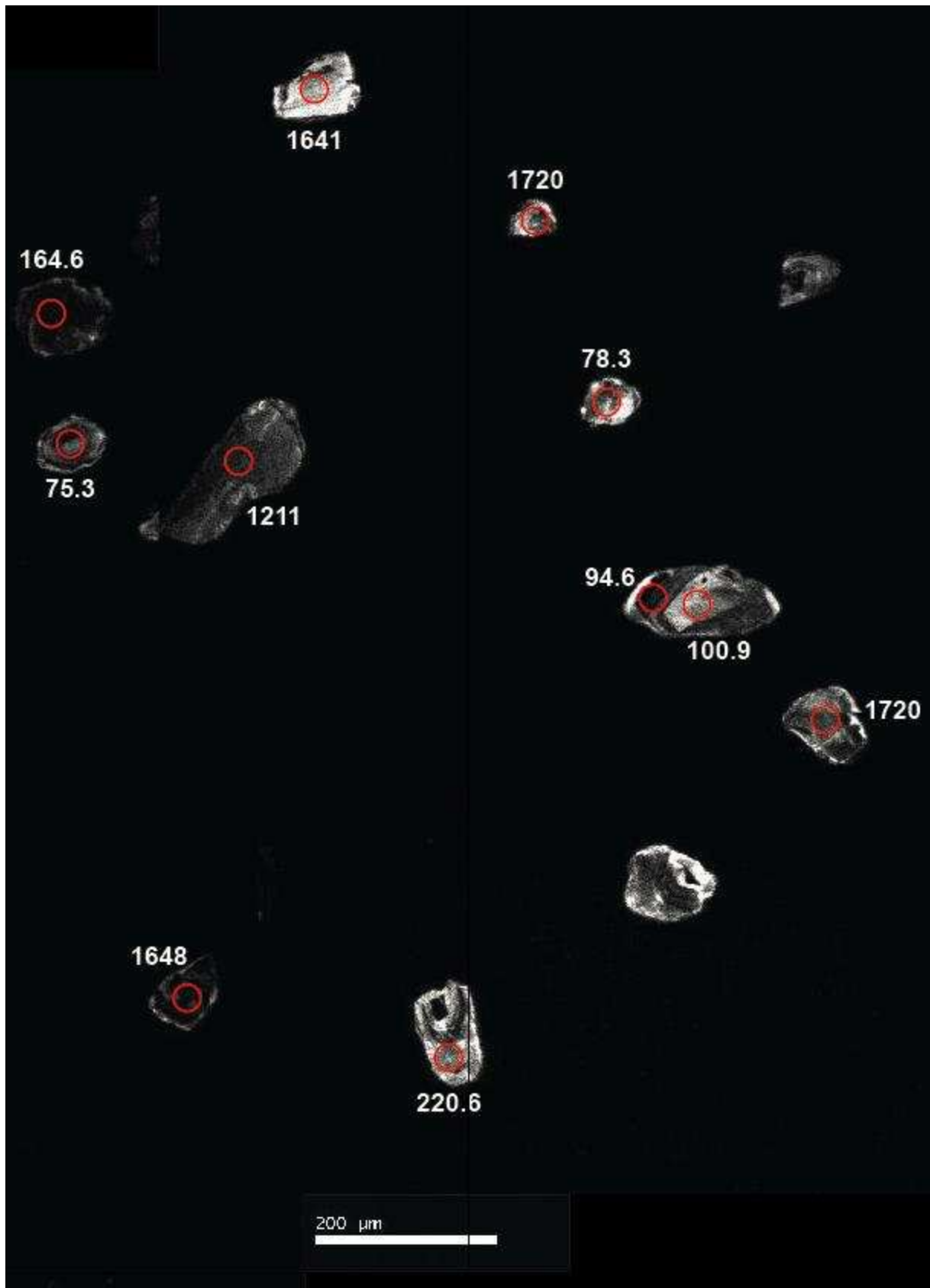


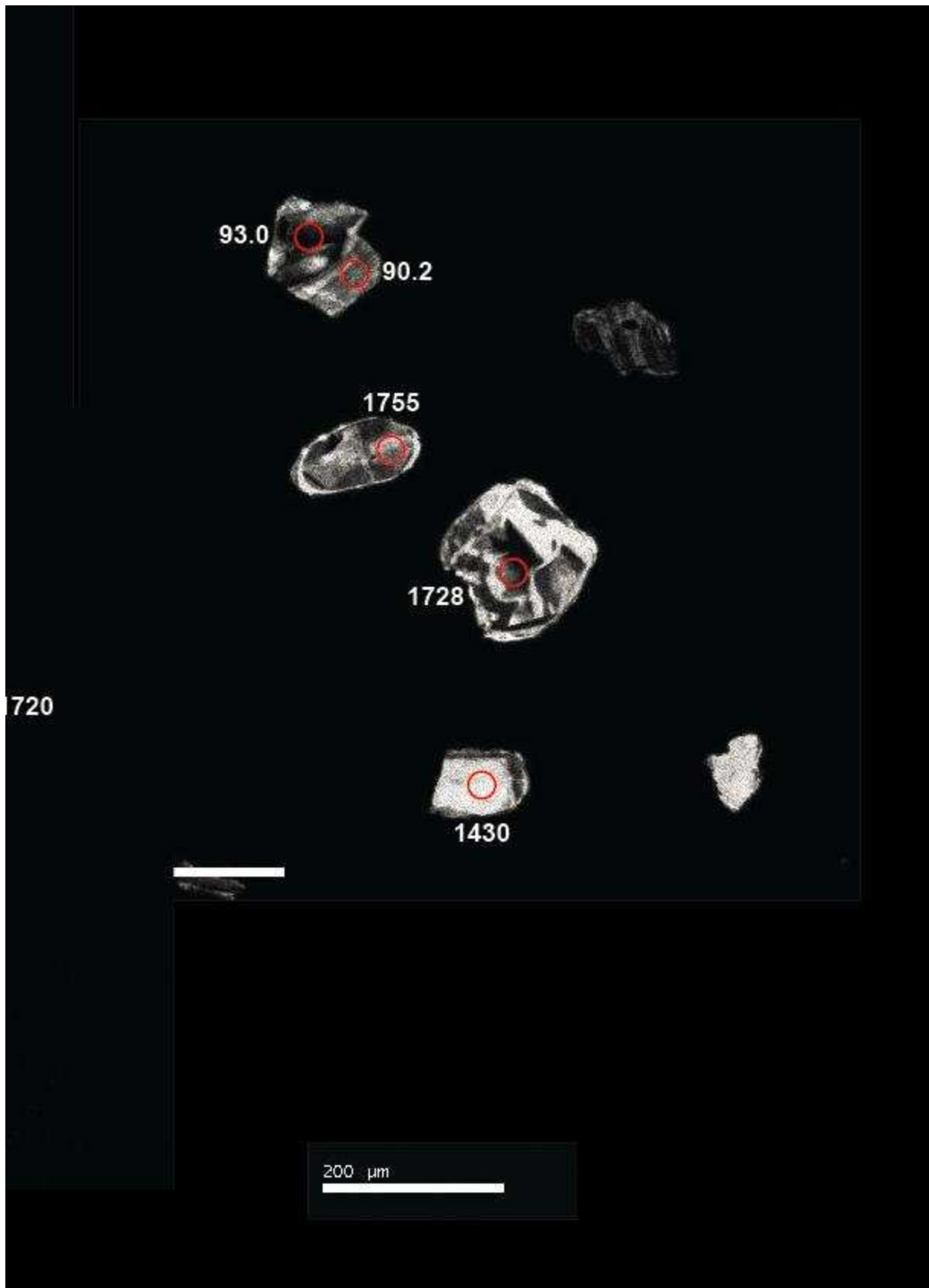




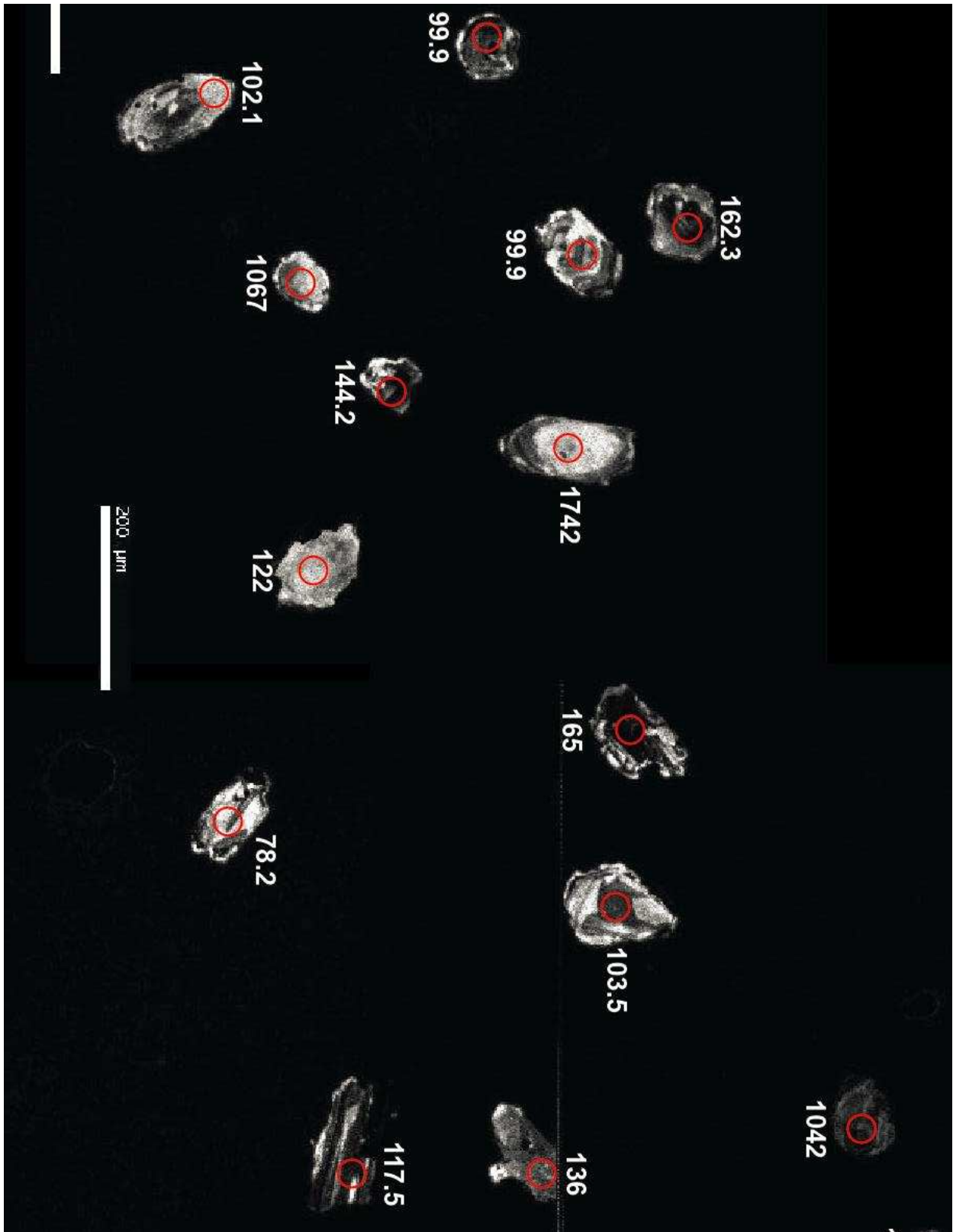


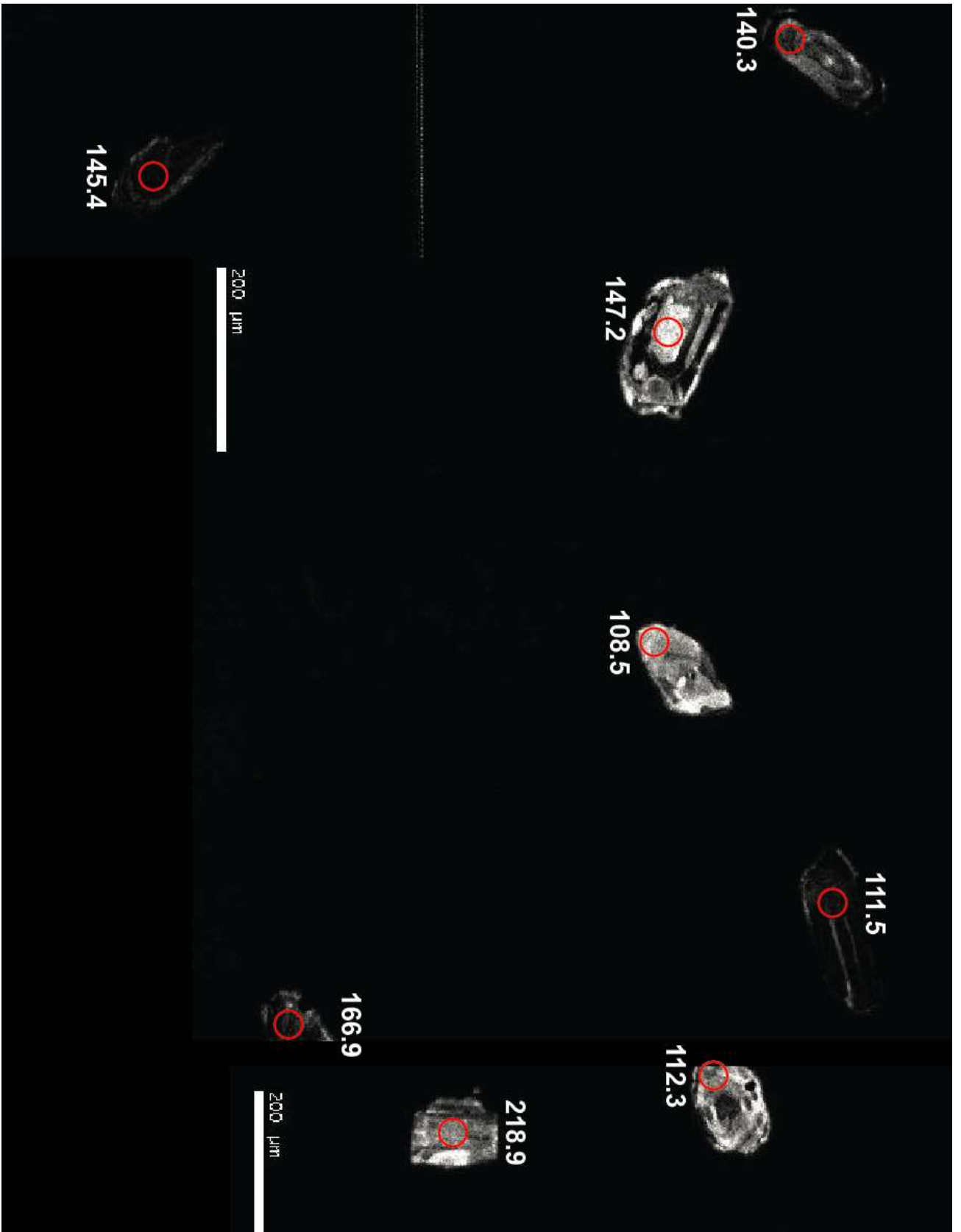


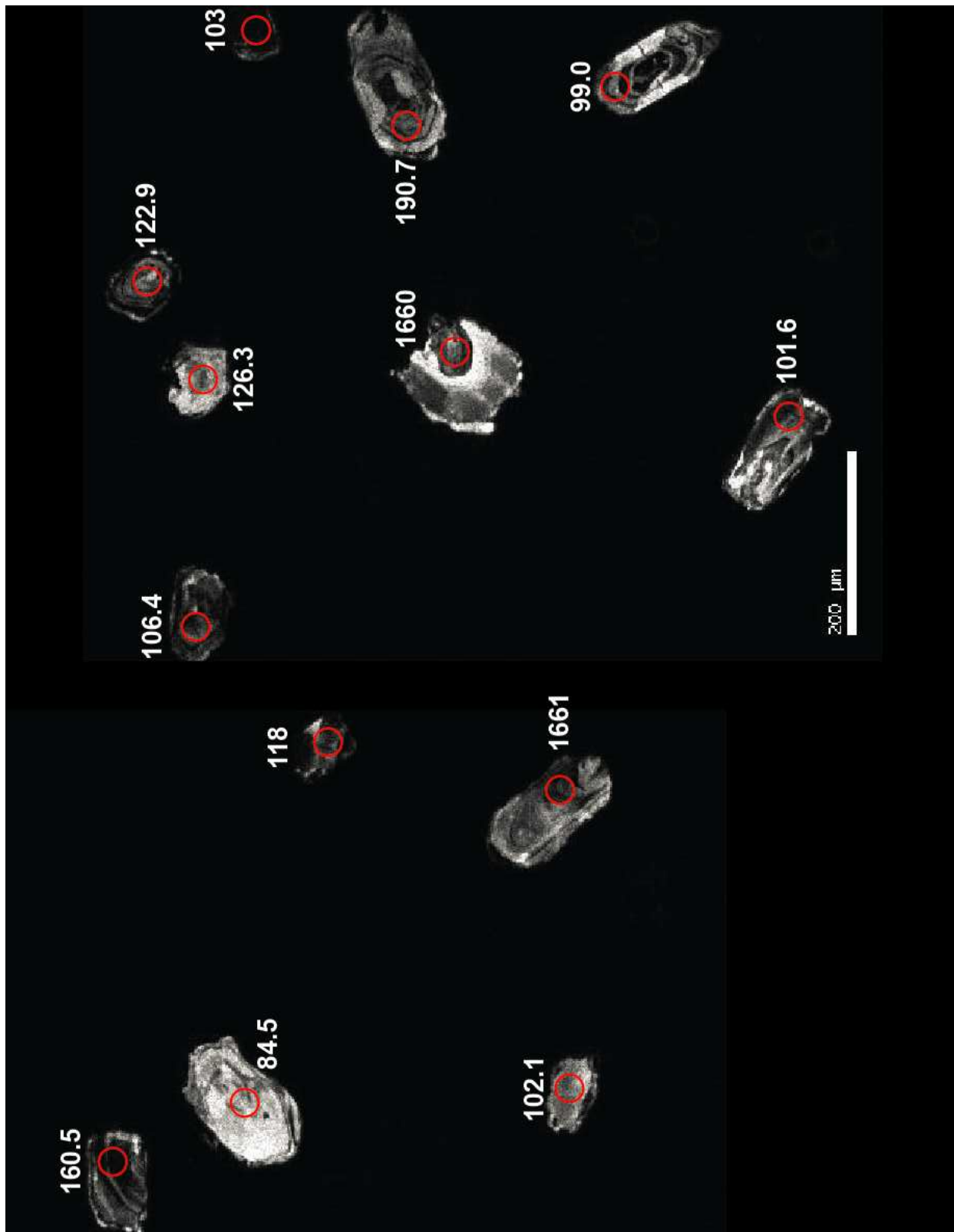


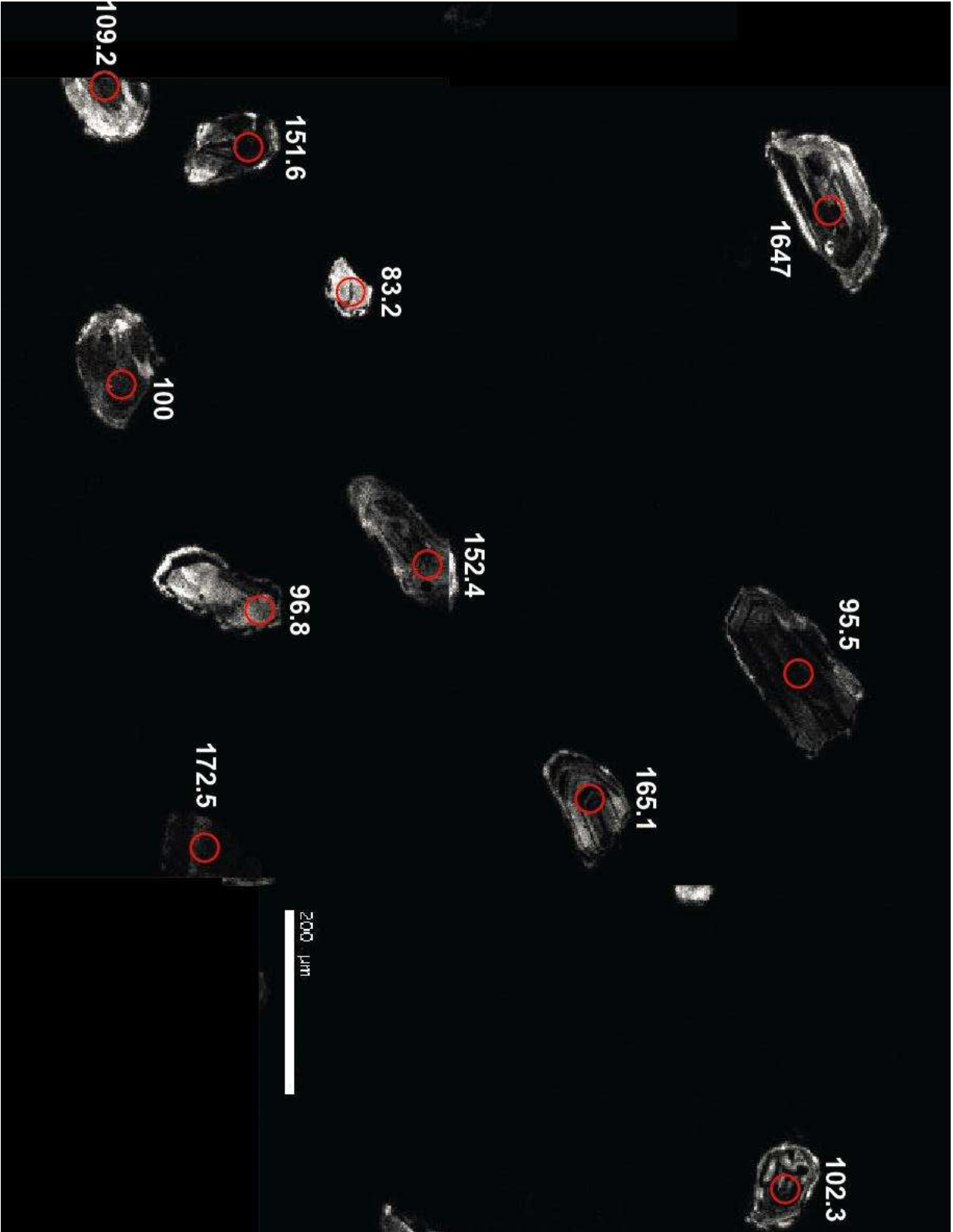


Sample 1015-P57

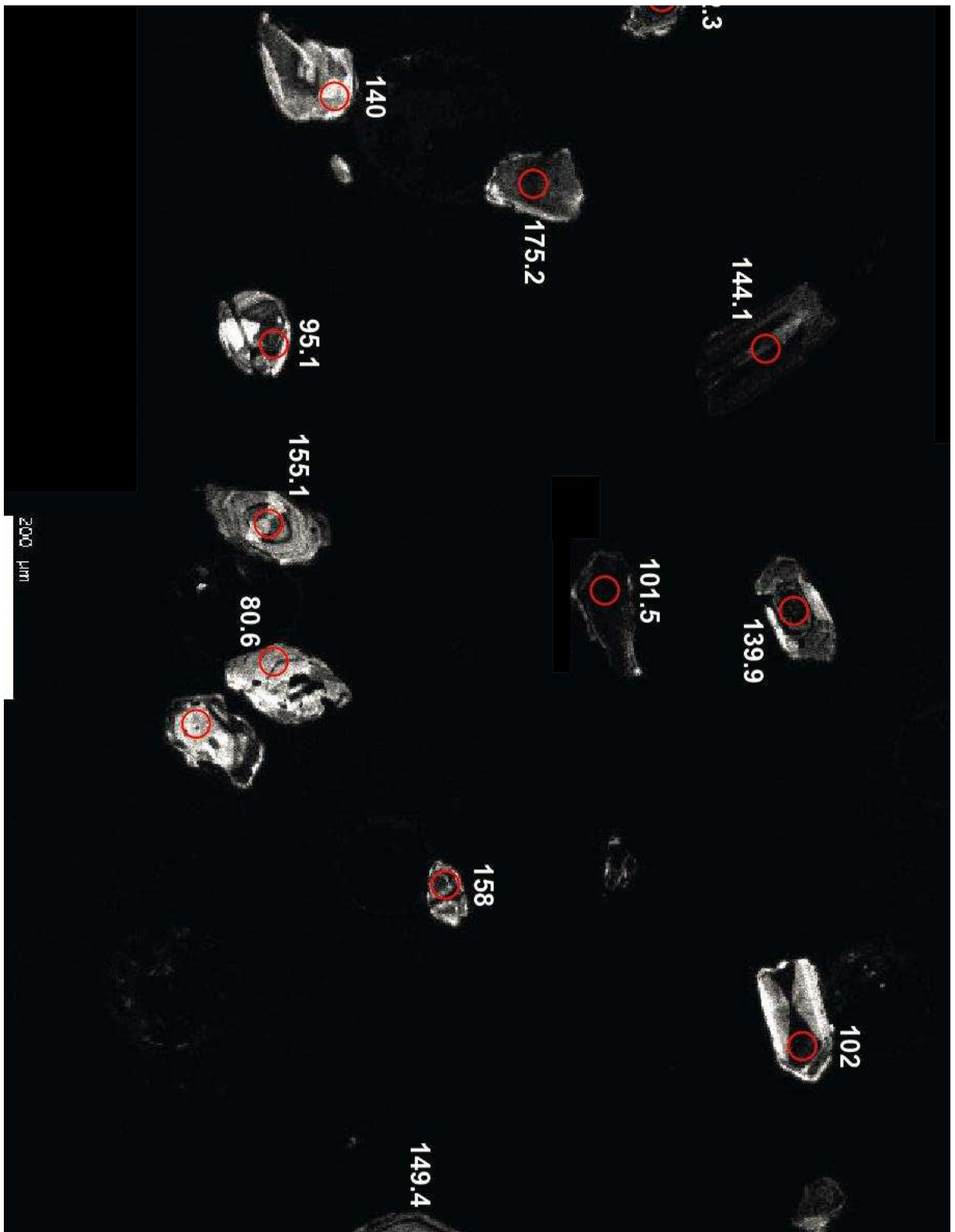


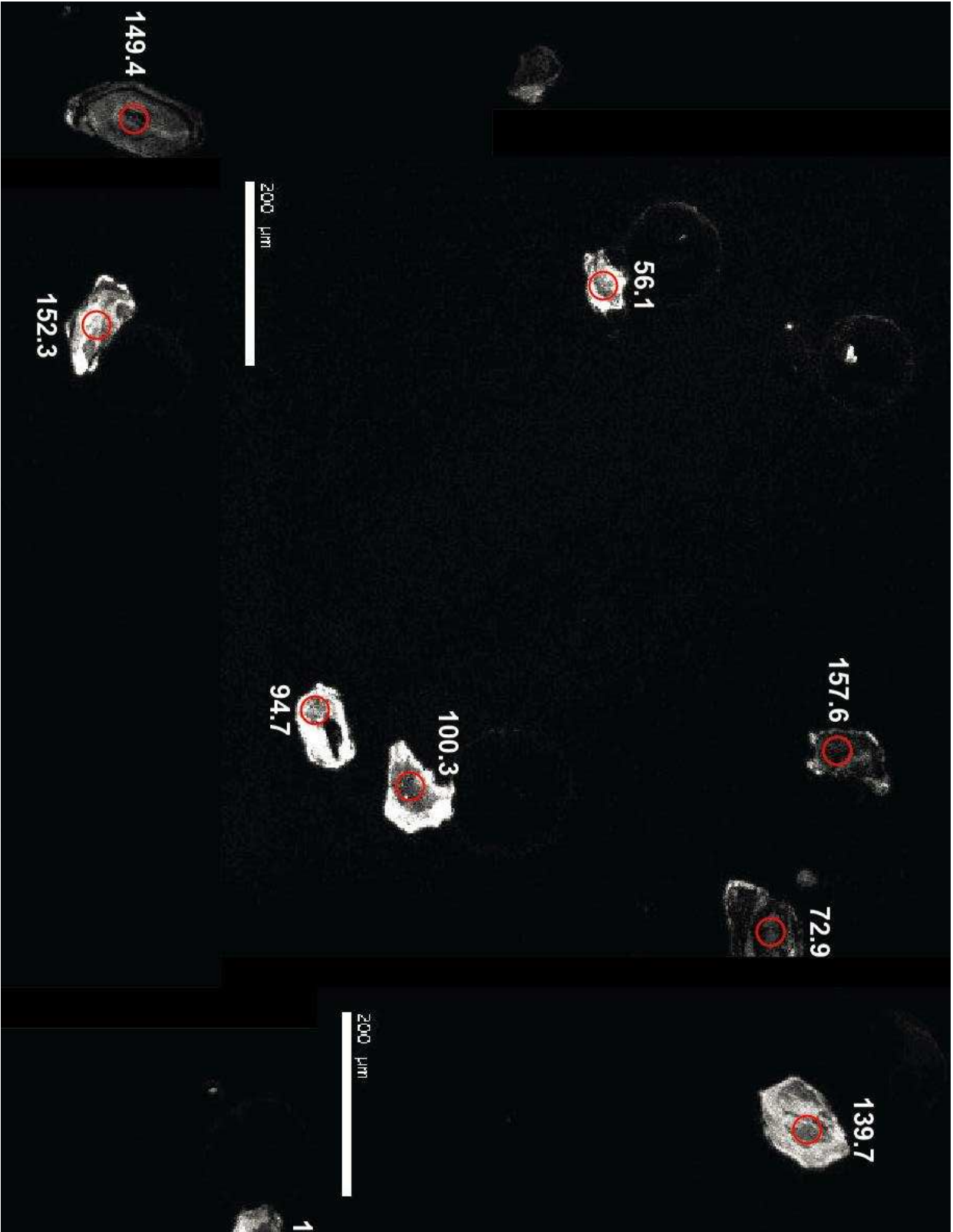




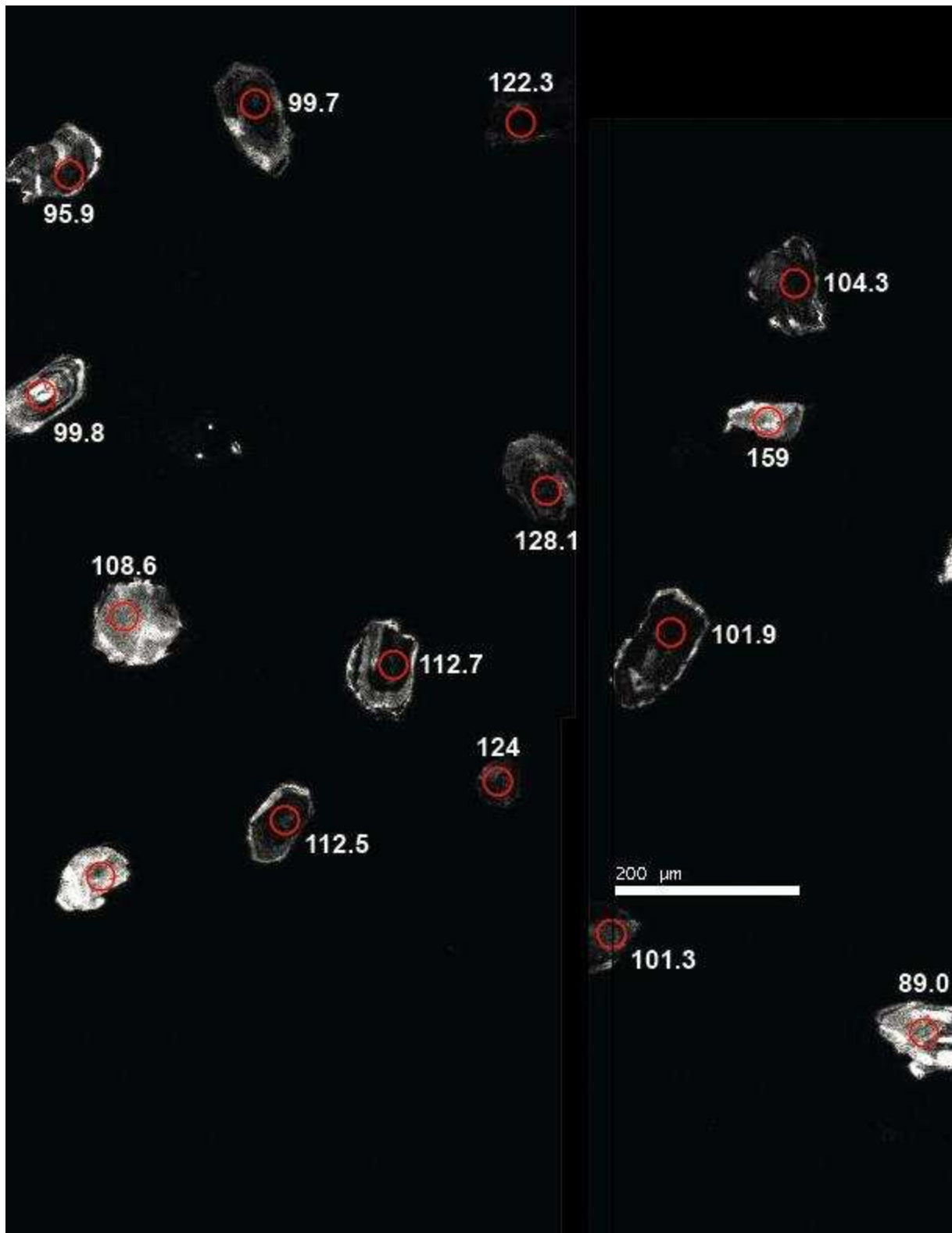


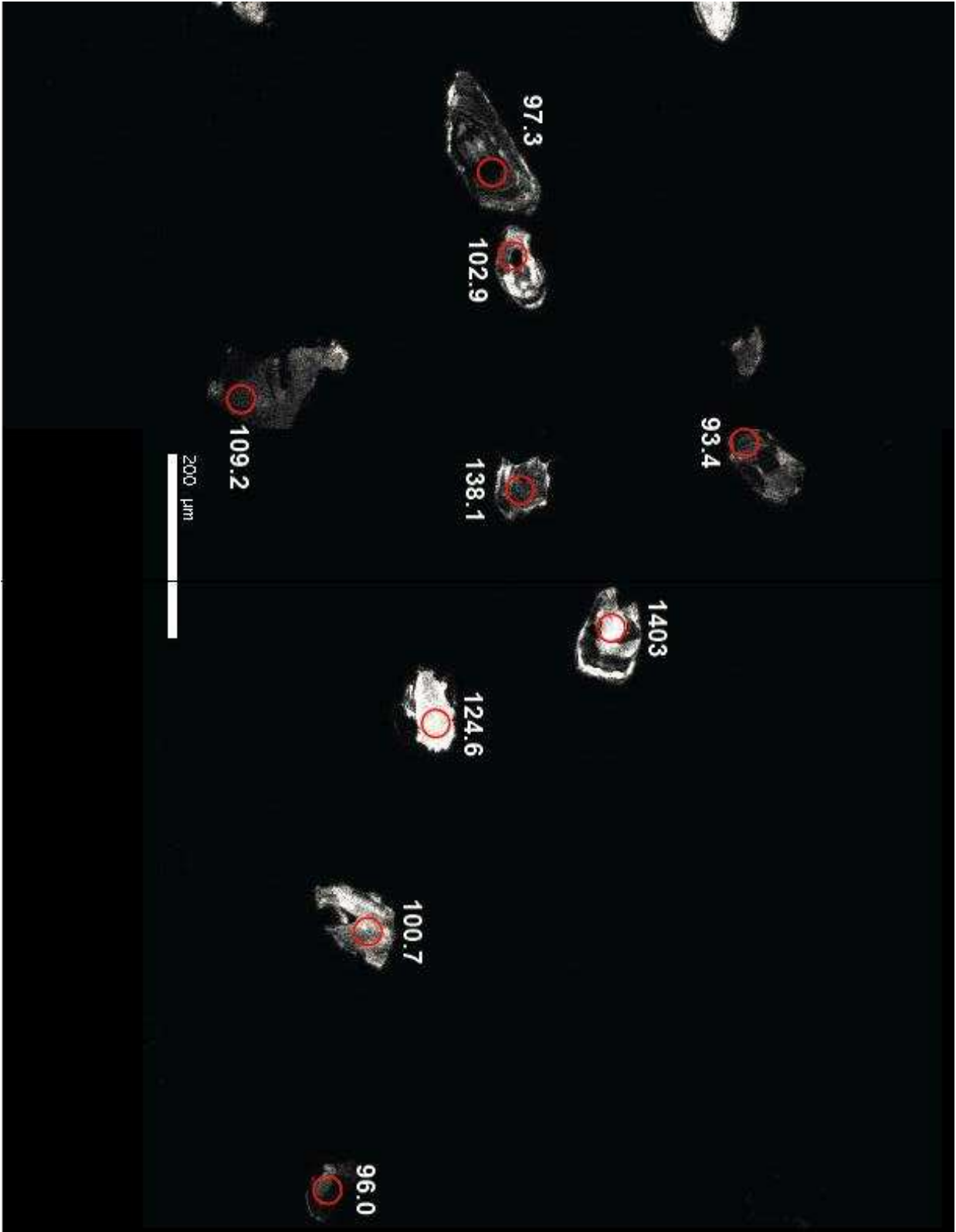




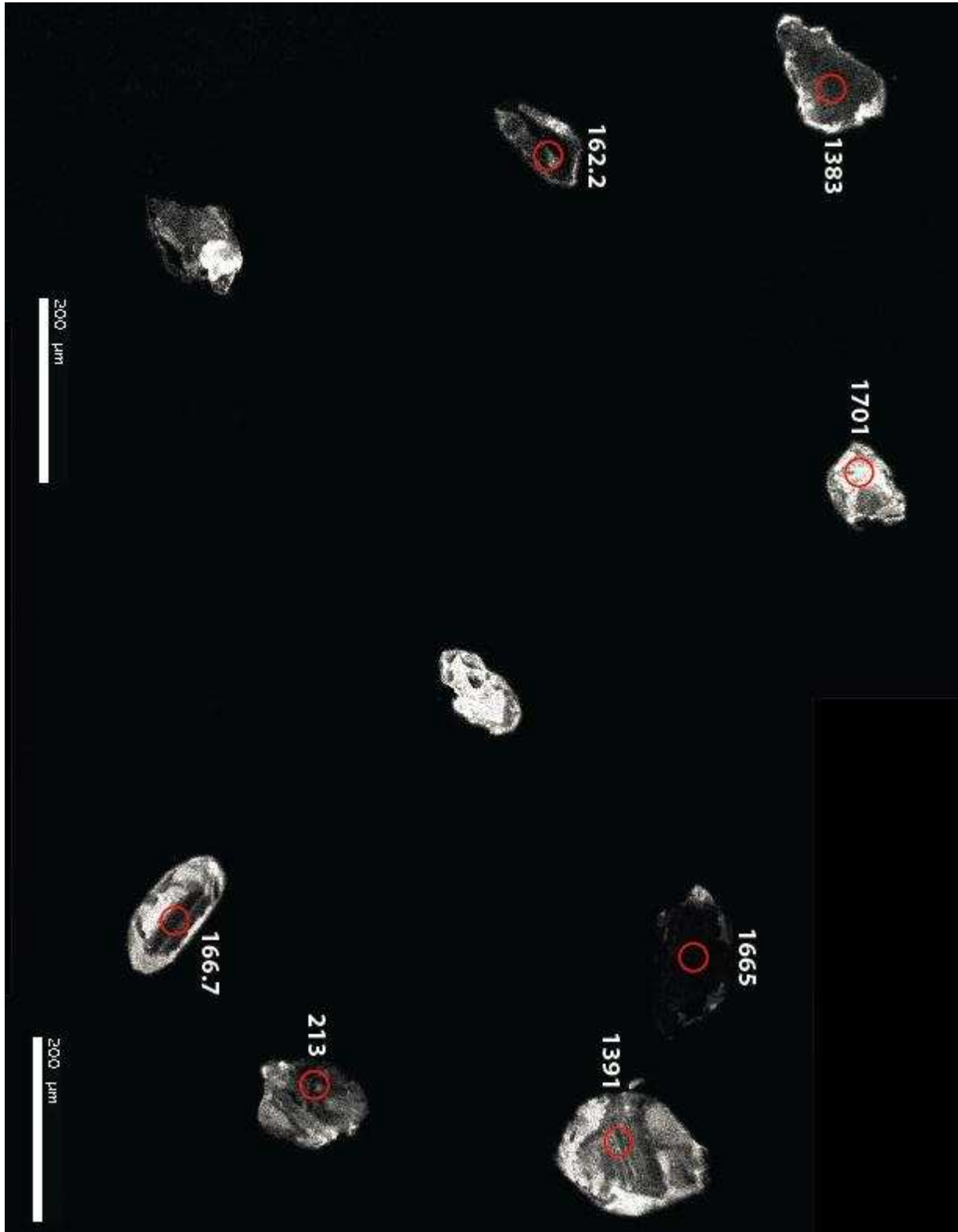


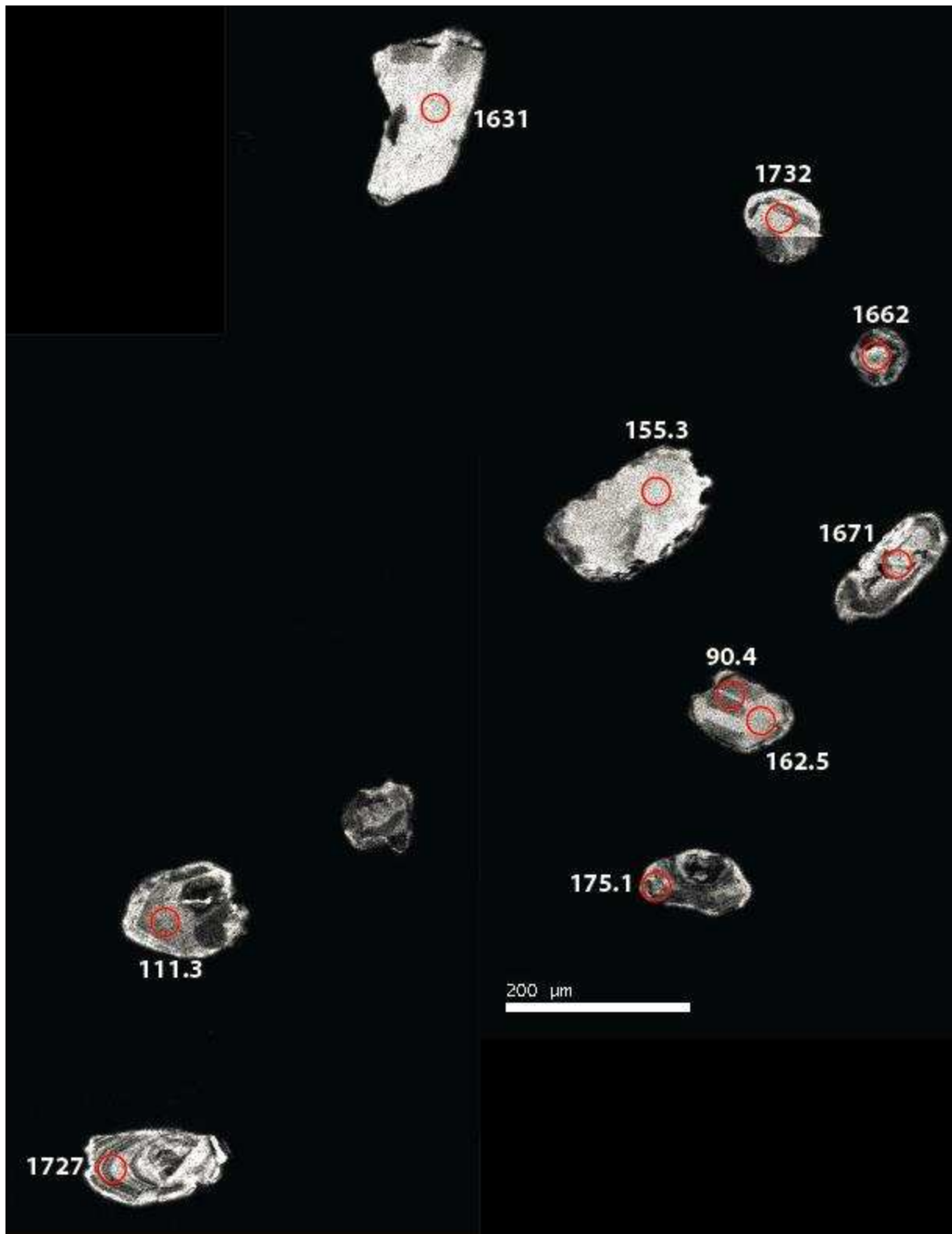


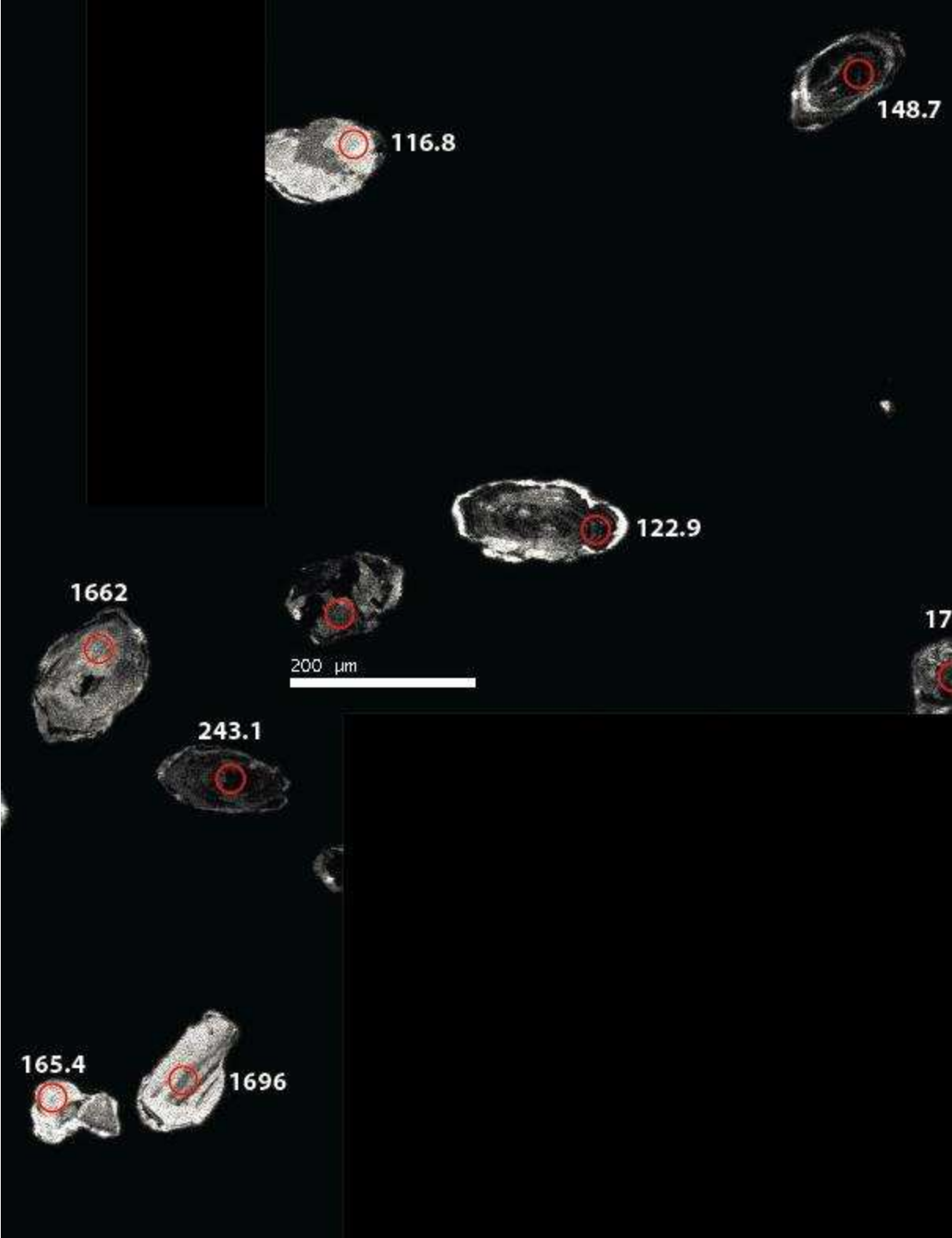




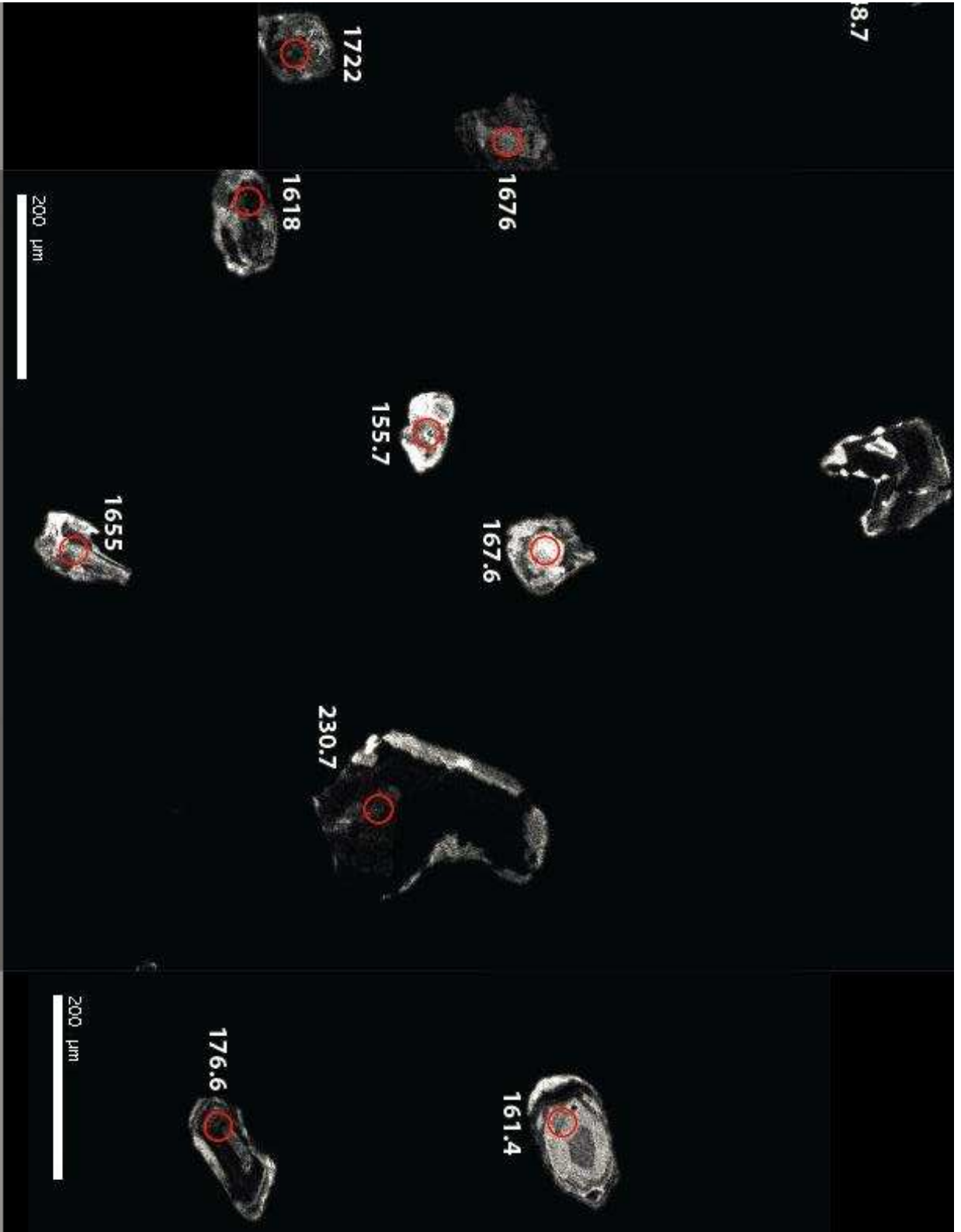
Sample 0316-P80a



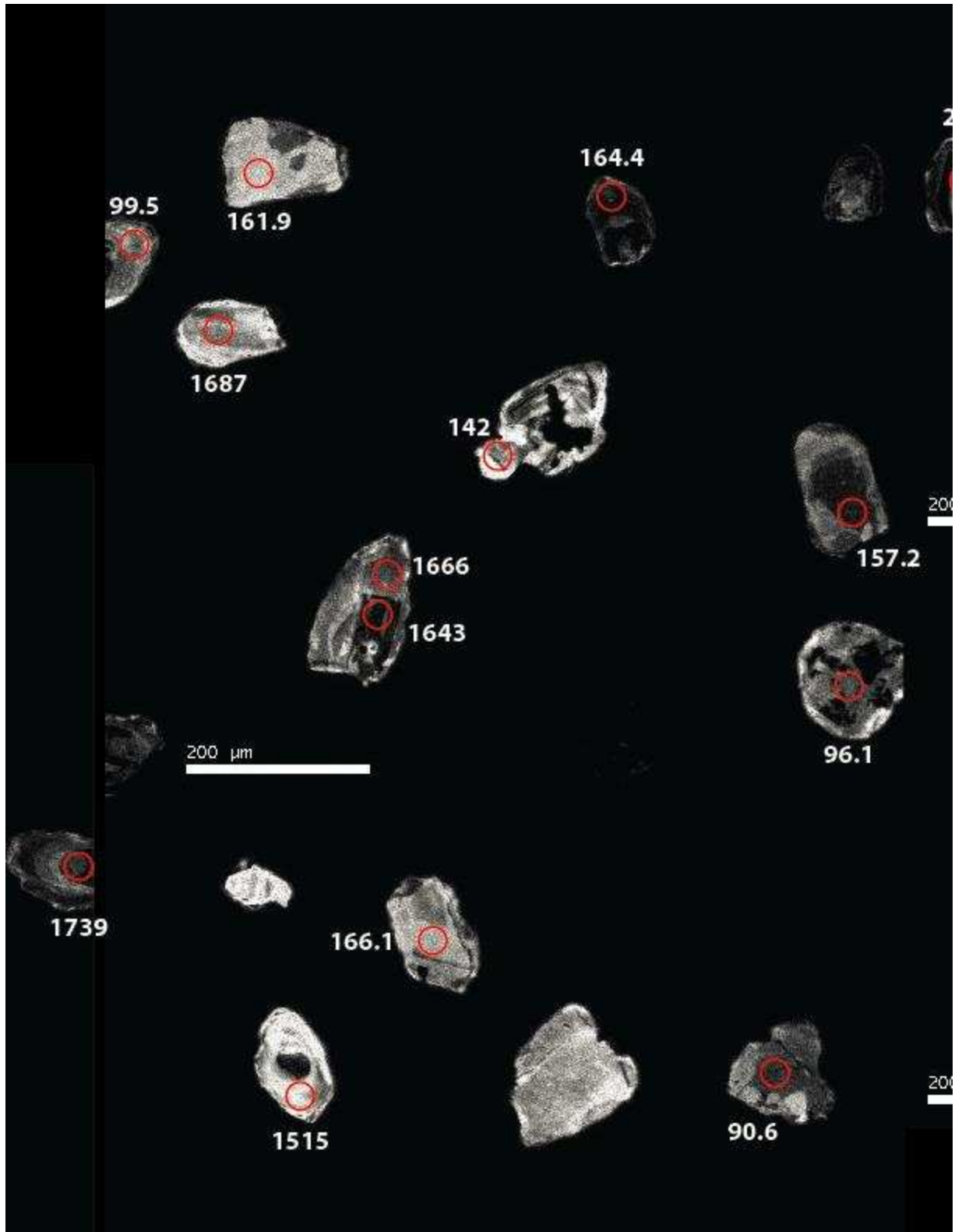


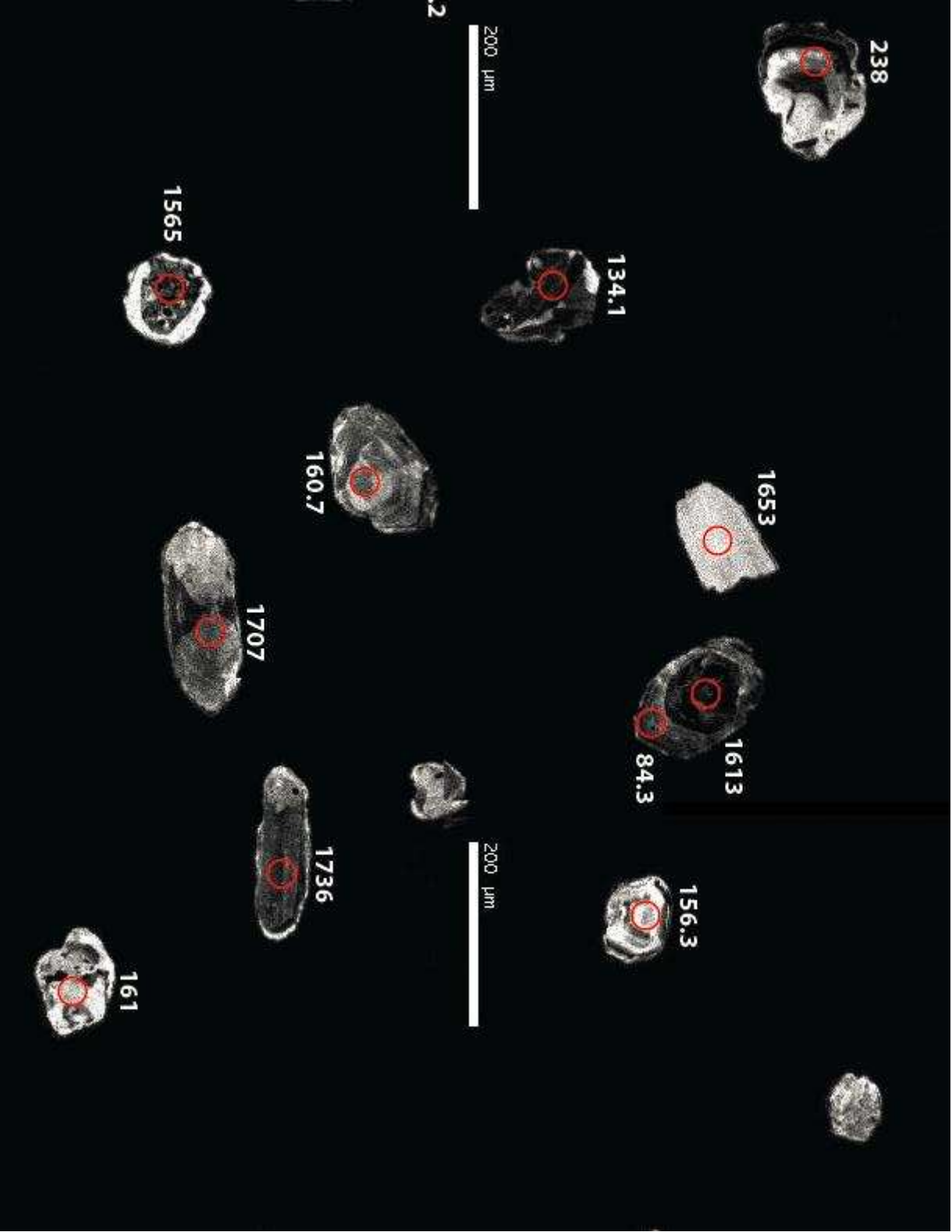


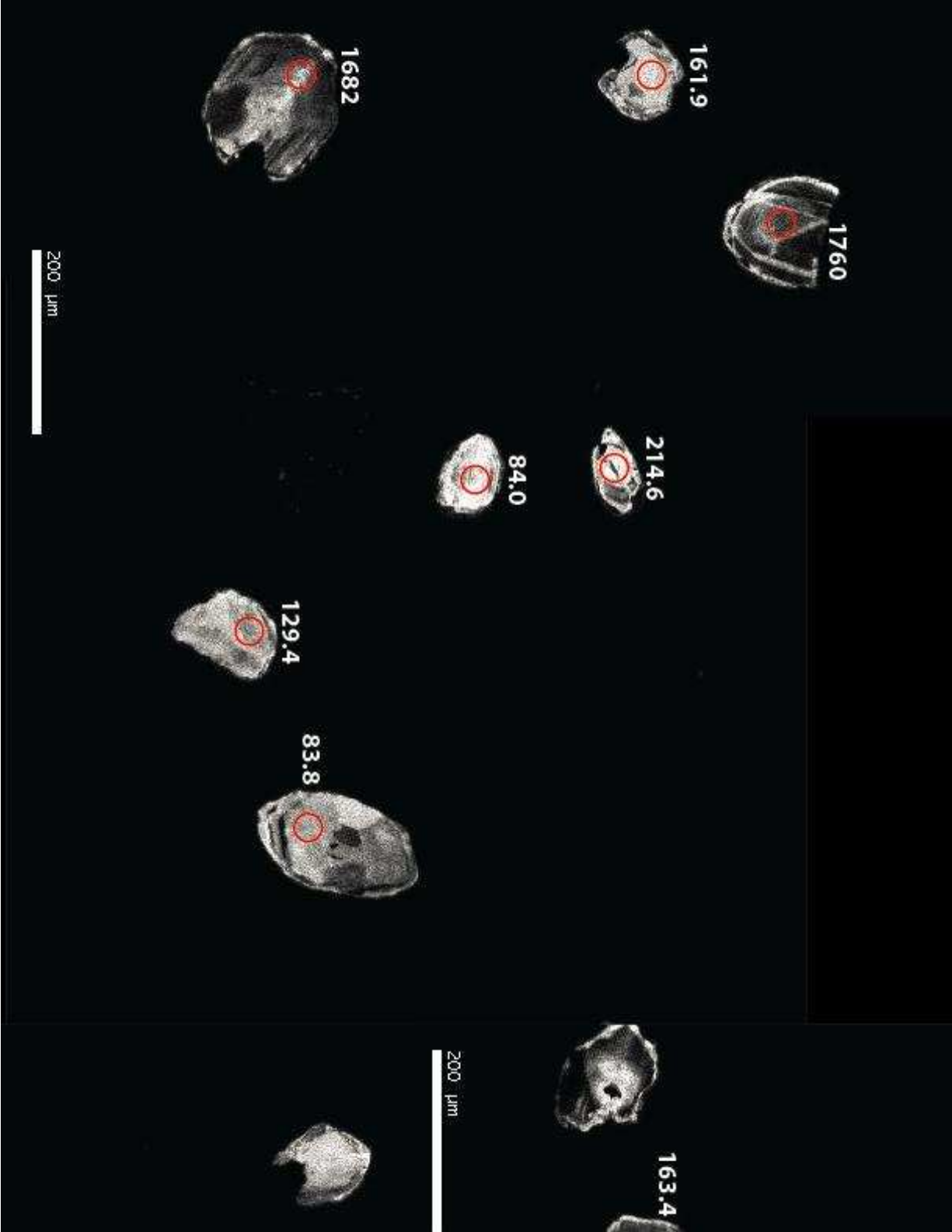


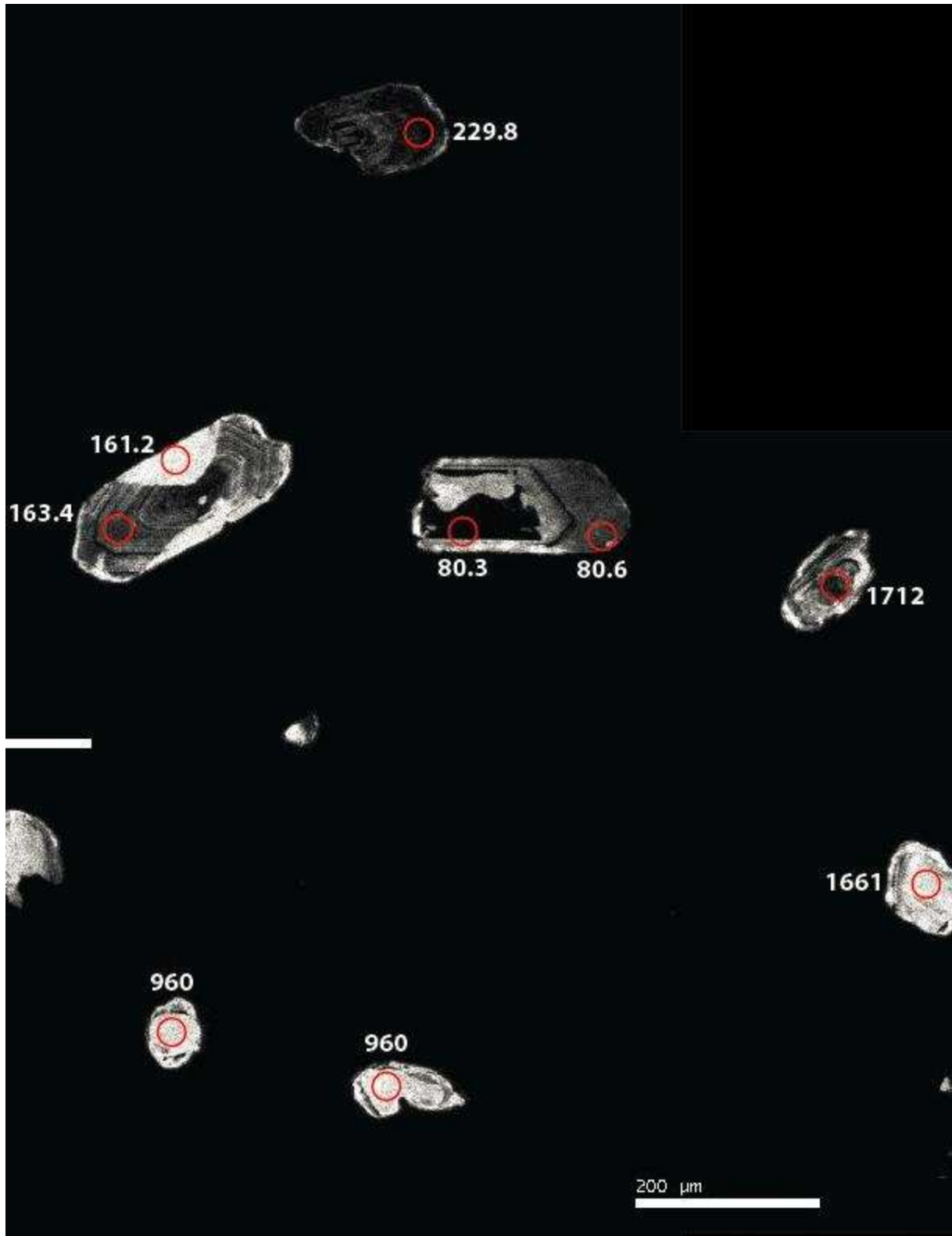


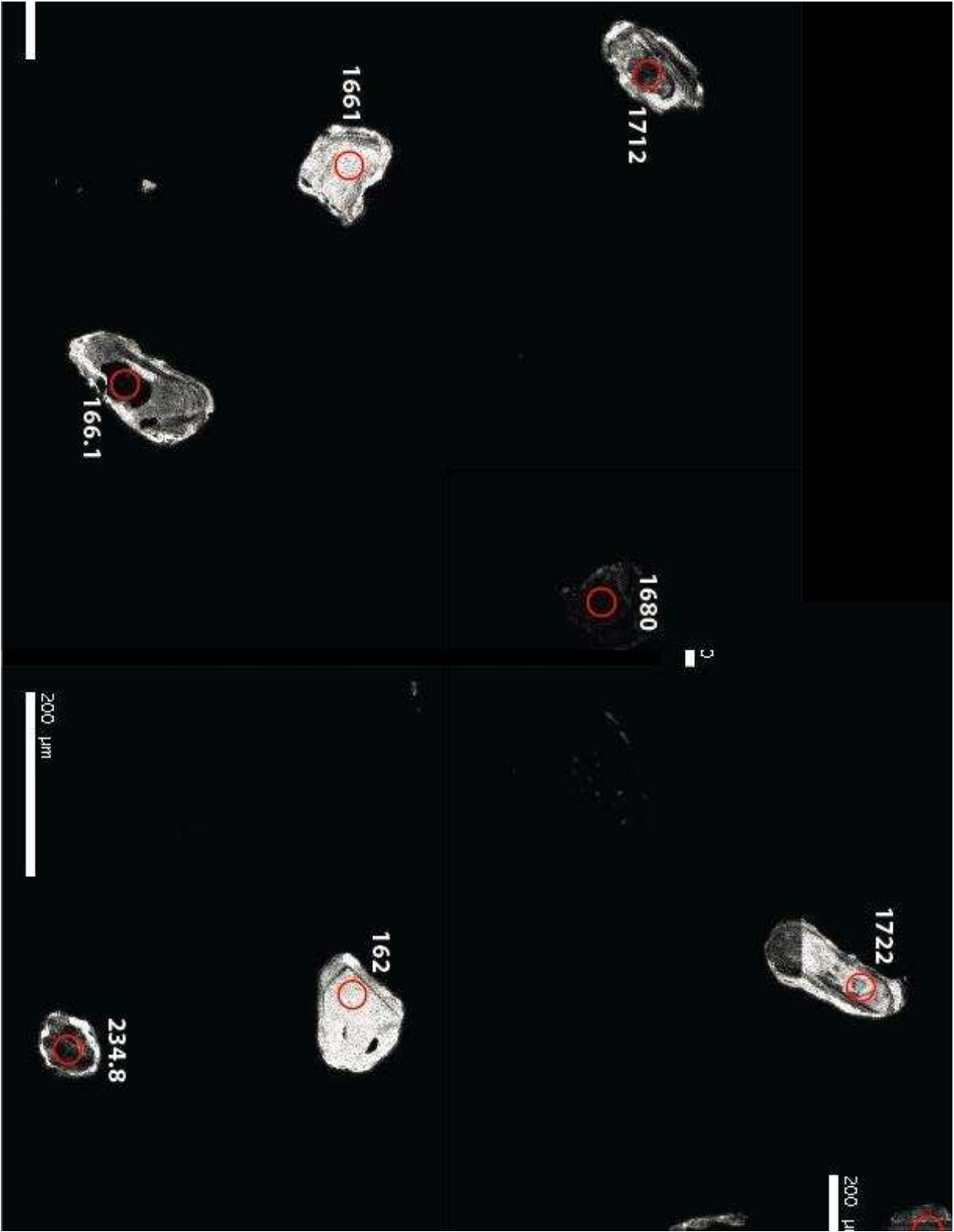


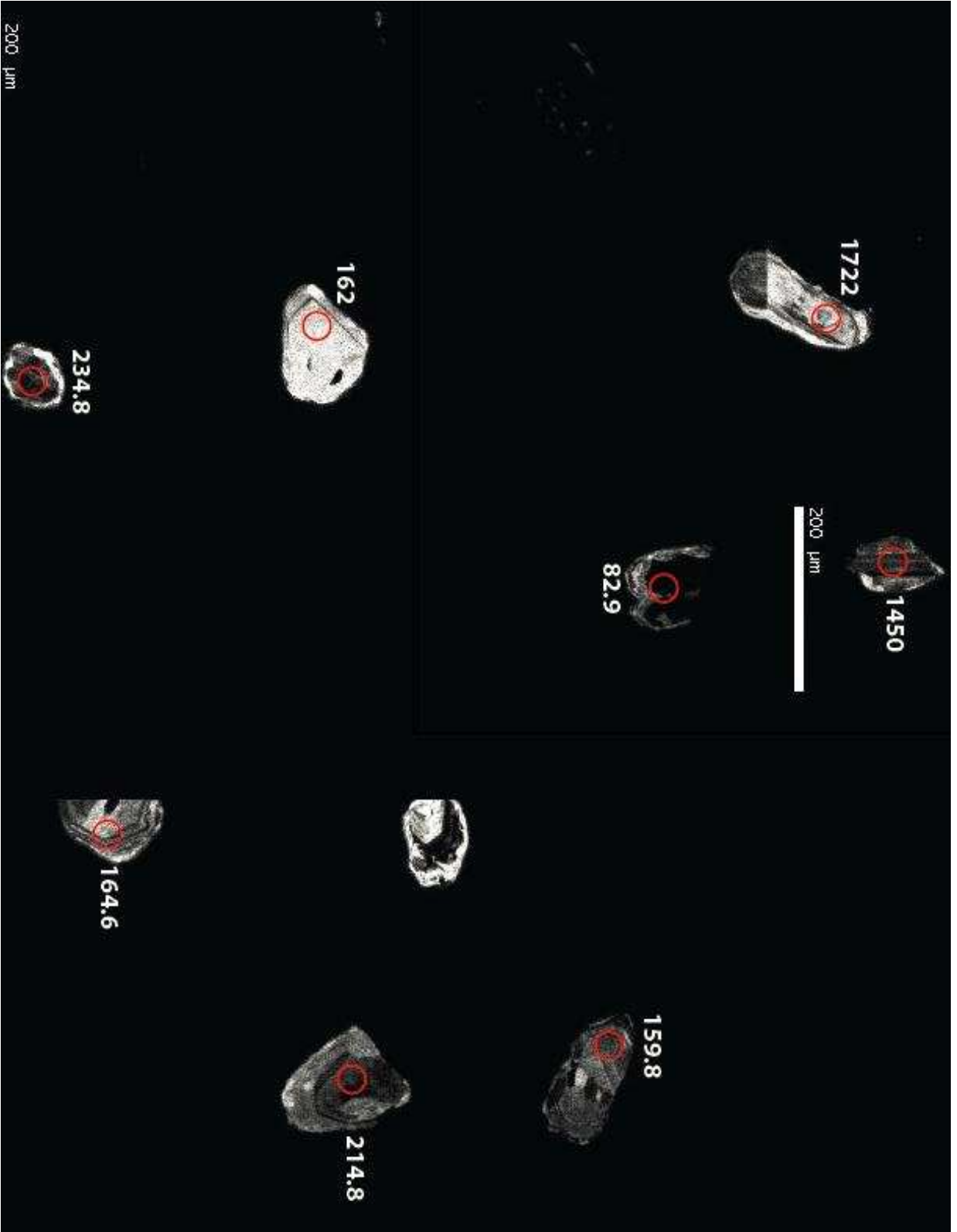




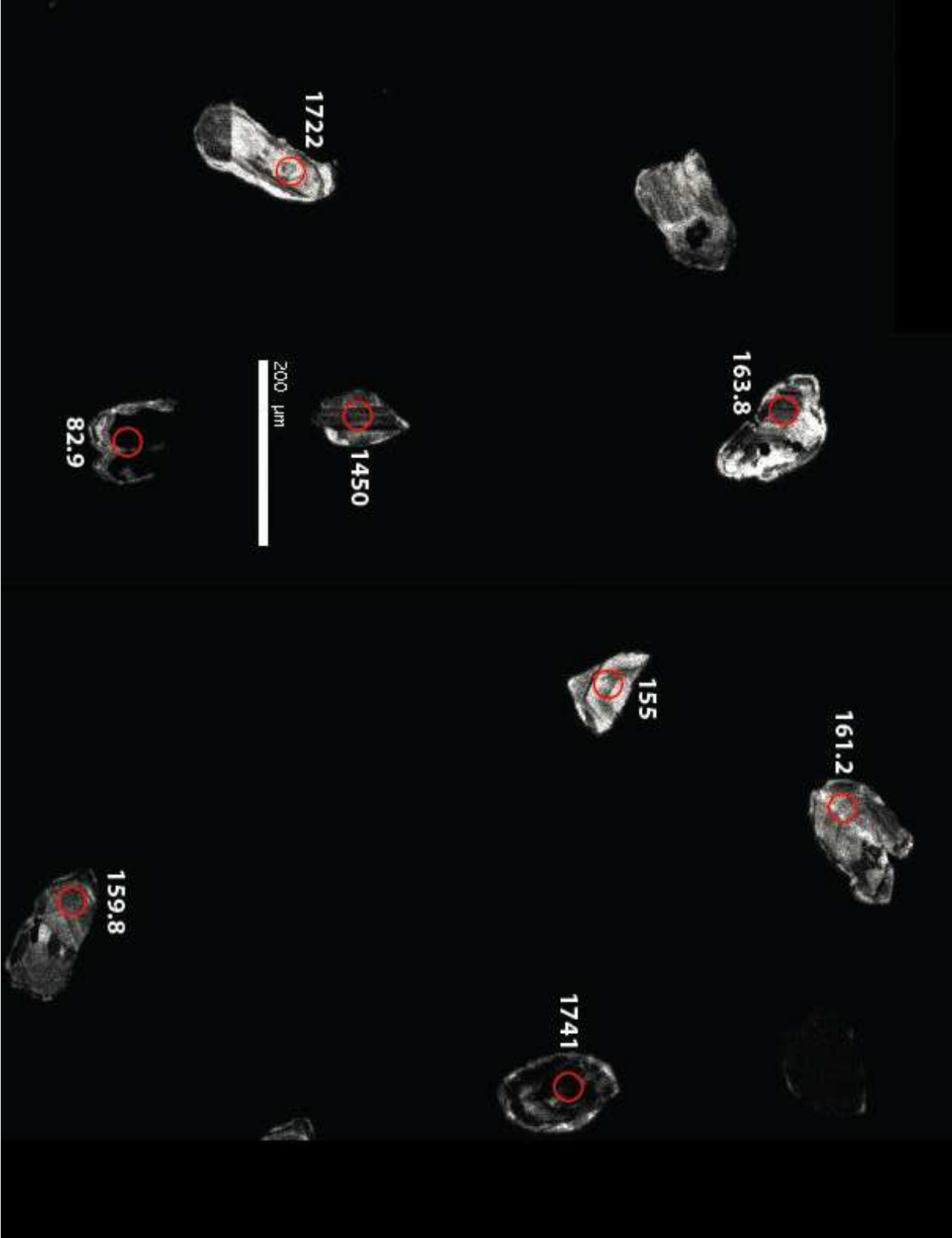






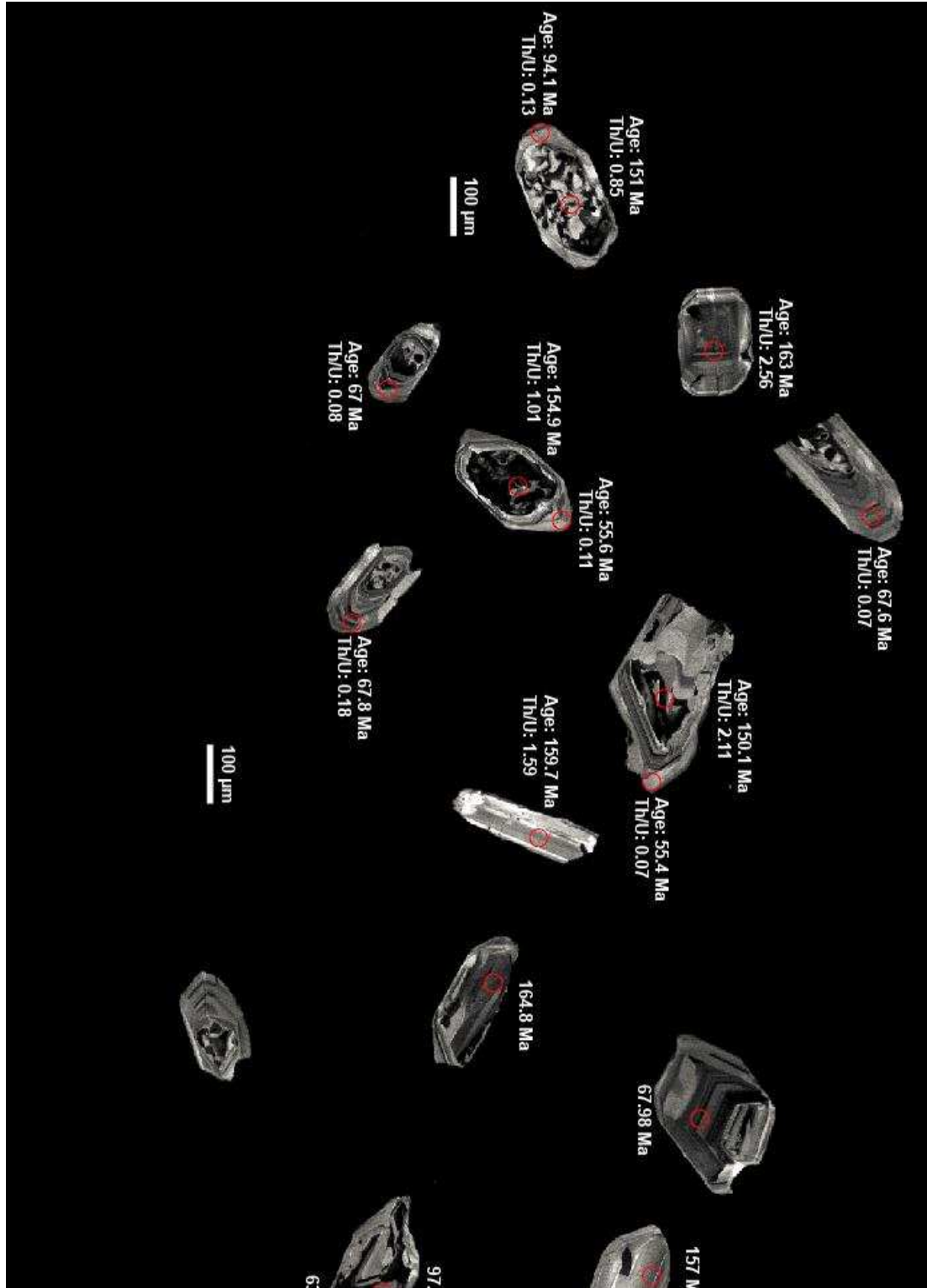


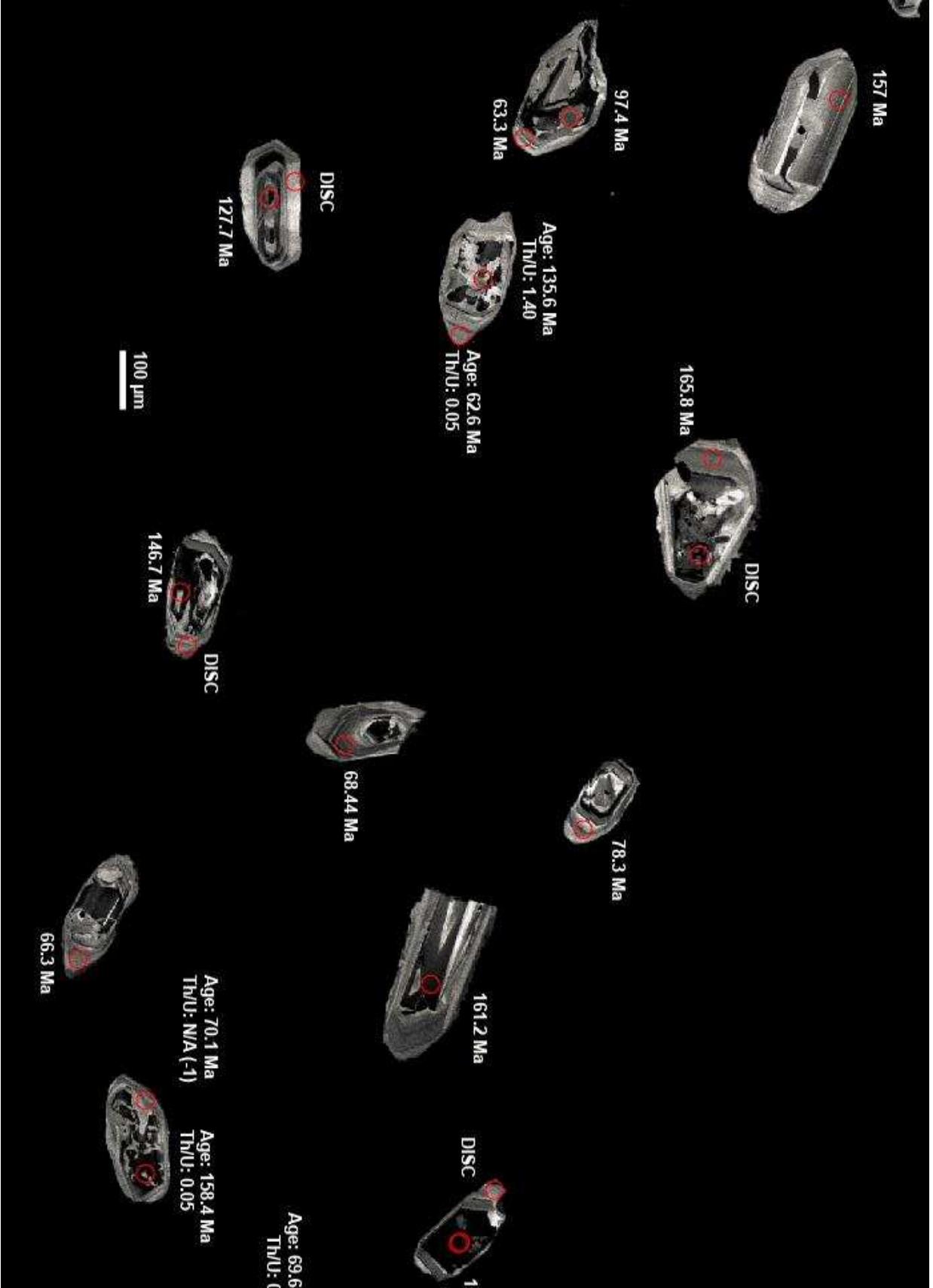


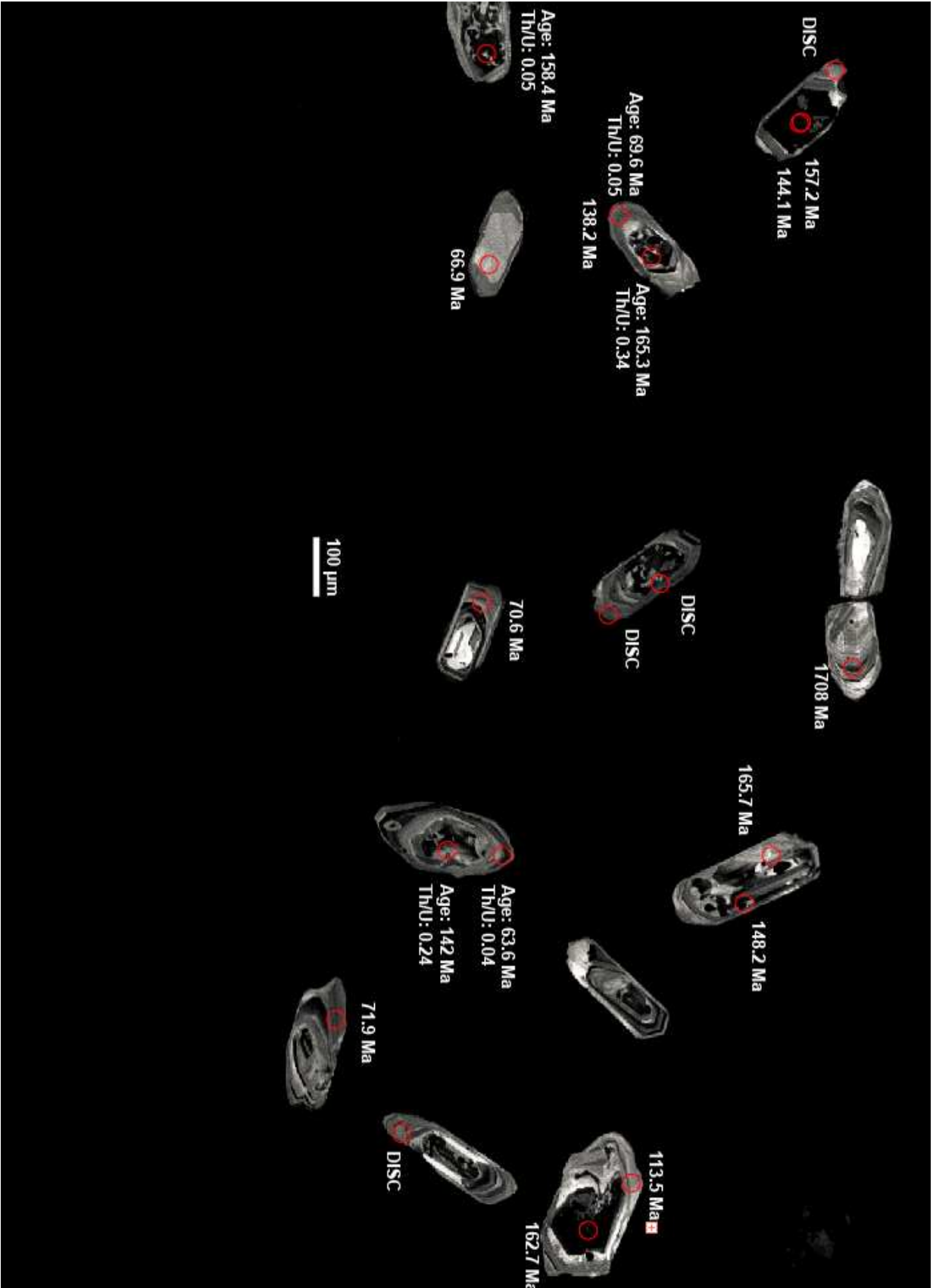


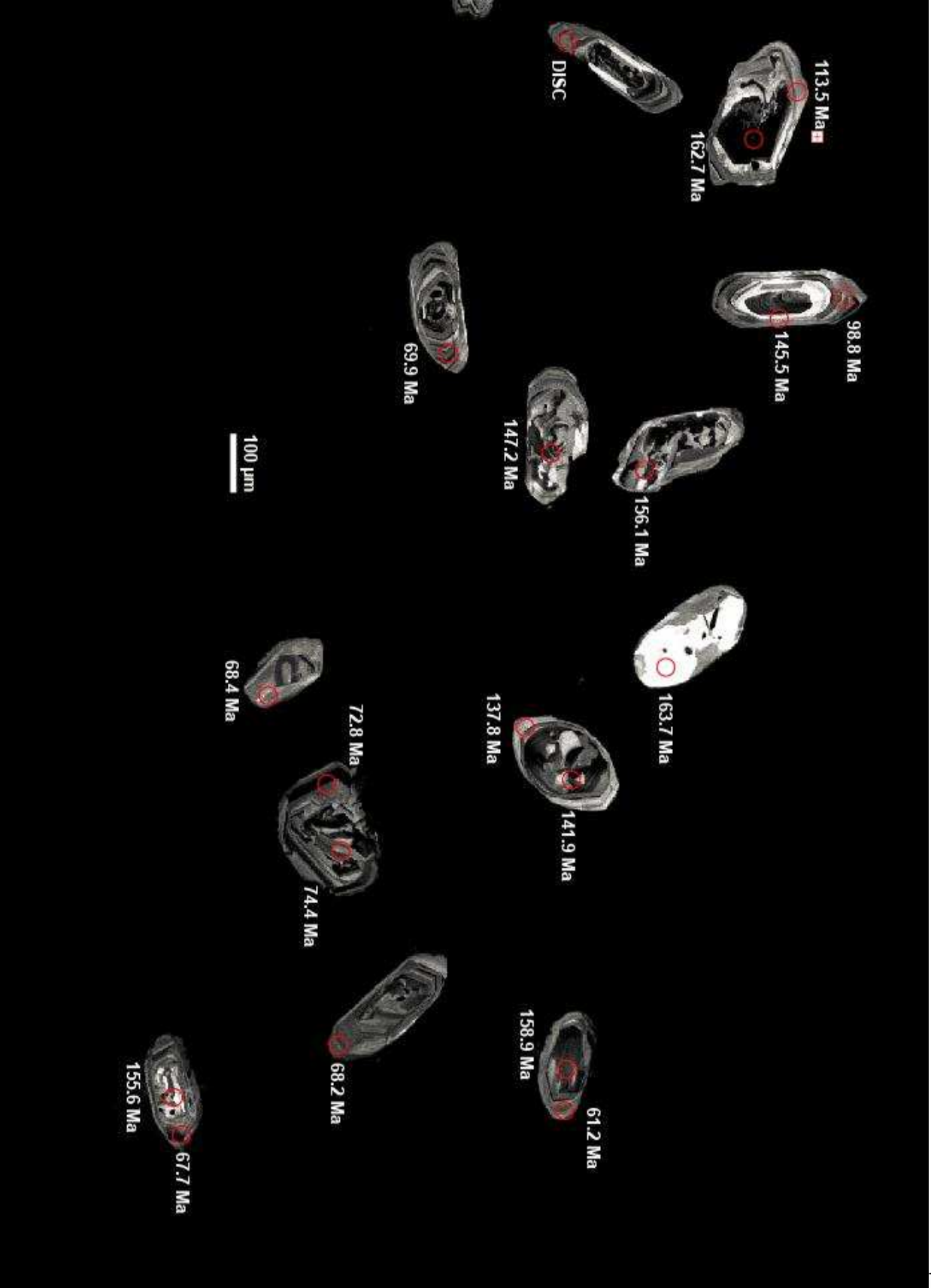
# Appendix 10: CL Imagery of zircons from Igneous Intrusions

## Sample 0217-P43









Sample 0217-P47

